ON THE INVERSE IDENTIFICATION PROBLEM IN A THREE-DIMENSIONAL LAYER

PHD THESIS

By
Alejandro E. Martínez Castro
Civil Engineer

Advisor
Rafael Gallego Sevilla

Departament of Structural Mechanics and Hydraulic Engineering ,
University of Granada
Edificio Politécnico Fuentenueva, C/ Severo Ochoa s/n, CP 18002
Granada (España)

March 2011

Editor: Editorial de la Universidad de Granada
Autor: Alejandro E. Martínez Castro
D.L.: GR 770-2012
ISBN: 978-84-694-5755-9

This work has been done as a part of the doctoral program "Planificación, fiabilidad y riesgo en ingeniería civil" at the University of Granada. The work has been supervised by Prof. Dr. Rafael Gallego Sevilla. On this work I have included the resuls of my own work. Parts of this work have been published or submitted at international scientific journals. Also, the work has been presented at relevants international conferences in the context of boundary elements.

The work presented here includes a review of the state of the art, the development of an specific fundamental solution in time-harmonic elastodynamics for the layer, the development of singular elements to treat stress singularities at corners and edges, and the analysis of the identification inverse problem based on gradient techniques and an image method (topological derivative approach). It has not been declared as new work published previously, written, by different authors, nor material required to obtain academic degrees.

Alejandro E. Martínez Castro

Resume

At the engineering practice non destructive techniques are required in order to analyse the presence of deffects in materials. To obtain practical solutions, it is necessary to solve the so-called Inverse Identification Problem with numerical techniques. After it, the experimental tests will provide input data that permits the identification and inspection of specimens.

The focus of this work is the Inverse Identification Problem, stated at an important domain for the industry sector in practice: an infinite plate. An elastic, homogeneous and isotropic material is considered, and a three dimensional infinite domain, limited between two parallel planes defines the layer domain. Inside of this plate there exists defects, in form of ellipsoid cavities. In order to identify such cavities, an elastodynamic problem is stated: at an accesible part of the boundary, a set of excitation points are defined; at different locations, a set of measurement points are fixed. The misfit between the experimental and the measured data for a parametrized given location of the cavity generates a cost function. Such cost function might be enriched with some kind of a-priori information, such as volume of deffects. The inverse problem is stated as an Optimization Problem. The Adjoint Variable Method is adopted in order to compute semi-analytic gradients required for BFGS algorithm. The forward problem is solved with a Boundary Element code based on the Regularized Boundary Integral Equation. An specific Green function has been developed in order to require a mesh only at the cavity boundary. A set of numerical tests have been carried out in order to test de dependence on some parameters of the optimization process: position of sources/receivers, random noise at measurement, material damping, number of parameters, etc.

The analysis of singular tractions at sharp corners and edges is also considered in the analysis. The development of an specific set of traction singular elements has been carried out. It has been used in the context of inverse analysis. The presence of corners and edges generates new difracted fields that must be properly modelized, to obtain the shape of the hidden cavities. The sensitivity to traction shape functions has been carried out for two support configurations.

A different way to minimize the cost function is the linearization of the response in terms of the so-called Topological Derivative. The displacement expansion in the frequency domain is obtained. Based on it, the linearization of the cost function is carried out. At each three-dimensional point, an optimum volume is obtained for the case of single or multiple cavity. The evaluation of the approximed cost function is fast. This causes that zero order global optimization method, such as Genetic Algorithm, are proposed to find the optimum position and volume of cavities. The use of the Topological Sensitivity is also tested as an image method. A set of numerical benchmark is carried out, with interesting conclusions for the case of simple or multiple deffect search.

Acknowledgements

I wanted to express my gratitude first to my family, because of their tolerance during the working days involved in the development of this work. To my parents, Enrique and Loli. To my brother, Jorge. It is always a difficult task providing a PhD candidate the necessary conditions to produce research results.

I wanted to express an special acknowledgement to Prof. Dr. Rafael Gallego, for his pacient guidance during these years and the past years as an undergraduate student. I met him in 1997, when I was a degree student. We began working on Boundary Elements in the context of error estimation and mesh adaptation for fracture mechanics. He made me discover research work in the context of Boundary Element Method. This work fascinated myself. Some years later, I discovered also the pleasure of publishing the results of investigation, and the difficulties and satisfactions involved in writting good quality papers.

I wanted to extend my gratitude to Dr. Bojan B. Guzina (Department of Civil Engineering, University of Minnesota at Twin Cities) for his guidance during my short stay in 2004, in particular to details of singular elements, fundamental solution and boundary elements based on the regularized boundary integral equation; I visited him in 2003; I learnt the methodology involved in writting and debugging good quality codes, and running computational time-consuming processes in a Linux cluster environment, based on the MPICH technology. Special gratitude to my colleages at Minneapolis: Dr. Sylvain Nintcheu Fata, Dr. Andrew Madyarov, and Dr. Ivan Chikichev.

I also extend and special acknowledgement to Dr. Marc Bonnet (LMS, École Polytechnique, Palaisseau Cedex, France), in aspects related with the Adjoint Variable Method. I visited him in 2004.

To my collegues and friends at the Department of Structural Mechanics at the University of Granada. In particular, to Msc. Inas Hatem Faris, for her contributions in aspects related with the topological sensitivity analysis for three-dimensional solids. I am deeply in debt with her. Also, I extend my acknowledgement to my collegues, PhD candidates working at the Mechanics of Solids and Structures Group, leadered by Rafael Gallego: Miguel A. Riveiro Taboada, Roberto Palma Guerrero, Rafael Bravo Pareja, Esther Puertas García and to Dr. Guillermo Rus Carlborg, Juan José Granados Romera, Lucía Comino Mateos and Francisco Javier Suárez Medina. I extend an special acknowledgement to Dr. Pedro Museros Romero, for his friendship and good advices. Also to Prof. Eng. Alejandro Castillo Linares.

To Dr. Hao Bai (Lakehead University, Canada), for providing tabulated material shown in the validation section of the fundamental solution; his comments are also gratefully acknowledged.

I also extend my acknowledgement to the Spanish Ministery of Education, for the FPU Grant AP-2001, that permited visiting the USA and France during the development of this PhD Thesis work.

Dedicated to my beloved Ángela, and my twin-sons Alejandro and Pedro, which were borned during the writting period of this PhD Thesis.

Contents

List of Tables

List of Figures

CHAPTER 1

Introduction, objetives and methodology

1.1 Introduction

Testing of materials by non destructive methods requires a set of numerical and experimental tools. This PhD work is focused on the numerical solution of the Inverse Identification problem, stated at a three-dimensional viscoelastic layer. The aim of the IIP stated is the identification of hidden cavities inner in a three-dimensional viscoelastic layer, based on the scattering of time-harmonic waves. This particular domain is very interesting for industrial aplications. Despite the use of guided waves in testing of materials is a classical topic in the literature, the number of papers focused on the Inverse Problem stated as an optimization problem for the layer domain is reduced. The main reason is that no closed form or fully integrable numerical solutions exists in the state of the art to solve the direct problem at a viscoelastic three-dimensional layer. Thus, the aim of this PhD work is the aplication of a reduced set of numerical techniques at the layer domain, obtaining conclusions to enrich the knowledgement about inverse problems for this particular configuration.

To reach the proposed objective, a first necessary previous work is the solution of the dificculties involved in the forward problem. The solution of the direct scattering of waves coming from sources and measured at selected testing points has to be programed in a numerical code. The radiation of waves and the traction-free boundary conditions constitutes the main difficulties that the direct code must solve for the infinite plate problem. The direct solution is going to be evaluated at each iteration in a general non-linear optimization algorithm; thus, a fast and accurate evaluation of the solution is required. The Boundary Element Method (BEM) permits an accurate and fast direct solution, as it consider the radiation boundary condition as a natural property of the BEM when the adequate Green function is included. Thus, a first objective of this PhD work was the development of an adequate elastodynamic Green function stated a the three-dimensional layer. Such fundamental solution requires only meshig the surface of deffects and some auxiliary surfaces (e.g. supports).

The solution obtained by the BEM depends strongly on two main aspects: the Green function used and the quality of the interpolation space used to approxime tractions and displacements. The use of the numerical codes in testing of materials require the consideration of realistic geometries existing in testing, such as supports, boxed geometries, etc. A secondary objective is the definition of an adequate set of approximation shape functions to represent tractions and displacements. Sharp geometries give rise to the presence of singularities that strongly affects to the quality of the results; in the context of elastic waves, sharp geometries changes the wave patterns, with must be taken into account in the numerical code. A second objective of this PhD was the development of specific traction shape functions to enhance the solution when sharp geometries are included.

The proposed fundamental solution with the new developed traction shape functions have been included in a BEM code based on the Regularized Boundary Integral Equation. With this methodology, no explicit regularization is required at any boundary point.

The Inverse Problem is stated as an optimization problem, in which the hidden cavity is parametrized as an ellipsoid and a regularized cost function depending on the misfit between experimental and computed displacements at selected points is minimized. The Inverse Problem is general nonlinear ill-posed problem. In this sense, solution is not unique, and it does not depends continously on the experimental data. Also, solution is strongly affected by errors obtained at the measurement points. The analysis of this inversion process is the next objective of this PhD work. The IIP is solved and discussed in the context of two different approach: i) minimization based on gradient methods, in which a direct solution is computed at the parametrized damaged layer; ii) the use of zero-order global search algorithms to identify hidden cavities, based on an approximation of the cost function by way of the Topological expansion of displacements.

First order algorithms are explored in the context of optimization methods. Such algorithms states the general nonlinear optimization problem, in which the shape and location of the hidden cavities is based on a parameter vector. At each iteration, the cost function and its first-order derivatives are computed. Second order derivatives are not required. In this sense, this group of methods are called *quasi-Newton*, in which no explicit second order Hessian matrix is computed. On this PhD work, a first analysis of the Inverse Problem based on the BFGS algorithm is discussed in a chapter.

The BFGS method requires the computation of the first-order derivatives. Such derivatives depends on the fundamental solution, and for the layer domain, the first order derivatives of the Green function does not exists in the literature. Gradients are computed by way of a semi-analytical integral carried out over the deffect surfaces, once the so-called Adjoint Problem is solved. The use of the Adjoint Variable Method (AVM) to compute gradients for the layer domain constitutes a novelty included at the corresponding chapter.

To obtain general conclusions that permit the comparison between algorithms, methods, and properties for inverse analysis of the layer domain, an exhaustive number of numerical tests have been carried out. The computational platform permits the computation and the analysis of the results. The consideration of a-priori volume information, the definition of error at measurements, the sensitivity to the number of sources/receivers, or the dependence on the initial guess point at each frequency is analysed at the corresponding chapter.

The last chapter is focused on the use of zero-order algorithms. Such techniques require a fast computation of the forward solution due to the fact that the minimum is obtained by testing the solution space. In this sense, the evaluation of the cost function requires the solution of a direct problem at each step. The computation of the direct cost function is expensive, in terms of number of operations and computing time. It requires the statement and solution of an equation system at each step. An alternative way to reduce the computational effort is the linealization of the problem, by way of the expansion of the displacement with computations carried out at the domain without deffects. The Topological Sensitivity approach permits the expansion of displacements, tractions, and integral cost function. An approximed cost function can be built at each point, which permit the fast evaluation of the direct problem. This important requirement permit the use of a particular zero-order method, such as Genetic Algorithms. The focus of the last chapter of this work is the analysis of the applications of the combined Genetic Algorithms and Topological Sensitivity approach. A numerical benchmark is carried out with interesting conclusions.

1.2 Objetives

The main objectives of this PhD work may be summarized at the following items:

- Development of an specific Green's function for the three dimensional viscoelastic layer in the frequency domain. The inversion is based on the scattering of elastic time-harmonic waves. The use of the Boundary Element Method permits a minimum mesh, only at the boundary of the deffects. Thus, this was the first objective to reach.
- Development of an specific code, in the context of Boundary Elements, to solve the direct problem. The code should be compared and contrasted with analytic or numeric solutions existing in the literature.
- Development of an specific set of tracion shape-functions to represent sharp geometries.
- Statement of the Inverse Identification Problem as an optimization problem. Development of the Adjoint Variable Approach to obtain the approximed gradientes.
- Numerical benchmark to obtain general properties of the IIP. Analysis of the stability of the algorithm. Analysis of the sensitivity of the results to random noise at the measurement, and dependence on some parameters. Comparing and contrasting the results with similar works existing in the literature.
- Development of the Topological Expansion of the cost function combined with Genetic Algorithms to obtain an approximed first guess spherical cavity, or to solve the IIP under certain conditions. Development of a numerical benchmark to obtain general properties of the use of the GA-TS tool as an identification of hidden cavities.

1.3 Methodology

To reach the previous objectives, the following methodology is applied.

- To develop the Green function, a general overview of the state of the art has been carried out. After the revision, the method of displacement potentials, with Thompson-Haskell transfer matrix system, has been explored. The use of cilindrical polar potentials, the Fourier transform in the angular direction, and the Hankel transform in the radial direction, permits the solution of the problem.

  To learn about the specific details of the method, the author visited Dr. Bojan B. Guzina in 2003, at the University of Minnesota at Twin Cities. Apart from the particularization of the multi-layer half space solution to the single layer, a new work was proposed, which is included in this PhD. The development of new variable-order traction shape functions that permits the modelization of sharp geometries. It must be mentioned that the author of this PhD worked on the main aspects concerning the new 8-noded singular elements, the determination of the basis for the traction shape functions, the rules to improve the integration of cuasi-singular integrals, and the numerical tests to confirm and validate the novel formulations for such elements. This work was also co-directed by Prof. Dr. R.Y.S. Pak. Results of this work were published in a paper. At this PhD document, this paper is reproduced in an specific chapter. The aim of this chapter is the introduction of such special functions. At this PhD Thesis, such traction singular shape functios have been used in the context of inverse analysis.

  The Green function was obtained and published [108]. Also, a paper about the new traction singular shape functions was published (see [70]).
- A numerical code has been developed and optimized based on the Regularized Boundary Element Method. In this sense, the work developed with Dr. Bojan Guzina was required to optimize the code, and test it. Also, the Green function has been compared with other references existing in the literature. The most important of them is the work by Dr. Hao Bai, which provided tabulated material.

The numerical code is based on Matlab and Fortran Language of Programming. The codes have been compiled and optimized in a Linux cluster. In this sense, the author applied the methodolgy learnt at Minnesota (Minneapolis Supercomputation Institute and Bojan Guzina's group). The specific hardware architecture required for intensive computation, the ways to parallelize computations, and the better options to carry out computations depending on high memory requeriments have been developed and optimized.

- The statement and solution of the IIP as an optimization problem was the next ofjective. To reach it, a careful revision of the state of the art was carried out. The IIP is stated as an optimization problem. The hidden deffect is parametrized. The cost function is built in terms of the discrepancy between the experimental measurement and the one obtained for a fixed set of parameters. Different optimization methods have been explored; the BFGS has been selected because it is common in the literature, and because less number of operations are required in comparison with Levenberg-Marquardt method and other quasi-Newton methods. The complexities of the Green function does not permit an easy Direct Differentiation Approach to obtain the necessary gradients. To obtain gradients, the Adjoint Variable method is used.
  To learn about the Adjoint Variable method, and generate and optimize the code, the author visited in 2004 Dr. Marc Bonnet (École Polytechnique, France). Working with Dr. Bonnet, the author learnt the main points of the Adjoint State implementation. The combined Matlab-Fortran is used to obtain a global solution.
- The numerical benchmark required an special treatment. The parametric analyses required to check the dependence of the solution respect to random noise, damping, parametrization of the ellipsoids, etc, required an important amount of time. A computational platform based on a Linux system has been developed. The use of specific scripts premitted the generation of analysis cases, and the postprocess of the resulting files.
- The Topological Expansion of the cost function is carried out based on the linearization of displacements in terms of the cavity volume. A rigorous analysis is carried out to obtain the first order displacement terms. Based on it, a quadratic approximed shape function is built. The cost function is computed based on the properties of the Non-Damaged state. This means that the forward problem is very fast to compute. The use of zero order methods, such as the Genetic Algorithm, seems to be a better option for this kind of problem in which gradients are no possible and the fordward solution is evaluated in a fast manner.
  The use of the Topological Sensitivity as an image method is also a technique reported in the literature. The way considered here is different, as the TS is used to define an approximed cost function. Both methods are compared by analysing the three dimensional mapping of the TS value versus the cost function. A numerical benchmark is carried out to analyse the dependence on the main parameters.
  The initial expansion of the cost function is extended for the case in which two or more cavities are considered. The interaction between cavities terms are neglected, which would be useful when radiation and material damping are given. The hypersingular traction kernel is required to obtain the interaction terms. When such term is not included, the interaction between deffects is ignored. It is possible at moderate damping rates with low frequencies. Numerical tests have been defined to test the identification of two cavities based on it. Also, the identification of less number of deffects than the number of trial cavities is explored.

1.4 Organization of this document

This PhD document is organized by independent chapters, in the sense that the revision of the state of the art, statement of the particular problem and conclusions follow the rules of an independent paper. The author consider that by this way reading each individual chapter is easier and more compact, linked with the structure of the papers already published by the author about the particular topics developed, or papers to be published from this work. The reference to general methods, such as the Boundary Element Method, or the Regularized Boundary Integral Equations, have been omitted. The reader can use the selected lectures on each chapter to find information about these topics.

The first chapter is focused on the Green's function for the viscoelastic layer. The formulation and solution method is exposed. Numerical test confirm the adequate implementation of the theoretical development.

At the second chapter, the work developed with Dr. Guzina and Prof. Dr. Pak is included. Formulation and numerical examples are presented to validate and enhance the convenience of using the new shape functions. The 8-noded shape functions are used in the context of inverse problems, at the third chapter.

The third chapter is focused on the solution of the Inverse Identification Problem with a quasi-Newton algorithm. The Adjoint Variable Method is presented to compute semi-analytical gradients. A set of numerical benchmark is presented, testing the stability of the inverse problem respect to the most relevant variables involved in the inversion.

At the fourth chapter, the topological sensitivity of displacement variables is developed for the time-harmonic problem stated at the layer. The expansion of displacements leads to a natural expansion of the cost function, which permits its combination with zero-order optimization methods to obtain the location and shape of hidden cavities.

CHAPTER 2

Green's function for a three dimensional elastodynamic viscous layer

2.1 Introduction

The numerical treatment of certain specific mixed boundary value problems involving layered media requires fundamental solutions in order to obtain accurate results which are compatible with low computing times. Numerical methods based on fundamental solutions, such as the boundary element method (BEM), would require such a demand. One of the high interest problems that demands such a solution is the analysis of single or multi-layered elastic plates. The main applications of waves in plates are ultrasonic non-destructive testing and parameter identification. Recent interest in guided waves in plates came from the developments of acoustic emission and ultrasonic testing. Recent references on this subject can be found in works by Cheeke(2002)[39], Kundu(2004)[88], and Malhotra and Carino(2004)[105].

The problem of wave propagation in infinite plates has been extensively studied since the work by Rayleigh(1888) [134] and Lamb(1917)[91], the main contribution of which was to introduce the concept of wave equations. One important advance in the context of dispersion relations and approximate theories can be found in the work by Mindlin(1960)[117].

The elastodynamic Green function for a homogeneous isotropic elastic plate has long been studied since Miklowitz(1978) [114]. Initial studies into fundamental solutions for wave propagation in plates deal with two-dimensional problems, in the context of axisymmetric problems e.g. Weaver(1982) [161], using the eigenfunction method. In the context of three-dimensional time-domain problems, the paper by Ceranoglu and Pao(1981)[27] shows a Green's function based on the generalized ray theory, using the Cagniard-De Hoop method to solve the double transform. The solutions based on the generalized ray theory require numerical evaluation of the results, and this is a critical aspect of the method. Vasudevan and Mal(1985)[159] present the transient solution due to an embedded dislocation. A transient Green's function has been published in the form of a `FORTRAN` code by Hsu(1985)[80], based on the ray theory solution.

In the context of approximated solutions, a semi-analytical formulation has been proposed: a 1D finite element mesh is introduced for the layering direction, and analytic (or semi-analytic) solutions are considered for the remaining coordinate directions. The layers are divided into sub-layers to introduce the FEM mesh and this method is called the thin-layer method (TLM). For two-dimensional problems, Galán and Abascal (2002-2003) [56, 57] show a method to analyse wave scattering due to defects in layered media, whereby a BEM mesh is used to model the defect neighbourhood and a FEM semi-analytical Green's function is used in the far-field. For 3D problems, Kausel and Peek (1982)[83] and Kausel(1994)[82] present the fundamental solution for layered media based on the TLM. Recently, Bai *et al.*(2004) [7] presented a fundamental solution based on modal superposition for homogeneous or multi-layered plates. A finite element mesh is introduced to approximate the

vertical component of displacements, while for planar directions, the spatial double Fourier transform leads to plane and antiplane modal equations, which provide the modal base for expanding the solution.

The work by Benitez and Rosakis(1985)[12] presents a general analytic approach for obtaining the three-dimensional Green's function for a multi-layered plate. The double Fourier transform and the propagator matrix technique lead to the analytic solution in the transformed domain. The authors define the solution without attempting numerical inversion and this work is carried out in Pintado and Benítez(1990)[131] for a uniformly moving source.

Matrix techniques have been used to analyse multilayered configurations (see the review work by Lowe(1995)[99]. The propagator matrix method is a technique which was initially developed by Thompson(1950)[156] and Haskell(1953)[76] to relate the tractions and displacements at the upper and lower surfaces of a layer. The initial technique was improved by Harkrider(1964)[75], Haskell(1964) [77], Apsel and Luco (1964)[4], Luco and Apsel(1983) [101], Franssens(1983) [52], Hisada(1994) [78], Hisada(1995) [79], among others.

Work by Kundu and Mal (1985)[89] and Xu and Mal (1985)[164], and recently for multilayered composites Banerjee and Mal (2005) [8], shows a solution method which has improved on the Haskell-Thompson matrix method. The numerical technique used is an integral transform approach in the frequency domain where only the surface response is computed. In this context, the solution cannot be considered to be a Green's function.

Work based on the double Fourier transform requires a large amount of computation time to evaluate the integrals of the inverse transform. The Hankel transform approach reduces the dimension of the integrals from two to one (only in the radial direction). Pak and Guzina (2002) [124] present the three-dimensional fundamental solution for a multilayered viscoelastic half-space, based on the original approach by Luco and Apsel (1983)[101]. The solution is built in three steps: a) potential displacements, b) angular Fourier series, c) radial Hankel transform. The propagator matrix approach is updated in order to define the solution, free of unbounded exponential terms. The evaluation of the fundamental solution requires the numerical evaluation of the inverse Hankel transform (henceforth IHT). A modified integration path is proposed in order to avoid the singularities along the real axis, see Guzina (2001)[69].

This work deals with the Green's function for the time-harmonic elastodynamic problem in a plate domain, including damping effects. The method proposed by Guzina and Pak is adopted here to develop the fundamental solution by including the boundary conditions of the plate, and the specific reflection matrices for the plate have been obtained. In order to compute the IHT, a modified integration path is introduced. A careful analysis has been carried out to identify the poles along the formal path which are specific for the plate domain. The result of this analysis is the identification of unbounded poles at low excitation frequencies, which correspond to the asymmetric Lamb modes. A numerical treatment is proposed to delineate the integration path. In order to validate the solution, a series of numerical tests are presented, in which the solution is checked and compared with other previously published results.

2.2 Problem Statement and Solution Method

The linear elastic response of a general three-dimensional homogeneous and isotropic solid may be analysed in terms of the Navier equation,

$$(\lambda + 2\,\mu)\ \nabla\nabla\cdot\boldsymbol{u} - \mu\,\nabla\times\nabla\times\boldsymbol{u} + \boldsymbol{f} = \rho\,\ddot{\boldsymbol{u}} \tag{2.1}$$

where λ and μ are the Lamé constants; ρ is the material mass density; $\boldsymbol{u}$ is the displacement field; $\ddot{\boldsymbol{u}}$ stands for the acceleration field; and $\boldsymbol{f}$ is a time-dependent volumetric force field. Eq. (2.1) may be analysed in the frequency domain by virtue of the Fourier transform leading to

$$(\lambda + 2\,\mu)\ \nabla\,\nabla\cdot\boldsymbol{u} - \mu\,\nabla\times\nabla\times\boldsymbol{u} + \rho\,\omega^2\,\boldsymbol{u} + \boldsymbol{f} = \boldsymbol{0} \tag{2.2}$$

where the factor $\mathrm{e}^{i\omega t}$ is omitted.

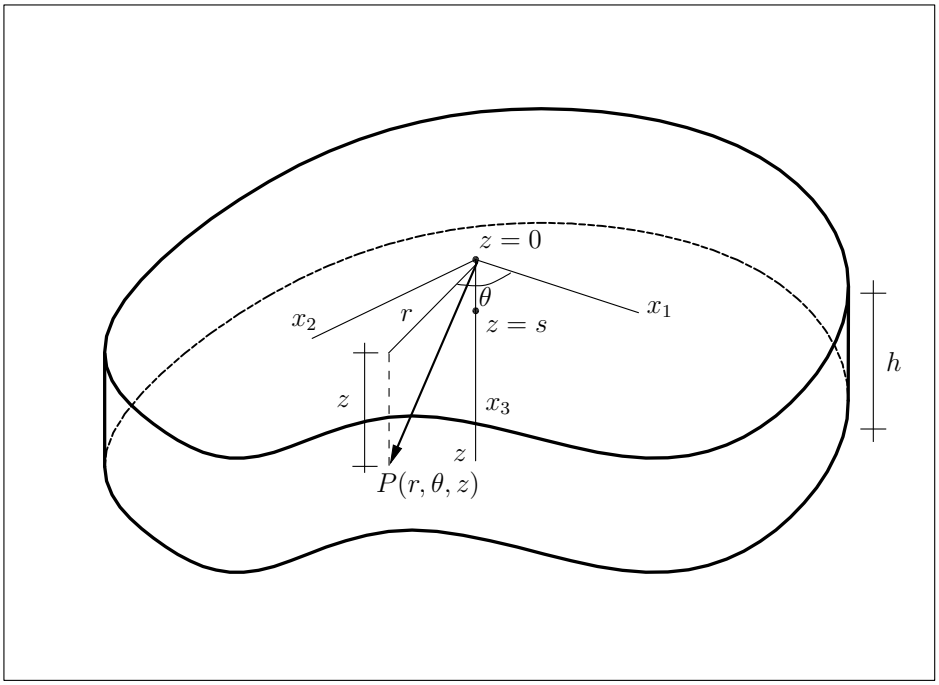

Figure 2.1: Infinite plate domain. Cartesian and polar references

Figure 2.1 shows the infinite plate domain with a thickness of h. The Cartesian reference, $\mathcal{R}_c = \{0;\, x_1, x_2, x_3\}$, and the polar coordinate system $\mathcal{R}_p = \{0;\, r, \theta, z\}$ are also shown. The plate domain $\Omega = \{(x_1, x_2, x_3) | 0 \leq x_3 \leq h\}$ is bounded by the free surfaces S_1 and S_2, with $S_1 = \{(x_1, x_2, x_3) | x_3 = 0\}$ and $S_2 = \{(x_1, x_2, x_3) | x_3 = h\}$. A time-harmonic point force is located at $z = s$. A displacement vector, which is the solution of Eq. (2.2), can be represented as a combination of three displacement potentials, ϕ_1, ϕ_2, and ϕ_3 Pak(1987)[123],

$$\boldsymbol{u}(r, \theta, z) = \nabla\,\phi_1(r, \theta, z) + \nabla\times\{\phi_2(r, \theta, z)\,\boldsymbol{e_z} + \nabla\times[\phi_3(r, \theta, z)\,\boldsymbol{e_z}]\} \tag{2.3}$$

with $\boldsymbol{e_z}$ being a unitary vector in the vertical direction (x_3 or z). Considering Eq. (2.3) in Eq. (2.2), it follows that the governing equation for each potential is Helmholtz-type,

$$\left(\nabla^2 + k_q^2\right)\,\phi_q = 0, \qquad q = 1, 2, 3 \tag{2.4}$$

where

$$k_1 = k_p \equiv \omega\sqrt{\frac{\rho}{\lambda + 2\mu}}; \qquad k_2 = k_3 = k_s \equiv \omega\sqrt{\frac{\rho}{\mu}}. \tag{2.5}$$

The viscosity effects may be included in the model by complex-valued material parameters *correspondence principle*, by Christiansen [30]. Thus, constants λ^* and μ^* are defined in terms of the frequency-dependent coefficients ξ_α and ξ_β:

$$\begin{array}{rcll} \lambda^* + 2\mu^* & = & (\lambda + 2\mu)\,[1 + 2\,i\,\xi_\alpha(\omega)]\,, & \xi_\alpha \geq 0 \\ \mu^* & = & \mu\,[1 + 2\,i\,\xi_\beta(\omega)]\,, & \xi_\beta \geq 0 \end{array} \tag{2.6}$$

In what follows, the elastic constants will be shown as λ and μ, allowing complex values for them by virtue of Eq. (2.6). In order to solve Eq. (2.4), the angular Fourier series is introduced

$$\phi_q(r,\theta,z) = \sum_{m=-\infty}^{\infty} \phi_{q_m}(r,z)\, e^{im\theta}, \qquad q = 1,2,3 \tag{2.7}$$

with analogous expressions for displacements and tractions.

At this point, the m-th order Hankel transform is introduced. Its direct and inverse forms are defined as follows [133]:

$$\tilde{f}^m(\xi,z) = \int_0^\infty f(r,z)\, r\, J_m(r\xi)\, \mathrm{d}r; \qquad f(r,z) = \int_0^\infty \tilde{f}^m(\xi,z)\, \xi\, J_m(r\xi)\, \mathrm{d}\xi \tag{2.8}$$

where $J_m(z)$ is the m-th order Bessel function.

Substituting Eqs. (2.7) in Eqs. (2.4) and taking the Hankel transform, the set of wave equations is reduced to a set of differential ordinary equations,

$$\left(\tilde{\phi}^m_{q_m}\right)'' + \left(k_q^2 - \xi^2\right)\tilde{\phi}_{q_m} = 0, \qquad q = 1,2,3 \tag{2.9}$$

in which $(\cdot)'$ stands for $\mathrm{d}(\cdot)/\mathrm{d}\,z$. The general solution of Eq. (2.9) may be written as

$$\begin{array}{rcll} \tilde{\phi}^n_{1_m}(\xi,z) & = & A^n_{1_m}(\xi)\, e^{\alpha z} + B^n_{1_m}(\xi)\, e^{-\alpha z} & \\ \tilde{\phi}^n_{q_m}(\xi,z) & = & A^n_{q_m}(\xi)\, e^{\beta z} + B^n_{q_m}(\xi)\, e^{-\beta z}, & q = 2,3 \end{array} \tag{2.10}$$

where,

$$\alpha = \sqrt{\xi^2 - k_p^2}, \quad \beta = \sqrt{\xi^2 - k_s^2}. \tag{2.11}$$

Constants $A^n_{q_m}$, $B^n_{q_m}$ will be computed from the following boundary conditions: traction free at $z = 0$; $z = h$ and source at $z = s$. The roots α and β are located in the first quadrant so both their real and imaginary parts are positive. Displacement and traction Cartesian components u_i, τ_{ij}, respectively, can be related with potential derivatives through the polar components. In order to prescribe the source condition, a general distributed load at $z = s$ is applied as a traction jump,

$$\begin{array}{rcccl} \tau_{zr}(r,\theta,s^-) - \tau_{zr}(r,\theta,s^+) & = & P(r,\theta) & = & \displaystyle\sum_{m=-\infty}^{\infty} P_m(r)\, e^{im\theta} \\ \tau_{z\theta}(r,\theta,s^-) - \tau_{z\theta}(r,\theta,s^+) & = & Q(r,\theta) & = & \displaystyle\sum_{m=-\infty}^{\infty} Q_m(r)\, e^{im\theta} \\ \tau_{zz}(r,\theta,s^-) - \tau_{zz}(r,\theta,s^+) & = & R(r,\theta) & = & \displaystyle\sum_{m=-\infty}^{\infty} R_m(r)\, e^{im\theta}. \end{array} \tag{2.12}$$

In particular, a point force located at $z = s$ is represented by the Dirac Delta function in polar coordinates,

$$\begin{aligned} \mathrm{f}_h(r,\theta,z) &= \mathcal{F}_h \,\frac{\delta(r)}{2\pi r}\,\delta(z-s)\,\boldsymbol{e}_h \\ \mathrm{f}_v(r,\theta,z) &= \mathcal{F}_v \,\frac{\delta(r)}{2\pi r}\,\delta(z-s)\,\boldsymbol{e_z} \end{aligned}$$

where $\boldsymbol{e}_h$ is a unit horizontal vector in the $\theta = \theta_0$ direction and $\mathcal{F}_h$ and $\mathcal{F}_v$ are the magnitudes of the point load components.

Each angular Fourier series, Eq. (2.12), of $f_h(r,\theta,z)$ and $f_v(r,\theta,z)$ contains only three terms, $m = -1, 0, 1$, with

$$\begin{aligned} P_{\pm1}(r) &= \mathcal{F}_h\, e^{\mp i\theta_0}\,\frac{\delta(r)}{4\pi r}, & P_m(r) = 0,\ m \neq \pm 1 \\ Q_{\pm1}(r) &= \pm i\,\mathcal{F}_h\, e^{\mp i\theta_0}\,\frac{\delta(r)}{4\pi r}, & Q_m(r) = 0,\ m \neq \pm 1 \\ R_0(r) &= \mathcal{F}_v \frac{\delta(r)}{2\pi r}, & R_m(r) = 0, m \neq 0 \end{aligned} \tag{2.13}$$

Henceforth, source magnitude loads will be indexed as

$$\mathcal{F}_0 = \mathcal{F}_v; \quad \mathcal{F}_{\pm1} = \mathcal{F}_h; \quad \mathcal{F}_m = 0,\ |m| > 1. \tag{2.14}$$

2.2.1 Uncoupled PS and S Wave Propagation Systems

For numerical purposes, it is convenient to introduce a set of dimensionless parameters,

$$\begin{array}{lllll} \bar{r} = k_0\, r, & \bar{z} = k_0\, z, & \bar{s} = k_0\, s, & \zeta = \xi/k_0, & \bar{\mu} = \mu/\mu_0, \\ \bar{\lambda} = \lambda/\mu_0, & \bar{\rho} = \rho/\rho_0, & \bar{k}_q = k_q/k_0, & \bar{\alpha}_q = \sqrt{\zeta^2 - \bar{k}_q^2}, & \bar{h} = k_0\, h \end{array} \tag{2.15}$$

where μ_0 and ρ_0 are the reference values for shear stiffness and mass density. In what follows, such values will be fixed as $\mu_0 = \mathrm{Re}(\mu)$ and $\rho_0 = \rho$. The parameter $k_0 = \omega\sqrt{\rho_0/\mu_0}$ is the reference wavenumber.

An additional change of variables leads to the dimensionless displacements,

$$\begin{aligned} v_{1_m}(\zeta,\bar{z};\bar{s}) &= \frac{\mu_0\, k_0}{2\,\mathcal{F}_m}\left\{\left(\tilde{u}_{r_m}^{m+1} + i\,\tilde{u}_{\theta_m}^{m+1}\right) - \left(\tilde{u}_{r_m}^{m-1} - i\,\tilde{u}_{\theta_m}^{m-1}\right)\right\} \\ v_{2_m}(\zeta,\bar{z};\bar{s}) &= \frac{\mu_0\, k_0}{\mathcal{F}_m}\tilde{u}_{z_m}^{m} \\ v_{3_m}(\zeta,\bar{z};\bar{s}) &= \frac{\mu_0\, k_0}{2\,\mathcal{F}_m}\left\{\left(\tilde{u}_{r_m}^{m+1} + i\,\tilde{u}_{\theta_m}^{m+1}\right) + \left(\tilde{u}_{r_m}^{m-1} - i\,\tilde{u}_{\theta_m}^{m-1}\right)\right\} \end{aligned} \tag{2.16}$$

and dimensionless tractions

$$
\begin{aligned}
\sigma_{21_m}(\zeta,\bar{z};\bar{s}) &= \frac{1}{2\,\mathcal{F}_m}\left\{\left(\tilde{\tau}^{m+1}_{zr_m}+i\,\tilde{\tau}^{m+1}_{z\theta_m}\right)-\left(\tilde{\tau}^{m-1}_{zr_m}-i\,\tilde{\tau}^{m-1}_{z\theta_m}\right)\right\}\\
\sigma_{22_m}(\zeta,\bar{z};\bar{s}) &= \frac{1}{\mathcal{F}_m}\tilde{\tau}^{m}_{zz_m}\\
\sigma_{23_m}(\zeta,\bar{z};\bar{s}) &= \frac{1}{2\,\mathcal{F}_m}\left\{\left(\tilde{\tau}^{m+1}_{zr_m}+i\,\tilde{\tau}^{m+1}_{z\theta_m}\right)+\left(\tilde{\tau}^{m-1}_{zr_m}-i\,\tilde{\tau}^{m-1}_{z\theta_m}\right)\right\}\\
\sigma_{11_m}(\zeta,\bar{z};\bar{s}) &= \frac{1}{\mathcal{F}_m}\left\{\tilde{\tau}^{m}_{rr_m}+2\mu_0 k_0\bar{\mu}\left(\widetilde{\frac{u_{r_m}}{\bar{r}}+i\,m\frac{u_{\theta_m}}{\bar{r}}}\right)^m\right\}\\
\sigma_{33_m}(\zeta,\bar{z};\bar{s}) &= \frac{1}{\mathcal{F}_m}\left\{\tilde{\tau}^{m}_{\theta\theta_m}-2\mu_0 k_0\bar{\mu}\left(\widetilde{\frac{u_{r_m}}{\bar{r}}+i\,m\frac{u_{\theta_m}}{\bar{r}}}\right)^m\right\}\\
\sigma_{13_m}(\zeta,\bar{z};\bar{s}) &= \frac{1}{\mathcal{F}_m}\left\{\tilde{\tau}^{m}_{r\theta_m}+2\mu_0 k_0\bar{\mu}\left(\widetilde{\frac{u_{\theta_m}}{\bar{r}}-i\,m\frac{u_{r_m}}{\bar{r}}}\right)^m\right\}
\end{aligned}
\tag{2.17}
$$

where $\mathcal{F}_m$ is the source series defined in Eq. (2.14). Thanks to these changes of variable, two uncoupled propagation systems [101, 78, 124] may be written in matrix form as

$$
\begin{bmatrix} v_{1_m}\\ v_{2_m}\\ \sigma_{21_m}\\ \sigma_{22_m}\\ \sigma_{33_m}\\ \sigma_{11_m}\end{bmatrix}=\begin{bmatrix} -\zeta & \bar{\beta} & -\zeta & -\bar{\beta}\\ -\bar{\alpha} & \zeta & \bar{\alpha} & \zeta\\ 2\bar{\mu}\zeta\bar{\alpha} & -\bar{\mu}(\bar{\beta}^2+\zeta^2) & -2\bar{\mu}\zeta\bar{\alpha} & -\mu(\bar{\beta}^2+\zeta^2)\\ \bar{\mu}(\bar{\beta}^2+\zeta^2) & -2\bar{\mu}\zeta\bar{\beta} & \bar{\mu}(\bar{\beta}^2+\zeta^2) & 2\bar{\mu}\zeta\bar{\beta}\\ \bar{\lambda}(\bar{\alpha}^2-\zeta^2) & 0 & \bar{\lambda}(\bar{\alpha}^2-\zeta^2) & 0\\ \bar{\lambda}\bar{\alpha}^2-(\bar{\lambda}+2\bar{\mu})\zeta^2 & 2\bar{\mu}\xi\bar{\beta} & \bar{\lambda}\bar{\alpha}^2-(\bar{\lambda}+2\bar{\mu})\zeta^2 & -2\bar{\mu}\zeta\bar{\beta}\end{bmatrix}\begin{bmatrix}\mathbf{w_{d_m}}(\zeta,\bar{z};\bar{s})\\ \mathbf{w_{u_m}}(\zeta,\bar{z};\bar{s})\end{bmatrix}
\tag{2.18}
$$

for PS-waves, and

$$
\begin{pmatrix} v_{3_m}\\ \sigma_{23_m}\\ \sigma_{13_m}\end{pmatrix}=\begin{bmatrix} i\,\zeta & i\,\zeta\\ -i\,\bar{\mu}\,\zeta\,\bar{\beta} & i\,\bar{\mu}\,\zeta\,\bar{\beta}\\ \bar{\mu}\,\zeta^2 & \bar{\mu}\,\zeta^2\end{bmatrix}\cdot\begin{pmatrix} w_{d_m}(\zeta,\bar{z};\bar{s})\\ w_{u_m}(\zeta,\bar{z};\bar{s})\end{pmatrix}
\tag{2.19}
$$

for S-waves.

The terms $\mathbf{w_{d_m}}$, $\mathbf{w_{u_m}}$, w_{d_m} and w_{u_m} are interpreted as downward and upward propagating components of the PS and S wave vectors, respectively. It is possible to obtain the expressions for these vectors by applying the specific plate boundary conditions. The decomposition for PS vector is

$$
\begin{aligned}
\mathbf{w_{d_m}}(\zeta,\bar{z};\bar{s}) &= \mathbf{E}(\bar{z})\cdot{\mathbf{G_d}}^{-1}\cdot\left[\mathbf{R}^u\cdot\mathbf{E}(\bar{s})\cdot\mathbf{S_{u_m}}+\mathbf{R}^u\cdot\mathbf{E}(\bar{h})\cdot\mathbf{R}^d\cdot\mathbf{E}(\bar{h}-\bar{s})\,\mathbf{S_{d_m}}\right]+\\
&\quad H(\bar{z}-\bar{s})\cdot\mathbf{E}(\bar{z}-\bar{s})\,\mathbf{S_{d_m}} \qquad (2.20)\\
\mathbf{w_{u_m}}(\zeta,\bar{z};\bar{s}) &= \mathbf{E}(\bar{h}-\bar{z})\cdot{\mathbf{G_u}}^{-1}\cdot\left[\mathbf{R}^d\cdot\mathbf{E}(\bar{h}-\bar{s})\cdot\mathbf{S_{d_m}}+\mathbf{R}^d\cdot\mathbf{E}(\bar{h})\cdot\mathbf{R}^u\cdot\mathbf{E}(\bar{s})\,\mathbf{S_{u_m}}\right]+\\
&\quad H(\bar{s}-\bar{z})\cdot\mathbf{E}(\bar{s}-\bar{z})\,\mathbf{S_{u_m}} \qquad (2.21)
\end{aligned}
$$

where,

$$
\mathbf{G_d} = \left[\mathbf{I}-\mathbf{R}^u\,\mathbf{E}(\bar{h})\,\mathbf{R}^d\,\mathbf{E}(\bar{h})\right] \tag{2.22}
$$

$$
\mathbf{G_u} = \left[\mathbf{I}-\mathbf{R}^d\,\mathbf{E}(\bar{h})\,\mathbf{R}^u\,\mathbf{E}(\bar{h})\right] \tag{2.23}
$$

Matrices $\mathbf{R}^u$ and $\mathbf{R}^q$ are given by,

$$\mathbf{R}^u(\zeta) = \frac{1}{R(\zeta)} \cdot \begin{bmatrix} R_{11}(\zeta) & R_{12}(\zeta) \\ R_{21}(\zeta) & R_{11}(\zeta) \end{bmatrix} \tag{2.24}$$

$$\mathbf{R}_d(\zeta) = \frac{1}{R(\zeta)} \cdot \begin{bmatrix} R_{11}(\zeta) & -R_{12}(\zeta) \\ -R_{21}(\zeta) & R_{11}(\zeta) \end{bmatrix} \tag{2.25}$$

where

$$\begin{aligned} R_{11}(\zeta) &= -\left(4\,\bar{\alpha}(\zeta)\,\bar{\beta}(\zeta)\,\zeta^2 + \left(\bar{\beta}^2(\zeta) + \zeta^2\right)^2\right) \\ R_{12}(\zeta) &= -4\bar{\beta}(\zeta)\,\zeta\,\left(\bar{\beta}^2(\zeta) + \zeta^2\right) \\ R_{21}(\zeta) &= -4\bar{\alpha}(\zeta)\,\zeta\,\left(\bar{\beta}^2(\zeta) + \zeta^2\right) \\ R(\zeta) &= \left(\bar{\beta}^2(\zeta) + \zeta^2\right)^2 - 4\,\bar{\alpha}(\zeta)\,\bar{\beta}(\zeta)\,\zeta^2 \end{aligned} \tag{2.26}$$

$R(\zeta)$ is the Rayleigh wave function whose zeroes provide the Rayleigh wave numbers. It can be shown that det $\mathbf{R}_d$ = det $\mathbf{R}_u$. The zeroes of this determinant would play an important role in the definition of the integration path for the IHT, as shown below.

(2.27)

It should be noted that the determinant of Matrix $\mathbf{E}(\bar{z})$ is

$$\mathbf{E}(\bar{z}) = \begin{bmatrix} \mathrm{e}^{-\bar{\alpha}(\zeta)\,\bar{z}} & 0 \\ 0 & \mathrm{e}^{-\bar{\beta}(\zeta)\,\bar{z}} \end{bmatrix} \tag{2.28}$$

while the source terms $\mathbf{S}_{\mathbf{u_m}}$ and $\mathbf{S}_{\mathbf{d_m}}$ have the following expressions:

$$\begin{aligned} \mathbf{S}^T_{\mathbf{u_m}}(\zeta) &= \frac{-1}{2\,\bar{\rho}}\left(\bar{Z}_m - \frac{\zeta}{2\,\bar{\alpha}}\,(\bar{X}_m - \bar{Y}_m)\,,\ \bar{Z}_m\,\frac{-\zeta}{\bar{\beta}(\zeta)} + \frac{1}{2}(\bar{X}_m - \bar{Y}_m)\right) \\ \mathbf{S}^T_{\mathbf{d_m}}(\zeta) &= \frac{1}{2\,\bar{\rho}}\left(\bar{Z}_m + \frac{\zeta}{2\,\bar{\alpha}}\,(\bar{X}_m - \bar{Y}_m)\,,\ \bar{Z}_m\,\frac{\zeta}{\bar{\beta}(\zeta)} + \frac{1}{2}(\bar{X}_m - \bar{Y}_m)\right). \end{aligned} \tag{2.29}$$

The Heaviside function is represented by H and $\mathbf{I}$ is the 2×2 identity matrix.

The pure shear wave propagating system is defined in terms of the scalar functions

$$\begin{aligned} w_{d_m}(\zeta, \bar{z}; \bar{s}) &= e^{-\bar{\beta}\,\bar{z}}\left(1 - e^{-2\,\bar{\beta}\,\bar{h}}\right)^{-1}\left[e^{-\bar{\beta}\,\bar{s}} + e^{-\bar{\beta}\,\bar{h}}\,e^{-\bar{\beta}(\bar{h}-\bar{s})}\right]\,S_m + \\ &\quad H(\bar{z} - \bar{s})\,e^{-\bar{\beta}\,(\bar{z}-\bar{s})}\,S_m \\ w_{u_m}(\zeta, \bar{z}; \bar{s}) &= e^{-\bar{\beta}\,(\bar{h}-\bar{z})}\left(1 - e^{-2\,\bar{\beta}\,\bar{h}}\right)^{-1}\left[e^{-\bar{\beta}(\bar{h}-\bar{s})} + e^{-\bar{\beta}\,\bar{h}}\,e^{-\bar{\beta}\,\bar{s}}\right]\,S_m + \\ &\quad H(\bar{s} - \bar{z})\,e^{-\bar{\beta}\,(\bar{s}-\bar{z})}\,S_m \end{aligned} \tag{2.30}$$

with

$$S_m = \frac{-i}{4\,\bar{\mu}\,\zeta\,\bar{\beta}(\zeta)}\,\left(\bar{X}_m + \bar{Y}_m\right) \tag{2.31}$$

the dimensionless coefficients for the source series are given by

$$\begin{aligned} \bar{X}_1(\zeta) &= \frac{1}{2\,\pi}\,e^{-i\,\theta_0}, \quad & \bar{X}_m(\zeta) = 0,\ m \neq 1 \\ \bar{Y}_{-1}(\zeta) &= \frac{1}{2\,\pi}\,e^{i\,\theta_0}, \quad & \bar{Y}_m(\zeta) = 0,\ m \neq -1 \\ \bar{Z}_0(\zeta) &= \frac{1}{2\,\pi}, & \bar{Z}_m(\zeta) = 0,\ m \neq 0 \end{aligned} \tag{2.32}$$

where a unit load in vertical and horizontal directions has been assumed.

2.2.2 *Asymptotic Decomposition*

In order to evaluate the displacement and traction components of the elastodynamic fundamental solution, the semi-infinite integrals corresponding to the IHT must be computed. Denoting the source direction by superscript $s = \{h.v\}$, the displacement components can be obtained:

$$\begin{aligned}
\hat{u}^s_r + i\,\hat{u}^s_\theta &= \frac{k_0}{\mu_0}\sum_{m=-1}^{1}\mathcal{F}^s_m\, e^{i\,m\,\theta}\int_0^\infty (v_{3_m}+v_{1_m})\,\zeta\,J_{m+1}(\bar{r}\,\zeta)\,\mathrm{d}\zeta \\
\hat{u}^s_r - i\,\hat{u}^s_\theta &= \frac{k_0}{\mu_0}\sum_{m=-1}^{1}\mathcal{F}^s_m\, e^{i\,m\,\theta}\int_0^\infty (v_{3_m}-v_{1_m})\,\zeta\,J_{m-1}(\bar{r}\,\zeta)\,\mathrm{d}\zeta \\
\hat{u}^s_z &= \frac{k_0}{\mu_0}\sum_{m=-1}^{1}\mathcal{F}^s_m\, e^{i\,m\,\theta}\int_0^\infty v_{2_m}\,\zeta\,J_m(\bar{r}\,\zeta)\,\mathrm{d}\zeta
\end{aligned} \tag{2.33}$$

while for tractions,

$$\begin{aligned}
\hat{\tau}^s_{zz} &= k_0^2\sum_{m=-1}^{1}\mathcal{F}^s_m\, e^{i\,m\,\theta}\int_0^\infty \sigma_{22_m}\,\zeta\,J_m(\bar{r}\,\zeta)\mathrm{d}\zeta \\
\hat{\tau}^s_{zr} + i\,\hat{\tau}^s_{z\theta} &= k_0^2\sum_{m=1}^{1}\mathcal{F}^s_m\, e^{i\,m\,\theta}\int_0^\infty (\sigma_{23_m}+\sigma_{21_m})\,\zeta\,J_{m+1}(\bar{r}\,\zeta)\,\mathrm{d}\zeta \\
\hat{\tau}^s_{zr} - i\,\hat{\tau}^s_{z\theta} &= k_0^2\sum_{m=1}^{1}\mathcal{F}^s_m\, e^{i\,m\,\theta}\int_0^\infty (\sigma_{23_m}-\sigma_{21_m})\,\zeta\,J_{m-1}(\bar{r}\,\zeta)\,\mathrm{d}\zeta
\end{aligned} \tag{2.34}$$

$$\begin{aligned}
\hat{\tau}^s_{rr} + \frac{2\,\mu_0\,k_0\,\bar{\mu}}{\bar{r}}\sum_{m=-1}^{1}\left\{\hat{u}^s_{r_m} + i\,m\,\hat{u}^s_{\theta_m}\right\}e^{i\,m\,\theta} &= k_0^2\sum_{m=-1}^{1}\mathcal{F}^s_m\, e^{i\,m\,\theta}\int_0^\infty \sigma_{11_m}\zeta J_m(\bar{r}\,\zeta)\,\mathrm{d}\zeta \\
\hat{\tau}^s_{\theta\theta} - \frac{2\,\mu_0\,k_0\,\bar{\mu}}{\bar{r}}\sum_{m=-1}^{1}\left\{\hat{u}^s_{r_m} + i\,m\,\hat{u}^s_{\theta_m}\right\}e^{i\,m\,\theta} &= k_0^2\sum_{m=-1}^{1}\mathcal{F}^s_m\, e^{i\,m\,\theta}\int_0^\infty \sigma_{33_m}\zeta J_m(\bar{r}\,\zeta)\,\mathrm{d}\zeta \\
\hat{\tau}^s_{r\theta} + \frac{2\,\mu_0\,k_0\,\bar{\mu}}{\bar{r}}\sum_{m=-1}^{1}\left\{\hat{u}^s_{\theta_m} - i\,m\,\hat{u}^s_{r_m}\right\}e^{i\,m\,\theta} &= k_0^2\sum_{m=-1}^{1}\mathcal{F}^s_m\, e^{i\,m\,\theta}\int_0^\infty \sigma_{13_m}\zeta J_m(\bar{r}\,\zeta)\,\mathrm{d}\zeta.
\end{aligned} \tag{2.35}$$

The fundamental solution (displacements and traction components) becomes singular at the source point. The integrals that define the fields become singular when the area to integrate is unbounded and the integrand is low decaying. In order to compute the IHT integrals, the integrands may be split into a strong decaying term plus a term which is integrated in closed-form, which represents the singular component.

The leading asymptotic expansions, see Pak(1987) [123], Pak(1994) [127] of the displacements and traction functions are termed $v^a_{i_m}(\zeta,\bar{z})$ and $\sigma^a_{ij_m}(\zeta,\bar{z})$.

The components of $v^a_{i_m}(\zeta)$ may be factorised as follows:

$$\begin{aligned}
v^a_{1_m}(\zeta,\bar{z}) &= \gamma_1(\zeta,\bar{z})\,\frac{\bar{Y}_m - \bar{X}_m}{2\bar{\mu}} - \gamma_3(\zeta,\bar{z})\,\frac{\bar{Z}_m}{\bar{\mu}} \\
v^a_{2_m}(\zeta,\bar{z}) &= \Omega_1(\zeta,\bar{z})\,\frac{\bar{X}_m - \bar{Y}_m}{2\bar{\mu}} + \Omega_2(\zeta,\bar{z})\,\frac{\bar{Z}_m}{\bar{\mu}} \\
v^a_{3_m}(\zeta,\bar{z}) &= \gamma_2(\zeta,\bar{z})\,\frac{\bar{X}_m + \bar{Y}_m}{2\bar{\mu}}
\end{aligned} \tag{2.36}$$

where the functions γ_1,γ_2, γ_3, Ω_1 and Ω_2 correspond to the bi-material full-space fundamental solution functions Guzina(1999) [64], with the interphase plane located at $x_3 = 0$ for $0 < s \leq h/2$ or $x_3 = h$ for $h/2 < s \leq h$; the half-space fundamental solution functions are obtained from these

taking $\mu = 0$ for the unloaded half-material. Complex parameters μ, ν are assigned to the loaded half-space.

The asymptotic kernels $v^a_{i_m}(\zeta)$ admit closed-form IHT integrals in Eq. (2.33), corresponding with the displacement field in a half-space, the closed-form expressions of which were obtained by Mindlin(1936) [116]. The fundamental solution displacement field will therefore be given by

$$\mathbf{u} = \mathbf{u}^{\text{half-space}} + \mathbf{u}^R \tag{2.37}$$

where superscript R denotes the regular kernel. As occurs with displacements, traction components $\sigma^a_{i j_m}$ can also be factorized Guzina(1999) [64]. The IHT traction integrals also lead to closed-form expressions, given by Mindlin(1936) [116], and an analogous kernel decomposition may be written for tractions.

At this point, we should mention that an alternative decomposition may be set by defining the asymptotic part of the solution by considering the static point-load solution for an infinite slab. This approach is possible, and it is easy to prove that such a solution can be split into Mindlin's solution plus a regular function (thus, the singularity is similarly removed). This alternative approach seems to present certain advantages in the context of its use in a numerical method such as the boundary element method. The static solution for a slab, on the other hand, involves more complexities than Mindlin's solution: the integrated form requires more floating-point operations, and there are fewer references in literature to it; moreover its representation in the Hankel transformed domain does not exist in the literature. This alternative method might therefore be explored, but it is not trivial to argue that it is better than the one proposed here. In computing codes and in the context of the boundary element method, the use of Mindlin's static part introduces additional integrals for particular geometries, but depending on the problem, such an approach would be faster than the one which considers the slab's static part.

2.3 Evaluation of the Inverse Hankel Transform Integrals

The regular part of the fundamental solution is given as a set of integrals for displacements

$$\begin{aligned}
u^{s,R}_r + i\, u^{s,R}_\theta &= \frac{k_0}{\mu_0} \sum_{m=-1}^{1} \mathcal{F}^s_m\, e^{i\,m\,\theta} \int_0^\infty (v_{3_m} + v_{1_m} - (v^a_{3_m} + v^a_{1_m}))\, \zeta\, J_{m+1}(\bar{r}\,\zeta)\, \mathrm{d}\zeta \\
u^{s,R}_r - i\, u^{s,R}_\theta &= \frac{k_0}{\mu_0} \sum_{m=-1}^{1} \mathcal{F}^s_m\, e^{i\,m\,\theta} \int_0^\infty (v_{3_m} - v_{1_m} - (v^a_{3_m} - v^a_{1_m}))\, \zeta\, J_{m-1}(\bar{r}\,\zeta)\, \mathrm{d}\zeta \\
u^{s,R}_z &= \frac{k_0}{\mu_0} \sum_{m=-1}^{1} \mathcal{F}^s_m\, e^{i\,m\,\theta} \int_0^\infty (v_{2_m} - v^a_{2_m})\, \zeta\, J_m(\bar{r}\,\zeta)\, \mathrm{d}\zeta
\end{aligned} \tag{2.38}$$

and tractions.

The strong decay of the integrand in Eq. (2.38) allows numerical evaluation in a truncated interval. The main drawback of the integration is the presence of poles along the formal path (when no damping is considered), or quasi-singular behaviour for poles close to the integration points (when damping is included). In order to solve these problems, a common technique consists in delineating a deformed complex integration path Levy(1976)[94], Greenfield(1995) [61] and Guzina (2001) [69], which smoothes the integrands. Figure 2.2 shows the modified contour, which is characterized by the initial slope $\tan(\phi)$ and the ζ-abscissas η_1, η_2, η_3. The path is completed from η_3 along the real axis, with $\eta_{\max}$ being the end point of the truncated interval. The method requires delineation of

the adequate path, avoiding the poles which remain in the shaded areas. The poles are given by the zeroes of the determinant det $\mathbf{G_d} = \det \mathbf{G_u}$ and $\mathbf{G_u}$, Eqs. (2.22) and (2.23).

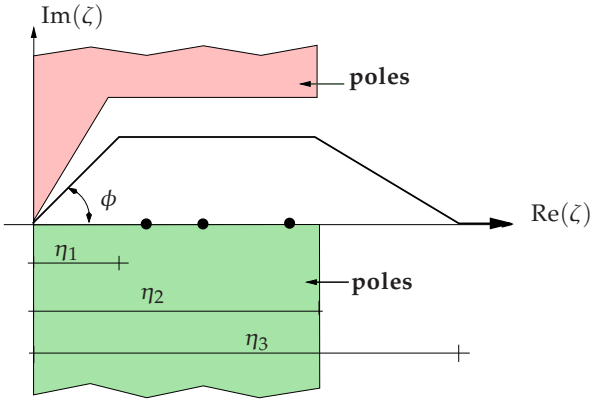

Figure 2.2: Modified integration path

2.3.1 *Asymptotic Plane-wave Limits*

Although the poles may be directly obtained by finding the roots $\bar{k}^*$ of det $\mathbf{G_d} = 0$, no closed-form expressions are available for these roots. Parameter η_2 must be chosen so that $\max \mathrm{Re}\{\bar{k}^*\} \leq \eta_2$. The way to bound the real part of the poles proposed in this chapter is to analyse plane-wave propagation problems for long values of the radial variable. The eigenfrequencies for the limiting plane problems are included in det $\mathbf{G_d} = 0$, as the radial dependence is only introduced by the Bessel functions. The PS and SH plane problems are governed by Rayleigh-Lamb waves and antiplane modes, respectively. Further details of plane-wave analysis can be found in Kundu(2004) [88].

Rayleigh Waves

Rayleigh waves are the PS waves that propagate along the free surface in a homogeneous half-space. Equation $R(\zeta) = 0$, with $R(\zeta)$ shown in Eq. (2.26), gives the normalized wavenumbers corresponding to Rayleigh waves. Let c_s and c_p be the speeds of the P and S waves, and k_s, k_p the P and S wavenumbers, respectively. The equation $R(\zeta) = 0$ is written as

$$(2k^2 - k_s^2)^2 - 4k^2\alpha\beta = 0; \tag{2.39}$$

where $\alpha = \sqrt{k^2 - k_p^2}$ and $\beta = \sqrt{k^2 - k_s^2}$. This formula can be written in dimensionless format as

$$(2 - \tau^2)^2 - 4\sqrt{(1 - \tau^2)\left(1 - \frac{\tau^2}{\kappa^2}\right)} = 0 \tag{2.40}$$

with $\tau = \dfrac{v}{v_s}$ and $\kappa = \dfrac{v_p}{v_s}$.

Since $\kappa > 1$, it can be proved Mal(1991) [103] that there is only one zero in Eq. (2.40), $\tau_R \in [0, 1]$. Thus, $\bar{k}_R = 1/\tau_R \in [0, 1]$. The phase velocity of Rayleigh waves depends on Poisson's ratio and the S-wave speed. There are two expressions for estimating v_R: Eq. (2.41) due to Viktorov(1967) [160], and Eq. (2.42) due to Schmerr(1998) [139].

$$v_R \simeq \frac{0.87 + 1.12\nu}{1 + \nu} v_s \tag{2.41}$$

$$v_R \simeq \frac{0.862 + 1.14\nu}{1 + \nu} v_s \tag{2.42}$$

Poisson's ratio is bounded by $\nu \in [0, 0.5]$; thus, considering Eqs. (2.41) and (2.42), the Rayleigh wave speed may be bounded by $v_R \in [0.87\, v_s,\ 0.96\, v_s]$. In terms of the normalized wavenumber, $\bar{k}_R \in [1.0416, 1.1494]$. In [69], the bound for the maximum pole for a multilayered half-space configuration is fixed to $\eta_2 = 1.25$, which verifies $\eta_2 > 1.1494$, defining the normalization constants ρ_0 and μ_0 from their values in the lowest-velocity layer. Such a bound is imposed in terms of the Rayleigh wave, and the proposed bound is confirmed for various multi-layered configurations by numerical experiments, in which smoothly heterogeneous configurations are tested.

Lamb Waves

Lamb waves are known as the in-plane waves for a plate and consist of P and SV waves which propagate along the planar direction. The traction-free conditions lead to two equations, the roots of which provide the symmetric or asymmetric modes.

- *Symmetric Lamb modes*. The dispersion equation is

$$\frac{\tanh(\alpha h/2)}{\tanh(\beta h/2)} = \frac{(2k^2 - k_s^2)^2}{4\, k^2\, \alpha\, \beta} \tag{2.43}$$

  Roots k in Eq. (2.43) depend on the excitation frequency ω. The mode which corresponds to zero frequency is the fundamental symmetric mode, denoted by S_0. At low frequency functions, α and β are small. Thus, the left-hand side term in Eq. (2.43) may be approximated as

$$\frac{\tanh(\alpha h/2)}{\tanh(\beta h/2)} \simeq \frac{\alpha}{\beta} \tag{2.44}$$

  With this approximation, the solution of Eq. (2.43) is

$$k_L^S = \frac{k_s^2}{2\sqrt{k_s^2 - k_p^2}}. \tag{2.45}$$

  where k_L^S stands for the symmetric Lamb wavenumber. The speed v_L^S is

$$v_L^S = 2 v_s \sqrt{1 - \frac{v_s^2}{v_p^2}} \tag{2.46}$$

  Therefore, the speed of symmetric Lamb modes at near-zero frequency is a finite value. The normalised wavenumber $\bar{k}_L^S = k_L^S / k_s$ is bounded by $1/2 < \bar{k}_L^S < 1/\sqrt{2}$, since the ratio v_s^2/v_p^2 depends only on Poisson's ratio ν. Thus, the maximum value for $\bar{k}_L^S$ from symmetric Lamb modes is $\bar{k}_L^S = 1/\sqrt{2} \simeq 0.7071$.
  In the high frequency range, the left-hand side term in Eq. (2.43) tends to the unity; thus, in this case, symmetric Lamb modes tend to Rayleigh modes, in which no unbounded wavenumbers were obtained.
- *Asymmetric Lamb modes*. The dispersion equation for these modes is

$$\frac{\tanh(\alpha h/2)}{\tanh(\beta h/2)} = \frac{4\, k^2\, \alpha\, \beta}{(2k^2 - k_s^2)^2}. \tag{2.47}$$

  The solution at zero frequency corresponds with the fundamental asymmetric mode, denoted by A_0. The solution for v_L^A in Eq. (2.47) at low frequency can be obtained by the perturbation

method [14, 103]

$$v_L^A \simeq v_s \left\{ \frac{4}{3} \left(1 - \frac{v_s^2}{v_p^2} \right) \right\}^{1/4} \left(\frac{\omega h}{2 v_s} \right)^{1/2} \tag{2.48}$$

Thus, the wavenumber k_L^A is $O(\sqrt{\omega})$ when $\omega \to 0$. As k_s is $O(\omega)$, it follows

$$\bar{k}_L^A = \frac{k_L^A}{k_s} = \frac{O(\sqrt{\omega})}{O(\omega)} = O(\frac{1}{\sqrt{\omega}}) \tag{2.49}$$

thus,

$$\lim_{\omega \to 0} \bar{k}_L^A(\omega) = +\infty. \tag{2.50}$$

The approximation defined by Eq. (2.48) is a good predicting value for the root in Eq. (2.47). From this equation, the dimensionless wavenumber for this mode is:

$$\mathrm{Re}(\bar{k}_L^A) \simeq \left[\frac{\bar{h}^2}{3} \left(1 - \mathrm{Re}(\bar{k}_p^2) \right) \right]^{-1/4} \tag{2.51}$$

The asymmetric Lamb modes are included in the solutions of $\det \mathbf{G_d} = 0$. This pole is such that the lower the frequency, the higher the value for $\mathrm{Re}\{\bar{k}_L^A\}$. Therefore, in the low frequency range, the position η_2 is defined by the condition $\eta_2 > \mathrm{Re}\{\bar{k}_L^A\}$. On the other hand, the asymmetric Lamb modes at high frequency tend to Rayleigh modes, as they do for the symmetric modes.

Antiplane Waves in a Plate

The SH eigenvalues and eigenfunctions constitute the free vibration for the antiplane modes. The propagation velocity at a fixed frequency is given by

$$v_m^{SH} = \frac{v_s}{\sqrt{1 - \left(\frac{m\,\pi}{h} \right)^2 \left(\frac{v_s}{\omega} \right)^2}}, \; m = 0, 1, 2, \ldots \tag{2.52}$$

The velocity v_s depends on ω. The 0-th mode is not dispersive, whereas modes $m = 1, 2, \ldots$ are. The dimensionless wavenumber

$$\bar{k}_m^{SH} = \sqrt{1 - \left(\frac{m\,\pi}{\bar{h}} \right)^2} \tag{2.53}$$

is bounded by $\mathrm{Re}\{\bar{k}_m^{SH}\} \leq 1$. The antiplane modes are poles in the S uncoupled propagation system. Eq. (2.30) shows that poles are given by $(1 - e^{-2\bar{\beta}\bar{h}}) = 0$, which leads to Eq. (2.53).

2.3.2 Modified Contour Path Delineation

The analysis for parameters ϕ, η_1, η_2 and η_3 proposed by [69] for the multilayered half-space problem is checked and updated for the plate solution.

- Initial angle ϕ and η_1. [69] proposed the limits of the initial slope and the height of the contour path, $\pi/8 \leq \phi \leq 3\pi/8$, and $0.05 \leq \tan(\phi) \cdot \eta_1 \leq 0.36$. For the plate domain, numerical experiments confirm the validity of these limits.
- Parameter η_2. This variable requires special attention due to the presence of Lamb modes in the plates. For the multilayered half-space problem, the bound $\eta_2 > 1.25$ was proposed, on the basis of numerical tests for multilayered configurations, in which smooth stiffness transitions were adopted. When the plate domain is tested, such a limit is not valid in the low frequency

range. It was shown in Section 2.3.1 how normalized asymmetric wavenumbers become unbounded at low frequencies, thus

$$\lim_{\omega \to 0} \mathrm{Re}\{\bar{k}_L\} = \infty \Rightarrow \lim_{\omega \to 0} \eta_2 = \infty.$$

Although the adopted criterium should be $\eta_2 = \max\{\mathrm{Re}\{\bar{k}_R\}, \mathrm{Re}\{\bar{k}_L\}\}$, with $\bar{k}_R$ being the Rayleigh wavenumber, a more practical approach is proposed in this chapter (see below).

- Parameter η_3. This is required for adequate smoothing of the integrand. A value $\eta_3 = 2 \cdot \eta_2$ is valid for any situation.

Integrals involving Bessel functions are performed by means of an advanced adaptive numerical procedure which is presented in [71] and [69].

The practical delineation of the integration path for parameter η_2 consists of the identification of situations in which the real part of the furthest pole to the imaginary axis is greater than a certain fixed parameter. The value $\eta_2 = 1.25$ has been adopted and this covers a wide range of situations in which the modified contour path is valid. In order to consider all the plate configurations, the dimensionless parameter $\gamma = \lambda_s/h$ is introduced (S-wavelength to thickness). Figure 2.3 shows the solution γ in Eq. (2.47) with $k = 1.25$ and $h/2 = \pi/(\gamma k_s)$ for $\nu \in [0, 0.5]$. It can be seen that ratios $\gamma \leq 1.575$ validate the limit $\eta_2 = 1.25$. When the ratio is $\gamma > 1.575$, the solution of Eq (2.47) provides the Lamb mode, and $\eta_2 = \mathrm{Re}\{\bar{k}_L^A\}$ must be adopted in case the value is greater than 1.25 (this depends on ν).

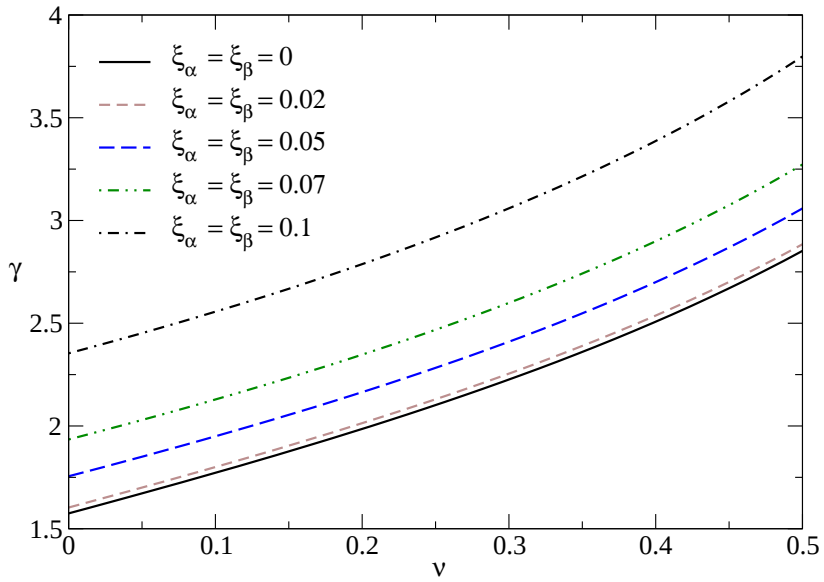

Figure 2.3: Value $\gamma = \lambda_s/h$ such that $\eta_2 = 1.25$ vs. Poisson's ratio ν.

The situations in which the upper limit corresponds to the asymmetric Lamb modes are limited to the low frequency range. Table 2.1 shows the values obtained for $\bar{k}_L^A$ when Poisson's ratio $\nu = 0$ and no damping is given, which constitutes the limiting case. The value $\gamma = 1000$ would be considered a practical maximum value to use the dynamic solution instead of the static Green's function. The

numerical procedure for integration in the interval $[\eta_1, \eta_2]$ consists of an adaptive method, fixing η_2 and iterating until the required accuracy is attained.

γ	$\bar{k}_L$
1	1.1797
2	1.3067
10	2.1826
100	6.3116
1000	19.766

Table 2.1: Normalized Lamb wavenumbers at $\nu = 0$; no damping.

Figure 2.4 shows an example of function $v_{2_m} - v^a_{2_m}$ defined in Eq. (2.38). A vertical source at position $s/h = 0.25$ and an observation point at $z/h = 0.1$, $r = 0$ have been considered. For a pure-vertical load, $m = 0$ is the only term in the series. Two integration paths have been delineated, with $\eta_1 = 0.5$, $\eta_2 = 7$, $\eta_3 = 8$; paths differ only in the initial slope: $\tan(\phi) = 0.5$ for "Path 1", and $\tan(\phi) = 0.1$ for "Path 2". Four frequencies have been tested, at $\gamma \in \{1, 2, 10, 100\}$. The figure shows:

- The maximum pole locations (pole positions agree with the results shown in Table 2.1).
- The role of the initial slope (the initial slope $\tan(\phi) = 0.5$ produces a smoother integrand than $\tan(\phi) = 0.1$ since it is further from the real axis).

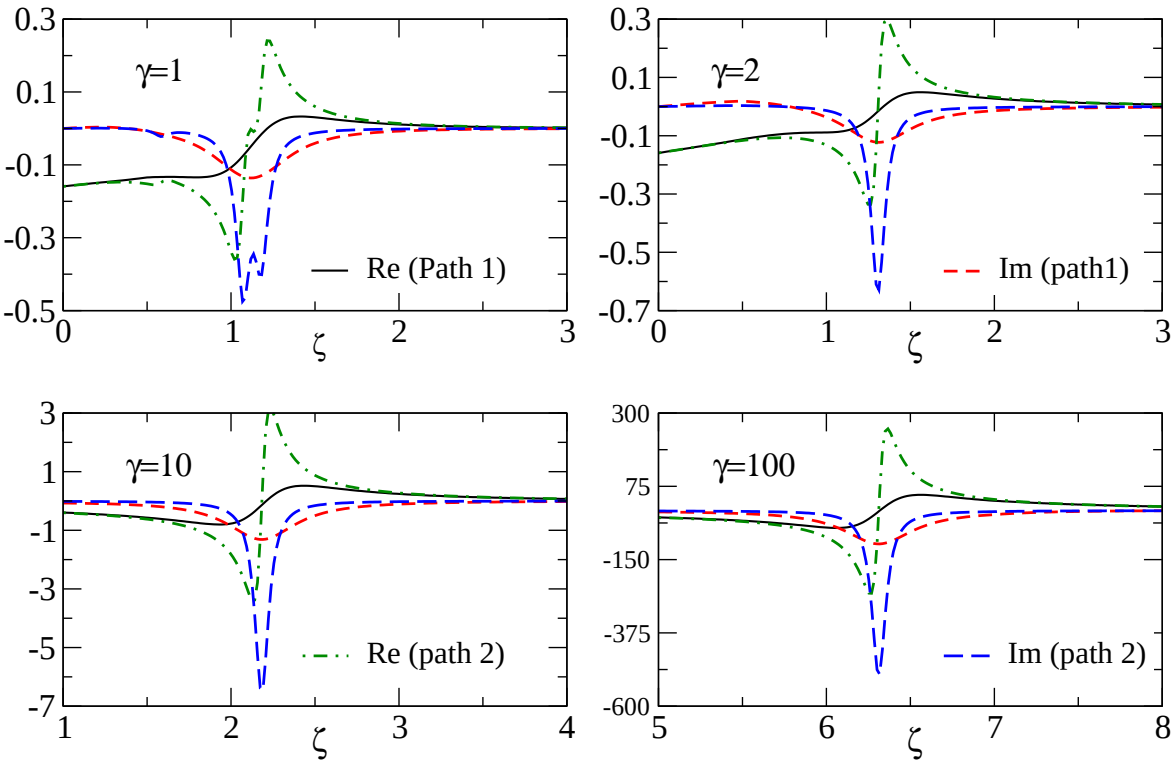

Figure 2.4: Curves $v_{2_0} - v^a_{2_0}$ along the integration path

2.4 Validation

In this section, the Green's function is validated by means of a series of tests and a double consideration:

a) Tests based on the reciprocity theorem for displacement and layer geometry for stresses, in which the basic properties of the fundamental solution are tested using only the approach presented in this chapter;

b) A direct comparison with previously published plots in which the layer's fundamental solution is obtained using different techniques.

2.4.1 Reciprocity Check

The elastodynamic displacement field corresponding with any fundamental solution must fulfill a basic identity,

$$u_i^j(\mathbf{x}, \mathbf{y}, \omega) = u_j^i(\mathbf{y}, \mathbf{x}, \omega) \tag{2.54}$$

called *Maxwell-Betti's reciprocity identity*, where $\mathbf{x}$ and $\mathbf{y}$ are the positions of the receiver and source points, respectively. Superscript j denotes the Cartesian component of the source force. The subscript i stands for the Cartesian component of the displacement field.

Figure 2.5 shows the reciprocity comparison. A layer, thickness h, and parameters μ, $\nu = 1/3$, is considered. The point force value is μh^2. A dimensionless excitation frequency $\Omega = 12$, with $\Omega = \omega h/\sqrt{\mu/\rho}$ is set. The figure represents the real and imaginary parts for two solutions. For the first one, u_3/h displacement is computed for a source pointing to the x_1 direction located at $(0, 0, 0.25h)$ and receivers at $(h, 0, z)$. The second distribution shows u_1/h corresponding with a set of sources pointing to the x_3 direction in $(h, 0, z)$ at the observation point $(0, 0, 0.25h)$. The contrast between both solutions shows a perfect agreement. Although this test shows that the displacement components fulfil the Maxwell-Betti identity, the result is not exclusive to the layered solution. In order to check specific properties of the plate domain, the following test is proposed for tractions.

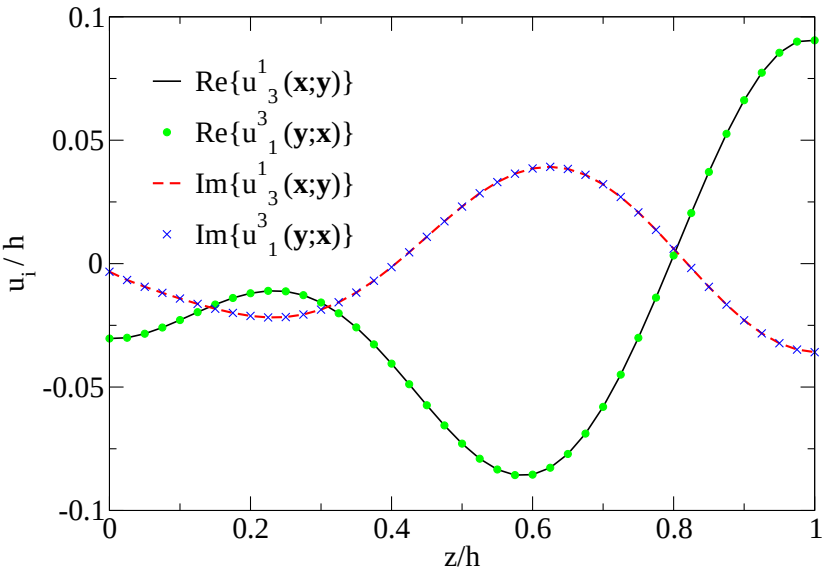

Figure 2.5: Reciprocity theorem check

2.4.2 *Traction Fundamental Solution Symmetry Check*

The layer fundamental solution shows certain symmetries or asymmetries with respect to the plane $z = h/2$, due to the geometric configuration and the boundary conditions prescribed. This aspect may be tested in traction fields by comparing two solutions. A layer, thickness h, stiffness μ and Poisson's ratio $\nu = 0.3$ is considered. "Solution 1" consists of a point source μh^2 located at $(x_1, x_2, x_3) = (0, 0, 1/3h)$. Two source directions (in x_1 and x_3 directions) are considered in two independent tests. Traction profiles τ_{ij} are computed at $(h, 0.5h, \chi)$, $\chi = x_3 \in [0, h]$. "Solution 2" consists of a source μh^2 located at $(x_1, x_2, x_3) = (0, 0, 2/3h)$, for which traction profiles are computed at $(h, 0.5h, \chi)$, with $\chi = h - x_3$. Both solutions show $\tau_{ij}^{\text{Sol.1}}(h, 0.5h, \chi) = \pm\tau_{ij}^{\text{Sol.2}}(h, 0.5h, \chi)$, where the sign depends on the source location (symmetric or asymmetric profiles). The x-axis represents the dimensionless abscissa χ/h. For both problems, a dimensionless excitation frequency $\Omega = \omega h/(\sqrt{\mu/\rho}) = 12$ is given as input data.

Figure 2.6 represents the comparison between both solutions for a source load pointing to the x_3 direction (vertical load). The relation between traction components is

$$\begin{array}{lll} \tau_{11}^{\text{Sol.1}} = -\tau_{11}^{\text{Sol.2}}; & \tau_{22}^{\text{Sol.1}} = -\tau_{22}^{\text{Sol.2}}; & \tau_{33}^{\text{Sol.1}} = -\tau_{33}^{\text{Sol.2}}; \\ \tau_{12}^{\text{Sol.1}} = -\tau_{12}^{\text{Sol.2}}; & \tau_{13}^{\text{Sol.1}} = \tau_{13}^{\text{Sol.2}}; & \tau_{23}^{\text{Sol.1}} = \tau_{23}^{\text{Sol.2}}. \end{array} \tag{2.55}$$

Perfect agreement is observed. Figure 2.7 shows the traction profiles for a source pointing to the x_1 direction (horizontal load). For this problem,

$$\begin{array}{lll} \tau_{11}^{\text{Sol.1}} = \tau_{11}^{\text{Sol.2}}; & \tau_{22}^{\text{Sol.1}} = \tau_{22}^{\text{Sol.2}}; & \tau_{33}^{\text{Sol.1}} = \tau_{33}^{\text{Sol.2}}; \\ \tau_{12}^{\text{Sol.1}} = \tau_{12}^{\text{Sol.2}}; & \tau_{13}^{\text{Sol.1}} = -\tau_{13}^{\text{Sol.2}}; & \tau_{23}^{\text{Sol.1}} = -\tau_{23}^{\text{Sol.2}}. \end{array} \tag{2.56}$$

Perfect agreement is also observed for this case.

2.4.3 *Comparison with Results based on Different Methods*

The aim of these tests is the direct comparison with previously published results. The source for comparison is found in [7] which described the solution for a layered isotropic plate based on the double Fourier transform. The solution is built through modal superposition. An alternative solution is shown for a pure-vertical load (axisymmetric problem) based on a hybrid model, also reported by [7], in which the Hankel functions of the first kind constitute the modal base at the near-field.

A plate, thickness h, elastic moduli μ and Poisson's ratio $\nu = 1/3$ is considered. A vertical source μh^2 is located at $(x_1, x_2, x_3) = (0, 0, h/4)$. The receiver is located at $(h, 0, z)$, where $z \in [0, h]$. The u_3/h dimensionless displacement is computed at z. The dimensionless frequency $\Omega = \omega h/\sqrt{\mu/\rho} = 20$ is considered. The factor $e^{-i\omega t}$ is considered at Bai's solution; thus, the conjugate complex of the solution proposed here is compared with the ones obtained by the hybrid and modal superposition methods.

Figure 2.8 shows the comparison between three methods. Although agreement is quite good, better agreement is observed with the hybrid method, and this is due to the similar near-field representation between the hybrid method and the solution proposed here which is based on the Hankel transform. Both representations better reproduce singular behaviour at the source neighbourhood. Since the modal superposition method is based on the addition of planar waves (rather than singular solutions), the near-field behaviour therefore requires more terms in order to give an accurate result.

The comparison for a horizontal source is shown in Figure 2.9. A source μh^2 pointing to the x_1 direction is located at $(0, 0, h/4)$. The dimensionless vertical displacement u_3/h is computed at $(h, 0, z)$. The value $\Omega = 20$ has been considered. For this problem, only the modal superposition solution is available (the hybrid method is valid only for vertical load). Agreement between the

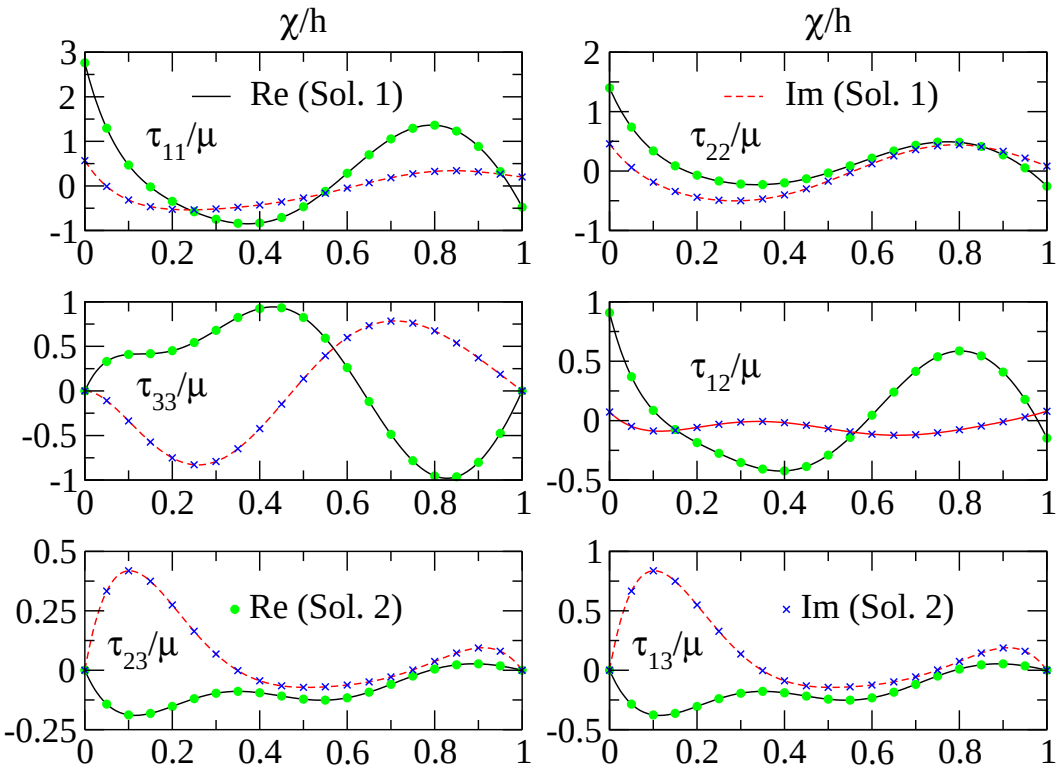

Figure 2.6: Symmetry cross-check for a vertical source, force μh^2, $\Omega = 12$

results is good, and small differences are observed due to the different representations at the near field.

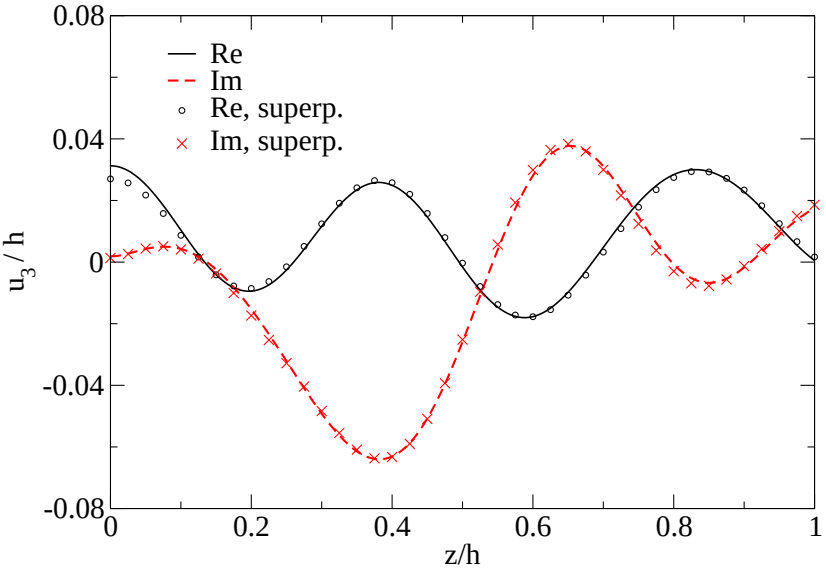

Figure 2.9: Comparison with Bai *et al.* (2004) results, horizontal source μh^2, vertical displacement. $\Omega = 20$. Source at $(0, 0, h/4)$. Results at (h,0,z)

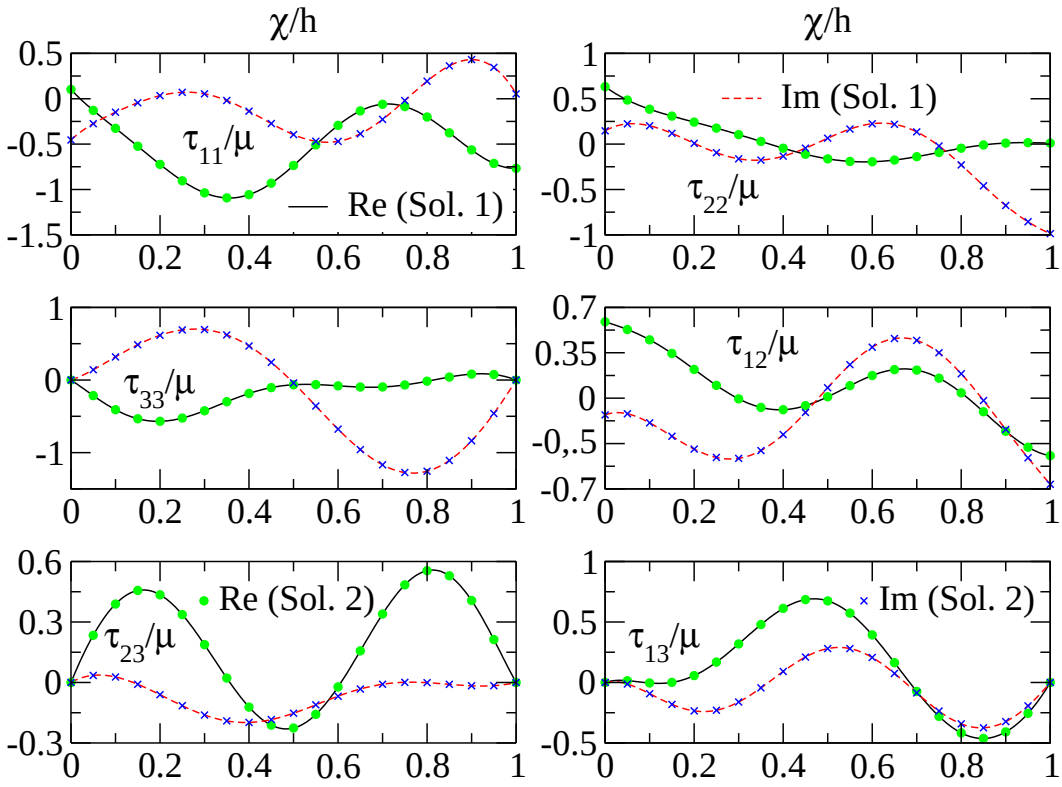

Figure 2.7: Symmetry cross-check for a horizontal source, force $\mu\, h^2$, $\Omega = 12$

2.5 Concluding Remarks

This chapter presents the fundamental solution for the three-dimensional elastodynamic problem for an isotropic layer domain. Time-harmonic formulation has been considered, and damping is included by complex-valued material parameters. The solution method based on the propagator matrix method, including updates by [124], has been adopted to develop the Green's function, and the specific reflection matrix components for the plate domain are presented. Displacement and traction components are given by two adding terms: an analytical closed-form solution (corresponding with the static half-space problem) and a regular integral (which must be evaluated by numerical methods). The modified integration path technique is used to obtain a smooth integrand. A careful analysis of poles reveals that the asymmetric Lamb's normalized wavenumber becomes unbounded when the frequency decreases. A specific treatment is proposed to identify the position of such poles, which may be extended to multilayered configurations, in which a strong stiffness transition permits the presence of Lamb waves, not only for plates, but for some multilayered half-space configurations. Numerical tests confirm theoretical and practical aspects have been correctly developed.

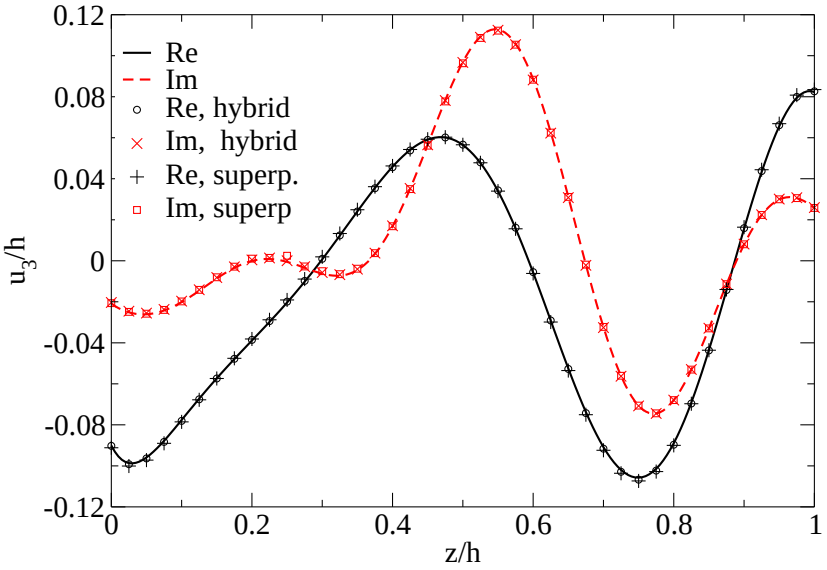

Figure 2.8: Comparison with Bai *et al.* (2004) results, vertical source μh^2, vertical displacement. $\Omega = 20$. Source at $(0, 0, h/4)$. Results at (h,0,z)

CHAPTER 3

Singular boundary elements for three-dimensional elasticity problems

3.1 Introduction

One of the common features of mixed boundary value problems in solid mechanics is the presence of non-smooth boundary and interfacial surfaces. As demonstrated by a number of studies (see works by Williams or Dempsey, [163, 42]), sharp geometries such as those involved in punch problems (Fig. 3.1) often give rise to the theoretical occurrence of singular contact tractions which can cause inaccuracy and poor convergence in numerical analyses. To address these computational issues and pursue a truly rigorous solution to solid mechanics problems in the context of Boundary Integral Equation (BIE) formulations, the development of specialized boundary elements capable of representing singular contact tractions would clearly be beneficial. Beyond its inherent utility as a tool for establishing 3D benchmark results, such careful treatment may also elevate the analysis of nano-indentation unloading response (e.g. Pha (2002)[130]) involving sharp indenters of arbitrary shape.

Usage of traction-singular elements in BIE dates back to Cruse (1977)[38] dealing with 2D problems in linear fracture mechanics. This work was followed by a series of studies (e.g. Ingra, Martínez or Gray, [15, 106, 60]) on the development and use of a so-called "quarter-point" boundary element that is consistent with the occurrence of square-root singular tractions. Complicating the issue further, however, is the coincidental presence of non-unique tractions at boundary corners and edges. The latter problem can be mitigated by the use of double nodes, tangential derivatives, or discontinuous boundary elements (e.g., Rego Silva (1993) [135], Stamos(1995) [146]). As an example of a comprehensive treatment of non-smooth boundaries in 2D elasticity, [98] have proposed a set of semi-discontinuous lineal boundary elements equipped to deal with both traction discontinuities and power-type singularities of variable order.

In three-dimensional BIE stress and deformation analyses, on the other hand, attention has mostly been focused on the treatment of fracture mechanics problems and associated square-root traction singularities. For instance, an eight-node crack tip element with singular traction shape functions was introduced in Luchi(1987)[100], while a nine-node surface analog of the lineal "quarter point" element was developed in Ariza(1997)[6]. More recently a continuous, variable-order boundary element was proposed in Zhou(2005)[166] for the specific purpose of calculating stress intensity factors featuring 3D multi-domain fracture problems. Despite its utility, however, the latter crack tip element requires the continuity of tractions across its "front", representing the material or crack edge. As such, it is not suited for the treatment of *non-unique* tractions occurring along the perimeter of smooth boundary surfaces that may intersect or terminate at arbitrary angles relative to each other.

To advance the rigorous BIE treatment of problems in 3D solid mechanics, the focus of this paper is a set of semi-discontinuous, surface boundary elements that are capable of representing *both*

traction discontinuities and integrable power-type traction singularities, while permitting a smooth transition to regular surface elements away from material edges. For generality, these variable-order singular elements are developed in their four-node (linear) and eight-node ("serendipity" quadratic) variants, allowing for situations when either one or two of the (adjacent) element's sides coincide with material edges. Enhanced by the proposed treatment of singular and non-unique surface tractions, the regularized BIE solution is found to perform well, with fast and stable convergence for both static and dynamic benchmark problems. Further uses of the proposed methodology may involve the analysis of 3D contact problems associated with sharp indenters, as well as the calculation of stress-intensity factors for intersecting boundary and interfacial surfaces.

3.2 Singularity of tractions at non-smooth material interfaces

In the analyses of 3D solids involving arbitrary geometric and material configurations, one often needs to consider domains that are bounded by surfaces containing curves across which the normal to the boundary exhibits a discontinuity. For further reference, the smooth segments of such curves will be denoted as *edges*, while the points of their intersection, contact, or termination will be referred to as *corners*. From the local analyses (e.g. Dempsey(1981)[42]), it is well known that the stress field at those locations may become singular. As a result, the convergence and accuracy of numerical solutions for this class of problems can be improved by incorporating such local characteristics into the computational scheme [9, 74, 126]. A rigorous treatment of the rigid punch problems in Fig. 3.1, for instance, would demand such an analysis. To determine the singular character of stresses in the vicinity of material edges and corners, the following analytical observations are relevant:

- For points at a fixed distance from boundary corners, the near-edge displacement and stress gradients in the direction parallel to an edge are usually negligible compared to the ones in the perpendicular direction (ver Bažant[10]). As a result, the problem may be analyzed as that of either plane or anti-plane strain depending on loading conditions.

- The singular character of stresses is unaffected by the (regular) inertial forces. Consequently, one may explore singular dynamic stresses by considering the corresponding static problem. This statement can be established by assuming a power-type, time-harmonic behavior of the displacement field, $\boldsymbol{u}(r,\theta,t) = \boldsymbol{f}(\theta,\omega)\, e^{i\omega t}\, r^{\lambda}$, $Re(\lambda) < 1$ in the vertex neighborhood, where (r,θ) are the local polar coordinates (see Fig. 3.1) and ω is the frequency of vibration. Substitution of the foregoing format into Navier equations reveals that the inertia term remains finite for all points. As such, it becomes negligible relative to (unbounded) displacement gradients as $r \to 0$.

3.2.1 Edge singularity

The edge-induced singularity of the stress fields for various multi-material (or equivalently multi-wedge) configurations in the context of *plane strain* has been explored in studies ranging from the classical works of Williams(1952) [163] and Bogy(1968, 1971) [16, 18] to more recent developments [154, 150, 29, 121, 165]. As shown in Bogy, for example, singular behavior of the stress field at the apex of a bonded bi-material wedge such as those featured in Fig. 3.1 can be determined from an eigen-problem (signifying the existence of non-trivial stresses under zero body forces and surface tractions as $r \to 0$) that is formulated by means of the Airy stress function and Mellin integral transform [157].

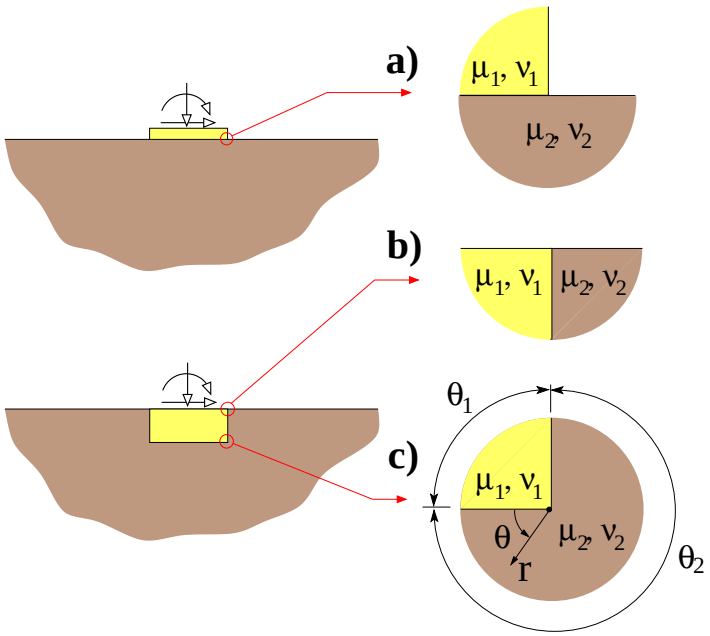

Figure 3.1: Rigid punch problems ($\mu_1 \to \infty$) involving bi-material edge configurations

With reference to a *closed* bi-material configuration depicted in Fig. 3.1c, the order of singularity in the stress field at the wedge apex can be shown, using the latter approach, to permit the representation

$$\tau_{ij}(r,\theta) = \left\{ \begin{array}{l} r^{-(\zeta+2)} \left\{ f_{ij}^{c}(\theta)\cos(\eta\log(r/r_o)) + f_{ij}^{s}(\theta)\sin(\eta\log(r/r_o)) \right\} \\ \qquad + o\left(r^{-(\zeta+2)}\right), \qquad \text{if} \quad \mathcal{D}_e(\lambda)=0, \quad \mathcal{D}_e'(\lambda)\neq 0 \quad (\lambda=\zeta+i\eta, \quad \zeta<-1), \\ r^{-(\zeta+2)}\log(r/r_o)\left\{ f_{ij}^{c}(\theta)\cos(\eta\log(r/r_o)) + f_{ij}^{s}(\theta)\sin(\eta\log(r/r_o)) \right\} \\ \qquad + o\left(r^{-(\zeta+2)}\right), \qquad \text{if} \quad \mathcal{D}_e(\lambda)=\mathcal{D}_e'(\lambda)=0. \quad (\lambda=\zeta+i\eta, \quad \zeta<-1) \end{array} \right\}, \quad r\to 0 \tag{3.1}$$

in the local polar coordinates (r,θ) centered at the material edge $r=0$. Here $f_{ij}^{c}(\theta)$ and $f_{ij}^{s}(\theta)$ are analytic functions of the angular coordinate; $i,j\in\{r,\theta\}$; r_o is a reference length, and λ is a zero, with the largest real part in the strip $-2<\mathrm{Re}(s)<-1$ [17], of the characteristic equation

$$\begin{aligned} \mathcal{D}_e(s) \;\equiv\; & \left\{(\mathcal{M}_1-\mathcal{M}_2)^2(1+s)^2\sin^2\theta_1 - (1-\mathcal{M}_2)^2\sin^2(1+s)\theta_1\right\}\times \\ & \left\{(1+\mathcal{M}_2)^2\sin^2(1+s)\theta_2 - (\mathcal{M}_1-\mathcal{M}_2)^2(1+s)^2\sin^2\theta_2\right\} \\ & +\; (\mathcal{M}_1^2-1)\sin^2(1+s)(\pi-\theta_2)\left\{2(\mathcal{M}_1-\mathcal{M}_2)^2(1+s)^2\sin^2\theta_2 + \right. \\ & \left. 2(1-\mathcal{M}_2^2)\sin(1+s)\theta_1\sin(1+s)\theta_2 - (\mathcal{M}_1^2-1)\sin^2(1+s)(\pi-\theta_2)\right\} \;=\; 0, \end{aligned} \tag{3.2}$$

where θ_k ($k=\overline{1,2}$) is the angle subtended by the kth material wedge with shear modulus μ_k and Poisson's ratio ν_k, and

$$\mathcal{M}_1 = \frac{\mu_1(1-\nu_2)-\mu_2(1-\nu_1)}{\mu_1(1-\nu_2)+\mu_2(1-\nu_1)}, \qquad \mathcal{M}_2 = \frac{\mu_1(\frac{1}{2}-\nu_2)-\mu_2(\frac{1}{2}-\nu_1)}{\mu_1(1-\nu_2)+\mu_2(1-\nu_1)}. \tag{3.3}$$

One may observe that (3.1) encompasses oscillating ($\eta\neq 0$) as well as non-oscillating ($\eta=0$) power, logarithmic and power-logarithmic type singularities of the stress field. It is also worth noting that the stress field τ_{ij} exhibits no singularities for $Re(\lambda)<-2$, while the pure logarithmic type singularity

occurs when $\lambda = -2$ is a second-order zero of $\mathcal{D}_e(s)$. Higher powers of $\log(r/r_o)$ may also be deduced by considering the n^{th} order poles, $n > 2$. This type of singularity, however, has not been found to occur in elasticity problems [41].

In the case of an *open* bi-material edge featured in Figs. 3.1a and 3.1b, formula (3.1) still applies provided that the determinant function $\mathcal{D}_e(s)$ is replaced by the expression [18]

$$\begin{aligned}
\mathcal{D}_s(s) &= 4\mathcal{M}_2^2\,\mathcal{K}(s,\theta_2)\,\mathcal{K}(s,\theta_1) + 4\mathcal{M}_1\,\mathcal{M}_2\,(1{+}s)^2\,\Big\{\mathcal{K}(s,\theta_1)\,\sin^2\theta_2 + \mathcal{K}(s,\theta_2)\,\sin^2\theta_1\Big\} \\
&+ \mathcal{M}_1^2\,\Big\{4(1{+}s)^2(2s+s^2)\sin^2\theta_2\,\sin^2\theta_1 + \mathcal{K}(s,\theta_2{-}\theta_1)\Big\} \\
&+ 4\mathcal{M}_2\,(1{+}s)^2\,\Big\{\mathcal{K}(s,\theta_1)\,\sin^2\theta_2 - \mathcal{K}(s,\theta_2)\,\sin^2\theta_1\Big\} \\
&+ 2\mathcal{M}_1\Big\{2(1{+}s)^2\Big(\mathcal{K}(s,\theta_2)\,\sin^2\theta_1 - \mathcal{K}(s,\theta_1)\,\sin^2\theta_2\Big) + \mathcal{K}(s,\theta_1) - \mathcal{K}(s,\theta_2)\Big\} + \\
&+ \mathcal{K}(s,\theta_2{+}\theta_1), \qquad \mathcal{K}(s,\theta) = \sin^2(1{+}s)\theta - (1{+}s)^2\sin^2\theta.
\end{aligned} \tag{3.4}$$

in which $\mathcal{M}_1$ and $\mathcal{M}_2$ are given in (3.3).

From the analyses of this kind, it is generally understood that the local, near-edge variation of the stress field components is of the form

$$\log^m(r/r_o)\ \mathrm{Re}\left(\frac{f_\gamma(\theta)}{r^\gamma}\right) \quad \text{as} \quad r\to 0, \qquad \mathrm{Re}(\gamma)<1, \quad m=0,1 \tag{3.5}$$

where $f_\gamma(\theta)$ is complex-valued and regular, and $\gamma \equiv \lambda{+}2$ is an eigenvalue (so-called singularity exponent) that is obtained as a solution of the characteristic equation associated with the relevant edge configuration in terms of the angles, material properties, and interfacial conditions of participating wedges. Here it is again useful to note that $\mathrm{Im}(\gamma)$ gives rise to an oscillating-type singularity [165].

In deciding suitable values of γ in (3.5) via local analysis such as that in (3.2)–(3.4), however, it should be noted that:

- Taking the root of a featured characteristic equation, e.g. (3.2) or (3.4), with the *largest* real part takes into account only the *strongest possible* singularity predicted by the local analysis. In situations where multiple characteristic values with $-2 < \mathrm{Re}(\lambda) < -1$ exist, their participation in the elastic response depends on a particular (global) boundary value problem and transcends the predictive capabilities of local analyses [41].
- Likewise, the relevance of either *plane-strain* local analysis (illustrated in this study) or its *anti-plane* counterpart (e.g. [110, 107]) again depends on the global conditions, e.g. the mode of crack loading in the context of linear fracture mechanics.

To provide a focus in the study, the performance of proposed singular elements is illustrated on the basis of these two simplifying assumptions, namely i) the relevance of the characteristic value λ with the largest real part, and ii) that of the plane-strain singularity analysis. The computational platform established with the aid of these special elements however transcends these limitations.

3.2.2 Corner singularity

To determine the singular character of stresses in the neighborhood of corner points where two-dimensional solutions are no longer applicable, one may employ for instance 3D asymptotic eigen-analyses as in [10, 11, 145, 120, 84] where the local, power-type expansion of the stress field is coupled with a suitable (finite element, finite difference or boundary element) discretization of the multi-material configuration characterizing the neighborhood of the corner point. Notwithstanding their

theoretical importance, however, the corner singularities are often highly localized and tend to be less critical to the global solution than their edge counterparts.

In this paper, a practical computational platform that can utilize the foregoing asymptotic analyses for the enhancement of three-dimensional Boundary Integral Equation (BIE) methods is developed. To cater for engineering applications, the study is focused on the derivation of specialized boundary elements that are capable of effectively incorporating the discontinuous and locally-singular nature of surface tractions occurring along material *edges*. Depending on the problem configuration, local asymptotic analyses predict power, logarithmic, or power-logarithmic type singularities of the stress field (as well as their oscillatory variants) in the vicinity of material edges. By their nature, however, the logarithmic and oscillatory features of local stress concentrations typically have a limited effect on the overall resultant of boundary tractions, and thus on the global BIE solution. To deal with the key effects of non-smooth material boundaries, this investigation is accordingly concerned with a local, boundary element treatment of *power-type* traction singularities corresponding to $m=0$ and $\mathrm{Im}(\gamma)=0$ in (3.5).

3.3 Singular four–node elements

With reference to the parent domain $\{\eta_1,\eta_2|\ -1\le\eta_1\le 1,-1\le\eta_2\le 1\}$ of an M-node quadrilateral boundary element whose geometry (x_i), displacements (u_i) and tractions (t_i) are interpolated as

$$\begin{array}{rcll} x_i(\eta_1,\eta_2) & = & \sum_{m=1}^{M} x_i^m\,\phi_m^g(\eta_1,\eta_2), & \\ u_i(\eta_1,\eta_2) & = & \sum_{m=1}^{M} u_i^m\,\phi_m^d(\eta_1,\eta_2), & i=1,2,3 \\ t_i(\eta_1,\eta_2) & = & \sum_{m=1}^{M} t_i^m\,\phi_m^t(\eta_1,\eta_2), & \end{array} \tag{3.6}$$

in terms of their respective nodal values, the task at hand can be readily reduced to the development of specialized traction shape functions ϕ_m^t (and their companions ϕ_m^g and ϕ_m^d) that properly account for both singularity and discontinuity of interfacial tractions in situations when selected element sides coincide with material edges.

3.3.1 Edge element

As a canonic configuration of interest, one may consider the four-node quadrilateral element ($M=4$) with the parent domain $\{\eta_1,\eta_2|\ -1\le\eta_1\le 1,-1\le\eta_2\le 1\}$ whose side $\eta_1=1$ coincides with a sharp boundary edge. Consistent with the previous discussion, the singular traction behavior is assumed to be of the form

$$t_i(\eta_1,\eta_2)=\frac{\psi_i(\eta_1,\eta_2)}{(1-\eta_1)^{\alpha}}\quad\text{as}\quad \eta_1\to 1,\quad -1\le\eta_2\le 1,\quad 0\le\alpha<1,\qquad i=1,2,3 \tag{3.7}$$

where t_i are the Cartesian components of a traction vector; ψ_i are smooth and regular over the parent domain, and α is the order of traction singularity as $\eta_1\to 1$. To adequately represent (3.7) in the context of piecewise-smooth boundary and interfacial geometries, the sought "edge" element must obviously be *sub-parametric* in terms of its shape functions. To mirror the non-uniqueness of edge tractions, on the other hand, the element should also allow for their discontinuity across side $\eta_1=1$. With reference to Fig. 3.2a, the latter requirement can be met by introducing a semi-discontinuous, four-node boundary element whose nodes 2 and 3 are shifted away from the singular edge. In what follows, such nodal shifting will be imposed in terms of *both* traction, displacement, and geometry shape functions for "back-compatibility" with conventional collocation schemes, and in particular the regularized BIE method [125] employed in this study. Here it is useful to note that the featured

perturbation of geometric description, while deemed inessential for the examples presented, maintains the uniqueness of a normal to the boundary; a feature that that may facilitate the treatment of elasticity problems involving moving boundaries (see Guzina(2003)[67]).

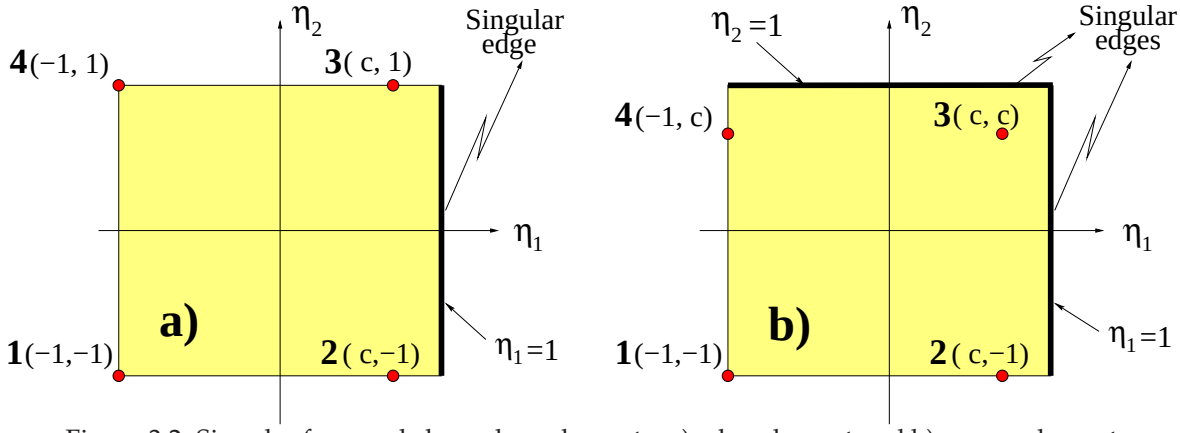

Figure 3.2: Singular four-node boundary elements: a) edge element and b) corner element

The basic requirement for the *geometry* shape functions $\phi^g_m(\eta_1,\eta_2)$, $m=\overline{1,4}$ characterizing any boundary element is the one of completeness, i.e. the element's ability to exactly reproduce planar geometries. To satisfy the completeness requirement while maintaining compatibility with the neighboring regular (isoparametric) element along side $\eta_1=-1$, the geometry shape functions for the "edge" element are assumed in the bilinear form

$$\begin{aligned}
\phi^g_1(\eta_1,\eta_2) &= \frac{(c-\eta_1)(1-\eta_2)}{2\,(1+c)},\\
\phi^g_2(\eta_1,\eta_2) &= \frac{(1+\eta_1)(1-\eta_2)}{2\,(1+c)},\\
\phi^g_3(\eta_1,\eta_2) &= \frac{(1+\eta_1)(1+\eta_2)}{2\,(1+c)},\\
\phi^g_4(\eta_1,\eta_2) &= \frac{(c-\eta_1)(1+\eta_2)}{2\,(1+c)},
\end{aligned} \tag{3.8}$$

where $0<c<1$ is a pre-defined parameter which specifies the location of internal nodes 2 and 3 as shown in Fig. 3.2a.

For the class of boundary value problems of interest in this study, requirements for the *displacement* shape functions, $\phi^d_m(\eta_1,\eta_2)$, $m=\overline{1,4}$ are similar: they must be able to i) exactly represent the rigid-body motions of the domain boundary, and ii) maintain the C_0-compatibility of the displacement field with the neighboring isoparametric element along side $\eta_1=-1$. Accordingly, one may assume

$$\phi^d_m(\eta_1,\eta_2) = \phi^g_m(\eta_1,\eta_2), \qquad -1\le\eta_1\le 1, \quad -1\le\eta_2\le 1, \qquad m=\overline{1,4}. \tag{3.9}$$

On expanding the regular auxiliary functions $\psi_i(\eta_1,\eta_2)$ over the parent domain in Taylor series at $\eta_1=1$, the *traction* shape functions $\phi^t_m(\eta_1,\eta_2)$, $m=\overline{1,4}$ which can correctly represent the singular

traction behavior (3.7) can be written as

$$\begin{aligned}
\phi_1^t(\eta_1,\eta_2) &= \left\{a_1(1-\eta_1)^{-\alpha}+b_1(1-\eta_1)^{1-\alpha}\right\}(1-\eta_2),\\
\phi_2^t(\eta_1,\eta_2) &= \left\{a_2(1-\eta_1)^{-\alpha}+b_2(1-\eta_1)^{1-\alpha}\right\}(1-\eta_2),\\
\phi_3^t(\eta_1,\eta_2) &= \left\{a_3(1-\eta_1)^{-\alpha}+b_3(1-\eta_1)^{1-\alpha}\right\}(1+\eta_2),\\
\phi_4^t(\eta_1,\eta_2) &= \left\{a_4(1-\eta_1)^{-\alpha}+b_4(1-\eta_1)^{1-\alpha}\right\}(1+\eta_2),
\end{aligned} \tag{3.10}$$

for $-1<\eta_1<1,\ -1<\eta_2<1$ and $0\le\alpha<1$, where a_m and b_m ($m=\overline{1,4}$) are some constants. As can be seen from (3.10), ϕ_m^t are all characterized by a linear variation in the η_2-direction to maintain the C_0-compatibility of tractions with neighboring isoparametric elements along $\eta_2=\pm1$. The variation of tractions in the η_1-direction, on the other hand, is composed of the singular term $(1-\eta_1)^{-\alpha}$ and the higher-order, regular term $(1-\eta_1)^{1-\alpha}$. The unknown coefficients in (3.10) can be determined from the requirement that the traction shape functions are uncoupled, i.e. that $\phi_m^t(\eta_1^k,\eta_2^k)=\delta_{mk}$, $m,k=\overline{1,4}$ where (η_1^k,η_2^k) are the local coordinates of the k^{th} element node in Fig. 3.2a, and δ_{mk} denotes the Kronecker delta. With the aid of (3.10), this requirement yields the necessary linear algebraic equations for a_m and b_m resulting in the solution

$$\begin{aligned}
\phi_1^t(\eta_1,\eta_2) &= \frac{2^\alpha(c-\eta_1)(1-\eta_2)}{2(1+c)(1-\eta_1)^\alpha},\\
\phi_2^t(\eta_1,\eta_2) &= \frac{(1-c)^\alpha(1+\eta_1)(1-\eta_2)}{2(1+c)(1-\eta_1)^\alpha},\\
\phi_3^t(\eta_1,\eta_2) &= \frac{(1-c)^\alpha(1+\eta_1)(1+\eta_2)}{2(1+c)(1-\eta_1)^\alpha},\\
\phi_4^t(\eta_1,\eta_2) &= \frac{2^\alpha(c-\eta_1)(1+\eta_2)}{2(1+c)(1-\eta_1)^\alpha}.
\end{aligned} \tag{3.11}$$

In contrast to the surface singular elements in fracture mechanics where the square-root singularities are of primary interest (e.g. [100]), the proposed traction shape functions (3.11) are capable of representing power-type singularities of arbitrary order $0<\alpha<1$, and are thus able to deal with general multi-material edge configurations. Another useful property of the present developments is that (3.8), (3.9) and (3.11) can be reduced to the continuous isoparametric format associated with conventional four-node quadrilaterals [20] by setting $\alpha=0$ and $c=1$. Regarding the intermediate "offset" case $0<c<1$, on the other hand, it is useful to recall that the strict applicability of singular expansion (3.1) underlying (3.11) is limited to *infinitesimal* distances from the material edge. With reference to Fig. 3.3a plotting the variation of ϕ_2^t in (3.11) over a semi-open region $\{\eta_1,\eta_2|\ -1\le\eta_1<1,-1\le\eta_2<1\}$, parameter c should preferably take values close to unity for improved accuracy of singular traction computations. In the context of the collocation method, however, the latter choice results in a highly-localized variation of the Green's functions over the neighboring boundary element (sharing the singular edge) when either node 2 or 3 in Fig. 3.2a is the collocation point; a "side effect" that increases both the complexity and computational effort necessary to establish a discretized BIE. From a limited set of geometric and material configurations examined in this study, an "optimal" value of the shift parameter that balances the computational effort with numerical accuracy was found to be in the range $0.75<c<0.95$.

With reference to (3.8) and (3.9), one may note that the displacement shape functions are assumed to vary *linearly* in the η_1-direction as opposed to the *power-type* hypothesis

$$\tilde{\phi}_k^d(\eta_1,\eta_2) = \frac{(1-\eta_1)}{\phi_k^t(\eta_1^k,\eta_2^k)}\,\phi_k^t(\eta_1,\eta_2), \qquad k=\overline{1,4} \tag{3.12}$$

that is more consistent with the singular distribution of tractions in (3.11) (see, e.g., [100] for crack elements where $\alpha = 0.5$). In view of the indentation problems as a primary motivation for this study, however, bi-linear interpolation (3.9) is preferred owing to its ability to consistently represent the *rigid-body motion* of surface indenters; a requirement that could not be met with assumption (3.12).

3.3.2 Corner element

To deal with non-smooth boundary geometries in a realistic fashion, one must also allow for the presence of corners, i.e. terminal or intersection points of multiple material edges. To this end, it is useful to consider a quadrilateral boundary element shown in Fig. 3.2b whose sides $\eta_1 = 1$ and $\eta_2 = 1$ *both* coincide with material edges. For generality, it is assumed that

$$t_i(\eta_1,\eta_2) = \begin{cases} \frac{\psi_i(\eta_1,\eta_2)}{(1-\eta_1)^\alpha} & \text{as} \quad \eta_1 \to 1, \qquad -1 \le \eta_2 < 1, \qquad 0 \le \alpha < 1, \\ \frac{\psi_i(\eta_1,\eta_2)}{(1-\eta_1)^\beta} & \text{as} \quad \eta_2 \to 1, \qquad -1 \le \eta_1 < 1, \qquad 0 \le \beta < 1 \end{cases} \qquad i = 1,2,3 \tag{3.13}$$

i.e. that the orders of traction singularity along the two edges bordering the element can be distinct. With such premise and the nodal arrangement shown in Fig. 3.2b, the results from the previous section may now be extended to yield the geometry, displacement, and traction shape functions for the "corner" four-node element as

$$\begin{aligned} \phi^g_1(\eta_1,\eta_2) = \phi^d_1(\eta_1,\eta_2) &= \frac{(c-\eta_1)(c-\eta_2)}{(1+c)^2}, \\ \phi^g_2(\eta_1,\eta_2) = \phi^d_2(\eta_1,\eta_2) &= \frac{(1+\eta_1)(c-\eta_2)}{(1+c)^2}, \\ \phi^g_3(\eta_1,\eta_2) = \phi^d_3(\eta_1,\eta_2) &= \frac{(1+\eta_1)(1+\eta_2)}{(1+c)^2}, \\ \phi^g_4(\eta_1,\eta_2) = \phi^d_4(\eta_1,\eta_2) &= \frac{(c-\eta_1)(1+\eta_2)}{(1+c)^2}, \end{aligned} \tag{3.14}$$

and

$$\begin{aligned} \phi^t_1(\eta_1,\eta_2) &= \frac{2^{\alpha+\beta}(c-\eta_1)(c-\eta_2)}{(1+c)^2(1-\eta_1)^\alpha(1-\eta_2)^\beta}, \\ \phi^t_2(\eta_1,\eta_2) &= \frac{2^{\beta}(1-c)^\alpha(1+\eta_1)(c-\eta_2)}{(1+c)^2(1-\eta_1)^\alpha(1-\eta_2)^\beta}, \\ \phi^t_3(\eta_1,\eta_2) &= \frac{(1-c)^{\alpha+\beta}(1+\eta_1)(1+\eta_2)}{(1+c)^2(1-\eta_1)^\alpha(1-\eta_2)^\beta}, \\ \phi^t_4(\eta_1,\eta_2) &= \frac{2^{\alpha}(1-c)^\beta(c-\eta_1)(1+\eta_2)}{(1+c)^2(1-\eta_1)^\alpha(1-\eta_2)^\beta}. \end{aligned} \tag{3.15}$$

One may observe from (3.14) that the geometry shape functions ϕ^g_m and the displacement shape functions ϕ^g_m are again bilinear. Moreover, the C_0-continuity of the displacements and tractions between the corner element and neighboring edge elements across sides $\eta_1 = -1$ and $\eta_2 = -1$ is also maintained.

It should also be noted that the corner singularity of the traction field as $\eta_1 \to 1$ and $\eta_2 \to 1$ is modeled simply as a product of the corresponding edge behaviors. A more rigorous approach would include determination of the exact asymptotic behavior of corner tractions as examined e.g. in Koguchi works [84] and incorporation of the result in the numerical scheme. Owing to the negligible boundary area over which such behavior is exhibited, however, the current approach is found to be sufficient for all intended purposes.

As an illustration of the four-node developments, traction shape functions ϕ_2^t for the edge element and ϕ_3^t for the corner element are shown in Fig. 3.3. To avoid plotting singular values, the graphs are generated over a semi-open region $\{\eta_1, \eta_2 | -1 \leq \eta_1 < 1, -1 \leq \eta_2 < 1\}$.

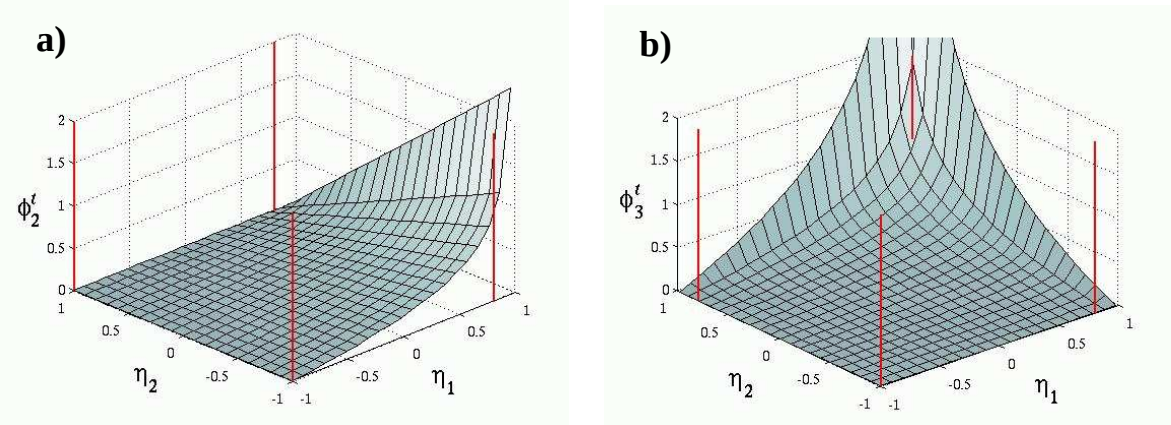

Figure 3.3: Four-node traction shape functions: a) ϕ_2^t for the edge element and b) ϕ_3^t for the corner element ($c = 0.8$, $\alpha = \beta = 0.5$)

In situations when the ability of a corner element to represent rigid-body motion is not essential, the displacement shape functions in (3.14) could be superseded, by analogy to (3.12), with their traction-compatible variants

$$\tilde{\phi}_k^d(\eta_1, \eta_2) \quad = \quad \frac{(1-\eta_1)(1-\eta_2)}{\phi_k^t(\eta_1^k, \eta_2^k)}\, \phi_k^t(\eta_1, \eta_2), \qquad k = \overline{1,4} \tag{3.16}$$

where ϕ_k^t are given by (3.15). Unless stated otherwise, however, the ensuing numerical results are based on bi-linear kinematic interpolations (3.9) and (3.14).

3.4 Singular eight–node elements

To permit more complex displacement and traction patterns such as those occurring in elastodynamics while maintaining the proper local representation of traction singularities, the foregoing four-node developments can be generalized to a set of eight-node ("serendipity") singular boundary elements which are compatible with conventional quadratic interpolation.

3.4.1 Edge element

With reference to Fig. 3.4a the eight-node, semi-discontinuous edge element ($M = 8$) is designed by shifting the nodes 2, 3, and 6 away from the material edge. As before, the nodal-shift parameter is denoted by c, while the local tractions are assumed to be power-type singular along side $\eta_1 = 1$ according to (3.7). In this setting, the geometry and displacement shape functions for the eight-node edge element that satisfy the completeness requirement can be derived as

$$
\begin{aligned}
\phi_1^g(\eta_1,\eta_2) = \phi_1^d(\eta_1,\eta_2) &= -\frac{(c-\eta_1)\,(1-\eta_2)\,(1+\eta_1+\eta_2)}{2\,(1+c)},\\
\phi_2^g(\eta_1,\eta_2) = \phi_2^d(\eta_1,\eta_2) &= -\frac{(1+\eta_1)\,(1-\eta_2)\,(c-\eta_1+c\,\eta_2)}{2\,c\,(1+c)},\\
\phi_3^g(\eta_1,\eta_2) = \phi_3^d(\eta_1,\eta_2) &= -\frac{(1+\eta_1)\,(1+\eta_2)\,(c-\eta_1-c\eta_2)}{2\,c\,(1+c)},\\
\phi_4^g(\eta_1,\eta_2) = \phi_4^d(\eta_1,\eta_2) &= -\frac{(c-\eta_1)\,(1+\eta_2)\,(1+\eta_1-\eta_2)}{2\,(1+c)},\\
\phi_5^g(\eta_1,\eta_2) = \phi_5^d(\eta_1,\eta_2) &= \frac{(c-\eta_1)\,(1+\eta_1)\,(1-\eta_2)}{2\,c},\\
\phi_6^g(\eta_1,\eta_2) = \phi_6^d(\eta_1,\eta_2) &= \frac{(1+\eta_1)\,(1-\eta_2^2)}{1+c},\\
\phi_7^g(\eta_1,\eta_2) = \phi_7^d(\eta_1,\eta_2) &= \frac{(c-\eta_1)\,(1+\eta_1)\,(1+\eta_2)}{2\,c},\\
\phi_8^g(\eta_1,\eta_2) = \phi_8^d(\eta_1,\eta_2) &= \frac{(c-\eta_1)\,(1-\eta_2^2)}{1+c}.
\end{aligned}
\tag{3.17}
$$

By design, interpolation functions in (3.17) maintain the C_0-continuity with i) singular edge elements across sides $\eta_2 = \pm 1$, and ii) regular (eight-node) isoparametric element across side $\eta_1 = -1$. The traction shape functions, on the other hand, that satisfy (3.6)-(3.7) while maintaining the quadratic variation in the η_2-direction across the edge element in Fig. 3.4a can be shown to take the form

$$
\begin{aligned}
\phi_1^t(\eta_1,\eta_2) &= -\frac{2^{\alpha-1}\,(c-\eta_1)\,(1-\eta_2)\,(1+\eta_1+\eta_2)}{(1+c)(1-\eta_1)^\alpha},\\
\phi_2^t(\eta_1,\eta_2) &= -\frac{(1-c)^\alpha\,(1+\eta_1)\,(1-\eta_2)\,(c-\eta_1+c\,\eta_2)}{2c\,(1+c)(1-\eta_1)^\alpha},\\
\phi_3^t(\eta_1,\eta_2) &= -\frac{(1-c)^\alpha\,(1+\eta_1)\,(1+\eta_2)\,(c-\eta_1-c\eta_2)}{2c\,(1+c)(1-\eta_1)^\alpha}\\
\phi_4^t(\eta_1,\eta_2) &= -\frac{2^{\alpha-1}\,(c-\eta_1)\,(1+\eta_2)\,(1+\eta_1-\eta_2)}{(1+c)(1-\eta_1)^\alpha},\\
\phi_5^t(\eta_1,\eta_2) &= \frac{(c-\eta_1)\,(1+\eta_1)\,(1-\eta_2)}{2c\,(1-\eta_1)^\alpha},\\
\phi_6^t(\eta_1,\eta_2) &= \frac{(1-c)^\alpha\,(1+\eta_1)\,(1-\eta_2^2)}{(1+c)(1-\eta_1)^\alpha},\\
\phi_7^t(\eta_1,\eta_2) &= \frac{(1+\eta_1)\,(c-\eta_1)\,(1+\eta_2)}{2c\,(1-\eta_1)^\alpha},\\
\phi_8^t(\eta_1,\eta_2) &= \frac{2^\alpha\,(c-\eta_1)\,(1-\eta_2^2)}{(1+c)(1-\eta_1)^\alpha}.
\end{aligned}
\tag{3.18}
$$

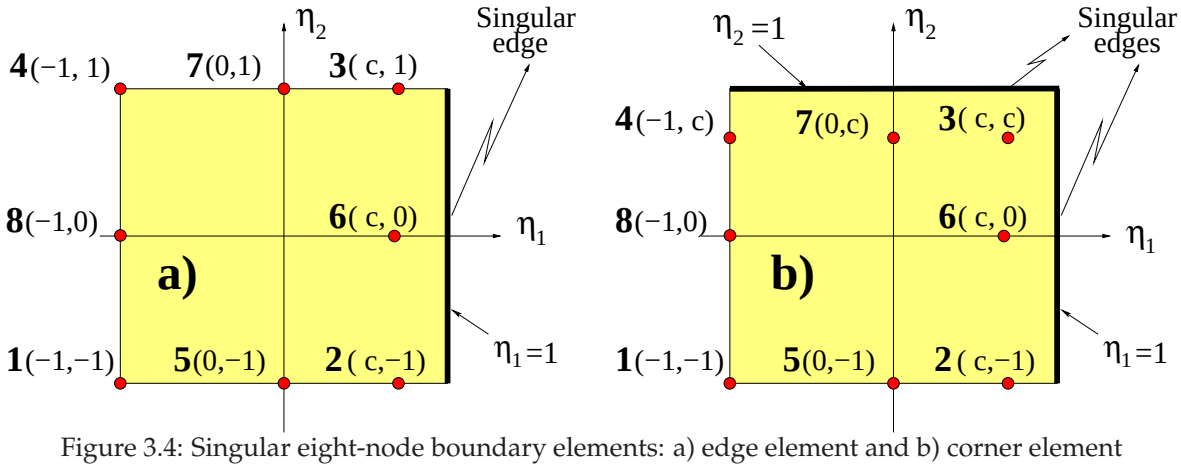

Figure 3.4: Singular eight-node boundary elements: a) edge element and b) corner element

3.4.2 *Corner element*

Following the approach outlined earlier, the relevant shape functions are next developed for the eight-node corner element depicted in Fig. 3.4b whose sides $\eta_1 = 1$ and $\eta_2 = 1$ *both* coincide with material edges. Here, the surface tractions over the element's parent domain are assumed to be singular according to (3.13). To properly account for the underlying traction discontinuities, nodes 2, 3, 4, 6 and 7 are "isotropically" shifted away from material edges by the amount c. With such assumptions, one finds that the boundary geometry and displacements are locally interpolated through the shape functions

$$
\begin{aligned}
\phi_1^g(\eta_1,\eta_2) = \phi_1^d(\eta_1,\eta_2) &= -\frac{(c-\eta_1)\,(c-\eta_2)\,(1+\eta_1+\eta_2)}{(1+c)^2},\\
\phi_2^g(\eta_1,\eta_2) = \phi_2^d(\eta_1,\eta_2) &= -\frac{(1+\eta_1)\,(c-\eta_2)\,(c-\eta_1+c\eta_2)}{c\,(1+c)^2},\\
\phi_3^g(\eta_1,\eta_2) = \phi_3^d(\eta_1,\eta_2) &= -\frac{(1+\eta_1)\,(1+\eta_2)\,(c-\eta_1-\eta_2)}{c\,(1+c)^2},\\
\phi_4^g(\eta_1,\eta_2) = \phi_4^d(\eta_1,\eta_2) &= -\frac{(c-\eta_1)\,(1+\eta_2)\,(c+c\eta_1-\eta_2)}{c\,(1+c)^2},\\
\phi_5^g(\eta_1,\eta_2) = \phi_5^d(\eta_1,\eta_2) &= \frac{(c-\eta_1)\,(1+\eta_1)\,(c-\eta_2)}{c\,(1+c)},\\
\phi_6^g(\eta_1,\eta_2) = \phi_6^d(\eta_1,\eta_2) &= \frac{(1+\eta_1)\,(c-\eta_2)\,(1+\eta_2)}{c\,(1+c)},\\
\phi_7^g(\eta_1,\eta_2) = \phi_7^d(\eta_1,\eta_2) &= \frac{(c-\eta_1)\,(1+\eta_1)\,(1+\eta_2)}{c\,(1+c)},\\
\phi_8^g(\eta_1,\eta_2) = \phi_8^d(\eta_1,\eta_2) &= \frac{(c-\eta_1)\,(c-\eta_2)\,(1+\eta_2)}{c\,(1+c)},
\end{aligned}
\tag{3.19}
$$

whereas the (singular) local variation of tractions permits the representation

$$
\begin{aligned}
\phi_1^t(\eta_1,\eta_2) &= -\frac{2^{\alpha+\beta}(c-\eta_1)\,(c-\eta_2)\,(1+\eta_1+\eta_2)}{(1+c)^2(1-\eta_1)^\alpha\,(1-\eta_2)^\beta},\\
\phi_2^t(\eta_1,\eta_2) &= -\frac{2^\beta(1-c)^\alpha(1+\eta_1)\,(c-\eta_2)\,(c-\eta_1+c\eta_2)}{c\,(1+c)^2(1-\eta_1)^\alpha(1-\eta_2)^\beta},\\
\phi_3^t(\eta_1,\eta_2) &= -\frac{(1-c)^{\alpha+\beta}(1+\eta_1)\,(1+\eta_2)\,(c-\eta_1-\eta_2)}{c\,(1+c)^2(1-\eta_1)^\alpha(1-\eta_2)^\beta},\\
\phi_4^t(\eta_1,\eta_2) &= -\frac{2^\alpha(1-c)^\beta\,(c-\eta_1)\,(c+c\eta_1-\eta_2)\,(1+\eta_2)}{c\,(1+c)^2\,(1-\eta_1)^\alpha\,(1-\eta_2)^\beta},\\
\phi_5^t(\eta_1,\eta_2) &= \frac{2^\beta(c-\eta_1)\,(1+\eta_1)\,(c-\eta_2)}{c\,(1+c)(1-\eta_1)^\alpha(1-\eta_2)^\beta},\\
\phi_6^t(\eta_1,\eta_2) &= \frac{(1-c)^\alpha(1+\eta_1)\,(c-\eta_2)\,(1+\eta_2)}{c\,(1+c)(1-\eta_1)^\alpha(1-\eta_2)^\beta},\\
\phi_7^t(\eta_1,\eta_2) &= \frac{(1-c)^\beta(c-\eta_1)\,(1+\eta_1)\,(1+\eta_2)}{c\,(1+c)(1-\eta_1)^\alpha(1-\eta_2)^\beta},\\
\phi_8^t(\eta_1,\eta_2) &= \frac{2^\alpha(c-\eta_1)\,(c-\eta_2)\,(1+\eta_2)}{c\,(1+c)(1-\eta_1)^\alpha(1-\eta_2)^\beta}.
\end{aligned}
\tag{3.20}
$$

Similar to the four-node developments in Section 3.3, setting $\alpha = \beta = 0$ and $c = 1$ in (3.17)–(3.20) reduces the eight-node edge and corner elements to a continuous isoparametric format associated with conventional eight-node quadrilaterals. As an illustration, eight-node traction shape functions ϕ_8^t for the edge element and ϕ_3^t for the corner element are plotted over a semi-open region $\{\eta_1, \eta_2 | -1 \le \eta_1 < 1, -1 \le \eta_2 < 1\}$ in Fig. 3.5.

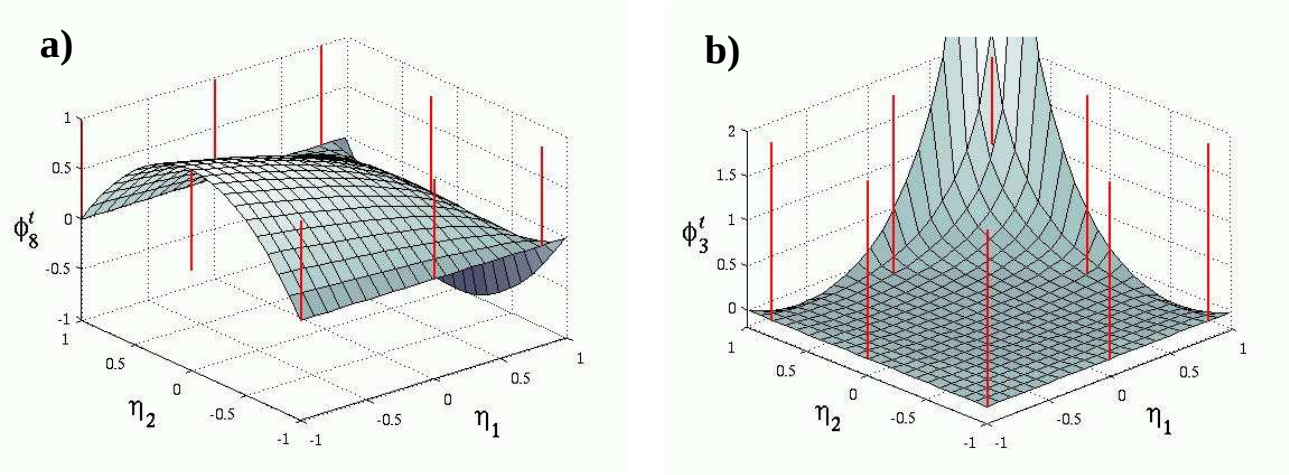

Figure 3.5: Eight-node traction shape functions: a) ϕ_8^t for the edge element and b) ϕ_3^t for the corner element ($c=0.8$, $\alpha=\beta=0.5$)

3.5 Numerical integration

To examine the performance of singular elements, it is useful to consider their implementation within the framework of regularized boundary integral equations [125]

$$\int_{\Gamma^n} t_i(\boldsymbol{\xi})\,\hat{u}_i^{k,n}(\boldsymbol{\xi},\boldsymbol{y})\,d\Gamma_\xi - \int_{\Gamma^n}[u_i(\boldsymbol{\xi})-u_i(\boldsymbol{y})]\;[\hat{t}_i^{k,n}(\boldsymbol{\xi},\boldsymbol{y})]_1\,d\Gamma_\xi \tag{3.21}$$
$$-\int_{\Gamma^n} u_i(\boldsymbol{\xi})\,[\hat{t}_i^{k,n}(\boldsymbol{\xi},\boldsymbol{y})]_2\,d\Gamma_\xi + \int_{\Omega^n} f_i(\boldsymbol{\xi})\,\hat{u}_i^{k,n}(\boldsymbol{\xi},\boldsymbol{y})\,d\Omega_\xi = \Upsilon\,u_k(\boldsymbol{y}),\quad \boldsymbol{y}\in\Gamma^n,\quad n=\overline{1,N}$$

written respectively for each material Ω^n in a piecewise-homogeneous body $\Omega=\bigcup_{n=1}^N \Omega^n$. Here, Γ^n is a piecewise-smooth boundary of the homogeneous piece Ω^n; $i,k=\overline{1,3}$; summation is assumed over the repeated indexes; u_i and t_i are the respective Cartesian components of the boundary displacements and tractions; $\hat{u}_i^{k,n}$ and $\hat{t}_i^{k,n}$ are suitable (displacement and traction) Green's functions characterizing the n^{th} material; $[\cdot]_1$ and $[\cdot]_2$ denote the respective singular and regular components of their argument; f_i stands for the body force; $\boldsymbol{n}$ is the normal to Γ^n pointing outward from Ω^n, and Υ equals 0 and 1 for the interior and exterior boundary value problem, respectively.

On approximating Γ^n by a boundary element mesh: $\Gamma_h^n=\bigcup_{q=1}^Q E_q$ where E_q are e.g. four- or eight-node quadrilateral surface elements, (3.21) can be reduced (via the collocation method) to a set of linear algebraic systems

$$\sum_{q=1}^{Q}\sum_{m=1}^{M_q}\sum_{i=1}^{3} t_i^{m_q}\int_{E_q}\phi_m^{t,q}(\boldsymbol{\xi})\,\hat{u}_i^{k,n}(\boldsymbol{\xi},\boldsymbol{y}^s)\,d\Gamma_\xi - \sum_{q=1}^{Q}\sum_{m=1}^{M_q}\sum_{i=1}^{3} u_i^{m_q}\int_{E_q}(\phi_m^{d,q}(\boldsymbol{\xi})-\delta_{sm_q})\,[\hat{t}_i^{k,n}(\boldsymbol{\xi},\boldsymbol{y}^s)]_1\,d\Gamma_\xi$$
$$-\sum_{q=1}^{Q}\sum_{m=1}^{M_q}\sum_{i=1}^{3} u_i^{m_q}\int_{E_q}\phi_m^{d,q}(\boldsymbol{\xi})\,[\hat{t}_i^{k,n}(\boldsymbol{\xi},\boldsymbol{y}^s)]_2\,d\Gamma_\xi + \int_{\Omega} f_i(\boldsymbol{\xi})\,\hat{u}_i^{k,n}(\boldsymbol{\xi},\boldsymbol{y}^s)\,d\Omega_\xi = \Upsilon\,u_k^s,\quad s=\overline{1,S} \tag{3.22}$$

written respectively for each Ω^n in terms of the nodal values of boundary displacements (u_k^s) and tractions (t_k^s) evaluated at collocation points $\boldsymbol{y}^s$. In (3.22), Q and S are respectively the numbers of boundary elements and nodes featuring Γ_h^n; M_q is the number of nodes for the q^{th} element whose displacement and traction shape functions are denoted respectively by $\phi_m^{d,q}$ and $\phi_m^{t,q}$, and m_q is the global number of the m^{th} element node. As all integrals in (3.22) exist in the ordinary sense, standard

(two-dimensional) Gaussian quadrature can formally be applied to all boundary elements, including: i) edge and corner elements, and ii) elements containing the collocation point. For boundary elements over which the featuring integrands are singular (due to either singularity of the Green's function or the shape function), however, standard quadrature proves to be notably inefficient and some modifications are required to maintain the desired accuracy.

3.5.1 Integration over regular elements containing the collocation point

Even though (3.22) is free of Cauchy principal values, its evaluation is complicated by the fact that the featured 3D Green's functions are characterized by the singular behavior

$$\hat{u}_i^{k,n}(\boldsymbol{\xi}, \boldsymbol{y}^s) = O(r^{-1}), \qquad \hat{t}_i^{k,n}(\boldsymbol{\xi}, \boldsymbol{y}^s) = O(r^{-2}) \qquad \text{as} \quad r = |\boldsymbol{\xi} - \boldsymbol{y}^s| \to 0,$$

for some $i, j \in \{1, 2, 3\}$ in the context of both elastostatic and elastodynamic problems (e.g. [20]). As a result, the corresponding elemental integrals demand substantial numerical integration effort. To provide a remedy, use is made of a regularizing mapping technique originally proposed in Lachat(1976) [90]. With reference to a standard four- or eight-node quadrilateral element E_q containing the collocation point as one of its *corner nodes*, the idea is to subdivide the element's parent domain into two triangles, e.g. Triangle A and Triangle B, with a common vertex at the collocation point P (see Fig. 3.6a). On denoting the global coordinates of the singular point P by $\boldsymbol{y}^n$, the advantage of this mapping procedure is that the Jacobian of the underlying transformation is of the order: $J(\boldsymbol{\xi}) = O(|\boldsymbol{\xi} - \boldsymbol{y}^n|)$ as $E_q \ni \boldsymbol{\xi} \to \boldsymbol{y}^n$ which weakens the singularity of featured kernels and thus improves the integration accuracy. With reference to Fig. 3.6a, the approach may be illustrated by introducing the set of auxiliary coordinates $\{\eta_1', \eta_2' | -1 \le \eta_1' \le 1, -1 \le \eta_2' \le 1\}$ to describe Triangle A, and requiring that the side $\eta_1' = 1$ collapses onto the singular point P (see Fig. 3.6b). On generalizing to a situation where P coincides with the k^{th} quadrilateral element node $(k = \overline{1,4})$ with coordinates (η_1^k, η_2^k), the above-described mapping can be synthesized as

$$\begin{aligned}
&\eta_1 = \eta_1^k \eta_1', \qquad \eta_2 = \eta_2^k \left\{ 1 - \frac{1}{2}(1 - \eta_1')(1 - \eta_1^k \eta_2^k \eta_2') \right\}, \quad \text{Triangle } A \\
&\eta_2 = \eta_2^k \eta_1', \qquad \eta_1 = \eta_1^k \left\{ 1 - \frac{1}{2}(1 - \eta_1')(1 + \eta_1^k \eta_2^k \eta_2') \right\}, \quad \text{Triangle } B, \quad k = \overline{1,4}
\end{aligned} \tag{3.23}$$

where $-1 < \eta_1' < 1$, $-1 < \eta_2' < 1$, and the partition is arranged so that the side of Triangle A that is parallel to the η_2-axis contains the collocation point. One may note that the Jacobian of transformation (3.23) is $(\eta_1^k \eta_2^k)^2 (1 - \eta_1')/2$ for both participating triangles. Owing to the fact that $|\boldsymbol{\xi} - \boldsymbol{\xi}^k| = O(1 - \eta_1')$ as $\boldsymbol{\xi} \to \boldsymbol{\xi}^k \equiv \boldsymbol{\xi}(\eta_1^k, \eta_2^k)$, this yields the desired behavior: $J(\boldsymbol{\xi}) = O(|\boldsymbol{\xi} - \boldsymbol{y}^n|)$ when $\boldsymbol{\xi} \to \boldsymbol{y}^n$.

In situations where the collocation point P coincides with a *side node*, $\boldsymbol{\xi}^k \equiv \boldsymbol{\xi}(\eta_1^k, \eta_2^k)$ $(k = \overline{5,8})$ of a regular eight-node element (see Fig. 3.4 with $c = 1$), the foregoing procedure can be adapted by i) splitting the element's parent domain into two rectangular regions along the coordinate axis η_1 and η_2 respectively for $k \in \{6, 8\}$ and $k \in \{5, 7\}$, and ii) applying a suitable analogue of (3.23) to each rectangular subdomain.

3.5.2 Integration over singular elements

In the case of singular boundary elements, additional singularity in the integrands on the left-hand side of (3.22) arises from the traction shape functions ϕ_m^t given respectively by (3.11), (3.15), (3.18),

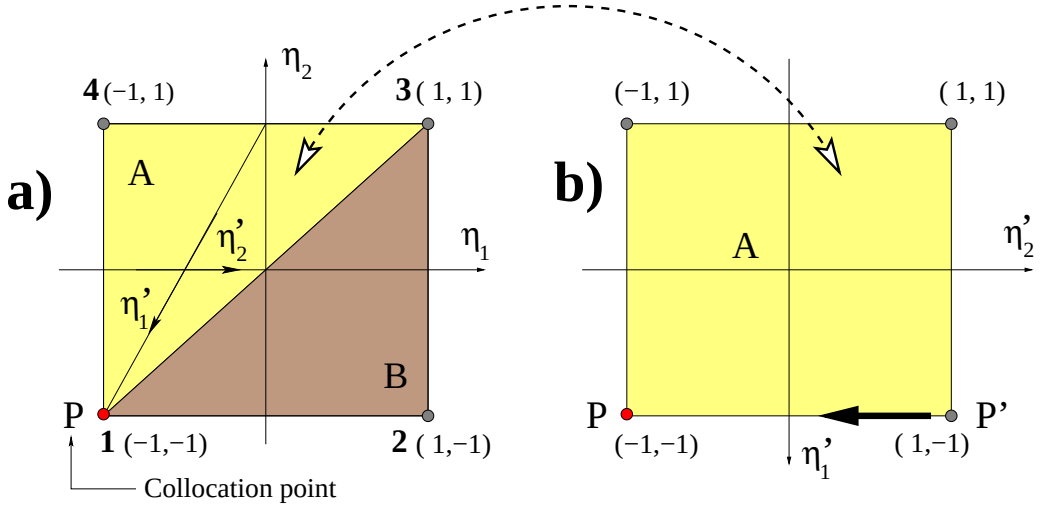

Figure 3.6: Partition and mapping of a regular element containing the collocation point P.

and (3.20) for the four-node edge, four-node corner, eight-node edge, and eight-node corner element, respectively. As an example, one may consider the four-node and eight-node *edge* elements in Figs. 3.2a and 3.4a whose traction shape functions are singular as

$$t_i(\eta_1,\eta_2) = O\left((1-\eta_1)^{-\alpha}\right) \quad \text{as} \quad \eta_1 \to 1, \quad -1 \le \eta_2 \le 1, \quad 0 \le \alpha < 1, \qquad i = 1,2,3 \tag{3.24}$$

For clarity, it is first assumed that none of the element nodes coincides with the collocation point. To improve the efficiency of numerical integration for this case, one may to introduce a 1-to-1 mapping of the local coordinates $\{\eta_1,\eta_2 \,|\, -1 \le \eta_1 \le 1, -1 \le \eta_2 \le 1\}$ into an auxiliary domain $\{\eta_1',\eta_2' \,|\, -1 \le \eta_1' \le 1, -1 \le \eta_2' \le 1\}$ so that the Jacobian of transformation nullifies the singular traction behavior (3.24). To this end, one may assume

$$\begin{aligned} \eta_1 &= A + B\left(1-\eta_1'\right)^C, && -1 \le \eta_1' \le 1, \\ \eta_2 &= \eta_2', && -1 \le \eta_2' \le 1, \end{aligned} \tag{3.25}$$

where A, B and C are the unknown constants for the mapping. By imposing the end conditions where $\eta_1(\pm 1,\eta_2') = \pm 1$, one finds that $A=1,\ B=-2^{(1-C)}$, and consequently

$$(1-\eta_1)^{-\alpha} d\eta_1 d\eta_2 \;=\; 2^{(1-\alpha)(1-C)}\, C\, \left(1-\eta_1'\right)^{(1-\alpha)C-1} d\eta_1' d\eta_2'. \tag{3.26}$$

For the exponent of $(1-\eta_1')$ in (3.26) to be unity, one must take $C = 1/(1-\alpha)$ and therefore

$$\begin{aligned} \eta_1 &= 1 - 2^{-\alpha/(1-\alpha)}\left(1-\eta_1'\right)^{1/(1-\alpha)}, && -1 \le \eta_1' \le 1, \\ \eta_2 &= \eta_2', && -1 < \eta_2' \le 1. \end{aligned} \tag{3.27}$$

In a similar fashion, one may find the appropriate mapping for the four- and eight-node *corner* elements (Figs. 3.2b and 3.4b) to be of the form

$$\eta_1 = 1 - 2^{-\alpha/(1-\alpha)}\left(1-\eta_1'\right)^{1/(1-\alpha)}, \qquad -1 \le \eta_1' \le 1, \tag{3.28}$$

$$\eta_2 = 1 - 2^{-\beta/(1-\beta)}\left(1-\eta_2'\right)^{1/(1-\beta)}, \qquad -1 \le \eta_2' \le 1, \tag{3.29}$$

where $0 \leq \beta < 1$ represents the order of singularity for the traction shape functions along side $\eta_2 = 1$, see also (3.13).

In the special case when the collocation point coincides with one of the nodes of a singular (edge or corner) element, the regularizing mapping technique exemplified by (3.23) should be superimposed over (3.28) and (3.29). For collocation points which coincide with a *side* or an *internal* (as opposed to *corner*) node of a singular element, however, the element's parent domain must first be subdivided into a number of rectangular sub-domains so that each subdomain contains the collocation point as one of its corners. This is illustrated in Fig. 3.7 using the eight-node corner element as an example. In the Figure, local nodes $\{1\}$, $\{2,4,5,8\}$, and $\{3,6,7\}$ are designated as the "corner" node, "side" nodes, and "internal" nodes, respectively.

For clarity, the complete mapping sequence for a generic rectangular patch (i.e. subdomain) $\{\eta_1, \eta_2 | d \leq \eta_1 \leq e,\ f \leq \eta_2 \leq g\}$ in Fig. 3.7 can be written as

$$\eta_1 = \frac{2}{e-d}\left(\eta_1' - \frac{e+d}{2}\right), \qquad \eta_2 = \frac{2}{g-f}\left(\eta_2' - \frac{g+f}{2}\right) \tag{3.30}$$

which maps the patch into a "unit" reference domain $\{\eta_1', \eta_2' | -1 \leq \eta_1 \leq 1, -1 \leq \eta_2 \leq 1\}$;

$$\begin{array}{llll}
\eta_1' = \eta_1'', & \eta_2' = \eta_2'' & \text{if} \quad \eta_1|_{\eta_1'=1} < 1, & \eta_2|_{\eta_2'=1} < 1, \\
\eta_1' = \chi(\eta_1'', \alpha), & \eta_2' = \eta_2'' & \text{if} \quad \eta_1|_{\eta_1'=1} = 1, & \eta_2|_{\eta_2'=1} < 1, \\
\eta_1' = \eta_1'', & \eta_2' = \chi(\eta_2'', \beta), & \text{if} \quad \eta_1|_{\eta_1'=1} < 1, & \eta_2|_{\eta_2'=1} = 1, \\
\eta_1' = \chi(\eta_1'', \alpha), & \eta_2' = \chi(\eta_2'', \beta), & \text{if} \quad \eta_1|_{\eta_1'=1} = 1, & \eta_2|_{\eta_2'=1} = 1,
\end{array} \tag{3.31}$$

where $-1 \leq \eta_1'' \leq 1,\ -1 \leq \eta_2'' \leq 1$, and

$$\chi(\eta_k'', \gamma) = 1 - 2^{-\gamma/(1-\gamma)}\left(1 - \eta_k''\right)^{1/(1-\gamma)}, \qquad k = \overline{1,2},$$

a transformation which deals with the shape-function singularity; and

$$\begin{array}{l}
\eta_1'' = \eta_1''^k \eta_1''' \qquad \eta_2'' = \eta_2''^k \left\{1 - \frac{1}{2}(1-\eta_1''')(1 - \eta_1''^k \eta_2''^k \eta_2''')\right\}, \quad \text{Triangle } A \\
\eta_2'' = \eta_2''^k \eta_1''', \qquad \eta_1'' = \eta_1''^k \left\{1 - \frac{1}{2}(1-\eta_1''')(1 + \eta_1''^k \eta_2''^k \eta_2''')\right\}, \quad \text{Triangle } B, \quad k = \overline{1,4} \\
\eta_1''^1 = \eta_1''^4 = \ \eta_2''^1 = \eta_2''^2 = -1, \quad \eta_1''^2 = \eta_1''^3 = \eta_2''^3 = \eta_2''^4 = 1, \quad -1 \leq \eta_1''' \leq 1,\ -1 \leq \eta_2''' \leq 1
\end{array} \tag{3.32}$$

that mitigates the Green's function singularity. By means of (3.30)-(3.32), numerical integration over each rectangular subdomain of a singular element containing the collocation point can be effectively performed in terms of η_1''' and η_2''' using standard quadrature formulae. For singular elements not containing the collocation point, (3.32) is dropped and the numerical integration is performed in terms of η_1'' and η_2'' with $e = g = -d = -f = 1$.

3.6 Results

In what follows, proposed singular elements are applied to a set of canonical boundary value problems (involving piecewise-planar boundary surfaces) to evaluate their numerical performance. To provide a reference in the absence of suitable 3D analytical solutions, results stemming from the use of "singular" boundary element meshes are compared to their "regular" counterparts. For the clarity of comparison, each "singular" mesh is converted to its "regular" companion by setting $\alpha = 0$ and

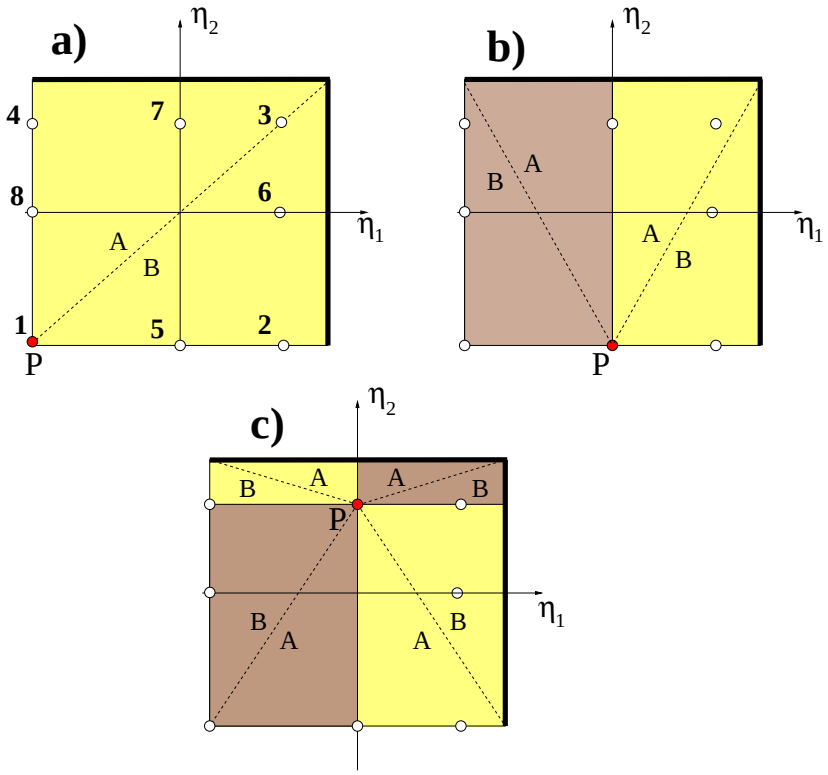

Figure 3.7: Partition of a singular eight-node corner element containing the collocation point P as: a) corner node, b) side node, and c) internal node.

$\beta = 0$ for all participating edge and corner elements. From a limited study, optimal value of the shift parameter c that controls the location of internal nodes within a singular element was found to be in the range $0.75 < c < 0.95$. In the sequel, *uniform* boundary element meshes (composed of equi-sized square elements) and the value of $c = 0.90$ are used throughout.

The first three examples deal with a rigid punch problem for the homogeneous isotropic half-space. Owing to the use of the exact half-space Green function (see Guzina(1999)[68]), these problems require only a minimal discretization that is limited to the contact surface. The fourth and the last example considers both the static and dynamic solution of a mixed boundary value problem for a solid cube, fixed at its bottom. For the latter problem, the full-space (static and dynamic) Green functions are employed.

3.6.1 Frictionless surface punch

As a first benchmark problem, Fig. 3.8 plots the results for the "vertical" static stiffness coefficient, K_{vv}, of a *frictionless* square surface punch ($|x_1| < a$, $|x_2| < a$) applied to the surface of a homogeneous elastic half-space ($x_3 > 0$) with shear modulus μ and Poisson's ratio $\nu = 1/3$. Under the frictionless interfacial conditions, the traction singularity associated with punch edges can be shown to be of the square-root type [43], which requires $\alpha = \beta = 0.5$.

The results obtained by the BEM approach are plotted against the solution of Dempsey and Li [40] who used an indirect integral equation approach and treated the singular contact tractions globally by assuming

$$t_3(x_1, x_2) = \frac{p(x_1, x_2)}{(a - |x_1|)^{0.5} (a - |x_2|)^{0.5}}, \qquad |x_1| < a, \quad |x_2| < a$$

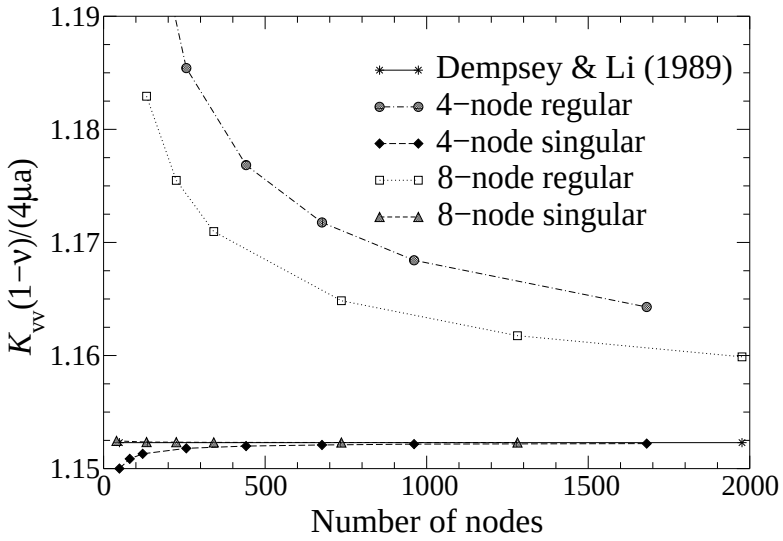

Figure 3.8: Static stiffness of a square surface punch $2a \times 2a$ (frictionless contact).

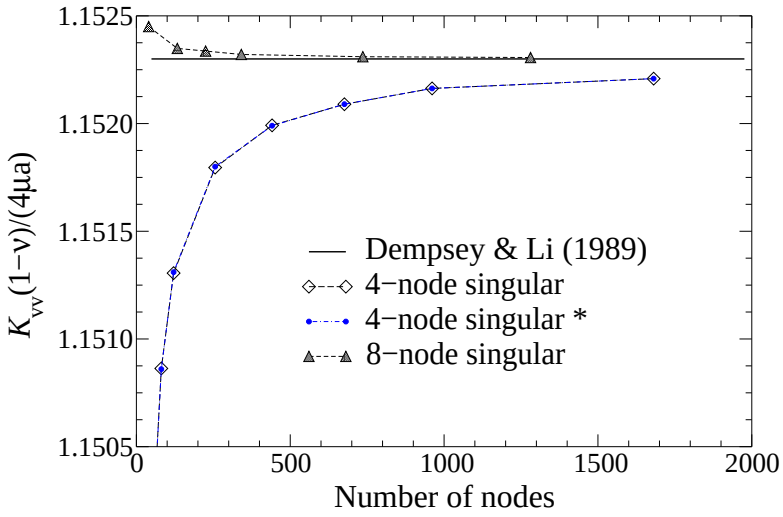

Figure 3.9: Effect of kinematic interpolation on the static stiffness of a square surface punch $2a \times 2a$ (frictionless contact).

and solving for the regular part $p(x_1, x_2)$. Their benchmark result

$$K_{vv} \;=\; 1.1523 \left(\frac{4\mu a}{1-\nu} \right)$$

was obtained by using 1024 elements, where the term in parentheses denotes the corresponding static stiffness of a frictionless circular punch with radius a. As can be seen from Fig. 3.8, the improved scheme with singular elements converges significantly faster to the asymptotic value 1.1523, especially when eight-node boundary elements are employed.

For completeness, a detail from Fig. 3.8 is re-plotted in Fig. 3.9 with an addition of the 4-node singular-element values (indicated by an asterisk) that are calculated using *traction-compatible* kinematic interpolations (3.12) and (3.16) in lieu of their (default) *bi-linear* counterparts (3.9) and (3.14). As can be seen from the display, the results obtained using two alternative kinematic descriptions are indistinguishable, which suggests that the choice of the displacement shape functions over traction-singular boundary elements may not be essential for the class of problems under consideration.

3.6.2 *Bonded surface punch*

The next example deals with a *bonded* square surface punch ($|x_1|<a$, $|x_2|<a$) applied to the half-space with shear modulus μ and Poisson's ratio $\nu = 1/3$. For this problem, relevant stiffness coefficients can be summarized as

$$K_{vv} = \frac{R_3^{\Delta_3}}{\Delta_3}, \quad K_{hh} = \frac{R_1^{\Delta_1}}{\Delta_1}, \quad K_{mm} = \frac{M_2^{\Theta_2}}{\Theta_2}$$
$$K_{mh} = \frac{M_2^{\Delta_1}}{\Delta_1}, \quad K_{hm} = \frac{R_1^{\Theta_2}}{\Theta_2}, \quad K_{tt} = \frac{M_3^{\Theta_3}}{\Theta_3} \tag{3.33}$$

where for instance $R_i^{\Delta_j}$ denotes the resultant contact force in the x_i-direction caused by the punch translation Δ_j in the x_j direction, and $M_i^{\Theta_j}$ is the resultant moment about the x_i-axis due to punch rotation Θ_j about the x_j axis.

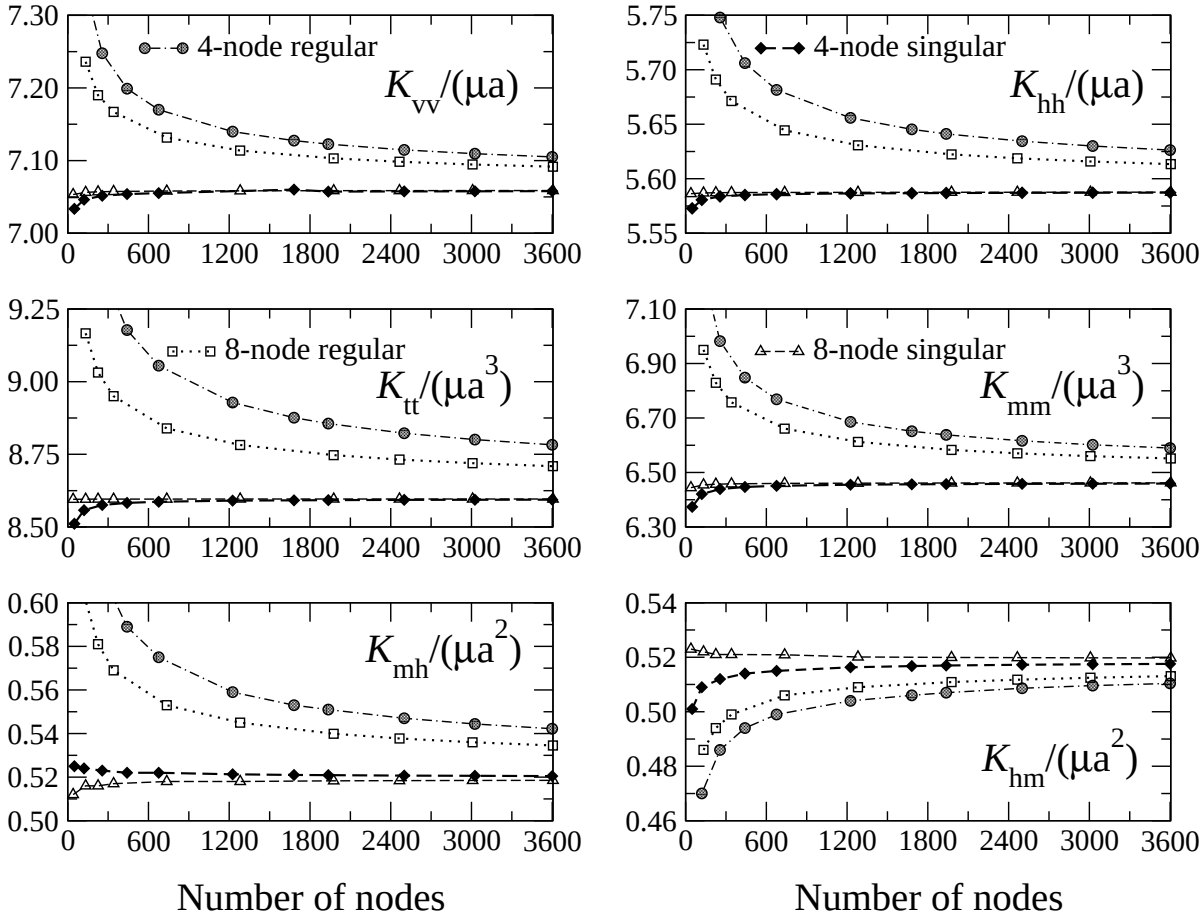

Figure 3.10: Static stiffness coefficients for a square surface punch $2a \times 2a$ (bonded contact, $\nu = 1/3$).

To characterize the singular contact tractions along punch edges in the case of a bonded contact, one may set $\theta_2 = 2\theta_1 = \pi$, $\mu_2 = \mu$, $\nu_2 = \nu$ and $\mu_2/\mu_1 \to 0$ in Fig. 3.1a, yielding

$$s = \lambda = -1.5 \pm \frac{i}{\pi} \tanh^{-1}\left(\frac{1-2\nu}{2-2\nu}\right), \tag{3.34}$$

Table 3.1: Surface punch problem: end values of stiffness coefficients

Stiffness coefficient	4-node regular $N = 3600$	4-node singular $N = 3600$	8-node regular $N = 3605$	8-node singular $N = 3605$
$K_{vv}/(\mu a)$	7.1050E0	7.0578E0	7.0915E0	7.0587E0
$K_{hh}/(\mu a)$	5.6262E0	5.5872E0	5.6133E0	5.5876E0
$K_{tt}/(\mu a^3)$	8.7827E0	8.5939E0	8.7091E0	8.5962E0
$K_{mm}/(\mu a^3)$	6.5896E0	6.4592E0	6.5515E0	6.4618E0
$K_{mh}/(\mu a^2)$	5.4222E-1	5.2048E-1	5.3453E-1	5.1852E-1
$K_{hm}/(\mu a^2)$	5.1040E-1	5.1758E-1	5.1306E-1	5.1974E-1

as the first-order zeros of $\mathcal{D}_s(s)$ in (3.4) with the largest real part in the strip $-2 < Re(s) < -1$ (see also [18]). On substituting (3.34) into (3.1), the above result implies oscillatory *square-root singular* tractions near the edges of the square foundation, for which again $\alpha = \beta = 0.5$ regardless of ν. Similar to the previous example, unbounded tractions are assumed to occur throughout the perimeter of the foundation regardless of the mode of loading. Accordingly, the singular elements are placed along edges $x_1 = \pm a$ and $x_2 = \pm a$. Fig. 3.10 illustrates the convergence of the boundary element solution, in terms of the stiffness coefficients (3.33), as a function of the number of boundary nodes N. As can be seen from the display, the use of singular boundary elements results in a faster overall convergence of the numerical solution. In particular, it is noted that the "singular mesh" with four-node elements outperforms its eight-node "regular" (i.e. quadratic) counterpart for all modes of loading.

Notwithstanding the apparent convergence of the results in Fig. 3.10 (and in particular those obtained using singular elements), however, it is important to examine whether the featured "asymptotic" values are reasonable. In the absence of a suitable analytical solution, one can make reference to the Maxwell-Betti reciprocity identity which requires that $K_{hm} = K_{mh}$. In this regard, Table 3.1 lists the "limiting" values of all stiffness coefficients, where N denotes the number of nodes in the boundary element mesh. The results indicate that the difference between K_{hm} and K_{mh} is 5.8%, 0.5%, 4.0% and 0.2% for the 4-node regular, 4-node singular, 8-node regular and 8-node singular mesh, respectively; a result that should be weighted with the fact that K_{hm} and K_{mh} are order-of-magnitude smaller than the remaining stiffness coefficients.

To provide a broader perspective for the study, the distribution of contact tractions t_3, produced by the unit punch translation ($\Delta_1 = 1$) in the ξ_1-direction, is plotted in Fig. 3.11 for three boundary element discretizations. To minimize the bias in the results, calculations are performed using two "regular" 8-node meshes with $N = 341$ and $N = 1281$, and a "regular" 4-node mesh with $N = 441$. As inferred by (3.33), this translational mode of loading is used to calculate the stiffness coefficients K_{hh} and K_{mh}. Subject to the limitations of assumed discretization and related interpolation issues, two observations are prevalent. In the vicinity of the $\xi_1 = \pm a$ edges, the contact tractions appear to exhibit oscillatory singular behavior that is resemblant of (3.34). In contrast, the distribution of tractions near the $\xi_2 = \pm a$ edges is considerably smoother. While illustrating the utility of local analyses e.g. in terms of exposing an oscillatory singular behavior, these results also serve as a reminder that the relevance of any local analysis to a particular boundary value problem is dependent on the (global) loading conditions. In this regard, a retarded convergence of the K_{mh} coefficient in Fig. 3.10 can be attributed to the fact that the assumed singular (4- and 8-node) boundary element meshes do not properly account for the local (near-edge) features in Fig. 3.11. For completeness, it is noted that the numerical contact tractions for the remaining modes of loading in (3.33), namely $\Delta_3 = 1, \Theta_2 = 1$ and $\Theta_3 = 1$ (omitted for brevity), indicate apparent singularity of contact tractions *throughout* the perimeter of the punch as assumed by the numerical analysis.

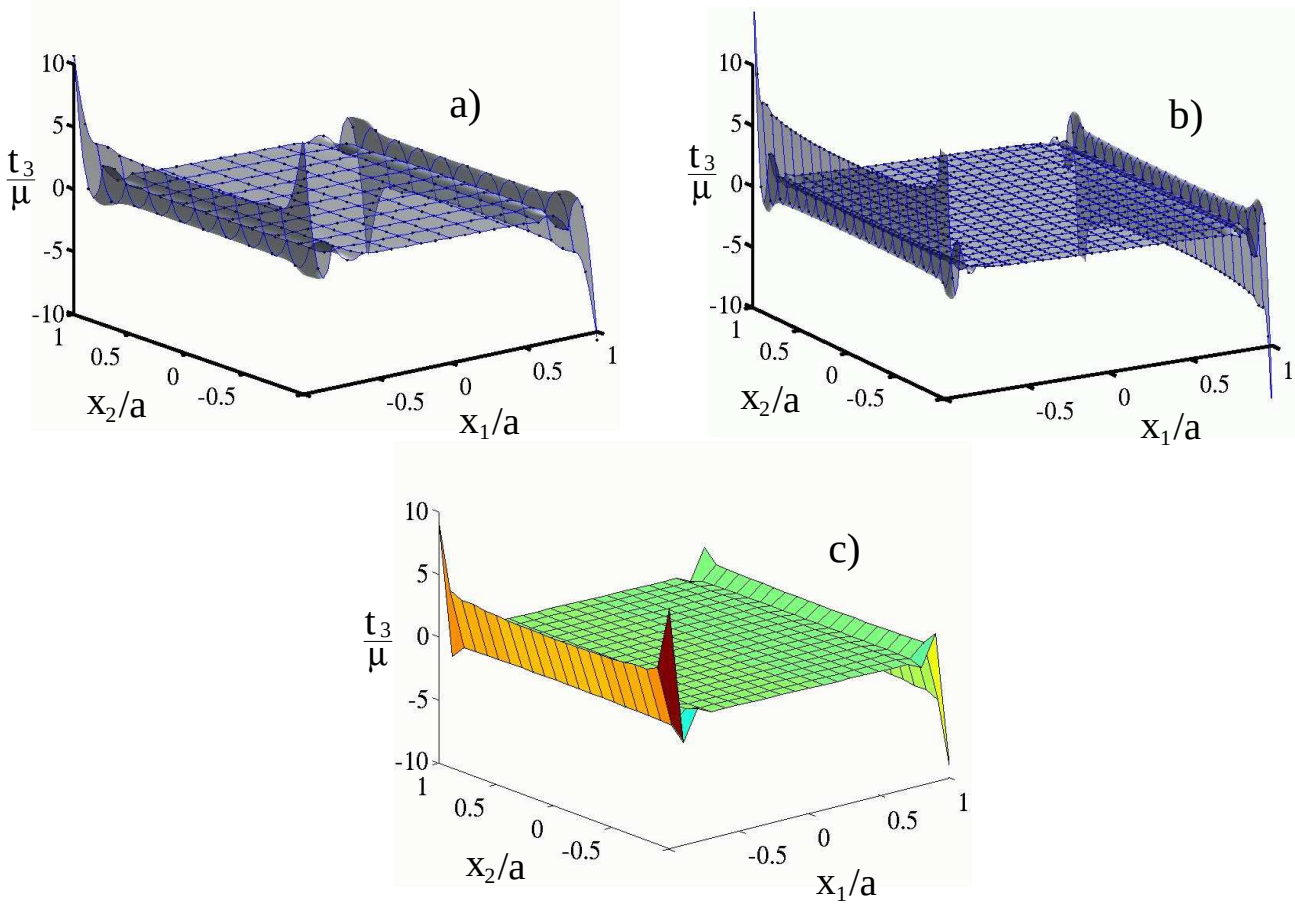

Figure 3.11: Normal contact tractions induced by the unit translation of a bonded punch in the ξ_1-direction: results obtained using a) 10×10 "regular" 8-node mesh ($N=341$), ii) 20×20 "regular' 8-node mesh ($N=1281$), and c) 20×20 "regular' 4-node mesh ($N=441$).

3.6.3 Embedded punch

In what follows, interfacial stiffness coefficients (3.33) are computed for the rigid cubical punch ($|x_1|<a,\ |x_2|<a,\ 0<x_3<2a$) embedded in, and bonded to a homogeneous elastic half-space, $x_3>0$ (see also Fig. 3.1). The half-space is characterized by the shear modulus μ and Poisson's ratio $\nu=1/3$. To examine the singularity of contact tractions along the edges of an embedded block, it is useful to make a distinction between the surface and embedded edge, shown respectively in Figs. 3.1b and 3.1c. Accordingly, all boundary edges lying in the plane $x_3=0$ will be designated as *surface* edges, while the remaining eight edges will be understood as being *embedded*.

In the case of a surface edge, a substitution $\theta_1=\theta_2=\pi/2,\ \nu_2=1/3$ and $\mu_2/\mu_1\to0$ in (3.4) yields a numerical solution

$$s=\lambda\approx-1.690 \tag{3.35}$$

for the first-order zero of $\mathcal{D}_s(s)$, with the largest real part, in the strip $-2<Re(s)<-1$. On the basis of (3.1) and (3.35), the singularity orders α or β for all participating surface edges are set to 0.310. For an embedded edge, on the other hand, the relevant characteristic equation is (3.2). On setting $\theta_2=3\theta_1=3\pi/2,\ \nu_2=1/3$ and $\mu_2/\mu_1\to0$, the relevant zero of (3.2) with the largest real part can be found as

$$s=\lambda\approx-1.590; \tag{3.36}$$

a result that, by virtue of (3.1), requires that α or β for embedded edges be set to 0.410. One may note that the values in (3.35) and (3.36) are consistent with the results of the two-dimensional analysis for the clamped-free wedge of angle $\pi/2$ and the clamped-clamped wedge of angle $3\pi/2$, respectively (see Williams(1952) [163]).

Fig. 3.12 illustrates the convergence of the stiffness coefficients in (3.33) for the embedded punch problem. The results again demonstrate the utility of singular boundary elements as a tool for improving the accuracy of numerical approximation. In contrast to the two earlier examples, on the other hand, it is seen that the "regular" mesh with eight-node elements exhibits a performance that is comparable to that stemming from the use of either "singular" mesh. This is perhaps not surprising in view the fact that the singularities for the embedded punch problem, being weaker than that for its surface counterpart, are inherently more amenable to a polynomial approximation. For completeness, Table 3.2 lists the "limiting" values of the stiffness coefficients in Fig. 3.12. Adopting a relative difference between the values of K_{hm} and K_{mh} as a measure of solution accuracy, comparison of the data in Tables 3.1 and 3.2 also reveals that the embedded punch results outperform those for the surface punch. This "anomalous" behavior apparently stems from the fact that the surface-punch traction singularity (3.34) has an oscillatory character that is *not captured* by the use of singular elements. In contrast, edge singularities (3.35)–(3.36) featuring the embedded punch problem exhibit no oscillatory behavior ($\lambda = 0$).

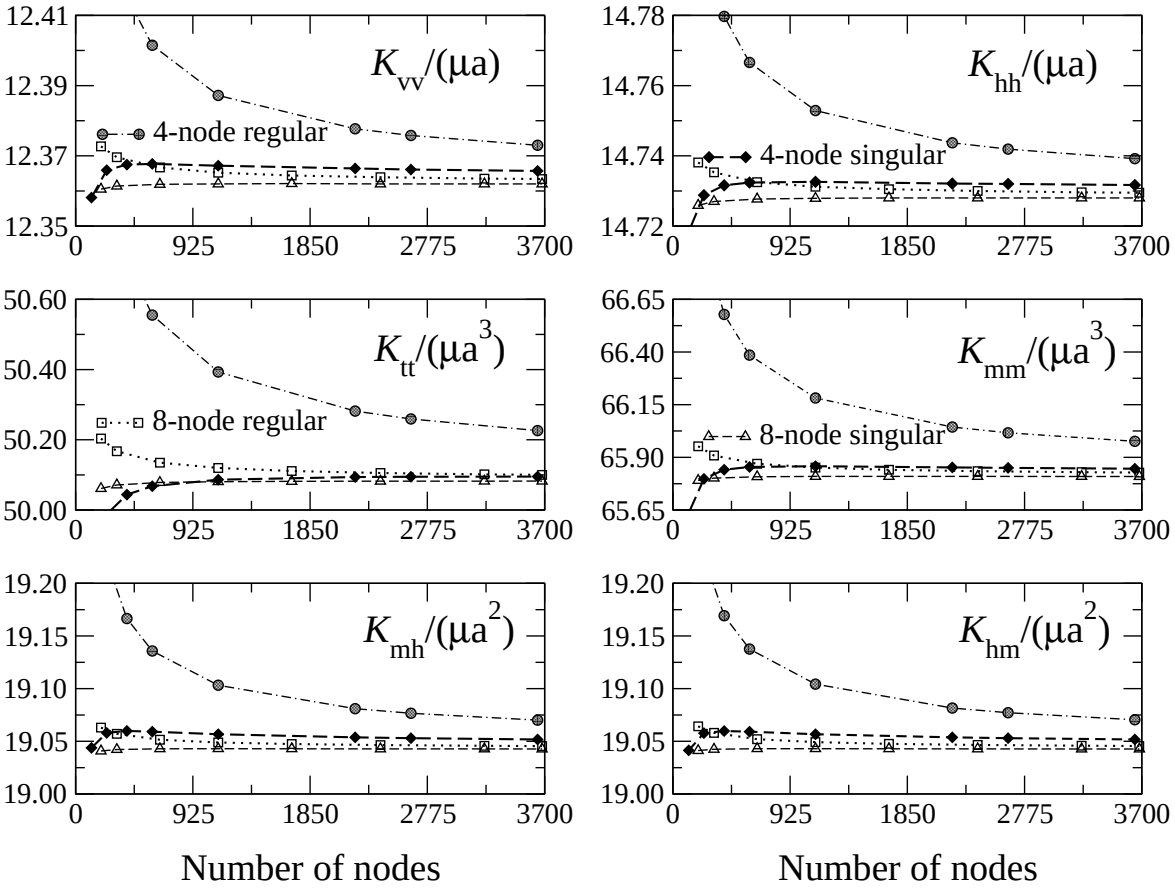

Figure 3.12: Static stiffness coefficients for an embedded cubical punch $2a \times 2a \times 2a$ (bonded contact, $\nu = 1/3$).

Table 3.2: Embedded punch problem: end values of stiffness coefficients

Stiffness coefficient	4-node regular $N = 3645$	4-node singular $N = 3645$	8-node regular $N = 3680$	8-node singular $N = 3680$
$K_{vv}/(\mu a)$	1.2373E1	1.2365E1	1.2363E1	1.2362E1
$K_{hh}/(\mu a)$	1.4739E1	1.4731E1	1.4729E1	1.4728E1
$K_{tt}/(\mu a^3)$	5.0226E1	5.0095E1	5.0100E1	5.0082E1
$K_{mm}/(\mu a^3)$	6.5976E1	6.5846E1	6.5828E1	6.5809E1
$K_{mh}/(\mu a^2)$	1.9070E1	1.9051E1	1.9045E1	1.9042E1
$K_{hm}/(\mu a^2)$	1.9070E1	1.9051E1	1.9045E1	1.9042E1

3.6.4 Solid cube

The focus of the next example is a mixed boundary value problem for a finite elastic body, involving either static or dynamic (time-harmonic) loading. The problem domain is a solid cube $|x_k| < 3a$ ($k = 1, 2, 3$) that is fixed along its bottom, $x_3 = -3a$. The cube has a shear modulus μ, Poisson's ratio $\nu = 0.3$ and mass density ρ. An internal point load of magnitude μa^2 is applied at $(1.5a, 0, 0)$ in the x_1-direction. For the dynamic case, the frequency of excitation is $\omega = \sqrt{\mu/\rho}/a$. For the edge and corner elements along the bottom face, a local eigenvalue analysis identical to that in Section 3.6.3 shows that $\alpha = \beta = 0.310$. Beyond their merit as benchmarks, this class of testing configurations may also be relevant to elastic imaging problems [23], especially those involving biological tissues where the internal forcing is realized with the aid of a confocal ultrasound beam [50].

Figs. 3.13 and 3.14 illustrate the convergence of the BIE solution in terms of the boundary displacement $u_x(3a, 0, 0)/a$ for the static and dynamic case, respectively. In both instances, the use of singular elements accelerates the convergence of the numerical solution relative to that obtained using regular elements only ($\alpha = \beta = 0$). For the dynamic problem, however, Fig. 3.14 shows that the improvement due to the use of quadratic (instead of linear) elements is far more significant than that achieved by the use of singular (in lieu of regular) elements. Such behavior is apparently caused by the inertial forces which not only complicate the displacement patterns, but also minimize the magnitude of the bottom reaction and thus the effect of singular contact tractions.

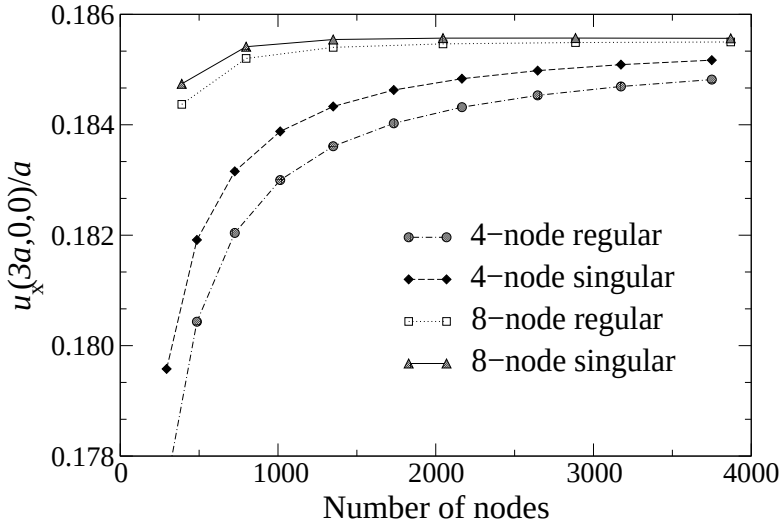

Figure 3.13: Normal displacement on the boundary of a solid cube $6a \times 6a \times 6a$, interior static force.

As a final comparison, Tables 3.3 and 3.4 list the values of $u_x(3a, y, 0)/a$, $0 \le y \le 2.7a$ for the static and dynamic problem, respectively. The boundary discretization used to obtain the results is uniform

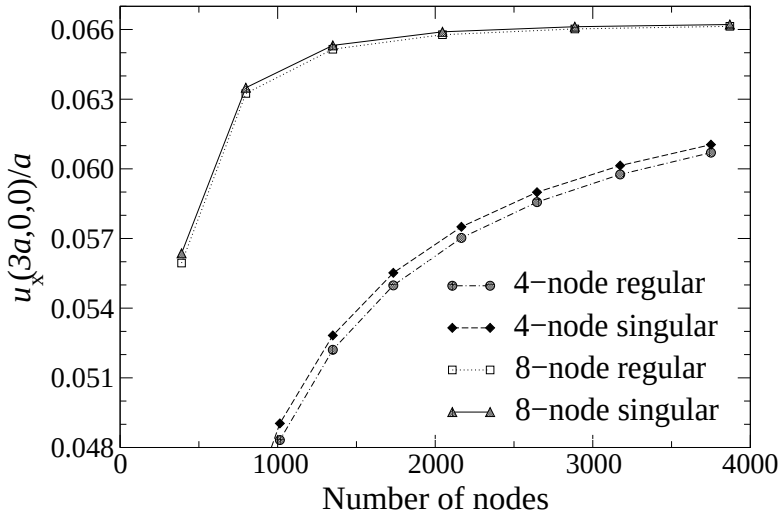

Figure 3.14: Normal displacement on the boundary of a solid cube $6a \times 6a \times 6a$, interior dynamic force.

Table 3.3: Solid cube problem, static loading: boundary displacement $u_x(3a, y, 0)/a$

y/a	4-node regular $N=2646$	4-node singular $N=2646$	8-node regular $N=2046$	8-node singular $N=2046$	FEM $N=60625$
0.0	1.8453E-1	1.8498E-1	1.8546E-1	1.8556E-1	1.8533E-1
0.3	1.8019E-1	1.8064E-1	1.8096E-1	1.8107E-1	1.8092E-1
0.6	1.6909E-1	1.6954E-1	1.6976E-1	1.6986E-1	1.6965E-1
0.9	1.5518E-1	1.5563E-1	1.5573E-1	1.5583E-1	1.5560E-1
1.2	1.4166E-1	1.4211E-1	1.4208E-1	1.4219E-1	1.4201E-1
1.5	1.3003E-1	1.3048E-1	1.3044E-1	1.3055E-1	1.3035E-1
1.8	1.2053E-1	1.2098E-1	1.2090E-1	1.2101E-1	1.2084E-1
2.1	1.1287E-1	1.1332E-1	1.1324E-1	1.1335E-1	1.1317E-1
2.4	1.0657E-1	1.0702E-1	1.0693E-1	1.0703E-1	1.0686E-1
2.7	1.0113E-1	1.0158E-1	1.0148E-1	1.0159E-1	1.0142E-1

and consists of either $6 \times 20 \times 20$ linear elements, or $6 \times 10 \times 10$ quadratic elements. For completeness, the tables also list the finite element results (ANSYS 8.0) generated using a $24 \times 24 \times 24$ uniform mesh consisting of 20-node "brick" elements (quadratic interpolation). Not surprisingly, the use of both quadratic and singular boundary elements appears to improve the BEM performance, with the agreement between the eight-node BEM results and FEM computations maintaining a reasonable level for both static and dynamic excitation.

3.7 Conclusions

To advance the computational treatment of three-dimensional elasticity problems involving sharp material boundaries and interfaces, the focus of this study is the development of traction-singular, semi-discontinuous surface boundary elements. Designed to simultaneously deal with traction discontinuities and integrable traction singularities of arbitrary power, these four- and eight-node elements also provide a smooth transition to regular boundary elements away for material edges. For generality, the singular elements are developed in their both "edge" and "corner" variants, allowing respectively for situations where either one or two of the adjacent element sides coincide with material edges. To aid their incorporation into a boundary integral solution scheme, quadrature over the singular elements is aided by a sequence of mapping techniques that respectively mitigate and nullify the singularity of the Green's and (traction) shape functions. For an effective treatment of rigid indentation problems, the traction-singular elements are complemented with a (four-node) linear

Table 3.4: Solid cube problem, dynamic loading: boundary displacement $u_x(3a, y, 0)/a$

y/a	4-node regular $N=2646$	4-node singular $N=2646$	8-node regular $N=2046$	8-node singular $N=2046$	FEM $N=60625$
0.0	5.8567E-2	5.8992E-2	6.5776E-2	6.5900E-2	6.6002E-2
0.3	5.0527E-2	5.0946E-2	5.7246E-2	5.7367E-2	5.7569E-2
0.6	2.9109E-2	2.9506E-2	3.4869E-2	3.4982E-2	3.5054E-2
0.9	2.5826E-4	6.2080E-4	4.5566E-3	4.6558E-3	4.6410E-3
1.2	-3.0427E-2	-3.0109E-2	-2.8029E-2	-2.7947E-2	-2.7960E-2
1.5	-5.9284E-2	-5.9019E-2	-5.8888E-2	-5.8827E-2	-5.8998E-2
1.8	-8.4397E-2	-8.4188E-2	-8.6300E-2	-8.6261E-2	-8.6470E-2
2.1	-1.0504E-1	-1.0489E-1	-1.0924E-1	-1.0922E-1	-1.0957E-1
2.4	-1.2138E-1	-1.2128E-1	-1.2797E-1	-1.2798E-1	-1.2843E-1
2.7	-1.3442E-1	-1.3437E-1	-1.4346E-1	-1.4349E-1	-1.4405E-1

and (eight-node) quadratic kinematic description that permits exact representation of the rigid-body motion. In situations involving deformable wedge configurations, these elements can be modified in a straightforward manner to include traction-compatible, power-type displacement interpolation for computational accuracy. Owing to the fact that the singular character of stresses in the vicinity of material edges and corners is unaffected by inertial forces, the proposed developments are equally applicable to elastostatic and elastodynamic problems. Using a direct boundary integral formulation the singular elements are shown, through a set of benchmark results, to be an effective computational vehicle for incorporating local singularity analyses into global calculations involving sharp geometries. With the orders of traction singularities obtained via plane-strain analysis as an example, the enhanced BIE solution is found to perform well, with fast and stable convergence for both static and dynamic problems. Owing to its dependence on the global loading conditions, however, the relevance of any local (plane or anti-plane strain) analysis is very much an open research question and represents the next step in the rigorous treatment of solid mechanics problems involving non-smooth material surfaces. Extended uses of the proposed methodology may include the analysis of 3D contact problems associated with sharp indenters as well as the calculation of stress-intensity factors for intersecting boundary and interfacial surfaces.

CHAPTER 4

The Inverse Identification Problem as an optimization problem based on Elastodynamic Boundary Integral Equations and gradient–based methods

4.1 Introduction

The identification of deffects in materials by using Qualitative Non-Destructive Testing (QNDT) is an interesting problem for the industry, material testing, seismic prospecting, medical diagnosis and underground object identification. The solution requires numerical models. An Inverse Identification Problem (IIP) is a particular kind of inverse problem in which a hidden part of the boundary is identified. Kubo's work [87] shows a general overview about the different kind of inverse problems that might be stated at a solid.

A direct problem can be stated as the calculation of the response (certain field v) given the geometry of the domain (solid Ω with boundary Γ), the material mechanical properties k, physical model operator ($\mathcal{L}$ and sources b), and boundary conditions (in terms of some known values of v, or derivatives) at Γ. Thus, a generic forward problem can be stated as follows: finding v in:

$$\mathcal{L}(v) + b = 0 \text{ on } \Omega \tag{4.1}$$

with Dirichlet, Newmann or Robin boundary conditions.

An Inverse Identification Problem (IIP) consists on finding some hidden unknown part of the boundary Γ. In order to find it, additional data from the response have to be provided, besides the boundary conditions. This data is measured at the accesible part of the boundary Γ.

This is focused on the solution of the IIP when the unknown part of the domain is a hidden cavity and the host domain is a three-dimensional elastic layer, with a set of time-harmonic forces to provide the experimental additional data. The mathematical structure of the task is an optimization problem, in which a cost function is defined based on the response measured at selected observation points for a parametrized geometry and the experimental measurements taken at the same points. Also, additional a-priori information might be provieded in order to enrich the cost functional. The forward problem is solved by the Boundary Element Method (BEM in what follows).

This problem has long been analyzed in the literature. The numerical inversion requires computing the cost function and partial derivatives respect to parameters. Finite Difference Approach has been demonstrated to produce poor convergence results; to solve such difficulty, there has been proposed two ways to compute analytic gradients. First, the Direct Differentiation Approach, and second, the Adjoint Variable Method (AVM in what follows).

The Direct Differentiation Approach is based on the analytic computation of sensitivities of any response parameter. This approach was used by Lee and Kwak [93], Nishimura et al. [118], Meric et al. [112], Aithal and Saigal [1], Mellings and Aliabadi [111], Suárez and Gallego [151], Rus and

Gallego [53, 137, 138, 136]. Using this approach, any solution parameter can be differentiated via an analytic formula. In the context of the BEM, the derivative is done via a direct differenciation of the Green's function (tractions or displacements) involved in the integral equations. But for some problems, as it is the case of the single-layer domain presented at this PhD Thesis, such derivatives are not possible or they are not available at the literature.

An alternative approach is the one proposed by the AVM. Gradients are computed through a semi-analytic formula based on the solution of the so-called *adjoint problem*. The most important task is that it is not required any derivation of kernel functions. Bonnet et al. [26, 21, 19, 48] applied the adjoint state approach to find the sensitivity to geometry variation of a cavity in bidimensional elasticity and elastodynamics. Bonnet and Constantinescu [22] show a general overview about inverse problems in elasticity, and introduce the adjoint solution for the identification of elastic moduli and hidden cavities and cracks. Recently, Bonnet and Guzina [24] use the adjoint variable approach to solve inverse identification problems of inclusions in an elastic three dimensional half space, by elastodynamic measurements.

The purpose of this work is the analysis of the inversion properties of the three-dimensional elastic layer, when the hidden object is an ellipsoid. The forward problem is solved by the BEM, based on the regularized elastodynamic boundary integral equation, and using the Green's function for the layer, developed by the authors [108]. The IIP is stated as an optimization problem, in which a BFGS algorithm is used, as it is proposed in works by Bonnet and Guzina [48, 24]. The cost function is built in terms of the misfit between experimental measurements and the one obtained by the forward problem solution, considering a parametrized position (6 parameters) of the ellipsoid. The cost function is enriched by adding some a-priori volume information. The necessary gradients of the cost function are supplied by a semi-analytic approach, by the AVM, which is very interesting for this case, due to the difficulties of deriving the Green's function. As it is an ill-posed problem, the dependence on several parameters is analyzed: number of excitation/measurement points, initial guess, a-priori volume information, frequencies, and error in experimental measurements. An extensive number of numerical tests have been carried out, which permits the analysis of the inversion process at the single layer domain.

Apart from these basic properties of this particular Inverse Problem, a set of numerical tests have been carried out in order to analyse the effect on some patches with zero displacement boundary conditions, that represents supports for some plate domains. This part of the work is interesting, due to the important aplications of this domain for the industry. A single patch has been introduced, considering zero-displacement boundary condition. It can be proof that singular tractions arises in such case. The effect of considering traction singularities through a local analysis and adequate traction shape functions [70] is tested. Through numerical experiments, it is shown that the IP converges better when singular tractions are considered, as it strongly affects to the solution of the forward and adjoint problems.

4.2 Problem statement

This chapter deals with an inverse scattering problem in which an ellipsoid cavity is hidden inside a three dimensional viscoelastic single layer. Figure 4.1 shows the 3D layer domain Ω, thickness h. With reference to the cartesian basis $\mathcal{B} = \{x_1, x_2, x_3\}$, the layer is defined as the region $\Omega = \{(x_1, x_2, x_3) | 0 \leq x_3 \leq h\}$, bounded by both planes $S = \{(x_1, x_2, x_3) | x_3 = 0\} \cup \{(x_1, x_2, x_3) | x_3 = h\}$. The material is elastic, isotropic, characterized by density ρ, and elastic constants λ and ν. Let $\Omega_c \in \Omega$ be the cavity domain, bounded by surface Γ. Let Γ_R be an auxiliary surface, $\Gamma_R = \Sigma_R \cap \Omega$, where Σ_R denotes a sphere of radius R centered at point (0,0,h/2). The figure also represents the outward

normal vector $\mathbf{n}$ to Γ, pointing to the interior of the cavity. Let $\mathbf{x} \in \Omega^-$ be an internal point, with $\Omega^- = \Omega \setminus (\Omega_c \cup \Gamma)$, and Ω_R^- the subset of Ω^- limited by Γ_R.

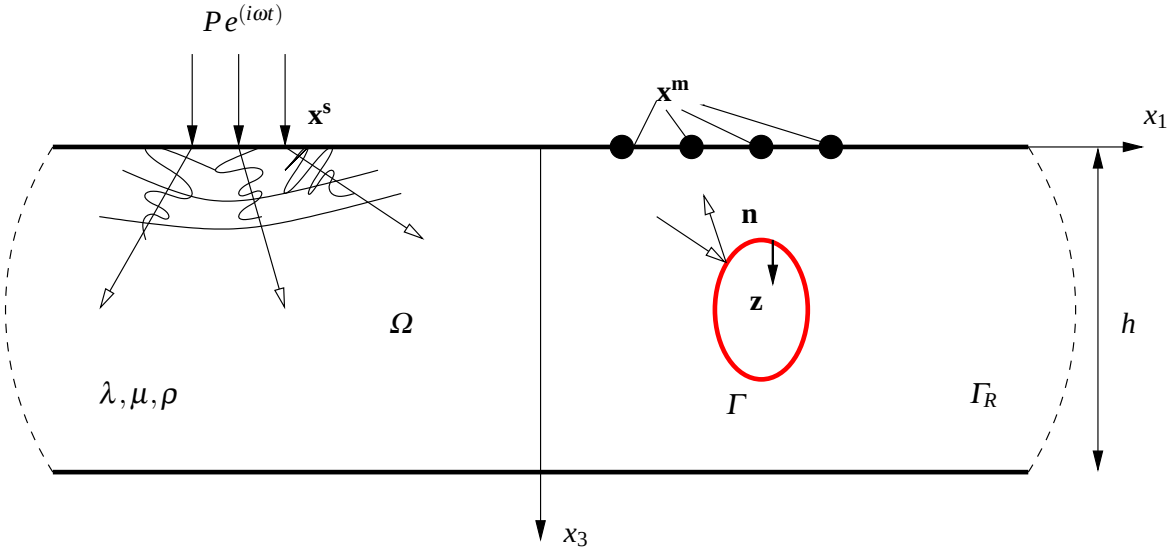

Figure 4.1: Ellipsoid cavity in a single layer domain. Sources and measurement points

At a finite set of NS points $\mathbf{x}_n^s$ corresponding to the upper layer, a set of time-harmonics sources are considered.

$$\mathbf{f}(\mathbf{x}) = \sum_{n=1}^{NS} P_n e^{i\omega t} \delta(\mathbf{x} - \mathbf{x}_n^s)\, \mathbf{e_3} \tag{4.2}$$

where δ stands for the three-dimensional Dirac delta function, P_n is the force magnitude and $\mathbf{e_3}$ is the unit vector in the x_3 direction. With this reference, the forward problem is stated:

$$\begin{aligned} \nabla \cdot (\mathbf{C} : \nabla \mathbf{u}) + \mathbf{f} + \rho\, \omega^2\, \mathbf{u} = \mathbf{0}, \mathbf{x} \in \Omega^- \\ \mathbf{t} = \mathbf{0},\ \mathbf{y} \in \Gamma \cup S \\ \lim_{R \to \infty} \int_{\Gamma_R} \{\hat{\mathbf{u}}^k(\mathbf{y}, \mathbf{x}) \cdot \mathbf{t}(\mathbf{y}) - \hat{\mathbf{t}}^k(\mathbf{y}, \mathbf{x}) \cdot \mathbf{u}(\mathbf{y})\} \mathrm{d}\Gamma = \mathbf{0} \\ \mathbf{x} \in\ \Omega_R^-,\ k = 1, 2, 3 \end{aligned} \tag{4.3}$$

with $\mathbf{t}$ is the traction unit vector, and $\mathbf{C}$ is the elastic tensor. The time-harmonic response includes damping, through the dampng rates ξ_α y ξ_β and the complex-valued material modules $\lambda = \lambda^*$ and $\mu = \mu^*$, by virtue of the *corresponding principle* [30].

$$\begin{aligned} \lambda^* + 2\mu^* &= (\lambda + 2\mu)\,[1 + 2i\xi_\alpha(\omega)]\,, \quad \xi_\alpha \geq 0 \\ \mu^* &= \mu\,[1 + 2i\xi_\beta(\omega)]\,, \quad \xi_\beta \geq 0 \end{aligned}$$

In Eq. (4.3), $\hat{\mathbf{u}}^k(\mathbf{y}, \mathbf{x})$ and $\hat{\mathbf{t}}^k(\mathbf{y}, \mathbf{x})$ are the displacement and traction functions of the fundamental solution.

4.3 Inverse Problem

The solution of the IIP requires the definition of a set of measurement points $\mathbf{x}^m$ at some accesible part of S in which displacements $\mathbf{u}$ are monitored for the true cavity position (see Figure 4.1). The statement of the optimization problem requires the definition of a cost function, as follows:

$$\mathcal{J}(\Gamma) = \frac{Q}{2} \sum_{m=1}^{NEP} \left(\overline{\mathbf{u}^m - \mathbf{u}^e}\right) \cdot \left(\mathbf{u}^m - \mathbf{u}^e\right) + \frac{G}{2} \left(V - V^{ref}\right)^2 \tag{4.4}$$

with $\mathbf{u}^m$ the measured displacements at a parametrized position of the cavity; $\mathbf{u}^e$ the experimental measurements for the true cavity; V is the volume of the parametrized cavity, and V^{ref} the a-priori known volume. The first term in Eq. (4.4) is the quadratic difference between experimental and computed measurements (considering the complex conjugate product). The second term is the quadratic difference between the reference volume and the cavity volume computed for a set of parameters. Parameters Q and G are weight constants required to provide more or less importance to the a-priori information, in order to regularize the cost function.

The cavity is modelled as an ellipsoid. The position and shape of it depends on d parameters p_d. In this case, 6 degrees of freedom have been considered: the center coordinates (c_1, c_2, c_3) and the semi-axis (a, b, c). Thus, a parameter vector is defined for the cavity, as follows:

$$\mathbf{p} = (c_1, c_2, c_3, a, b, c) \tag{4.5}$$

with p_d, $d = 1, \ldots 6$ the $d - th$ parameter. The volume V can be computed from axis dimensions,

$$V = \frac{4}{3} \pi \, a \, b \, c \tag{4.6}$$

In the literature, (e.g. see Nocedal and Wright [119]) there exists several optimization algorithms avaliable to find a local minimum with an iterative procedure in which, starting from a trial configuration, a solution is obtained by solving a local minimization problem in a quadratic approximation. In the context of BEM and IIP, Rus and Gallego [136] explore different algorithms and conclude that Levenberg-Marquardt's is the best option when the cost function is quadratic. Such conclusion is known in the literature: Levenberg Marquardt produces also faster convergence when the intial and end points are not close. At the present work, a quasi-Newton algorithm is explored, particularly the one proposed by Broyden, Fletcher, Goldfarb and Shanno (BFGS). This algorithm is also used by Fata et al. [48], to solve the IIP when the host domain is a three-dimensional half space. Despite it is known in the literature that, for such kind of quadratic cost functions, the Levenberg-Marquardt algorithm is a better option respect to convergence, the BFGS will be used. The reason to use it will be explained later, but basically for problems considered here, the Levenberg-Marquardt algorithm requires more computing time. The aim of this work is a first attempt to obtain general properties of inversion at the layer domain, comparing results with works published in the literature.

The BFGS algorithm requires the computation of the partial derivatives of the cost function respect to the design parameters, $\partial \mathcal{J} / \partial p_d$. Such gradients might be computed by the Finite Differences Approach. In the literature, it is well known that such approach produces poor convergence, and requires the computation of the direct problem too many times. The alternative to this approach is the computation of the analytic gradients. The Direct Differenciation Approach is the natural way to obtain such derivatives, but it requires the computation of derivatives of the Green function. In the context of this work, the fundamental solution for the layer is not evaluated by a closed-form

formula; displacements and traction fields requires the numerical evaluation of an inverse Hankel transform. The gradients of such functions are not avaliable in the literature. An alternative way to obtain gradients is the aplication of the Adjoint Variable Method (AVM), which requires only the solution of a forward adjoint problem, and gradients are obtained by a convolution integral over the cavity boundary Γ. In reference to the cost function defined in Eq. (4.4), gradient computations might be split into two terms: the first is the misfit between trial and experimental measurements, and partial derivatives are not analytic. On the contrary, the second term is explicit, and the derivative in Eq. (4.6) is done by a direct differentiation: thus, in what follows, the AVM is used to compute the partial derivatives of the first term.

4.4 The Adjoint Variable Method to compute gradients

The Adjoint Variable Method is used to compute the gradients respect to design parameters of the cost function. It is a useful technique avaliable in the literature that provides a semi-analytical formula to derive any function depending on some geometry-shape parametrers. The first step of the method consists on the definition of the so-called *adjoint problem*: the governing equation is the same than the one considered to solve the forward problem, Eq. (4.3), but:

- The original excitation sources are cancelled out. Instead of that, a set of point sources $\tilde{\mathbf{f}}$ are defined at the measurement points $\mathbf{x}^m$. The intensity of each source is equal to the difference between the measured and computed displacements (the conjugate complex number). Thus,

$$\tilde{\mathbf{f}}(\mathbf{x}) = Q \sum_{m=1}^{NEP} \left(\overline{\mathbf{u}^m - \mathbf{u}^e}\right) \delta(\mathbf{x} - \mathbf{x}^m) \tag{4.7}$$

- The boundary conditions of the adjoint problem are homogeneous, and same type than the direct problem. At this case, apart from traction-free condition at S, $\mathbf{t} = 0$ in Γ.

The partial derivative of the functional $\mathcal{J}$ respect to parameter p_d is computed by a numerical integral over boundary Γ.

$$\begin{aligned} \frac{\partial \mathcal{J}}{\partial p_d} \quad = \quad & \mathrm{Re}\Bigg\{ \int_\Gamma \Big[\rho\,\omega^2\,\mathbf{u}\cdot\tilde{\mathbf{u}} - \frac{2\lambda\mu}{\lambda+2\mu}\mathrm{div}_S\mathbf{u}\,\mathrm{div}_S\tilde{\mathbf{u}} - \mu\left(\nabla_S\mathbf{u} + \nabla_S^T\mathbf{u}\right) : \nabla_S^T\tilde{\mathbf{u}} \\ & + \mu\left(\nabla_S\mathbf{u}\cdot\mathbf{n}\right)\cdot\left(\nabla_S^T\tilde{\mathbf{u}}\cdot\mathbf{n}\right)\Big]\theta_n^d\,\mathrm{d}\Gamma \Bigg\} + G\left(V - V^{ref}\right)\frac{\partial V}{\partial p_d} \end{aligned} \tag{4.8}$$

In Equation (4.8), θ_n^d is the transformation velocity vector in the normal direction; $\theta_n^d \equiv \mathbf{n}\cdot\overline{\theta}^d$; considering the parametrizaton adopted here:

$$\theta_n^d = \left(n_1, n_2, n_3, \frac{x_1 - c_1}{a}\,n_1, \frac{x_2 - c_2}{b}\,n_2, \frac{x_3 - c_3}{c}\,n_3\right) \tag{4.9}$$

Equation (4.8) was obtained by Bonnet et al. (see [19, 48]) and involves a boundary only integral over Γ, in terms of the solution of the direct and adjoint solutions, and its surface divergence and gradient, with:

$$\mathrm{div}_S\mathbf{u} = u_{i,i} - n_i\,u_{i,n} \tag{4.10}$$

$$\nabla_S\mathbf{u} = \nabla\mathbf{u} - \mathbf{n}\otimes\mathbf{u}_{,n} \tag{4.11}$$

where subscript n denotes the normal derivative.

The volume term in cost function might be computed for the approximed cavity (e.g. see [48]). In the context of this work, numerical tests confirm that using the exact formula, Eq. (4.6) is a good

and simple option. Also, partial derivatives respect to axis a, b, c are easy to obtain from the volume closed-form expression.

4.5 Boundary Element and Computational Framework

The Inverse Problem solution requires some particularities respet to the numerical method chosen, when the solution is based on an iterative algorithm:

- A forward problem must be solved at each iteration, and the number of iterations required to find a local minimum usually is very large. Thus, a *minimum mesh* requirement is an interesting objective in order to minimize the global time to produce a result.
- The cavity moves from one to another iteration. Thus, a method that only involves meshing the deffects surface is desirable.
- For this layer problem, it is also desirable that the method includes the scattering conditions for the layer, without extra-meshing requirements.

For these reasons, the Boundary Element Method has been chosen to solve the forward problem at each iteration. In the context of IIP, the BEM is the natural technique to provide fast and accurate results. In this work, the formulation is based on the Regularized Boundary Integral Equation, and the elastodynamic three-dimensional solution for the layer is used as a Green's function [108]. For an internal point, the regularized BIE can be stated as follows,

$$u_k(\mathbf{y}) + \int_\Gamma \left[\hat{t}_i^k(\xi,\mathbf{y})\right]_1 \{u_i(\xi) - u_i(\mathbf{y})\} \mathrm{d}\Gamma_\xi + \int_\Gamma \left[\hat{t}_i^k(\xi,\mathbf{y})\right]_2 u_i(\xi) \mathrm{d}\Gamma_\xi = \sum_{n=1}^{NS} P_n \hat{u}_3^k(\mathbf{x}_n^s,\mathbf{y}) \tag{4.12}$$

where $[\hat{\mathbf{t}}^k]_1$ is the singular part of the elastodynamic Green's function, and $[\hat{\mathbf{t}}^k]_2$ is the regular part of the fundamental solution. In the context of the present formulation, the Mindlin's half-space solution has been adopted as a singular part, as it is shown in [108].

In order to use Equation (4.12), a set of isoparametric eight-noded element are introduced, allowing singular tractions when required [70]. The Gauss integration is performed, considering a refined mesh when the collocation point is close to the integration point, avoiding the quasi-singular integration problems. A matrix sistem is obtained, to solve the forward problem, written as:

$$\mathbf{HU} = \mathbf{F} \tag{4.13}$$

Once the direct problem is solved, the adjoint problem is stated and solved also by a regularized BIE:

$$\tilde{u}_k(\mathbf{y}) + \int_\Gamma \left[\hat{t}_i^k(\xi,\mathbf{y})\right]_1 \{\tilde{u}_i(\xi) - \tilde{u}_i(\mathbf{y})\} \mathrm{d}\Gamma_\xi + \int_\Gamma \left[\hat{t}_i^k(\xi,\mathbf{y})\right]_2 \tilde{u}_i(\xi) \mathrm{d}\Gamma_\xi = Q \sum_{m=1}^{NEP} \hat{u}_i^k(\mathbf{x}^m,\mathbf{y}) \times \left(\overline{u_i^m - u_i^e}\right) \tag{4.14}$$

$$\mathbf{H}\tilde{\mathbf{U}} = \tilde{\mathbf{F}} \tag{4.15}$$

where $\mathbf{H}$ is the same matrix than the one used to solve the direct problem; the only computation required is vector $\tilde{\mathbf{F}}$. The solution of the adjoint problem is the displacement field $\tilde{\mathbf{u}}$.

4.5.1 *Computational platform*

A FORTRAN code has been developed to compute the direct and adjoint problems. The BFGS algorithm is solved by Matlab, by using the Optimization Toolbox. Despite the problem is better understood in the context of constrained minimization (limiting the cavity size to avoid points out of the layer), there exists practical considerations to state the problem as an unconstrained nonlinear optimization one: i) the initial guess is close to the true position; in this sense, the shape and location of intial guess points could be carried out by image methods (linear sampling or topological derivative) or by an initial approximed minimization problem (combined genetic algorithms with an approximed linealization of the cost function): ii) the number of iterations increases with constrained minimization, and slower convergence is reached.

Respect to using Matlab, the main advantage is the linear search algorithm implemented, using quadratic and cubic interpolation, in order to produce a solution at each step that decreases the value of the cost function respect to the previous step. Nevertheless, the cost function must be normalized, as convergence criterium works with absolute values. Once the first solution is obtained, the root mean square for displacements is obtained (u^{rms}), and an alternative cost function is defined as follows:

$$\mathcal{J}(\Gamma) = \gamma \left(\sum_{m=1}^{NEP} \frac{1}{u^{rms}} \left(\overline{\mathbf{u}^m - \mathbf{u}^e} \right) \cdot \left(\mathbf{u}^m - \mathbf{u}^e \right) + \chi \left(\frac{V - V^{ref}}{V^{ref}} \right)^2 \right) \tag{4.16}$$

with γ a factor that controls the global stopping criterium (as it is defined by Matlab in terms of absolute value), and χ is a fractor that involves the a-priori volume information. Numerical tests have been carried out in order to callibrate such parameters.

4.6 Error in experimental measurements

To check the convergence and stability properties of the inverse algorithm, the sensitivity of the process respect to noise in experimental measurement is tested. It is a common task in the literature about Inverse Problems. Inverse problems are ill-conditioned. The algorithm proposed to solve the IIP determines the stability respect to noise in pseudo-experimental measurements. Also, the host domain plays a major role; noise is propagated inside the specimen, depending on damping. Radiation boundary conditions, as semi-space or this layer domain should avoid some problems involved with reflecting waves that amplifies the effect of noise at input data. One of the main objectives of this work is detecting if the particular layer domain permits stable inversion algorithms, with cost functions less sensitive to random noise, up to certain reasonable levels.

One common techinque to generate noise consists on applying a random distribution to the 'true' experimental observed measurements, at each component,

$$u_i^{e,noise} = u_i^e \left(1 + \varphi\right) \tag{4.17}$$

where φ is a random variable uniformly distributed over the interval $[-\eta, \eta]$. Values of η tested in this study cover range from η=0.02 to η=0.40. A set of numerical benchmarks, varying several aspects (numbers of experimental points, sources, a-priori data) gives an interesting result for this layer domain. Results will be commented at Numerical Benchmark section.

4.7 Singular tractions at supports

In order to link the applications of plate testing with industry, additional geometries must be explored, to represent supports. The aim of such test is the analysis of the inversion problem when

singular tractions occurs. In the context of ultrasound testing, the presence of sharp geometries usally causes singularities in tractions and displacement fields. Such behaviour change the response received at measurement points. Some corners and edges would act as new sources, with important implications in the inverse analysis. For direct codes, it is known in the literature that such singularities involves inaccuracy and poor convergence in numerical analysis. When gradients are supplied by the Adjoint Variable Method, the polluted data obtained by the fordward solution are the input date for the Adjoint Problem computation, in which also traction singularities occur. This causes that gradients computed by this techinque become more sensitive to tractions error that each the direct and adjoint problems.

The presence of supports in 3D plate testing is analysed at this work, as a particular case of sharp geometries. Other problems, such as the identification of boxed-cavities (with particular interest in underground facilities identification), are not considered here. Recently, Guzina *et al.* [70] developed specific singular elements for generic traction singularities. Traction singularity order is obtained by a local analysis, in which the power-type singularity exponent is solved as the main eigenvalue of the characteristic equation. Opened and closed bi-material configurations are analysed. Chapter 3 of this PhD document is focused on the development and numerical examples of such traction singular elements.

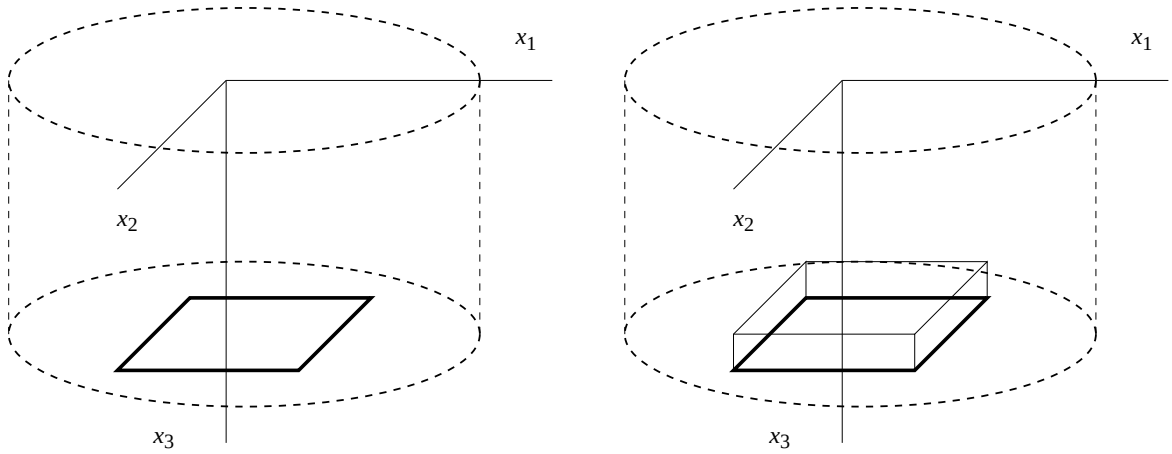

Figure 4.2: Rectangular patch and embedded support

4.8 Numerical tests

An exhaustive set of numerical tests have been carried out in order to conclude some general properties of this layer domain, in which the BFGS algorithm and the AVM are used to solve the Inverse Problem. The first step is the definition of a methodology that permits obtaining relevant conclusions of inversion process, based on statistical methods. In the literature, there exists no normalized tests that permit the comparison between domains and inversion techniques. At the present work, the relevant variables are analysed, the data are processed, and general conclusions based on statistical properties are obtained. The analysis carried out is similar than the one presented by Fata *et al.* [48] and Rus and Gallego [138].

A common task in the direct and inverse solution is the boundary element mesh used to represent the geometry and the solution. At the present work, the surface of the cavity is meshed by eight-noded quadratic boundary elements; in order to obtain a experimental solution, a fine mesh has

been used (294 elements), while the cavity is meshed by 54 boundary elements at each direct solution during the inverse analysis. Figures 5.2, 5.37 and 5.47 show the kind of boundary element mesh used.

The necessary experimental measurements might be simulated by the direct code, but a particular care must be taken when considering the same mesh and code. The *inverse crime* is a known problem that occurs when the inverse code is the same than the one used to solve the direct one. With this procedure it is difficult finding errors. In order to avoid it, a fine mesh is used to obtain the simulated experimental set of measurements. An alternative approach consists on obtaining the experimental solution by a different numerical method, such as the Finite Element Method, but this is not an easy task for the layer domain, due to its radiation boundary conditions. A coarse mesh is used to solve each forward problem during the inverse analysis. In addition, experimental errors are simulated. Thus, the effects of the inverse-crime are minimized and general conclusions can be obtained.

There are several parameters that affects the inverse analysis, in which gradients are computed by a semi-analytic formula, based on the Adjoint Variable Approach. The first required check is the quality of gradients obtained by such an approach.

The parameters tested may be summarized as follows:

- Arrays of excitation/measurement points. First, the relative position between both kind of points is considered. Two basic configurations are defined, to test the influence of symmetric or non-simmetric profiles in arrays of sources/receivers. At a second stage, the number of excitation/measurement points is increased, to test the sensitivity of the inversion algorithm to the dimension of the excitation/measurement points arrays.
- Frequency tested. In a plate there exists quasi-resonance frequencies; thus, the dependence on the excitation frequency is considered. There are better excitation frequencies in which the convergence of the algorithm is better. Also, the frequency determines the size of the deffects that might be found inner to the layer. Such frequency-dependence is analysed.
- True cavity position and initial guess points. The IP is an ill-posed problem. In this sense, the convergence is not guaranteed for all the relative configurations true/guess cavities. The resultant geometry is strongly dependent on the position of the initial guess. The solution, in a general domain, could be non-unique. The particularities of this domain is explored in order to fix the adequate range of cavity sizes and shapes, and relative distance of the initial guess point to guarantee the convergence.
- Parametrization of the cavity. The cavity can be parametrized up to 6 different parameters, but less parameters can be fixed. The dependence on the number of parameters is a common test in the literature, and it is also checked here.
- Consideration of a-priori volume information. The effect of this regularizing term is analysed; the definition of an adequate factor χ to give more or less importance to a-priori volume is tested.
- Consideration of noise in experimental measurements. First, a set of tests have been carried out without noise consideration; in a second step, the effect of noise in experimental measurements, by increasing noise levels, is analysed.
- The effect of additonal patches that represents supports for the layer. In this context, the consideration of traction singular elements have been tested.

4.8.1 Gradients checking

To show the advantages and special cares to use the Adjoint Variable Approach to compute gradients, a first numerical experiment has been carried out. An sphere of radius r is tested, centered at

Table 4.1: Gradient checking: Finite Differences vs. Adjoint Variable Method

Gradient component	96 elements Finite Diff.	$\mathcal{J} = 12.22\mu r^3$ Adjoint	294 elements Finite Diff	$\mathcal{J} = 12.43\mu r^3$ Adjoint
$1/(\mu r^2)\partial\mathcal{J}/\partial a$	1.2202	1.2009	1.2210	1.223
$1/(\mu r^2)\partial\mathcal{J}/\partial b$	-2.2021	-2.183	-1.992	-1.982
$1/(\mu r^2)\partial\mathcal{J}/\partial c$	0.3323	0.2935	0.3255	0.3203
$1/(\mu r^2)\partial\mathcal{J}/\partial c_1$	-4.342	-3.822	-4.288	-4.2901
$1/(\mu r^2)\partial\mathcal{J}/\partial c_2$	0.4434	0.429	0.4593	0.4584
$1/(\mu r^2)\partial\mathcal{J}/\partial c_3$	-0.7877	-0.7538	-0.7712	-0.7723

$(0, 0, 3r)$. The layer thickness is $h = 6r$. Elastic constants for the layer are μ, $\nu = 0.3$, and mass density ρ, whith $c_s = \sqrt{\mu/\rho}$ the speed of the S-waves. Damping rates are $\xi_\alpha = \xi_\beta = 0.05$. With $c_s = 1$, the excitation frequency $\bar{\omega} = \frac{\omega r}{\sqrt{\mu/\rho}} = 1$ concludes a wavelenght for s-waves $\lambda_s = 2\,\pi\,r \simeq 6.28\,r$, close to the thickness $h = 6r$ adopted. No a-priori volume information is considered.

Vector $\mathbf{p}_0 = (-0.5r, 1.2r, 2r, 1.5r, 0.5r, r)$ defines the 6 parameters of the initial guess ellipsoid. In reference to Figure (4.6) a set of 16 sources are considered, with $P_m = \mu r^2, m = 1, 16$, located in a square 4x4 mesh size 3r . Receptors are shown at the same figure, in a 3x3 squared mesh with size 2r. At receivers, displacements u_1, u_2 and u_3 are measured. Thus, $9 \times 3 = 27$ synthetic observation data are obtained.

The original cost function, Eq (4.4) is computed, with $Q = 1E6$, without a-priori information considered. The finite differences are computed for gradients $\partial\mathcal{J}/\partial p_d$, with central differences $\Delta p_d = 0.01r$. Table 4.1 compares the performance of the adjoint field vs. the finite differences, for two different meshes for the cavity. As it is known in the literature, the quality of the results computed via the AVM depends on the mesh used to discretize the cavity. Finite differences produces, in general, better results for coarse meshes. Nevertheless, gradients computed via the AVM are less computing-expensive, and the quality of the results are better when the point is close to the true position.

4.8.2 Quasi-resonance phenomena in infinite layers and excitation frequencies

The dependence on the frequency in the inversion process is an interesting task, with practical consequences. In a general solid, the existence of eigen frequencies determines resonance phenomena, wich affects the convergence of the inverse algorithm. In the context of infinite plates, and for the kind of sources tested, there are no pure eigenmodes, due to the radiation boundary condition. When the layer is excited, a system of symmetric and asymmetric Lamb waves are generated. The study of Lamb wave propagation in elastic waveguides is an active domain of research, notably because of the important applications it may have in nondestructive testing. It is remarkable that, for such topic, there remain fundamental open questions, such as the mathematical proof of the completeness of the Lamb modes [13]. There are other fundamental problems not fully treated in the literature, such as quasi-resonance phenomena (characterized by a large but finite amplitude response), reported in the literature, for the semi-infinite plate (e.g. [141, 158, 62, 92, 162, 122]). The physical phenomena is the dominance of the first symmetric mode S_0 respect to the initial A_0 asymmetric mode, which is the main mode at low frequencies. The phenomenon was first discovered by experimental techniques by Glazis, in 1956. For the layer domain, a practical tool to find quasi-resonances adopted in this work is testing the displacements at the upper and lower layer at a range of frequencies. Quasirresonance occurs when displacements are amplified in a symmetric profile (S_0 Lamb wave).

Numerical experiments have been carried out in a plate thickness $h = 6r$, to detect the amplification frequency. A point source, intensity μr^2 is located at the origin, pointing to the positive x_3 direction. Six point are fixed, 3 of them located at $x_3 = 0$ and the other 3 points at the same x_1, x_2 positions, but at the lower layer; $x = 3 = h$. Displacements u_1 and u_3 are computed at different frequencies. Figure 4.3 show the comparative results for displacements, for two points located at both traction-free layers, and coordinates $x_1 = 2r$, $x_2 = 0$. Analogous figures for points located at $x_1 = 4r$ and $x_1 = 6r$ are shown in Figures 4.4 and 4.4, respectively.

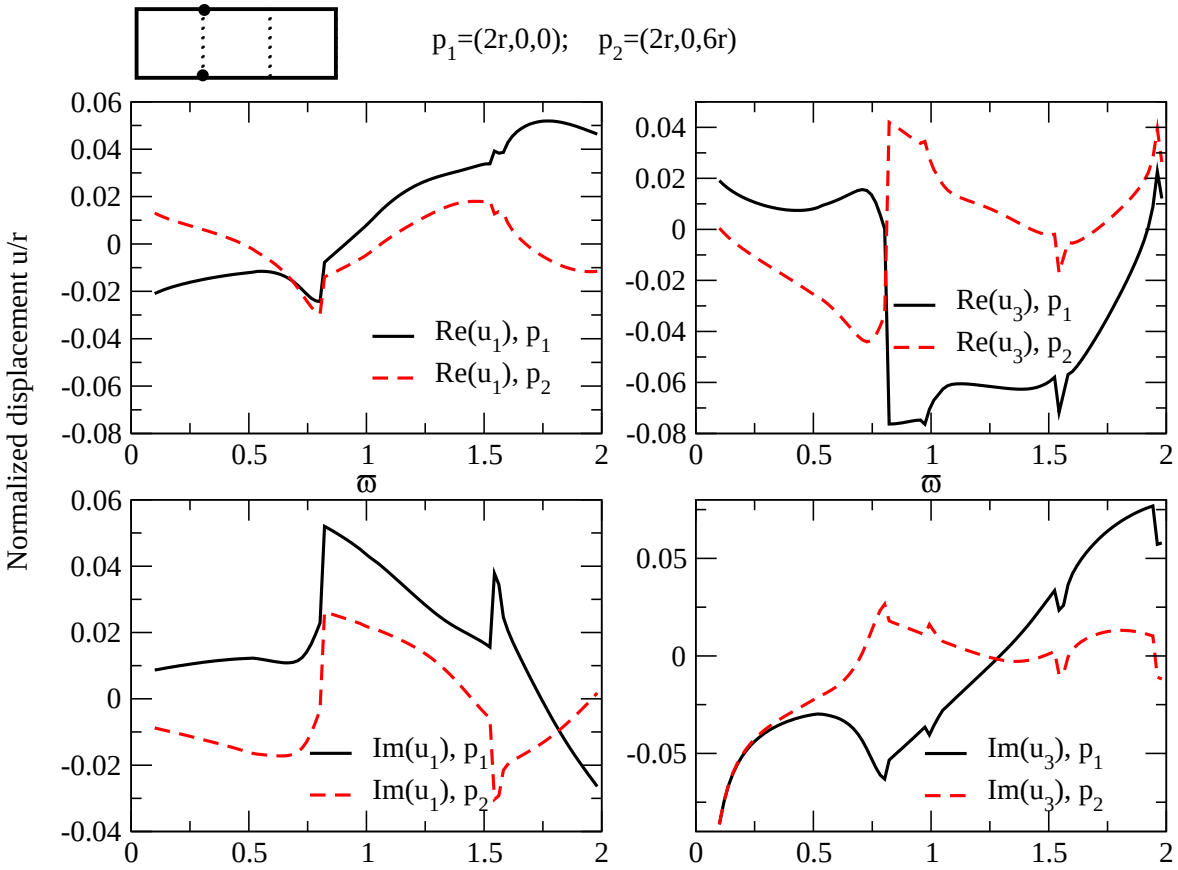

Figure 4.3: Quasirresonance test. Displacement patterns at $x_1 = 2r$

The quasirresonance frequency corresponds with $\bar{\omega} = 0.85$.Displacement pattern show that for frequencies below this value, a quasi-static (asymmetric) mode is the dominant one. On the contrary, for frequencies up to the quasirresonance, a symmetric propagating mode contains the main information. The quasirresonance in this sense might be interpreted as the frequency that activates the symmetric mode S_0.

From this analysis, four excitation frequencies have been fixed for subsequent tests: $\bar{\omega} = \frac{\omega r}{\sqrt{\mu/\rho}} = \{0.5, 1, 1.5, 2\}$. As it is observed in plots, frequency $\omega = 1$ is close to the quasirresonance frequency $\bar{\omega} = 1$.

4.8.3 Numerical benchmark

The inversion process depends on the relative positions of the excitation points and source points. At this domain in which layer waves are present two basic configurations are proposed. At the first of

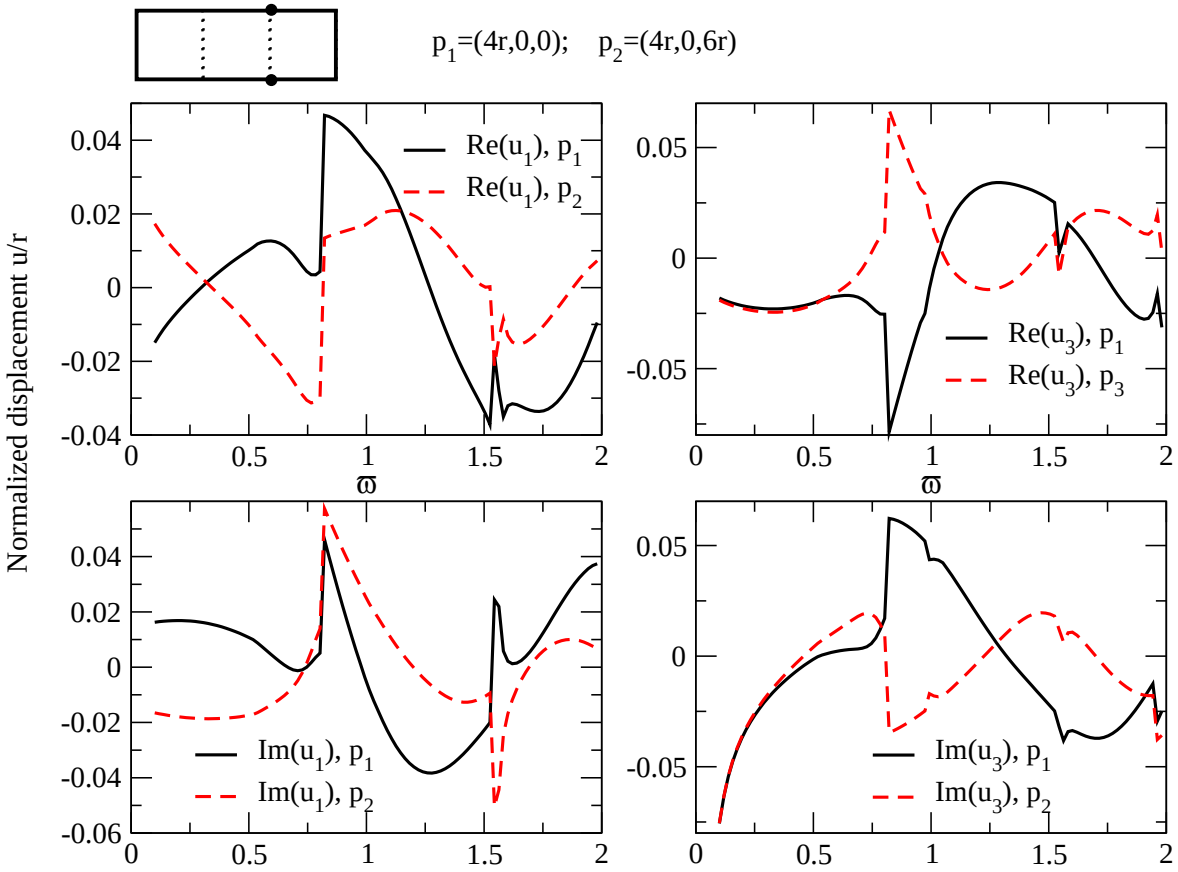

Figure 4.4: Quasirresonance test. Displacement patterns at $x_1 = 4r$

them, the source points and the receivers are disposed in a rectangular array with the same gravity center, located at the origin of coordinates, see Figure 4.6 with this profile, reported by Fata and Guzina's work [48], the buried cavity is identified with the refleced waves that comes from the cavity, but few of them coming from the lower bound (and less important when damping is included).

The second configuration checks the influence on waves coming from reflection from the lower layer. Figure 4.7 shows a typical configuration of the second kind used in this work. Sources and receivers are located in rectangular arrays whith different gravity centers. Waves received at measurement points comes from rebounds coming from the hidden cavity, and from the lower layer. The mirror effect coming from the lower layer is more important when low damping ratios are considered. For all the cases studied here, the distance between center coordinates from sources and receivers is fixed in $3r$, for all the problems. For both cases, a layer thickness $h = 6r$ has been fixed; material elastic properties μ, $\nu = 0.3$ have been adopted, with damping parameters $\xi_\alpha = \xi_\beta = 0.05$. Sources are time-harmonic, intensity $P_m = \mu r^2$.

For each configuration, the following parameter variation have been carried out:

- *Excitation points*: Rectangular meshes, sizes $r \times r$, $2r \times 2r$ and $3r \times 3r$, are set. For each size, 5 source-points arrays have been generated, varying the number of points: 4×4, 5×5, 6×6, 9×9 and 11×11. Thus, 3 sizes and 5 different sets of points = 15 configurations.
- *Measurement points*: Measurement points are located at the center of rectangular meshes, sized $r \times r$, $2r \times 2r$ and $3r \times 3r$. For each size, the arrays of measurement points are 3×3, 4×4, 5×5,

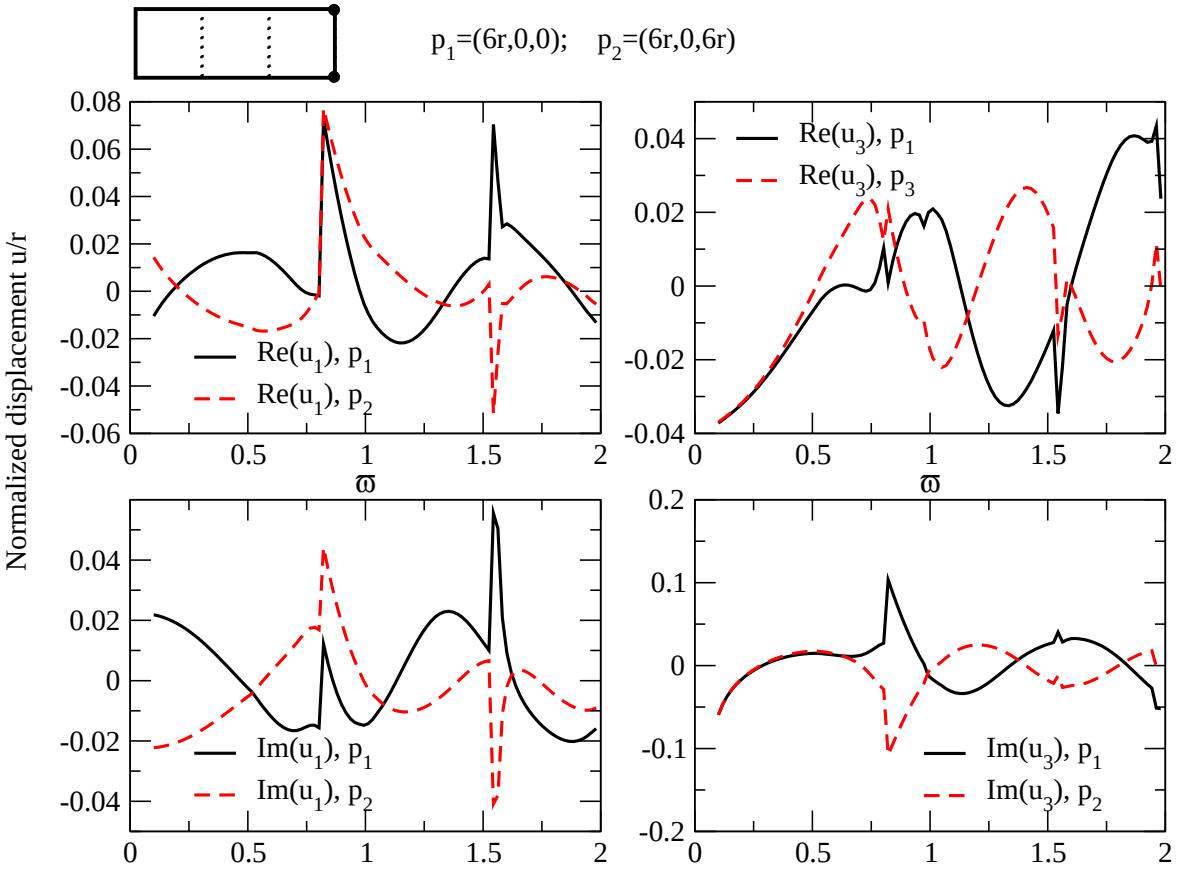

Figure 4.5: Quasirresonance test. Displacement patterns at $x_1 = 6r$

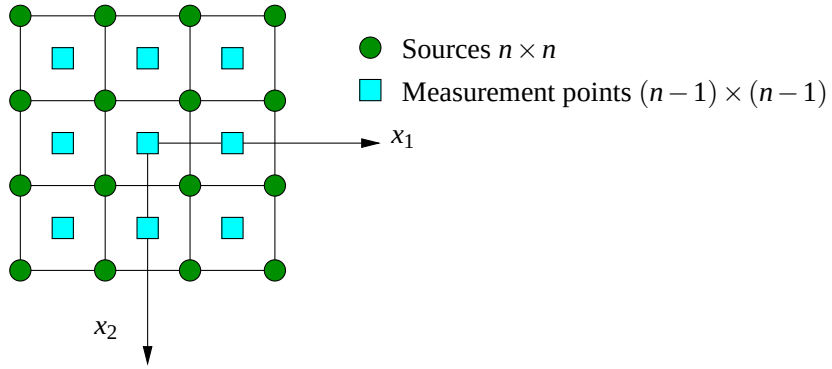

Figure 4.6: Sources and receivers, configuration 1, at $x_3 = 0$

8×8 and 10×10. Only the 15 configurations in which $n \times n$ sources with $(n-1) \times (n-1)$ receivers have been considered.

- *Excitation dimensionless frequencies* $\bar{\omega} = \{0.5, 1, 1.5, 2\}$ have been tested, with $\bar{\omega} = \frac{\omega r}{(\sqrt{\mu/\rho})}$.
- *True cavity position*: For each problem it has been considered 9 positions for the true cavity:
  - Cavity center: $(0, 0, 2r)$; $(0, 0, 3r)$ and $(0, 0, 4r)$.
  - Cavity semi-axis: $a = b = c = 0.5$; $a = b = 2c = 1.1$; $2a = 2b = c = 1.1$.

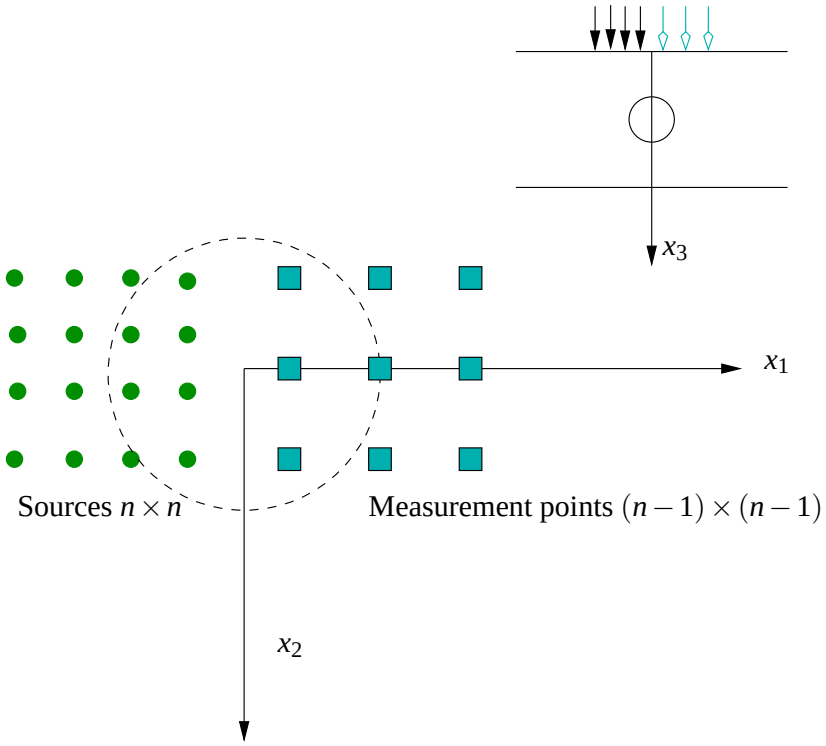

Figure 4.7: Sources and receivers, configuration 2, at $x_3 = 0$

- *Initial guess point*: For each problem, 5 random initial trial positions have been adopted. The distance given is limited to $2r$ in center coordinates, and r in cavity diameters. Initial guess are filtered in order to remain inside the plate domain. It is assumed that initial points are given after a mapping tool is checked at the domain (like Topological Sensitivity or Linear Sampling Method); thus, initial guess points remain close to the true parameters.
- *Parameter configurations*: 5 parameter configurations have been defined:
  - 2 parameters, (c_1, r), with r the cavity radius.
  - 3 parameters, (c_1, c_3, r).
  - 4 parameters, (c_1, c_2, c_3, r).
  - 4 parameters, (c_1, c_2, a, b).
  - 6 parameters, (c_1, c_2, c_3, a, b, c).

  For each parameter configuration, different cavity positions and guess points have been adopted.
- *A priori volume information*: The presence of a-priori known volume information is introduced. Value $\chi = 0.1$ is fixed, after numerical experiments.
- *Noise levels*: Levels $\eta = 0\%, 2\%, 10\%, 20\%, 30\%, 40\%$ have been considered.
- *Traction singular elements*: The effect of traction singularities at supports is tested. A reduced number of problems have been chosen. Two basic configurations, according to Figure 4.2 have been defined: a rectangular patch, size $r \times r$ centered at $(0, 0, 6r)$ is set. Singularity coefficients $\alpha = \beta = 0.5$ are fixed, with $c = 0.9$, for edge and corner elements. A 3×3 8-noded element mesh is defined. Apart from this, an embedded support is considered, $r \times r \times 0.5r$, centered at the same location. A $3 \times 3 \times 3$ mesh is defined, with $\alpha = \beta = 0.410$ for the embedded edges and corners, and $\alpha = \beta = 0.310$ for opened bi-material edges and corners. Also, parameter $c = 0.9$ defines the position of the shifted nodes.

A-priori volume information

The effect of providing the a-priori volume information produces changes in the shape of the cost function. It is known in the literature that the regularizing efect depends on the coefficient χ given to the a-priori known term. At the present work, parameters $\chi = \{0.05, 0.1, 1, 10\}$ have been explored. It has been observed that increasing the value χ produces a cost function in which the volume is more and more important, giving less importance to the misfit in measurement values term. This causes slow convergence in center coordinates parameters, and high convergence in size parameters (a, b, c). Parameter $\chi = 0.1$ produces a better regularizing effect, guiding the searching process by a fast convergence to the true size and reasonable number of iterations in cavity centers.

To analyse the effect of the a-priori volume information, a first set of tests have been defined, in which no noise is considered. Test have been designed in order to identify the dependence on the volume information respect to the main parameters involved in the inversion: number of excitation and measurement points, frequencies, noise, etc. In what follows results at different frequencies with a symmetric profile of sources and receptors, size 4×4, with 16 source points and 9 receptors are shown. General conclusions will be obtained.

To visualize the dependence on parameter χ, Figure 4.8 represents the number of iterations versus the values of parameters. It is observed that the higher the value of χ, the slowest convergence is reached. The shape of the cost function changes when a-priori volume information is provided. Cost function becomes less sensitive to center coordinates parameters. Thus, despite convergence is better, it requires an important amount of iterations. Parameter $\chi = 0.1$ reports the best results, in terms of convergence.

The regularizing efect of χ depends on the excitation frequency. At high frequencies, cost function is more irregular, providing several critical points. In problems considered at this work, initial points are close to the true point; thus, it is difficult obtaining as solutions based on gradient techniques points corresponding to other zeroes of the gradient. The effect on the excitation frequency is shown in Figure 4.9. At each frequency, the cummulative error parameter ι is computed, as follows,

$$\iota = \sum_{k=1}^{K} \left\| \mathbf{p} - \mathbf{p}^{true} \right\|_k \tag{4.18}$$

with

$$\left\| \mathbf{p} - \mathbf{p}^{true} \right\| = \sqrt{\sum_{d=1}^{6} \left(p_d - p_d^{true} \right)^2)} \tag{4.19}$$

Figure 4.9 represents parameter ι at frequencies $\bar{\omega} = \{0.5, 1, 1.5, 2\}$, computed for variuos a-priori parameters $\chi = \{0, 0.05, 0.1, 1, 10\}$. Parameter ι increases with the error level and the number of iterations required. It is observed the frequency dependence on the identification process. The best results are obtained at $\bar{\omega} = 1$, and $\chi = 0.1$. When parameter χ increases, the identification is less dependent on the excitation frequency, due to the fact that the cost function is based on the misfit between volumes. In general, increasing the frequency requires more iterations, but the regularizing efect of the a-priori volume information term is notorious. This fact can be concluded comparing with the results obtained at high frequency when no known volume is given.

The influence on other parameters, such as the number of excitation/measurement points, or the initial guess points, seems to play a minor role. Despite by increasing the number of excitation points the cost function increases at the measurement misfit term, the number of points chosen at the

present work is moderate. This could be the reason that parameter $\chi = 0.1$ reports the better results for all cases.

Figure 4.11 shows the iterates obtained during the optimization process, when no volume information is given. Optimization finishes after 11 iterations. The main characteristic is that cost function is sensitive both to center coordinates and to element shape. In contrast, figure 4.12 represents the iterates when a-priori volumen information is given. The parameters are adjusted in two steps: first, the cavity parameters related with size are adjusted. Second, the center coordinates are obtained. Providing more or less values for χ parameter, the second stage becomes more and more slow, but it converges to the true cavity position. Numerical experiments confirm that, for such configuration, parameter χ provides the less number of iterations, reaching the numerical convergence required.

When computations are carried out at configurations in which sources and receivers remain at different centers, a similar behaviour is observed, but the number of iterations required for convergence is higher. Figure 4.10 represents the dimensionless frequency $\bar{\omega}$ vs. the cummulative error parameter ι. With reference to Figure 4.9, a similar behaviour is observed, but more iterations and errors are obtained at the second configuration. Figure 4.13 shows the iterates for a particular problem ($\bar{\omega} = 1$), identification of an ellipsoid $a = b = 2c = 1.1$) when no a-priori volume information is given. In contrast with figure 4.14, the expected behaviour is observed: at the initial iterations, the volume is fitted, and the cavity centers are adjusted, with a reasonable number of iterations. Thus, also for this problem, volume parameter $\chi = 0.1$ seems to play an eficient role in the optimization process.

The main conclusion respect to volume information given by the numerical benchmark is that is an interesting regularization factor, but only providing the adequate weight coefficient. In configurations tested here, and up to the maximum frequency tested $\bar{\omega} = 2$, parameter $\chi = 0.1$ provides the best results, in terms of convergence and less number of iterations.

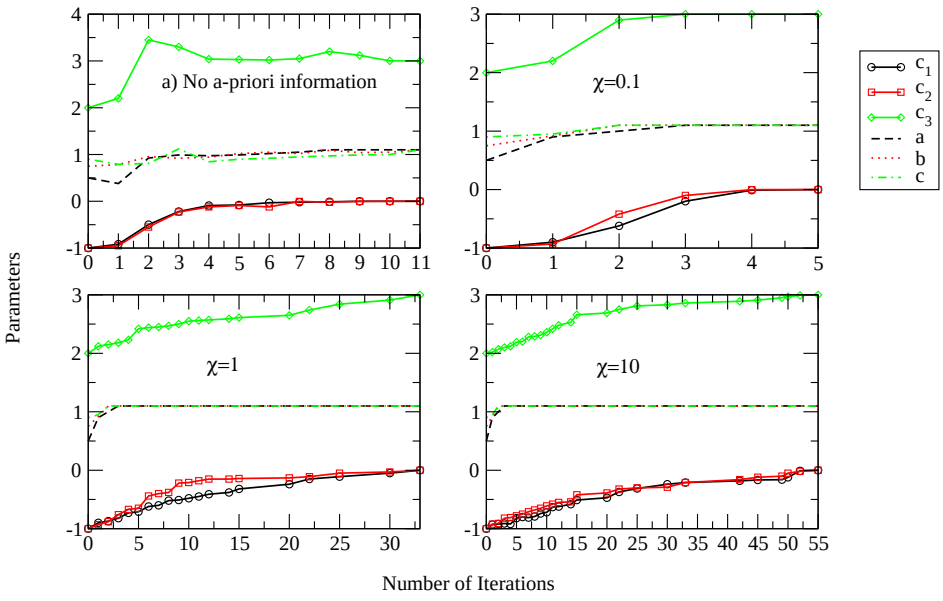

Figure 4.8: Effect of a-priori volume parameter χ on the inversion process. A 6-parameter identification at $\bar{\omega} = 1$

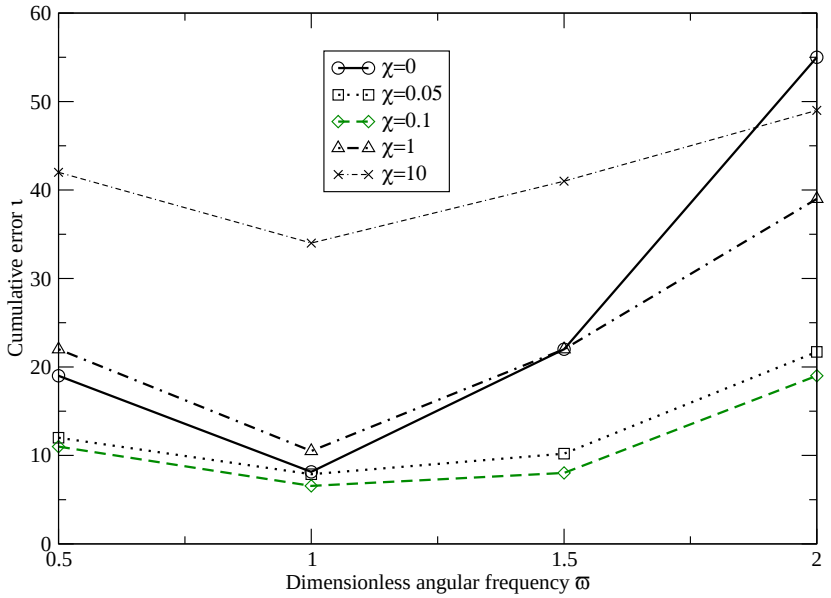

Figure 4.9: Effect of different a-priori volume parameter χ vs. the dimensionless frequency $\bar{\omega}$. Sources and receivers centers at the same location.

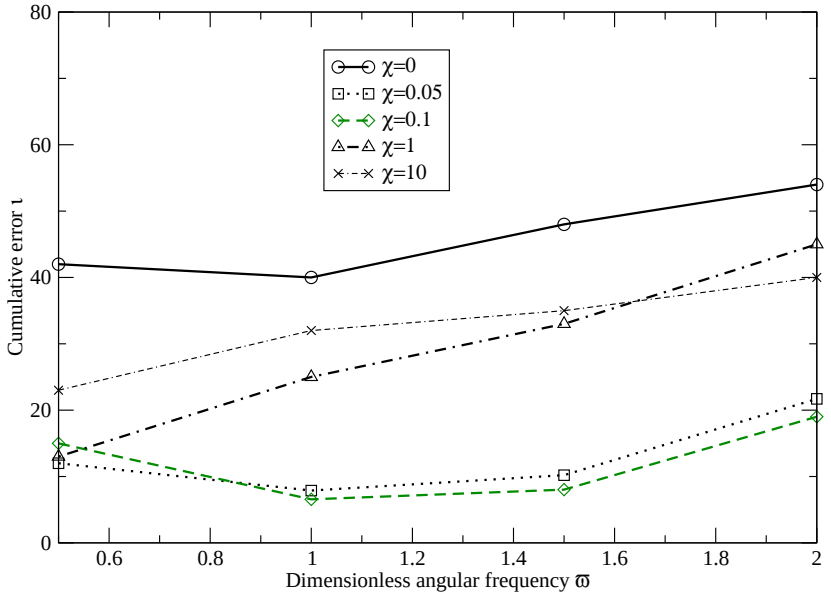

Figure 4.10: Effect of different a-priori volume parameter χ vs. the dimensionless frequency $\bar{\omega}$. Sources and receivers centers at different locations

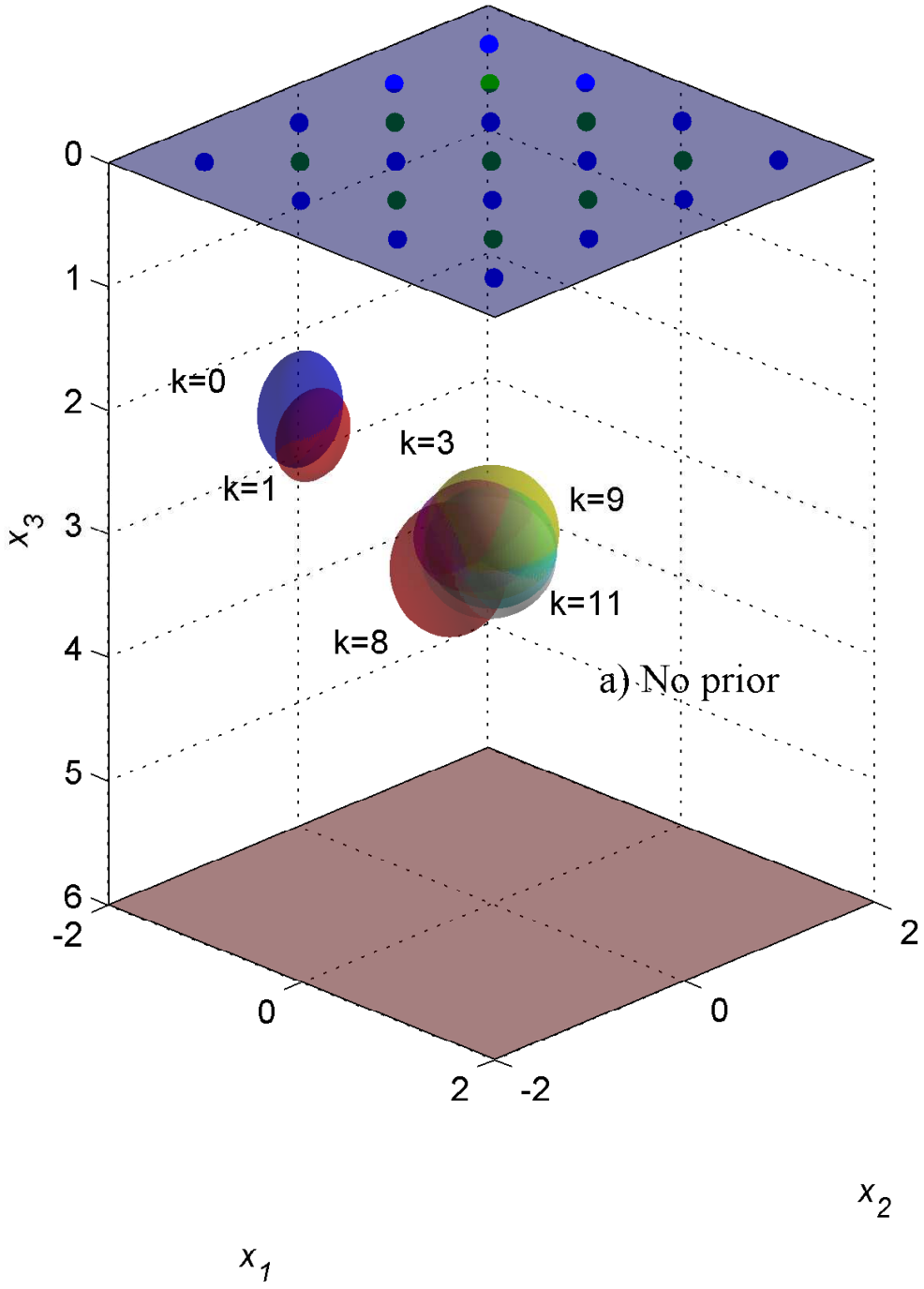

Figure 4.11: Sample of iterates during the optimization process. No prior information provided. Symmetric profile for sources/receivers.

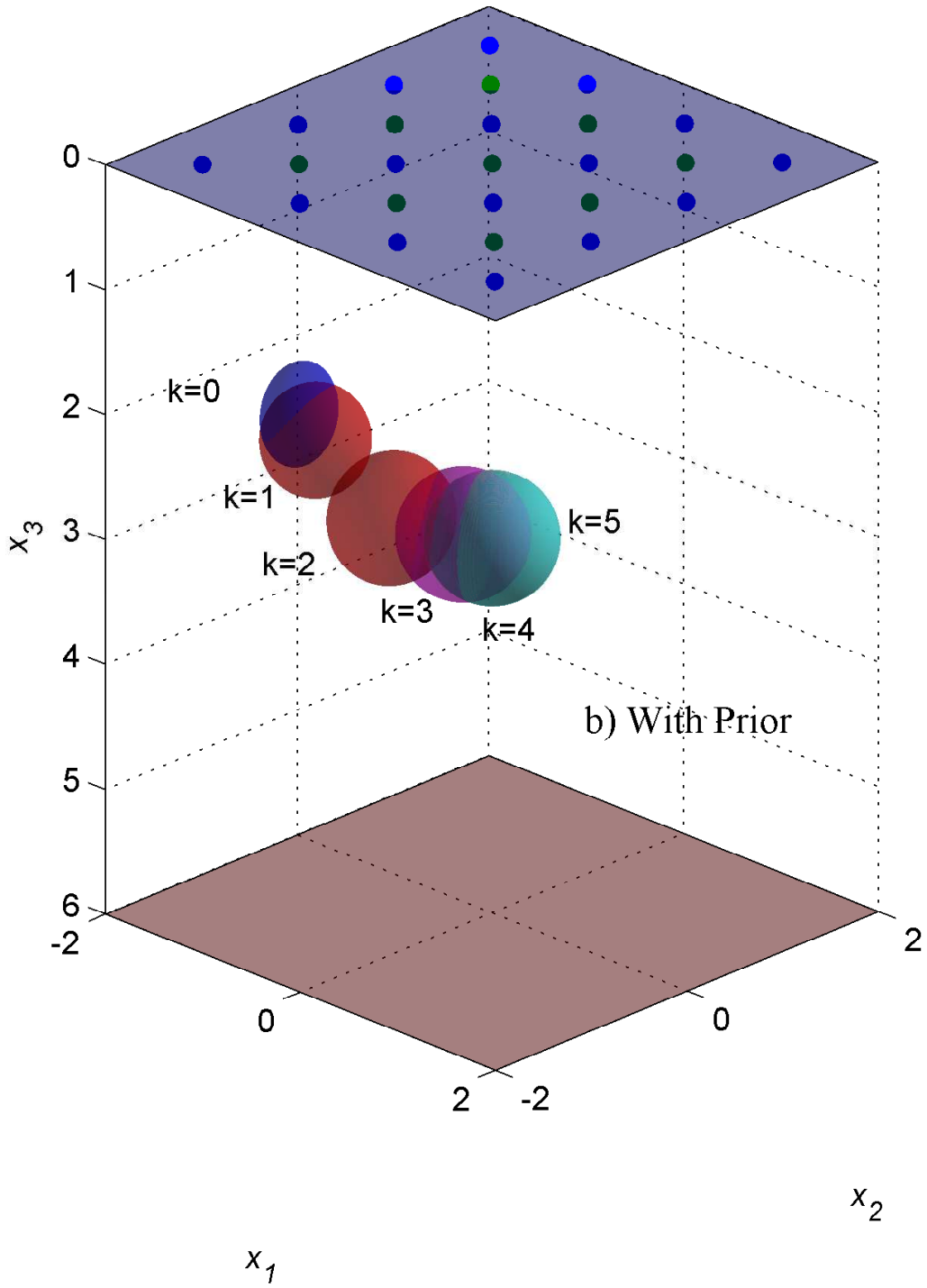

Figure 4.12: Sample of iterates during the optimization process. A-priori $\chi = 0.1$ information provided. Symmetric profile of sources/receivers.

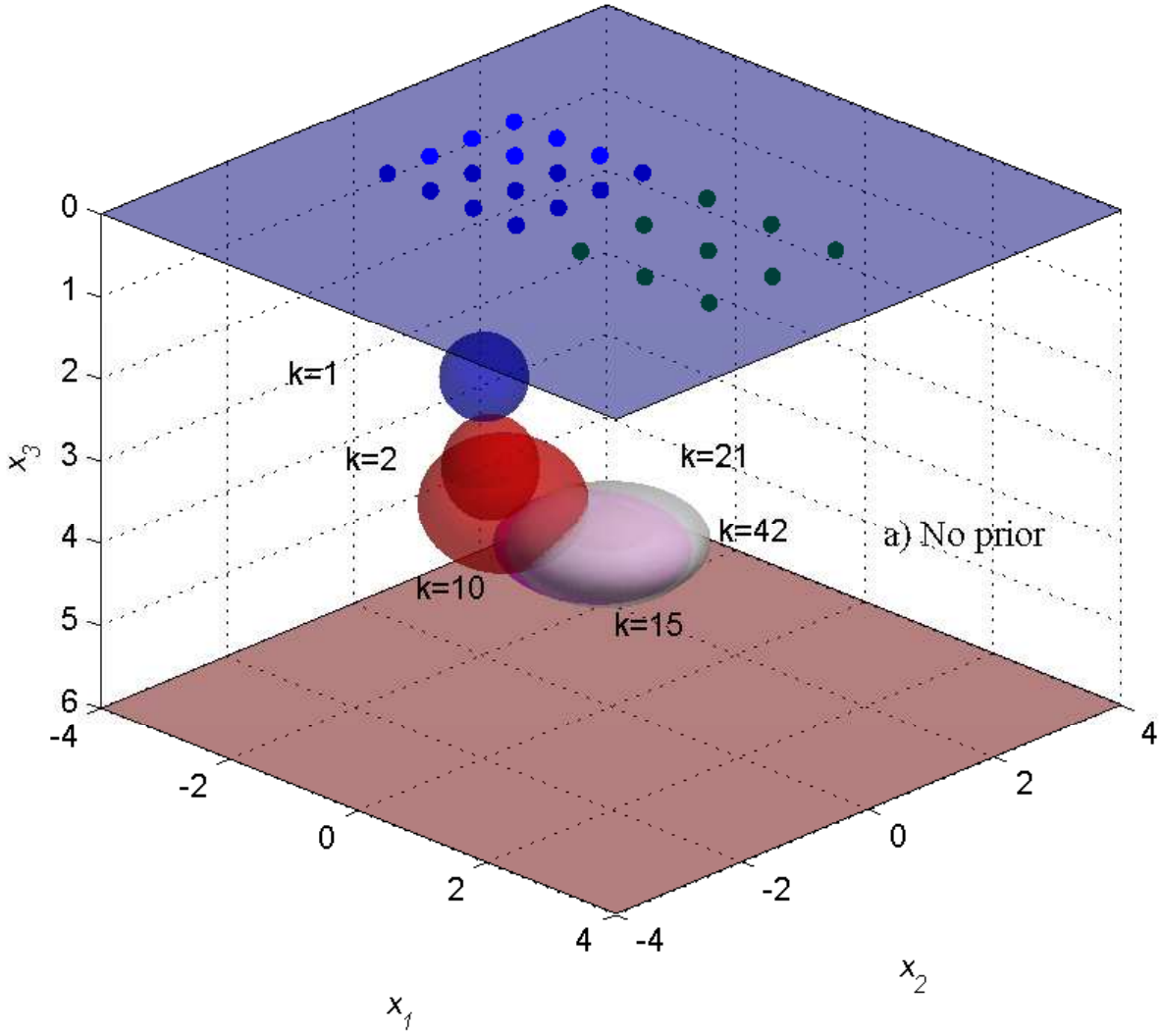

Figure 4.13: Sample of iterates during the optimization process. No prior information provided. Non-symmetric profile of sources/receivers.

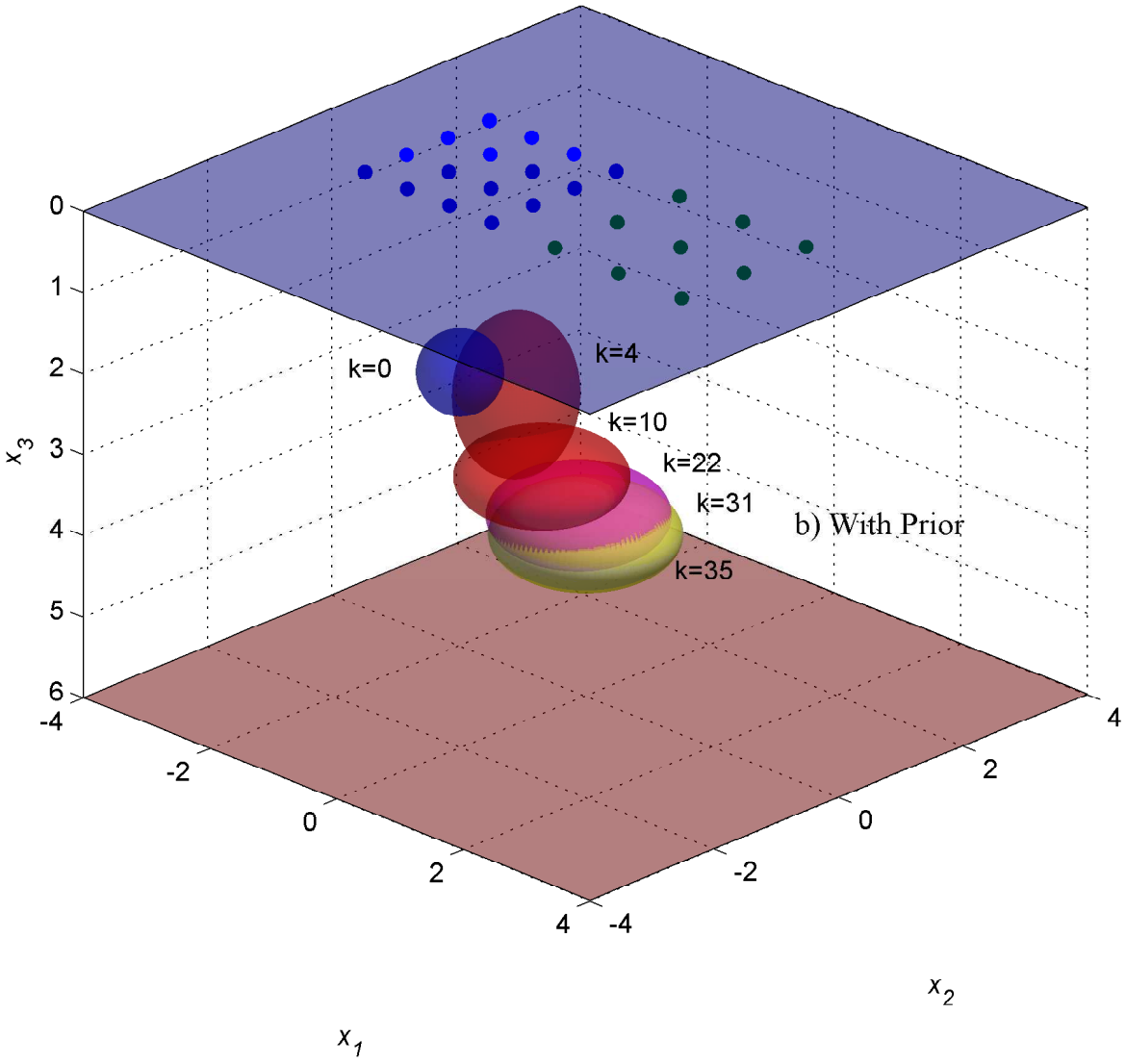

Figure 4.14: Sample of iterates during the optimization process. A-priori $\chi = 0.1$ information provided. Non-symmetric profile of sources/receivers.

Experimental data set and parameters

The number of sources and receivers play a major role at the identification process. The identification is based on measures taken at some receivers, excited by vertical sources at different points. The numbers of configurations chosen here are 5: from 16 sources and 9 receivers, to 121 sources and 100 measurement points. Three different sizes for arrays of sources/receivers have been tested. Thus, 15 configurations are considered. In order to obtain conclusions, no noise is given at measurement points.

Gallego and Rus [138] show that the number of measurements does not seem to play a major role in the convergence process. At that work, results are shown in double logarithmic scale. Results show that increasing the number of measurements does not increases the number of iterations required for convergence. It is remarked that for such configurations, more number of experimental points than parameters are provided. All the configurations chosen at the present work consider $(n-1) \times (n-1)$ receivers for $n \times n$. Thus, the number of experimental points and sources increases. This causes given a richer information when the number of points increases.

The methodology developed here to compare the results is obtaining the number of iterations required for convergence, at each frequency, and parameter configuration. At each problem, 9 configurations are tested, considering the center and semi-axis coordinates. Also, it is included the effect of providing 5 different initial guess points. Frequency and relative positions of sources and receivers remain as independent parameters.

A first plot is shown for $\bar{\omega} = 0.5$ and a symetric profile of sources and receivers. Figure 4.15 shows the dependence of convergence on the number of parameters at $\bar{\omega} = 0.5$, with few differences when more or less number of experimental points are chosen. Figure 4.16 shows the same result at $\bar{\omega} = 2$. Despite the number of iterations required at the higher frequency is higher, results shows that convergence depends more on the number of parameters chosen to define the ellipsoidal cavity.

In contrast, Figure 4.17 shows the same test carried out when sources and receivers are disposed in separated arrays without common center. Results when sources and receivers are located at separated spacial zones report poorer convergence.

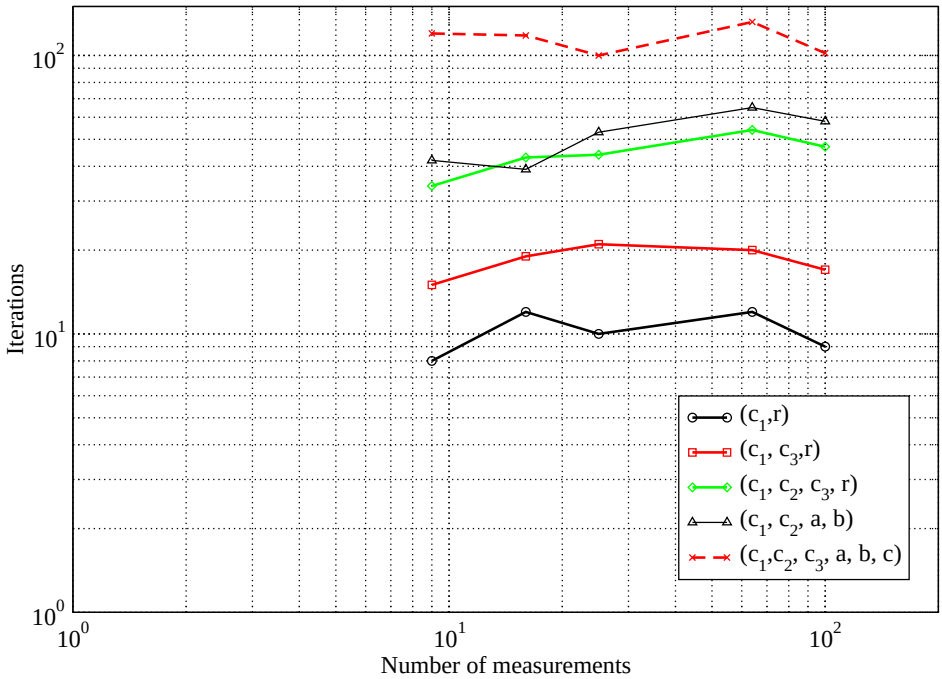

Figure 4.15: Convergence with different number of measurements and parameters. Excitation frequency $\bar{\omega} = 0.5$. Sources and receivers at symmetric profile configuration.

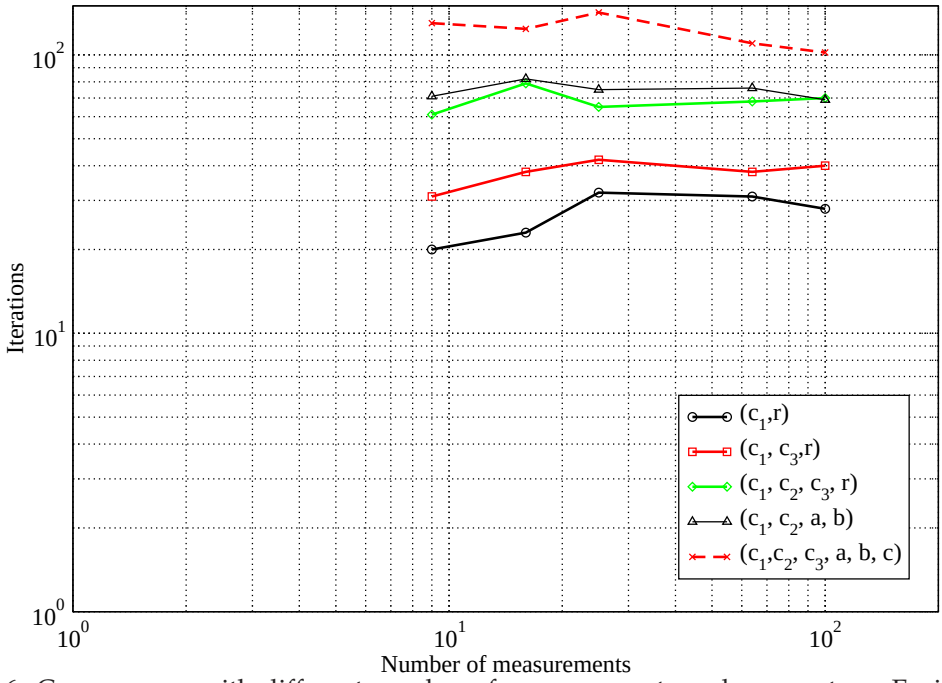

Figure 4.16: Convergence with different number of measurements and parameters. Excitation frequency $\bar{\omega} = 2$. Sources and receivers at symmetric profile configuration.

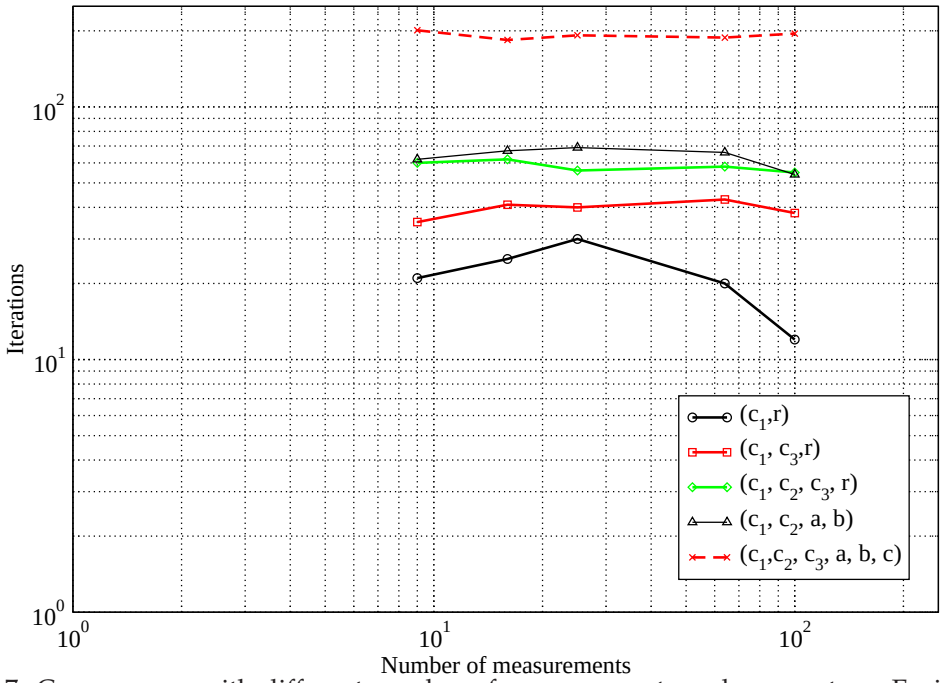

Figure 4.17: Convergence with different number of measurements and parameters. Excitation frequency $\bar{\omega} = 2$. Sources and receivers at aymmetric profile configuration.

Noise in experimental data

In inverse problem literature, the dependence on noise in experimental measurements is a common task. Noise considered here affects only to the quality of the experimental data, but other kind of noise is involved in the direct and inverse problem, such as geometry alteration, elastic parameters, frequency, etc (e.g. see [138]). In this work, errors in modelization of sharp geometries is considered in a different section.

Numerical errors are simulated with Equation 4.17, with aleatory variable $\eta = \{0.05, 0.1, 0.2, 0.3, 0.4\}$. Poor convergence is observed for error levels up to 40%. Following the methodology proposed by Rus and Gallego [138], the result reported at each problem involves a norm defined in terms of center coordinates and geometrical invariants.

$$I = \sqrt{1/r^2 * \left[(c_1 - c_1^{ref})^2 + (c_2 - c_2^{ref})^2 + (c_3 - c_3^{ref})^2)\right] + (I_x/I_x^{ref} - 1)^2 + (I_y/I_y^{ref} - 1)^2 + (I_z/I_z^{ref} - 1)^2} \tag{4.20}$$

with I_x, I_y, I_z the main inertia moment of ellipsoids, referred to the center of the ellipsoid at each configuration.

Parameter I is dimensionless, and it is sensitive to the difference in sizes and center coordinates. Inertia terms are more sensitive than center parameters (c_1, c_2, c_3).

The dependence on $\bar{\omega}$ is checked for a set of 2 parameters (c_1, r) inverse identification problems for variable levels of noise involved. No a-priori volume information is given. Sources are defined in an array sized $3r \times 3r$, with 6×6 source points and 5×5 measurement points, centered at $(0, 0, 0)$. It was shown in previous section that inversion is less sensitive to the number of sources and receivers. This kind of behaviour is also observed in tests involved in error levels in this section.

Figure 4.18 shows the dependence on measurement errors for different frequencies. The dependence on the initial guess point is considered by computing the mean value and the standard deviation of the geometrical invariants obtained as a result of the inversion process. At each abscissa point it is represented the error level: for each error level, it is plot the mean and the deviation in results in terms of a vertical bar. It is observed that the identification is sensitive to noise, but the inversion admits high error levels, up to 40% in parameter η. When the noise level is increased, parameter I increases and the optimization algorithm usually finishes after a criterium based on the number of iterations required to decrease the cost function reaches a certain level. When it occurs, the inversion is considered to be failed. In tests reported here, noise level up to $\eta = 0.4$ produces convergence, based on tolerances at the cost function.

The inversion is sensitive to the parametrization chosen for the ellipsoid. Figure 4.19 shows the results based on a 6-parameter optimization: (c_1, c_2, c_3, a, b, c). The same kind of behaviour is observed when comparing with Fig. 4.18, but higher values for both standard deviation and geometrical invariant residual are reported.

Results are more sensitive to the relative position of sources and receivers. Results selected here are computed with the same size and number of points for sources and receivers, but centers are $(-2, 0, 0)$ for sources and $(2, 0, 0)$ for receivers. Figures 4.20 and 4.21 shows the results when the parametrization is based on 2 or 6 parameters, respectively. The higher values for geometrical invariant norm are obtained; when the identification is based on 6 parameters, for the lower frequency it is reporeted lack of convergence (solid point) for error level $\eta = 0.4$.

The frequency dependece shows the same tendency observed in previous tests: the best results are reported for $\bar{\omega} = 1$, which is close to the quasi-resonance frequency. This result might be affected

by the sizes of the ellipsoids. When $\bar{\omega} = 1$, the wavelenght is $\lambda = 6.28r$, which is similar to the height of the layer $h = 6r$. Plots presented at this section shows that such frequency produces the better results in terms of geometrical invariant residuals, and noise levels.

Normalized error I is very sensitive to axis errors: thus, the regularizing effect of providing a-priori volume information is notorious. In tests reported here, an error $0.2r$ in axis parameter causes values of $I = 3.54$. When a-priori volumen is provided (χ=0.1), a better adjustement is done for axis values; differences in $0.05r$ in axis causes values $I = 0.55$. The effect of providing volume information acts as an scale factor for results: conclusions remain the same respect to noise in measurement data in inverse analysis and the dependence on frequency. Providing volume information decreases the number of iterations required for convergence, in all the problems.

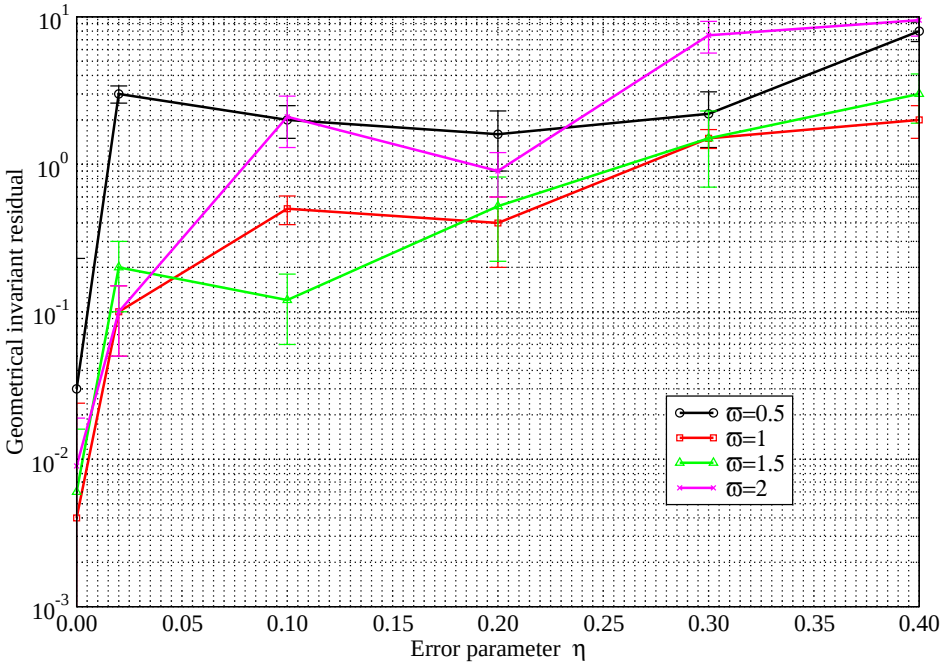

Figure 4.18: Geometrical invariant residual vs. error level. Results for a symmetric profile of sources/receivers, and 2-parameter identification

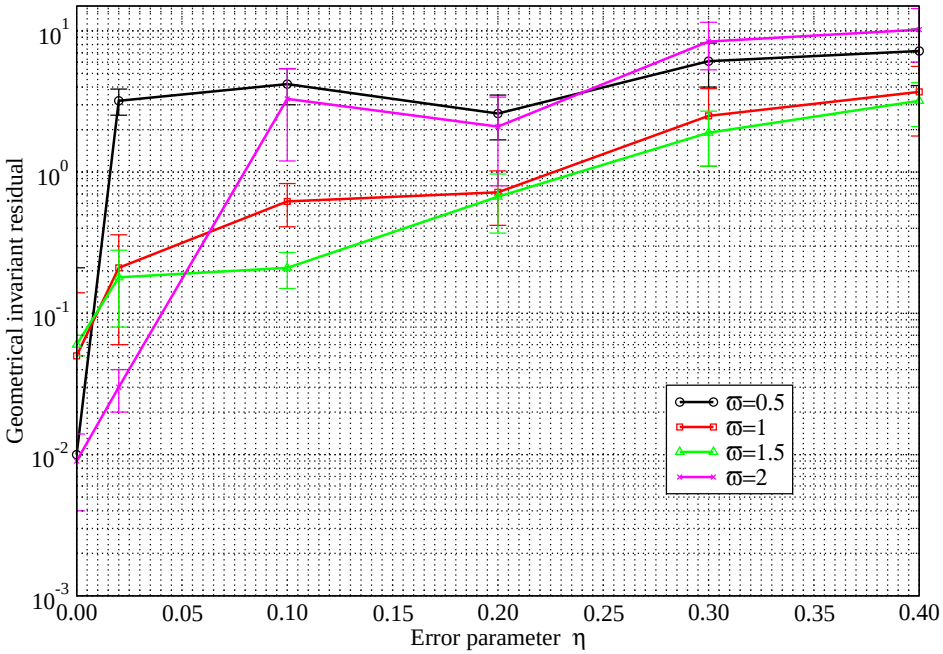

Figure 4.19: Geometrical invariant residual vs. error level. Results for a symmetric profile of sources/receivers, and 6-parameter identification

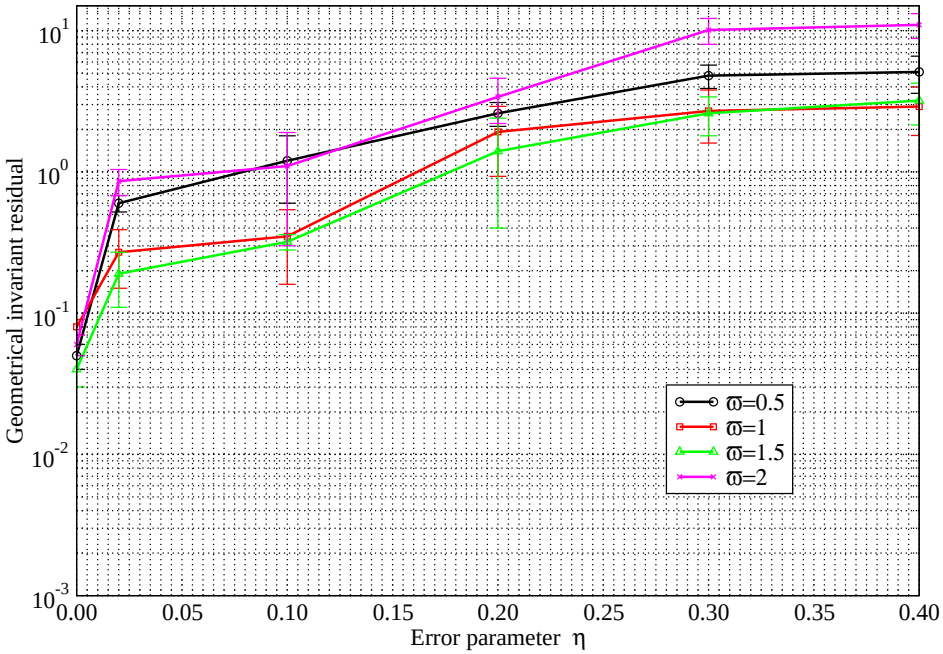

Figure 4.20: Geometrical invariant residual vs. error level. Results for non-symmetric profile of sources/receivers, and 2-parameter identification

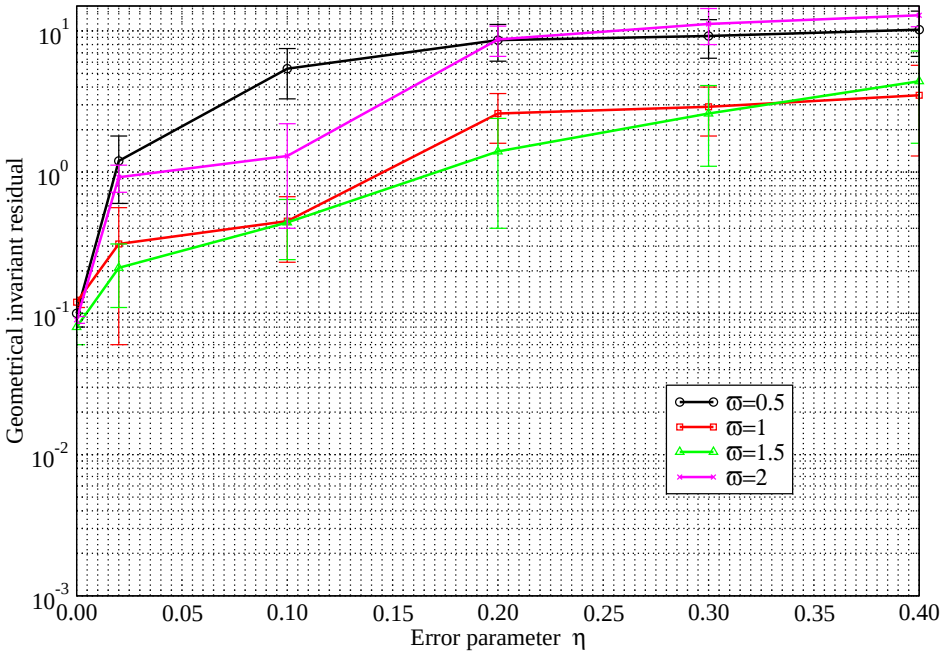

Figure 4.21: Geometrical invariant residual vs. error level. Results for a non-symmetric profile of sources/receivers, and 6-parameter identification

Traction singular elements

Error in representations of sharp geometries causes also error and noise in direct and inverse calculations. A particular case of sharp geometries occurs in representations of supports, in terms of patches or boxed shape. The kind error involved in representation of sharp contacts might be reported as a geometrical representation error. Similar considerations are included in the paper by Rus and Gallego [138], but the specific error involved in traction singularities is not analysed on that work.

To check the dependence on traction singular elements of results, two kind of configurations for supports have been fixed. Figure 4.2 shows a rectangular patch and a boxed support. For each configuration, the adequate singularity order has been provided through a rigorous local analysis, reported in [70]. It is known that singular elements are required in order to obtain accurate results with few elements: the dependence on singuarities is now analysed in the context of inverse problem.

For each configuration, the direct problem is solved by using traction singular elements and a general fine mesh for the cavity. It is stored as the pseudo-experimental solution. To solve the inverse problem, a coarse mesh is used, with regular or singular elements. The presence of additional geometries does not affect the way in which the forward and inverse problems are computed. The support configuration includes zero displacements boundary conditions. The inverse problem requires the computation of the Adjoint Problem, in order to compute integral over the cavity surface, Equation 4.8. Traction singularity errors affects to the quality of displacement results, which are the primary variable of inverse and adjoint problems. This mean that gradients supplied by the AVM are strongly affected by traction singular elements.

The next sections describe tests and results for both two configurations.

Table 4.2: Gradient checking: Influence on traction singular elements

Gradient component	3×3 regular	5×5 regular	10×10 regular	3×3 singular	5×5 singular
$1/(\mu r^2)\partial\mathcal{J}/\partial a$	3.433	2.833	2.432	2.371	2.372
$1/(\mu r^2)\partial\mathcal{J}/\partial b$	-4.386	-3.649	-3.328	-3.163	-3.165
$1/(\mu r^2)\partial\mathcal{J}/\partial c$	1.218	0.885	0.792	0.670	0.672
$1/(\mu r^2)\partial\mathcal{J}/\partial c_1$	-7.433	-6.789	-6.214	-5.792	-5.793
$1/(\mu r^2)\partial\mathcal{J}/\partial c_2$	1.434	1.063	0.938	0.857	0.855
$1/(\mu r^2)\partial\mathcal{J}/\partial c_3$	-1.827	-1.452	-1.321	-1.251	-1.254

Bonded surface support

This problem is represented by a layer, thickness $h = 6r$, with a support size $2r \times 2r$ centered at $(0, 0, 6r)$ (Fig. 4.2). Material parameter μ, ρ, and $\nu = 1/3$ are fixed. Zero-displacement boundary condition is given to the rigid surface support. When the local analysis is carried out, the singular coefficients $\alpha = \beta = 0.5$ are obtained; thus, an *square-root* singularity type is given to the shape functions in Eq. 3.20 for corner elements, but also for edge elements.

The direct problem is analysed by Guzina *et. al.* [70] in the context of static stiffnesses with a single half-space. That paper shows the influence on the quality of the results for computed stiffnesses when regular meshes are used, compared with singular element representation. The use of traction singular elements results in a faster convergence.

In the context of cavity identification presented at this work, the effect of traction singularities is first analysed to check the computation of gradients with the adjoint variable method. Gradients are computed by the convolution integral Eq 4.8, in wich displacements of the inverse and adjoint solutions are corrupted by traction errors. The problem tested is analogous to the one reported in section 4.8.1. An sphere of radius r, centered at $(0, 0, 3r)$, is located. Damping rates $\xi_\alpha = \xi_\beta = 0.05$ are fixed. No a-priori volume information is considered.

Vector $\mathbf{p}_0 = (-0.5r, 1.2r, 2r, 1.5r, 0.5r, r)$ defines the 6 parameters of the initial guess ellipsoid. The inversion is based on 16 sources with $P_m = \mu r^2, m = 1, 16$, located in a square 4x4 mesh size 3r centered at the origin of coordinates. Measurement points are disposed in a 3x3 squared mesh with size 2r, also centered at point $(0, 0, 0)$.

An accurate computation of gradients requires a fine mesh. For this problem, 294 8-noded elements are given for the ellipsoid. Patch is meshed with 3×3, 5×5, 10×10 regular elements; 3×3 and 5×5 singular elements are used to compare the results. Table 4.2 reports the results computed, at frequency $\bar{\omega} = 1$.

Results show the importance on providing the adequate singular elements to cause convergence due to the particular requeriments of the Adjoint Variable Method.

A different type of analysis have been carried out in order to check the dependence on noise in experimental data. The geometrical invariant I, computed with Equation (4.20) is obtained at four different frequencies, comparing the results with singular elements. Figure 4.22 allows the analysis of the results, in which error bars are included. In is observed that traction error decreases the maximum percentage error allowed to reach convergence for some frequencies. Also, it is observed that the standard deviation is greater when regular elements are obtained. The number of iterations required to reach the end point are considerably greater; up to 2 order of magnitudes greater for some problems; the higher the frequency, the higher the value for iterations.

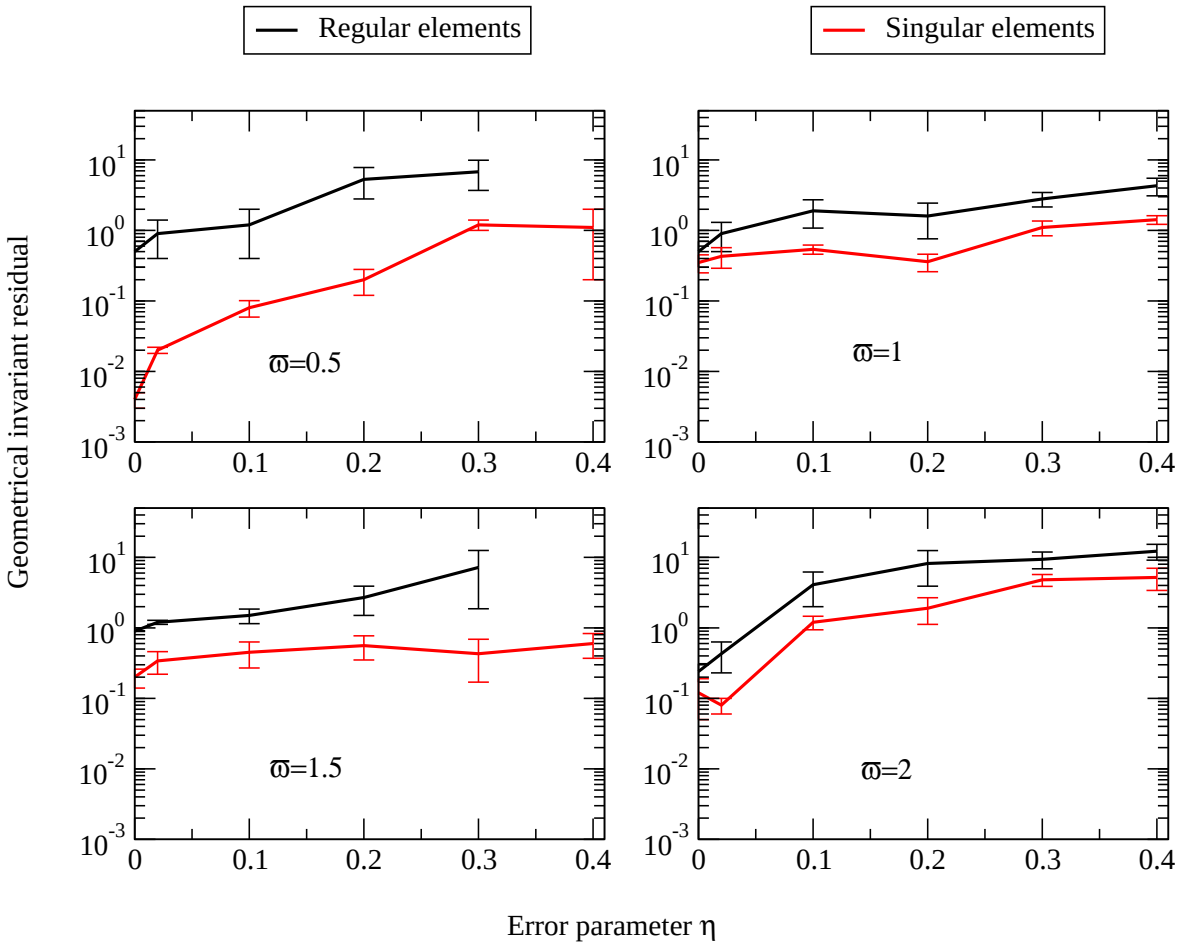

Figure 4.22: Geometrical invariant residual vs. error level. Effect of traction singular elements in a patch support

The effect of increasing or decreasing the number of parameters of the ellipsoid seems to play a minor dependence on the singularities. The general behaviour shown in section 4.8.3 remains the same here.

Embedded support

Figure 4.2 shows the basic configuration of an embedded support. Traction singularities are different, depending on the particular configuration of the edge adjacent to the lower layer, or the embedded edges. A local analysis is carried out (see [70]) with the resulting coefficients $\alpha = \beta = 0.310$ for the surface edges, and $\alpha = \beta = 0.410$ for the embedded edges.

A boxed support, sized $2r \times 2r$ by $0.5r$ is defined, centered at $(0, 0, 6r)$. The rest or properties, end point, and arrays of sources and receivers, remain the same than problem considered at the patch support. The only novelty here is a local restriction at the initial guess points, in order that the initial ellipsoid maintain a minimum separation respect to the boxed domain. This distance is fixed in $0.2r$ in the x_3 coordinate. This distance is required in order to avoid quasi-singular integral problems, wich in part are avoided by increasing the number of Gauss points when the source point and the integration point remain close. The experimental data are simulated

Results are similar than the one obtained for the patch support, except that the standard deviation of results is lower, due to the restrictions carried out in initial guess points. Figure 4.23 shows the geometrical invariant results evaluated at different frequencies, for 8-noded regular or singular

meshes. For this case, lack of convergence is obtained for some problems at the higher error levels. Also, it is observed that the regularization carried out by the volume parameter $\chi = 0.1$ provides better results, but it is observed that despite of this, gradients provided by the AVM computed with regular meshes produces poor convergence.

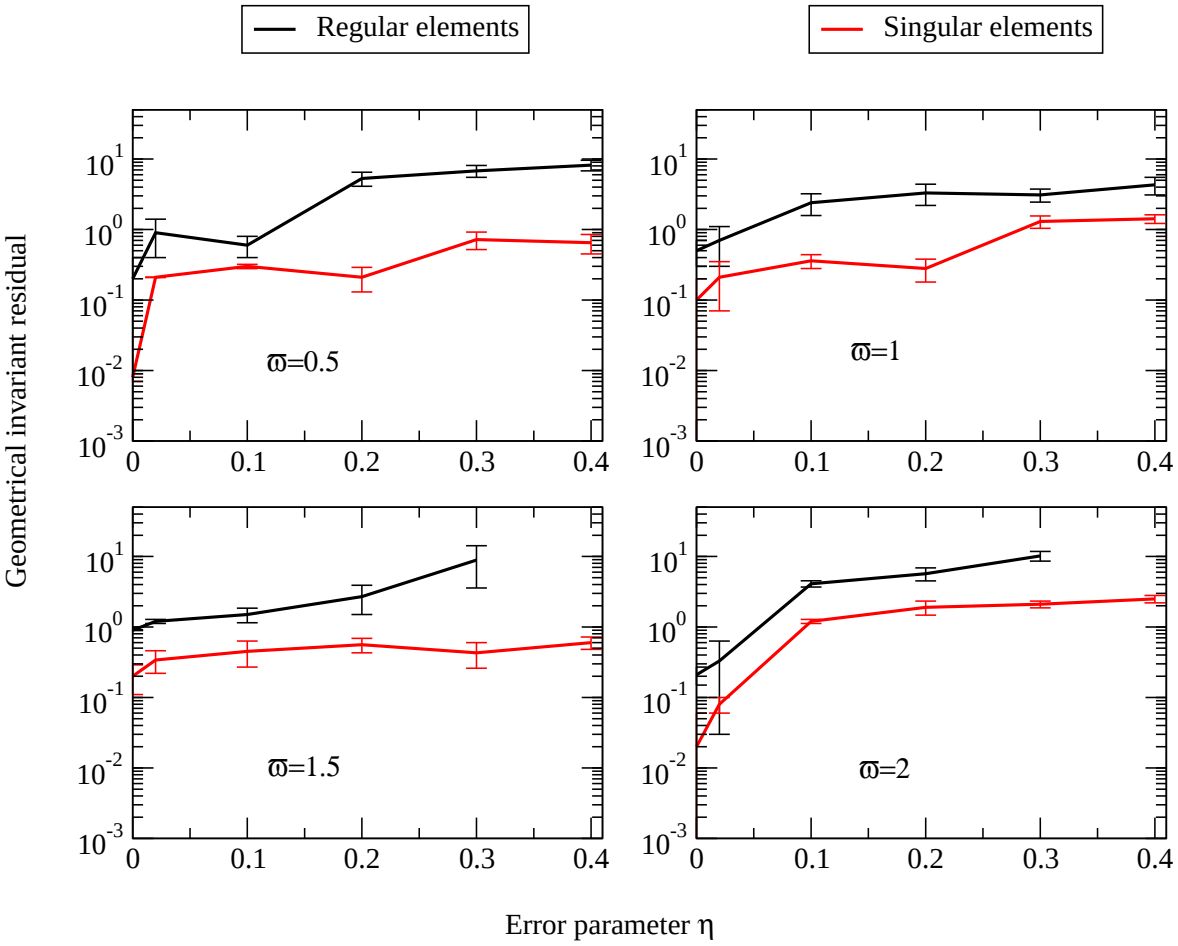

Figure 4.23: Geometrical invariant residual vs. error level. Effect of traction singular elements in an embedded support

4.9 Concluding remarks

The Inverse Identification Problem of finding hiddeng cavities embedded in a three dimensional viscoelastic layer is presented. The inverse algorithm is based on a BFGS optimization method. Gradients are computed by a semi-analytic formula.

The conclusions might be summarized as follows:

- Gradient computations based on the AVM are sensitive to mesh. A compromise between iteration numbers and precision level is required, in order to provide a mesh that produce medium quality gradients, decreasing the global number of iterations. In the literature, it is known that, despite finite differences give rise to instabilities and increase iteration number, gradient computations for coarse meshes at the ellipsoid are better. Numerical results obtained at this work

are based on a simple mesh for the ellipsoid. In experiments, the AVM has demonstrated to be an effective and powerful techinque to solve the optimization algorithm.

- The AVM requires good quality displacement patterns obtained by each direct code. Thus, when singularities occurs close to the ellipsoid surface, measurements for both the direct and the adjoint problems are affected by errors. Both error combined produces a gradient by the convolution integral over surface of the ellipsoid that causes errors in computed gradients. The resulting optimization point are sensitive to this fact.
- The problems computed here show that the optimization depends on the excitaition frequency. At frequencies over the quasi-resonance value, the optimization requires less iterations, with better convergence in terms of distance between the true configuration and the end points of the optimizations.
- The dependence on the number of experimental/source reamains a secondary factor, when compared with the number of parameters involved in the optimization. This conclusion is also observed in the literature.
- Better results are obtained in terms of convergence, number of iterations, and stability, when a symmetric profile of sources/receivers are selected. This could be caused by the multiple reflections of the hidden object with the lower layer, that acts as a mirror. This effect must be analysed by other techniques of inverse analysis at this domain, such as the Topological Sensitity, Linear Sampling Method, etc.

CHAPTER 5

Topological Sensitivity Analysis

5.1 Introduction

The identification of cavities embedded in an elastic solid is a long-standing problem in inverse analysis. The wide range of aplications cover from exploration seismology, medical imaging, non-destructive material testing, and underground facility detection. Among the techniques that tries to solve the identification problem, image methods are a kind of techniques focused on finding an image of the hidden objet by way of the sensitivity of domain points at the host domain to the cavity presence. The information of the so-called *non-damaged state* is used to find the hidden objects.

A group of image-method techniques are based on the far-field approximation of the wave equation, such as the ray theory [2, 142], or finite differences [132]. In a previous chapter, inverse analysis in the context of boundary integral equation and optimization problems is presented. Such techniques requires a common task: an extensive experimental an computational effort in order to fit and adjust general parametrized properties of the problem, based on experimental data. The nonlinear optimization problem requires direct computation of the parametrized damaged state. The quality of results depends on the initial guess configurations. The fordward problem requires solving an equation system to obtain displacements and tractions at the nodes of a mesh. Thus, global search methods are not a good option due the enormous time consuming in evaluating the different direct solutions.

An alternative approach to solve the problem is definition of some auxiliary integral functional to use the information of the initial non-damaged state to obtain internal shapes of the hidden cavities. Among this techniques, the Linear Sampling Method and the Topological Sensitivity are the two one reported in the literature.

The Linear Sampling method was first proposed by Colton *et al.* ([33, 36, 32, 31]) for far-field acoustic. With this approach an integral functional is developed and computed at an array of internal points. The equal-level surfaces at certain minimum values of the integral functional computed are related with the shapes of the actual internal cavities. Based on these works, this technique has been adapted in the field of electromagnetics ([34, 35, 73]), far-field elastic of scattering problems ([3, 5, 28, 59, 128]), and near-field of scattering problems [49].

The Topological Sensitivity (TS in what follows) approach is a different way to obtain information about the hidden objects based on a domain representation. The TS is the first-order derivative of the parametrized solution of the elasticity problem respect to the generation of a small cavity.

The first paper in which the TS is used in the context of optimization problems was presented by Eschenauer *et. al.* [44] and Schumacher [140]. On that work, a bubble method is defined based on the topological expansion of the cost function respect to cavity volume. The paper by Thierauf [155] also uses the bubble method ideas in the context of optimal topologies. The paper by Papadrakakis *et al.* [102] also links the topological expansion of cost functions with its applications in topology

optimization. The generalization to shape inverse problems was carried out by Sokołowski and coworkers [143, 144, 95, 96, 81, 97].

These initial works are based on the adjoint variable approach to obtain the volume derivatives of functionals involved in optimization problems [129]. Garreau *et al.* [58] use the adjoint method combined with a truncation domain technique in the context of linear elasticity problems. Millot *et al.* [115] applies the topological sensitivity approach in the context of finding buried objects.

The first work that introduces the idea of obtaining the topological sensitivity from boundary integral equations was presented by Gallego and Rus [54, 55]. In such work, the topological sensitivity boundary integral equation of displacements and tractions is derived in a closed-form formula for two-dimensional elasticity problems. The topological expansion of displacements and tractions leads to the definition of an approximed cost function, which permit the statement of a global optimization algorithm to find a minimum. All the computations related with the fordward problem require only the solution of the intial problem without deffects. The approximed cost function built can be minimized with global search techniques, such as the Genetic Algorithm approach. This way to combine the topological expansion of the cost function with zero-order global methods permits the definition of an initial guess points, defined in terms of center coordinates and size of deffects. The technique is extended to the analysis of anysotropic solids in bi-dimensional elastostatic problems [37]. With this approach, the TS is not used as an image method. It is used to define an approximed cost function to be used combined with Genetic Algorithms.

The use of Genetic Algorithms (GA) for the identification of deffects in the context of Boundary Integral Equation has been explored in the literature [85, 86, 152, 149, 148, 147]. On such works, the evaluation of the cost funciton requires the solution of a direct BE code, considering the geometry of the parametrized deffects. This approach leads to a very expensive algorithm, in terms of time required for the computations. However, the computation of the residual topological sensitivity requires the information of the non-damaged state. This approach reduces drastically the computation time required to find a global minimum.

The extension to the use of TS as an image method to find initial shapes of hidden objects for three-dimensional elasticity problems in the context of Boundary Integral Equations is carried out by Guzina and Bonnet in 2004 ([65, 23]). The idea developed is the use of the TS to define a three-dimensional map in which the level surfaces in which the TS is negative (or a certain fixed negative value) represents the shapes of the hidden objects. A three-dimensional half space in elastodynamics is considered in that work. The use of the topological sensitivity as a preliminary sampling technique to identify guess points in inverse-minimization methods is well reported in the literature for other related problems([63, 104, 51, 109])

In the present work, the linearized topological expansion of the cost function is used, combined with the GA tool, to find the initial center and size of spherical deffects. The host domain is the three-dimensional viscoelasticl layer. The forward problem is solved based on the Green function of the single-layered, obtained in this PhD work and published in [108]. The formulation is also extended to the case of multiple deffect identification, neglecting the interaction between deffect terms. A numerical benchmark is carried out in order to observe the dependence on different parameters of the minimization process. A comparison with the use ot the TS value as an image method is also carried out, in order to observe if the TS can be used to define initial shapes of deffects.

Recently, Faris and Gallego [47] have presented the use of the topological sensitivity in 3D elastic solids to determine the elastic response of three dimensional damaged solids. The research work is

based on the standard Boundary Integral Equation. The present work extends topological sensitivity approach to 3D elastodynamic problems.

5.2 Direct Problem

The three-dimensional viscoelastic layer domain, with a set of finite sources and a hidden spherical cavity is the basic problem considered. In reference to Figure 5.1, the host domain is the three–dimensional layer Ω, thickness h. In reference to the cartesian basis $\mathcal{B}\{O; x_1, x_2, x_3\}$, it is defined the region $\Omega = \{(x_1, x_2, x_3) | 0 \leq x_3 \leq h\}$, bounded by both traction-free planes $S = \{(x_1, x_2, x_3) | x_3 = 0\} \cup \{(x_1, x_2, x_3) | x_3 = h\}$. Let Γ_R be an auxiliary surface, $\Gamma_R = \Sigma_R \cap \Omega$, where Σ_R denotes a sphere of radius R centered at point (0,0,h/2).

The identification cavity is the sphere Ω_z, bounded by Γ_z. It is centered at $\mathbf{z}$ and its radius r. The figure represents the outward cavity normal $\mathbf{n}$, pointing at the interior direction to Γ_z, as it corresponds with a cavity interior to the material domain.

Let $\mathbf{x} \in \Omega^-$ be an internal point, with $\Omega^- = \Omega \setminus (\Omega_z \cup \Gamma)$, and Ω_R^- the subset of Ω^- limited by Γ_R. At certain points $\mathbf{x}^s$ corresponding to the upper layer, a set of time-harmonics sources are considered.

$$\mathbf{f}(\mathbf{x}) = \sum_{n=1}^{NS} P_n e^{i\omega t} \delta(\mathbf{x} - \mathbf{x}_n^s)\, \mathbf{e_3} \tag{5.1}$$

where δ stands for the three-dimensional Dirac delta function, P_n is the force magnitude and $\mathbf{e_3}$ is the unit vector in the x_3 direction. With this reference, the forward problem is stated:

$$\begin{aligned}
\nabla \cdot (\mathbf{C} : \nabla \mathbf{u}) + \mathbf{f} + \rho\, \omega^2\, \mathbf{u} = \mathbf{0}, \mathbf{x} \in \Omega^- \\
\mathbf{t} = \mathbf{0},\ \mathbf{y} \in \Gamma \cup S \\
\lim_{R \to \infty} \int_{\Gamma_R} \{\hat{\mathbf{u}}^k(\mathbf{y}, \mathbf{x}) \cdot \mathbf{t}(\mathbf{y}) - \hat{\mathbf{t}}^k(\mathbf{y}, \mathbf{x}) \cdot \mathbf{u}(\mathbf{y})\} \mathrm{d}\Gamma(\mathbf{y}) = \mathbf{0} \\
\mathbf{x} \in\ \Omega_R^-,\ k = 1, 2, 3
\end{aligned} \tag{5.2}$$

with $\mathbf{t}$ is the traction unit vector, and $\mathbf{C}$ is the elastic tensor. The time-harmonic response includes damping, through the damping rates ξ_α y ξ_β and the complex-valued material modules $\lambda = \lambda^*$ y $\mu = \mu^*$, by virtue of the *corresponding principle* [30].

$$\begin{aligned}
\lambda^* + 2\mu^* &= (\lambda + 2\mu)\left[1 + 2i\xi_\alpha(\omega)\right], \quad \xi_\alpha \geq 0 \\
\mu^* &= \mu\left[1 + 2i\xi_\beta(\omega)\right], \quad \xi_\beta \geq 0
\end{aligned}$$

In Eq. (5.2), $\hat{\mathbf{u}}^k(\mathbf{y}, \mathbf{x})$ and $\hat{\mathbf{t}}^k(\mathbf{y}, \mathbf{x})$ are the displacement and traction functions of the fundamental solution for the layer [108].

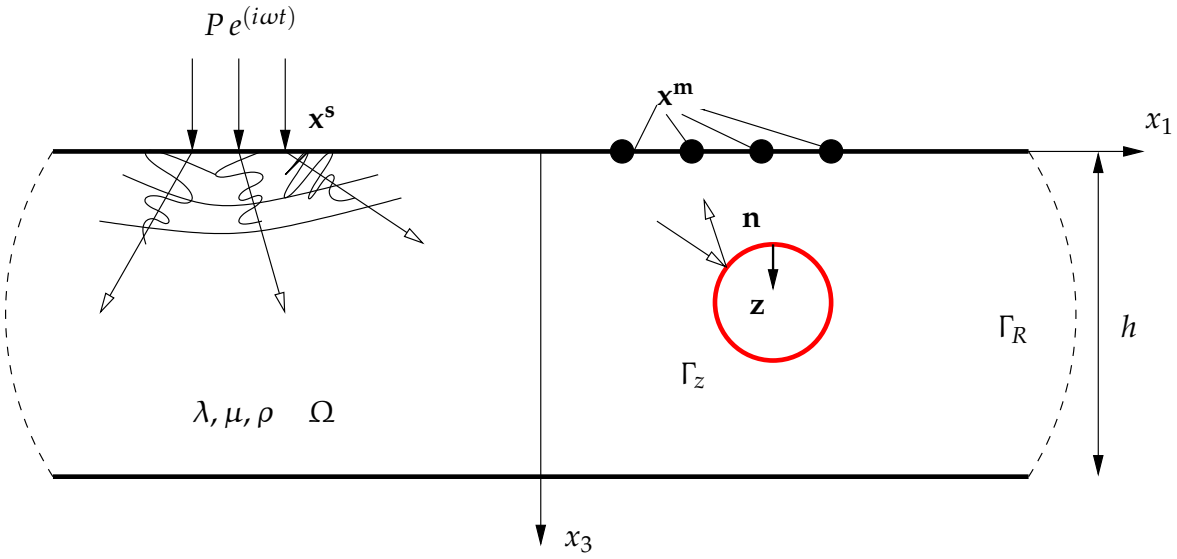

Figure 5.1: Spherical cavity in a single layer domain. Sources and measurement points

For point $\mathbf{x}$, the basic elastodynamic BIE can be estated as,

$$c_k^i(\mathbf{x})u_k(\mathbf{x}) + \int_{\Gamma_z} \hat{t}_k^i(\mathbf{y},\mathbf{x})\, u_k(\mathbf{y})\mathrm{d}\Gamma(\mathbf{y}) = \sum_{n=1}^{NS} P_n \hat{u}_3^i(\mathbf{x}_n^s,\mathbf{x}) \tag{5.3}$$

with c_k^i the Kronecker delta δ_k^i.

The previous equation, when stated at the Non Damaged State, consists on the direct collocation of the Fundamental Solution.

5.3 Inverse Problem

The inverse problem consists on the identification of the cavity Ω_Z based on the frequency-dependent displacement measurement $\mathbf{u}^m$ at points $\mathbf{x}^m$. Such values are obtained for any parametrized position of the sphere; the experimenta values of the displacement are the one obtained at the true position and size of the cavity. In the context of this work, such displacements will be noted as $\mathbf{u}^e$.

The identification of the cavity is stated as an optimization problem, as occured in the previous chapter. For this case, the cost function is stated without a-priori information of the volume. Thus:

$$\mathcal{J}(\Gamma) = \sum_{m=1}^{NEP} \frac{1}{2} \left(\overline{\mathbf{u}^m - \mathbf{u}^e}\right) \cdot \left(\mathbf{u}^m - \mathbf{u}^e\right) \tag{5.4}$$

with NEP the Number of Experimental Points. The overlined term represents the conjugate complex of the displacement difference.

5.4 Topological Sensitivity Boundary Integral Equation

The approach to obtain the Topological Sensitivity Boundary integral equation is well known in the literature, in the context of Boundary Integral Equation. It can be obtained by an analysis of the scattered waves from cavities (Guzina and Bonnet works, [23, 25, 66]) or by the decomposition in solid-rigid body motion plus an incremental field, proposed by Gallego and Rus [54]. This is the approach followed here. The main difference between both approaches is the way in which the elastic field is decomposed. The particularities of the decomposition will be remarked in this section.

At this domain Ω, bounded by the parallel planes Γ, the displacement $\mathbf{u}$ at an internal point $\mathbf{x} \in \Omega$ is computed by evaluating the Green function. This problem will be called the *Non–Damaged State* (NDS in what follows). The presence of a traction–free small cavity bounded by Γ_z located at $\mathbf{z}$ produces the modified displacement field $\tilde{\mathbf{u}}$ at $\mathbf{y}$. This second state will be called the *Damaged State* (DS). The Boundary Integral Equation (BIE) for the internal displacement field $\tilde{\mathbf{u}}$ is

$$c_k^i(\mathbf{x})\tilde{u}_k(\mathbf{x}) + \int_{\Gamma_z} \hat{t}_k^i(\mathbf{y},\mathbf{x})\, \tilde{u}_k(\mathbf{y})\mathrm{d}\Gamma(\mathbf{y}) = \sum_{n=1}^{NS} P_n \hat{u}_3^i(\mathbf{x}_n^s,\mathbf{x}) \tag{5.5}$$

The displacement field at the cavity boundary can be split as $\tilde{u}_k(\mathbf{y}) = u_k^0(\mathbf{y}) + \delta\bar{u}_k(\mathbf{y})$, where $u_k^0(\mathbf{y})$ is a rigid solid displacement, and $\delta\bar{u}_k(\mathbf{y})$ is the displacement field relative to the center $\mathbf{z}$ due to the local state of stresses.

The integral term in Eq. (5.5) can be transformed, by applying the Divergence Theorem at Γ_z, and taking into account the negative sign of the normal $\mathbf{n}$, as:

$$\int_{\Gamma_z} \hat{t}_k^i(\mathbf{y},\mathbf{x})\, \tilde{u}_k(\mathbf{y})\mathrm{d}\Gamma(\mathbf{y}) = u_k^0(\mathbf{z}) \int_{\Gamma_z} \hat{t}_k^i(\mathbf{y},\mathbf{x})\mathrm{d}\Gamma(\mathbf{y}) + \int_{\Gamma_z} \hat{t}_k^i(\mathbf{y},\mathbf{x})\, \delta\bar{u}_k(\mathbf{y})\mathrm{d}\Gamma(\mathbf{y}) \tag{5.6}$$

The first integral of the second term in Eq. 5.6 is zero for static problems, but for time-harmonic problems, the integral over a closed boundary of tractions, at cavities not containing the source, is related with the excitation frequency by the dynamic equilibrium of the problem. The equilibrium equation is $\sigma_{ij,j} + \rho\, b_i = -\rho\,\omega^2 u_i$; with $b_i = 0$ as no volume forces acts at the domain. Thus, the first term is evaluated as follows,

$$\int_{\Gamma_z} \hat{t}_k^i(\mathbf{y};\mathbf{x})\, \mathrm{d}\Gamma(\mathbf{y}) = -\int_{\Omega_z} \hat{\sigma}_{kj,j}^i(\mathbf{z},\,\mathbf{x})\mathrm{d}\Omega = \mathcal{V}(\mathbf{z})\rho\,\omega^2\, \hat{u}_k^i(\mathbf{z},\mathbf{x}) \tag{5.7}$$

with $\mathcal{V}(\mathbf{z}) = 4/3\,\pi\, r^3$, the spherical cavity volume at $\mathbf{z}$. The first integral of the right-hand side in Eq. 5.6 is:

$$u_k^0(\mathbf{z}) \int_{\Gamma_z} \hat{t}_k^i(\mathbf{y},\mathbf{x})\mathrm{d}\Gamma(\mathbf{y}) = \mathcal{V}(\mathbf{z})\, \rho\, \omega^2 \hat{u}_k^i(\mathbf{z},\mathbf{x})\, u_k^0(\mathbf{z}) \tag{5.8}$$

with $\hat{u}_k^i$ the Displacement Green's Function; u_k^0 is the displacement field at the Non Damaged State at the cavity center. The Non Damaged State is the traction-free infinite three-dimenisional layer; thus, to evaluate it, the Green function is used.

The second integral term at the right-hand side in Eq. (5.6) includes displacement field $\delta\bar{u}_k(\mathbf{y})$. The first order stresses at any point inside the domain far from the flaw location are equal to those of the primary state σ_{ij} and therefore, the displacements $\delta\bar{u}_k(\mathbf{y})$ along the vanishing flaw are equal to those due to a uniform remote stress field in an infinite layer.

$$\tilde{\sigma}_{ij}(\mathbf{y}) = \sigma_{ij}(\mathbf{z}) + \mathbf{h.o.t} \tag{5.9}$$

for $\mathbf{y}$ far from $\mathbf{z}$, where $\mathbf{h.o.t}$. stands for *higher order terms*, and,

$$\delta\bar{u}_k(\mathbf{y}) = \delta u_k^\infty(\mathbf{y}) + \mathbf{h.o.t} \tag{5.10}$$

where $\delta u_k^\infty(\mathbf{y})$ represents the solution of the remote traction uniform field $\sigma_{ij}(\mathbf{z})$. On the boundary of the cavity,

$$\hat{t}_k^i(\mathbf{y},\mathbf{x}) = \hat{\sigma}_{jk}^i(\mathbf{y},\mathbf{x})\, n_j(\mathbf{y}) = \hat{\sigma}_{jk}^i(\mathbf{z},\mathbf{x})\, n_j(\mathbf{y}) + \mathbf{h.o.t.} \tag{5.11}$$

The second integral term at the right-hand side in Eq. (5.6) is evaluated as:

$$\int_{\Gamma_z} \hat{t}_k^i(\mathbf{y},\mathbf{x})\,\delta\bar{u}_k(\mathbf{y})\mathrm{d}\Gamma(\mathbf{y}) = \hat{\sigma}_{jk}^i(\mathbf{z};\mathbf{x}) \int_{\Gamma_z} n_j(\mathbf{y})\delta u_k^\infty(\mathbf{y})\,\mathrm{d}\Gamma(\mathbf{y}) + \text{h.o.t} \tag{5.12}$$

Substractiong the resulting BIE for the DS, Eq. 5.5 from Eq. 5.3, stated at the NDS, and dividing by the cavity volume (to obtain sensitivities in terms of partial derivatives respect to the cavity volume), the so-called Topological Sensitivity Boundary Integral Equation is obtained [55], in which the displacement topological sensitivity is evaluated with a Boundary Integral Equation as follows:

$$c_k^i(\mathbf{x})\delta u_k(\mathbf{x}) = -\rho\,\omega^2\,\hat{u}_k^i(\mathbf{z},\mathbf{x}) - \hat{\sigma}_{jk}^i(\mathbf{z};\mathbf{x}) \int_{\Gamma_z} n_j(\mathbf{y})\delta u_k^\infty(\mathbf{y})\,\mathrm{d}\Gamma(\mathbf{y}) \tag{5.13}$$

At the previous equation, the last integral can be evaluated in a closed-form tensor (see works by Eshelby [45, 46]).

$$\int_{\Gamma_z} n_j(\mathbf{y})\delta u_k^\infty(\mathbf{y})\,\mathrm{d}\Gamma(\mathbf{y}) = I_{jk} \tag{5.14}$$

with,

$$\begin{aligned} I_{jk} &= -\left[A\sigma_{jk}^\infty - B\delta_{jk}\sigma_{ii}^\infty\right]\frac{1}{\mu} \\ A &= \frac{15(1-\nu)}{2(7-5\nu)} \\ B &= \frac{3(1-\nu)(1+5\nu)}{4(7-5\nu)(1+\nu)} \end{aligned} \tag{5.15}$$

Thus, the TSBIE for a single spherical cavity is:

$$c_k^i(\mathbf{x})\delta u_k(\mathbf{x}) = -\rho\,\omega^2\,\hat{u}_k^i(\mathbf{z},\mathbf{x}) - \hat{\sigma}_{jk}^i(\mathbf{z};\mathbf{x})I_{jk} \tag{5.16}$$

5.5 Topological Sensitivity of the Cost Function

Equation (5.16) permits the computation of the first volume derivative for all the displacements and related variables. In the context of the Inverse Problem stated, the interest is focused on the Cost Function (Eq. 5.4) and its sensitivity equation. The displacement field can be linearized as follows,

$$u_k = u_k^0 + \mathcal{V}\,\delta u_k \tag{5.17}$$

Based on the previous linearization, the approximed measured field $\mathbf{u}$ can be computed from the NDS; the cost function is linearized as:

$$\mathcal{J}(\Gamma) \simeq \sum_{n=1}^{NEP} \frac{1}{2}\left(\overline{\mathbf{u}^{m,0} + \mathcal{V}\,\delta\mathbf{u}^m - \mathbf{u}^e}\right)\cdot\left(\mathbf{u}^{m,0} + \mathcal{V}\,\delta\mathbf{u}^m - \mathbf{u}^e\right) \tag{5.18}$$

with $\mathbf{u}^{m,0}$ the measured displacement field at the NDS.

The previous equation can be expanded as,

$$\mathcal{J}(\Gamma) \simeq \sum_{n=1}^{NEP} \frac{1}{2}\left(\overline{\mathbf{u}^{m,0} - \mathbf{u}^e}\right)\cdot\left(\mathbf{u}^{m,0} - \mathbf{u}^e\right) + \mathcal{V}\left(\overline{\mathbf{u}^{m,0} - \mathbf{u}^e}\right)\cdot\delta\mathbf{u}^m + \frac{1}{2}\mathcal{V}^2\overline{\delta\mathbf{u}^m}\cdot\delta\mathbf{u}^m \tag{5.19}$$

The cost function evaluated at the NDS and the topological sensitivity of the cost function can be defined as:

$$\mathcal{J}^0 = \sum_{n=1}^{NEP} \frac{1}{2} \left(\overline{\mathbf{u}^{m,0} - \mathbf{u}^e} \right) \cdot \left(\mathbf{u}^{m,0} - \mathbf{u}^e \right) \tag{5.20}$$

$$\mathcal{T}(\mathbf{z}) = \sum_{n=1}^{NEP} \left(\overline{\mathbf{u}^{m,0} - \mathbf{u}^e} \right) \cdot \delta \mathbf{u}^m \tag{5.21}$$

Considering the previous definitions, the cost function can be expanded as:

$$\mathcal{J}(\Gamma) \simeq \mathcal{J}^0 + \mathcal{V}\,\mathcal{T} + \mathcal{V}^2 \cdot \sum_{n=1}^{NEP} \frac{1}{2} \overline{\delta \mathbf{u}^m} \cdot \delta \mathbf{u}^m \tag{5.22}$$

This expansion is based on the linearization of displacement, but it does not constitute a fully-quadratic expansion of the cost function. The quadratic expansion of displacements includes the second-order derivative (a quadratic term in volume), which leads to a quadratic term at the linearized cost function depending on the difference of measurements between the experimental displacements and the approximed one at the NDS. This kind of expansion, in the context of the use of the Topological Sensitivity as an image method, has been explored by Bonnet *et al.*.

At the present work, the topological expansion is based on the computation of the first-order topological sensitivity of displacements. The aim of such an approach is testing this expansion for the layer domain. The main advantage is that no second-order topological derivatives of displacements are required. Moreover, the wavelength consideration has not been explored at the formulation. This leads also to a more refined topological expansion of the cost function. The simplest one is the one considered in Eq. 5.22

In Equation 5.21, the topological sensitivity $\mathcal{T}(\mathbf{z})$ is a value depending on the position of the cavity. This parameter may be understood as a cavity locator: negative values means that the generation of a small cavity at the particular position or $\mathbf{z}$ decreases the value of the cost function. Thus, by heuristic considerations, the true cavity surface would be related with some negative or zero isosurfaces in $\mathcal{T}$. It must be remarked that this approach is not rigorously proof. Convergence, or isosurfaces, are not guaranteed. In the literature, works by Guzina and Bonnet emphasizes this use of the Topological Sensitivity of the cost function as an image method.

On the other hand, the approximed cost functional represented by equation 5.22 is evaluated by easy computations at the NDS. At each point, the cost function is evaluated in terms of the cavity volume $\mathcal{V}$. Thus, a local search of the optimum radius $\mathcal{V}^{opt}$ that minimizes the local expansion is possible. A local constrained minimization is stated, with the phisical restriction $\mathcal{V} \geq 0$. The search algorithm to identify the optimum volume at the cavity position $\mathbf{z}$ contains two steps:

a) Identify the optimum volume by a first derivative:

$$\mathcal{V}^{opt} = -\frac{\mathcal{T}}{\sum_{n=1}^{NEP} \overline{\delta \mathbf{u}^m} \cdot \delta \mathbf{u}^m}$$

b) In case that $\mathcal{V}^o pt$ is negative (which occurs when $\mathcal{T} < 0$), the optimum volume is asigned as $\mathcal{V}^{opt} = 0$

Once the optimum volume is computed, the optimum radius is also evaluated,

$$r^{opt} = \left(3\,\frac{\mathcal{V}^{opt}}{4\,\pi} \right)^{1/3} \tag{5.23}$$

At each point, the optimum volume is obtained and the cost function, depending on $\mathcal{V}$, is evaluated at the optimum volume. Thus, the cost function depends only on the coordinate center of the cavity, as the volume is fixed with $\mathcal{V}^{opt}$ at each point.

5.6 Multiple cavity identification

The topological expansion for the problem with n cavities requires the analysis of a new problem, in which a new sphere is generated in a domanin with $(n-1)$ existing deffects. The equation integral that defines the displacement sensitivity includes a term to consider the effect of the $(n-1)$ cavities on the new generated one.

At the present analysis, the interaction between cavities is ignored. Numerical examples confirm that the layer domain contains a radiation damping that permit for some problems ignoring such effect, when each cavity is far enough from the surrounding cavities.

Let $\mathbf{v}$ be a column vector whose v_j component contains the volume of the $j-th$ cavity located at $\mathbf{z}_j$. Let $\mathbf{T}$ be a matrix containing the Topological Sensitivities of displacements respect to cavities located at $\mathbf{z}_j$.

$$v_j = \mathcal{V}_j(\mathbf{z}_j) \tag{5.24}$$

$$T_{ij} = \frac{\partial u_i}{\partial \mathcal{V}_j} \tag{5.25}$$

Thus, the topological expansion of the displacement vector at a particular measurement point is written as:

$$\mathbf{u}^m = \mathbf{u}^0 + \mathbf{T}\,\mathbf{v} \tag{5.26}$$

Based on the linearized expansion of displacements, the topological expansion of the cost function is obtained as follows,

$$\mathcal{J}(\Gamma) \simeq \mathcal{J}^0 + \left(\overline{\mathbf{u}^{m,0} - \mathbf{u}^e}\right) \cdot \mathbf{T}\,\mathbf{v} + \frac{1}{2}\mathbf{v}^T\overline{\mathbf{T}^T}\,\mathbf{T}\,\mathbf{v} \tag{5.27}$$

Equation 5.27 is minimized at each position represented by the set of cavities. The optimum volume vector is computed by a local constrained minimization, which can be summarized as follows.

a) Compute the optimum volume vector $\mathbf{v}^{opt}$ by minimizing the cost function with its first order derivative. A local equation system is stated,

$$\overline{\mathbf{T}^T}\,\mathbf{T}\,\mathbf{v}^{opt} = -\left(\overline{\mathbf{u}^{m,0} - \mathbf{u}^e}\right) \cdot \mathbf{T} \tag{5.28}$$

b) If any component of vector $\mathbf{v}^{opt}$ is negative, obtain the minimum of $\mathbf{v}$ at the boundaries corresponding with $\mathcal{V}_i = 0$.

c) Choose the vector $\mathbf{v}^{opt}$ computing the cost function and choosing the configuration that provides the minimum value of $\mathcal{J}$.

The constrained minimization is necessary in the context of the present work. The physical limitation that volumes must be zero or positive lead to a cost function with an strong minimum point. Numerical experiments confirm that this kind of minimization is required, and it is more convenient for the highest frequencies, in which local pseudo-minimum points are obtained when negative volumes are allowed.

Once vector $\mathbf{v}^{opt}$ is obtained, the cost function is evaluated at $\mathbf{v} = \mathbf{v}^{opt}$.

5.7 Combined Genetic Algorithms with Topological Expansion of the cost function

The use of zero-order algorithms is convenient when the evaluation of the cost function is cheap, in terms of computing effort, and when gradients of the cost function respect to the design parameters are difficult to obtain. Such is the case of the approximed cost functional proposed. Among the different zero-order algorithms reported in the literature to solve the Inverse Problem (e.g. evolutionary algorithms [113] or parameter-space sampling methods [153]), Genetic Algorithms provides a fast and accurate solution for this problem. The combined use of GA-TS is reported in the literature, as it was commented at the introduction section; the particular kind of use of the GA analysed is simmilar to the one reported in works by Gallego and Rus, [54, 55].

Within the framework of genetic optimization, the set of design parameters, or *phenotype*, is encoded as a chain of variables, *chromosomes*. A population of individuals, is assumed. For the present study, each individual of the population consists of $3 - m$ design parameters, which are the coordinates of the defect centers. For each individual, the cost function is computed and is defined as the fitness function.

The code to solve the GA-TS search is based on the Matlab one developed by Haataja [72]. Parameters that define the GA are reported at the next section, for each case. As the fitness function $e(x)$ is maximized with such code, function $e(x) = -\mathcal{J}$, with $\mathcal{J}$ the approximed cost function and x the vector containing the cavity centers.

5.8 Numerical benchmark

At this section a numerical benchmark has been carried out in order to illustrate the aplications of topological sensitivity expansion in detection problems.

The first step is the validation of the topological sensitivity proposed in Equation (5.13). A practical way to do it is the comparison with the approximed topological sensitivity computed by a Finite Differences Approach (FDA). The comparison for displacement computations is shown in section 5.8.1.

Once Equation (5.13) is validated, a set of numerical tests have been done to validate the use of the Topological Derivative in the context of inverse identification problems.

5.8.1 Comparison with Finite Differences

In order to ilustrate the computation of the sensitivity, a direct comparative with finite diferences is shown. A layer thickness $h = 3r$, material parameters ρ, μ, Poisson rate $\nu = 0.3$, are chosen. A point source located at $(0, 0, 0)$ with load intensity $(0, 0, \mu r^2)$ is considered. A cavity is located at $\mathbf{z} = (0, 0, 1.5r)$. The displacement field is observed at $\mathbf{y} = (6r, 0, 1r)$. The Topological Sensitivity of displacements are computed at point $\mathbf{y}$, at dimensionless frequencies $\bar{\omega} = \frac{\omega r}{\sqrt{\mu/\rho}}\{0.3, 1, 1.5, 2\}$, in order to test Eq. (5.13). To compare the results, a Finite Differece of displacements respect to cavity volume is computed. Various cavity diameters have been tested. The consideration of small radius is limited to the accuracy of the direct code, due to quasi-singular integration problems. Table 5.1 shows the results for cavity radius $a_r = 0.25r$, for which volume $V = 0.0654r^3$. Only u_1 and u_3 components are computed, as $u_2 = 0$ due to the symmetry of the problem.

$\bar{\omega}$	Approach	$\mathrm{Re}(u_1)/r$	$\mathrm{Im}(u_1)/r$	$\mathrm{Re}(u_3)/r$	$\mathrm{Im}(u_3)/\mathrm{r}$
0.3	FD	5.651E-04	-3.780E-04	3.760E-03	-9.489E-04
0.3	TS	5.816E-04	-3.833E-04	-3.330E-04	-9.753E-04
1	FD	-3.592E-03	-2.174E-04	2.234E-03	1.400E-04
1	TS	-3.658E-03	-2.475E-04	2.447E-03	2.932E-04
1.5	FD	3.092E-02	1.175E-03	-2.124E-03	-1.672E-02
1.5	TS	3.046E-02	2.357E-03	-1.934E-03	-1.664E-02
2	FD	1.732E-02	7.164E-03	6.111E-03	-3.101E-02
2	TS	1.772E-02	9.241E-03	1.001E-02	-3.312E-02

Table 5.1: Comparison between Finite Differences (FD) and Topological Sensitivity (TS)

Table (5.1) shows that Eq.(5.13) is correct.

5.8.2 Single cavity detection

A this section, the basic reference configuration consists on an spherical cavity, radius $a_r = 0.5r$ centered at $(0, 0, 3r)$. The layer domain is thickness $h = 6r$. Material parameters are μ, ν, density ρ. For this configuration, a set of experiments have been designed to analyse the dependence on certain parameters.

Symmetric profile sources/receivers

For this set of tests, a symmetric profile of sources/receivers has been chosen. Both sources and receivers are centered at $(0, 0, 0)$. The sources array consists on 16 points disposed in an squared patch size $4r \times 4$; the receivers array consists on 9 points, disposed in an squared patch size $3r \times 3r$. Figure 5.2 show the basic configuration of arrays of sources, receivers, layer, and true cavity position. The figure also show the Boundary Element mesh used to compute the pseudo-experimental measurements. The sphere is meshed with 54 8-noded quadratic elements. The number of nodes is 164.

Cost function expansion

The approximed expansion of the cost function by way of the topological sensitivity is compared with the exact cost function for the problem considered at hand. The cost function is obtained for the single cavity identification. Point $(0, 0, 3r)$ is fixed. The only parameter is the cavity radius a_r. Figure 5.3 represents the exact and the approximed cost function, in terms of the cavity volume, at two different frequencies. The actual radius value is $r = 0.5$. At each frequency, two plots have been obtained, to shown the general shape of the cost function, and its values at radii close to the optimum.

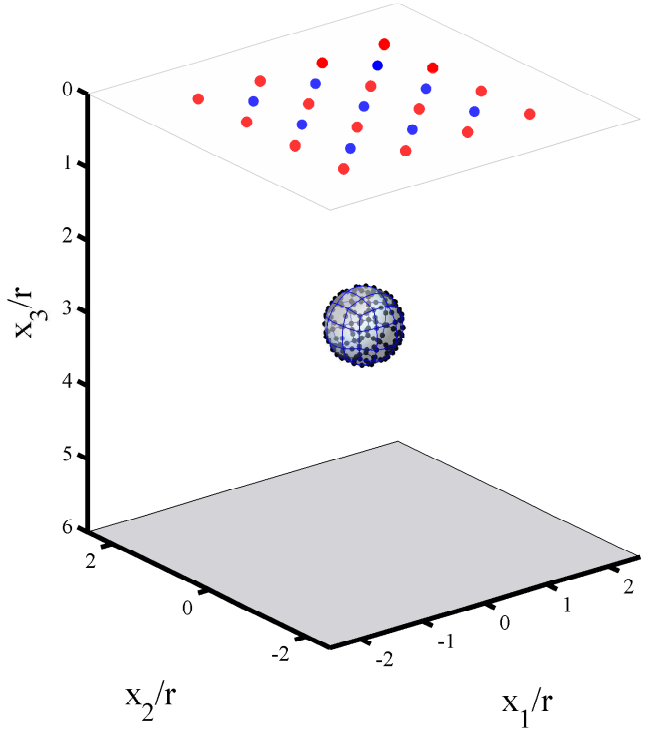

Figure 5.2: Configuration of sources (red) and receivers (blue). Identification of a centered cavity

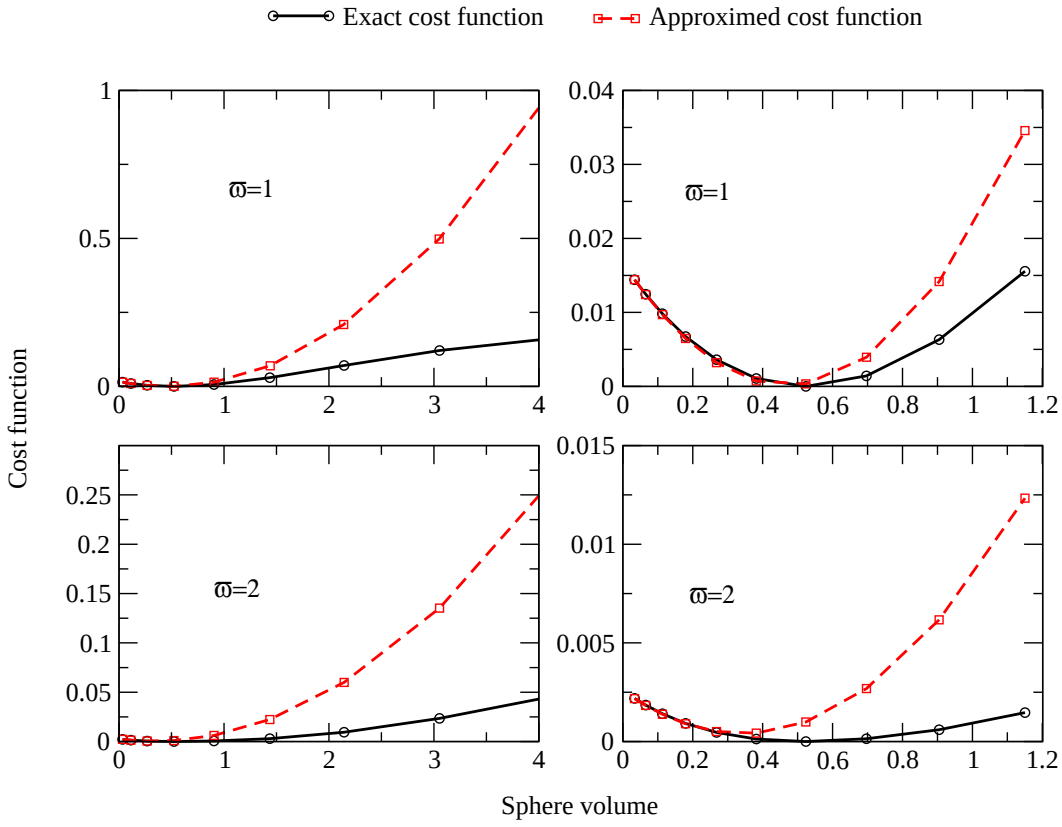

Figure 5.3: Comparison between the exact and the topological expansion cost function at two frequencies.

It is observed that the quality of the approximation depends on the excitation frequency. At frequency $\bar{\omega} = 1$, the optimum volume is quite the same, with error less than 1%. When the frequency is increased, the minimum value is reached at slightly different points. This mean that it is expected poorer results at higher frequencies. A different kind of topological expansion could be used to consider waves. Plot also shows that the approximation is good only for volumes close to the optimum one. The exact cost function behaves different to the quadratic one for higher volume values.

Effect of noise in experimental data

Inverse problems are ill-conditioned. Convergence is not guaranteed, and results do not depend continously on the data. In the ill-conditioned problems literature, it is a common task checking the dependence on errors in input data, in order to show the stability of the method. In this section, noise is introduced at the measurement data, through a random variable φ that pollutes the experimental data,

$$u_i^{e,noise} = u_i^e \, (1 + \varphi) \tag{5.29}$$

Variable φ is uniformly distributed over the interval $[-\eta, \eta]$. Values of η tested in this study cover the range $\eta = \{5\%, 10\%, 20\%\}$. To analyse the dependence on the excitation frequency, four excitation frequencies have been considered, $\bar{\omega} = \{1, 1.5, 2, 2.5\}$.

The GA is used to minimize the residual. Table 5.2 show the basic settings of the GA implemented.

Parameter	Value
Low constrain	$[-2.5, -2.5, .5]$
Up constrain	$[2.5, 2.5, 5.5]$
Number of parameters	3
Number of generations	50
Size of the population	20
Probability of crossover	0.8
Probability of mutation	0.02
Tournament probability	0.7
Scale for mutation	0.1

Table 5.2: Parameters of the GA for noise evaluation

Figures 5.4, 5.5,5.6 and 5.7 show the result of the combined GA-TS at the tested frequencies. Table 5.3 show the end values at each test, and the cost function. The last column is the normalized error, computed as:

$$\varepsilon = \sqrt{(c_1 - c_1^{ref})^2 + (c_2 - c_2^{ref})^2 + (c_3 - c_3^{ref})^2 + (a_r - a_r^{ref})^2} \tag{5.30}$$

with $(c_1^{ref}, c_2^{ref}, c_3^{ref}, a_r^{ref}) = (0, 0, 3r, 0.5r)$, the reference cavity parameters. Figure 5.8 shows the normalized error in terms of the excitation frequency and error level.

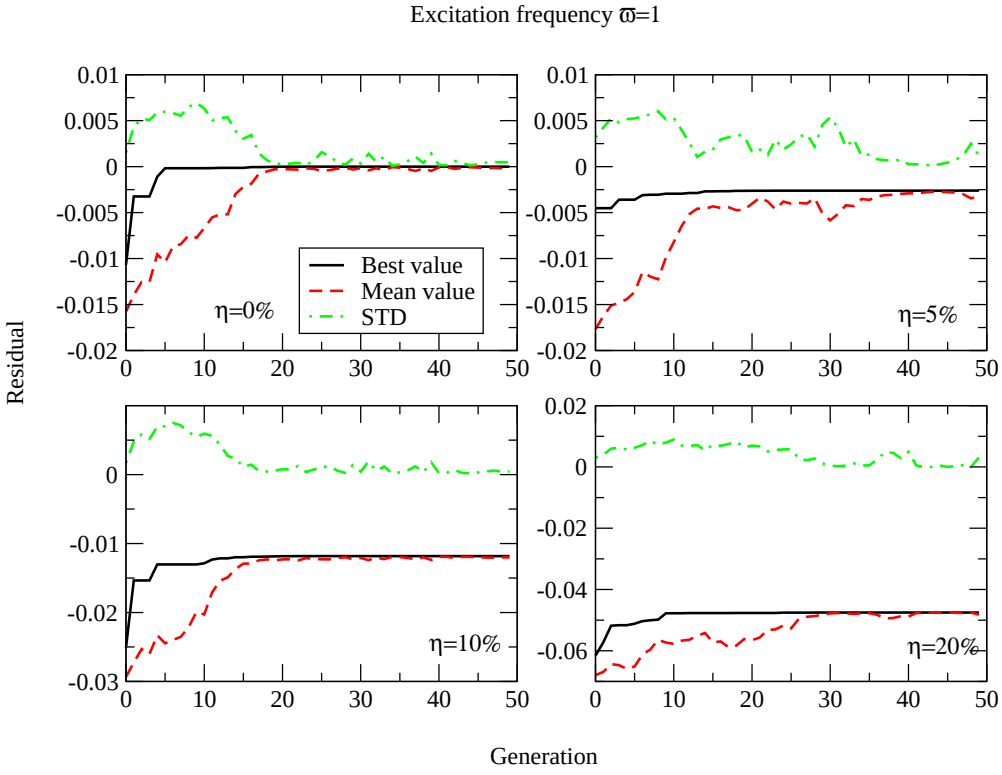

Figure 5.4: GA-TS identification of a cavity. Noise effect at $\bar{\omega} = 1$

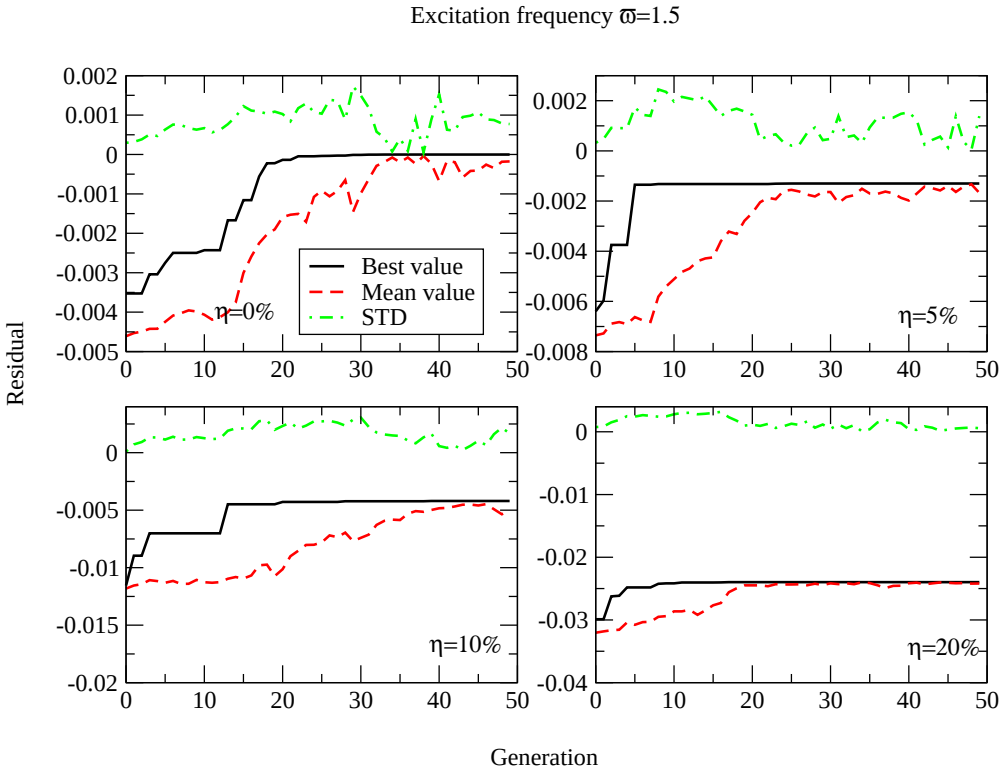

Figure 5.5: GA-TS identification of a cavity. Noise effect at $\bar{\omega} = 1.5$

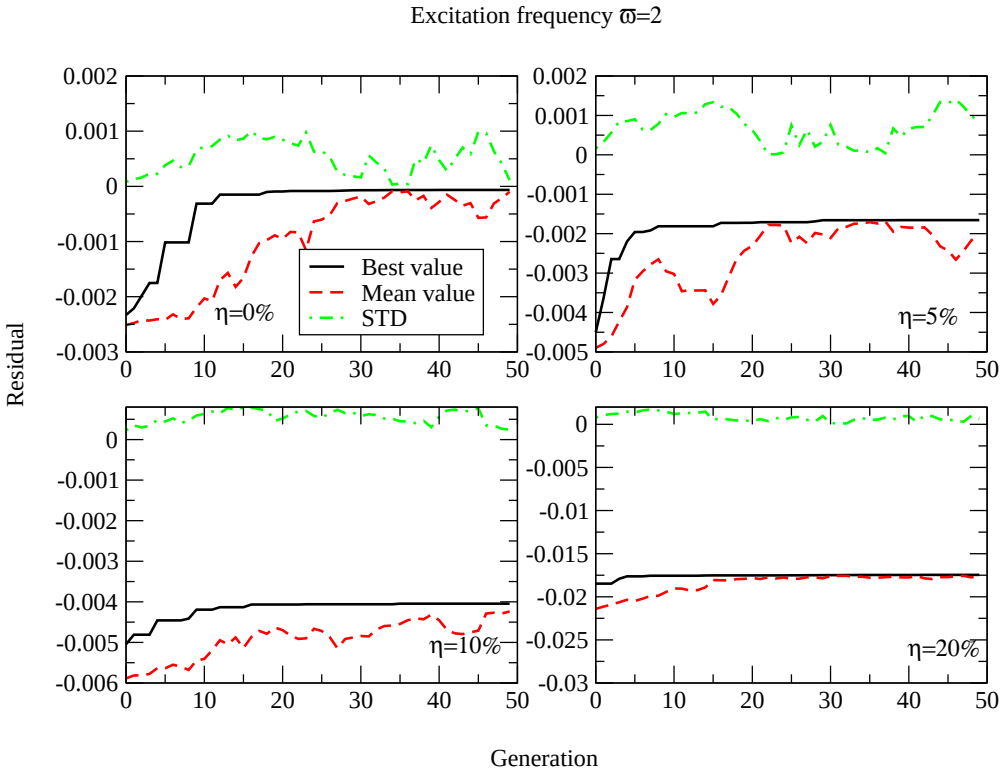

Figure 5.6: GA-TS identification of a cavity. Noise effect at $\bar{\omega} = 2$

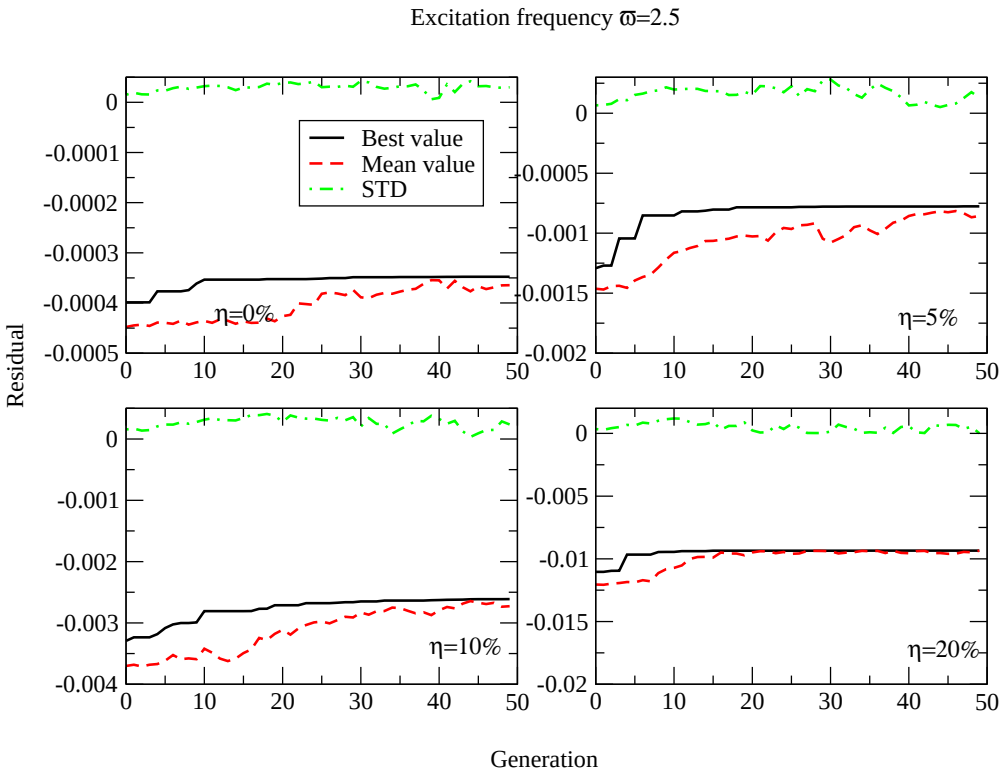

Figure 5.7: GA-TS identification of a cavity. Noise effect at $\bar{\omega} = 2.5$

Noise	c_1/r	c_2/r	c_3/r	a_r/r	$\tilde{\mathcal{J}}/(\mu r^3)$	ε/r
$\bar{\omega} = 1$						
0%	3.48E-04	5.39E-03	3.09	4.81E-01	2.26E-06	9.02E-2
5%	-1.09E-01	2.49E-03	3.22	4.78E-01	2.64E-03	2.47E-1
10%	1.52E-01	-1.24E-01	3.23	4.90E-01	1.18E-02	3.09E-1
20%	-2.43E-02	2.46E-01	3.34	5.04E-01	4.90E-02	4.20E-1
$\bar{\omega} = 1.5$						
0%	-1.98E-03	-1.39E-03	2.99	0.461	2.29E-01	4.03E-2
5%	4.48E-03	1.76E-01	2.88	0.464	1.30E-03	2.14E-01
10%	1.18E-02	-9.63E-02	2.91	0.485	4.19E-03	1.40E-01
20%	-2.77E-01	5.31E-02	2.73	0.469	2.39E-02	3.92E-01
$\bar{\omega} = 2$						
0%	5.06E-04	3.79E-03	3.15	0.455	6.54E-05	1.57E-01
5%	2.62E-02	-9.63E-02	3.20	0.485	1.65E-03	2.24E-1
10%	-2.04	1.73	5.11	0.703	4.04E-03	3.42
20%	2.07	1.82	1.94	0.393	1.74E-02	2.96
$\bar{\omega} = 2.5$						
0%	-7.44E-1	-4.44E-01	2.44	0.307	3.47E-04	1.12
5%	-3.43E-03	-7.78E-02	4.67	0.408	7.76E-04	1.67
10%	1.5	-1.92	4.43	0.523	2.60E-5	2.83
20%	-2.43	2.39	3.04	0.526	9.34E-03	3.41

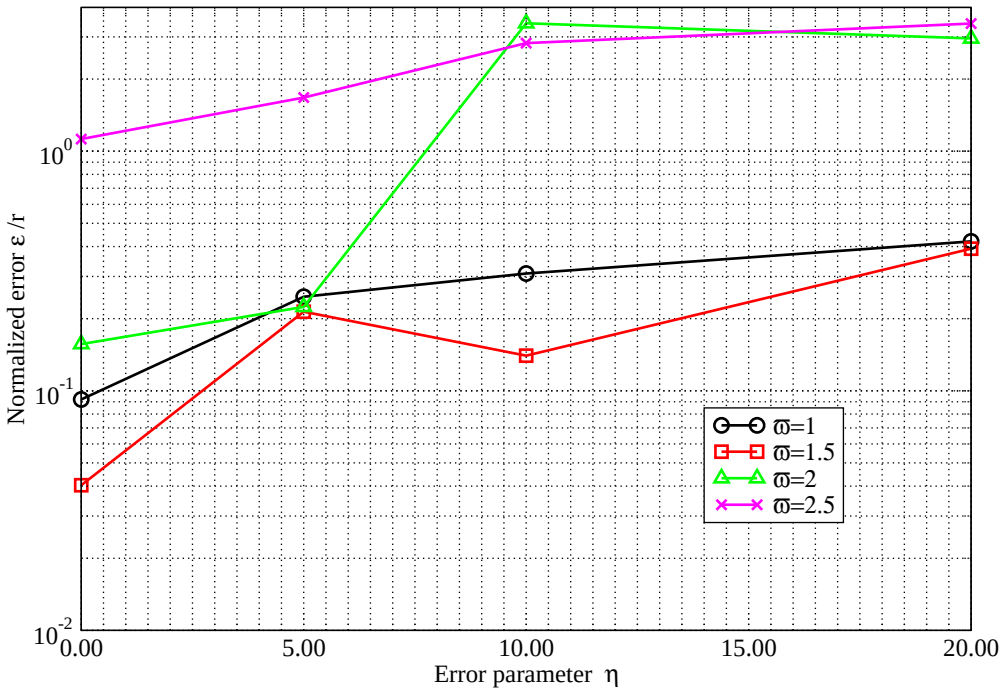

Figure 5.8: GA-TS global search. Effect of noise in measurements. Normalized errors. Dependence on the excitation frequency.

The optimization based on the GA is an stable algorithm, respect to noise in experimental measurements. Numerical tests confirm that noise levels up to 20% produces an end point close to the true cavity position. For each test, convergence is not guarateed for noise levels up to 30%. This

fact is related with the assumed errors that comes from the approximation of the cost function. The higher the frequency, the higher the errors.

Effect of material damping

Damping is included in the model through coefficients $\xi_\alpha(\omega)$ and $\xi_\beta(\omega)$. This kind of damping is inherent to the material, and depends on the velocity of the particles. There are other kind of numerical damping at the three-dimensional layer related with the radiation condition: the geometric damping. This mean that, in absence of material damping, the response to time-harmonic sources are progressive waves, and the resonance response can not occur.

Damping minimises the effect of waves reflected by solids. This fact permits a better inversion, and this result is known in the literature. At this section, three damping rates have been considered; $\xi_\alpha = \xi_\beta = \{2\%, 5\%, 10\%\}$. Table 5.4 shows the end values of the genetic algorithm search. The last column represents the error parameter ε, computed by Eq. (5.30). In all the cases, the error decreases when damping increases. This fact is also observed in figures 5.9 and 5.10, in which the evolution of the computed parameters during the GA-TS search is plot. Damping produces a fastest and stable identification: the Best Value curve require less iterations to obtain an stable value: the Standard Deviation and the Mean Value become more regular, with less STD values, when damping is increased.

Material damping improves the convergence properties of any global search method, and in this case, it is also observed. The layer medium contains a natural radiation damping, when $\xi_\alpha = \xi_\beta = 0\%$. In absence of material damping it is more critical to reach an stable last point. This is the reason that, in future sections, the absence of material damping will be considered and, in case of lack of convergence, it will be introduced a small damping rate, to observe the convergence properties. This procedure is very important in the context of multiple deffect identification.

The particular way in which damping has been introduced, with $\xi_\alpha = \xi_\beta$ involves that Poisson rate is real-valuated. Any case, the results are enough general, as damping effects on waves and results of inverse problems is a well known task in the literature. The aim of this section is only checking and concluding that, despite a radiation damping exists, material damping improves the convergence.

Damping (%)	c_1/r	c_2/r	c_3/r	a_r/r	$\check{\mathcal{J}}/(\mu r^3)$	ε/r
$\bar{\omega} = 1$						
0	3.48E-04	5.39E-03	3.09E+00	0.481	2.26E-06	9.02E-02
2	-2.98E-03	1.18E-03	3.09E+00	0.484	1.54E-06	9.32E-02
5	-1.09E-02	2.13E-02	3.07E+00	0.488	3.72E-06	7.46E-02
10	-2.91E-04	-6.22E-04	3.06E+00	0.492	3.25E-07	6.12E-02
$\bar{\omega} = 2$						
0	5.06E-04	3.79E-03	3.15E+00	0.455	6.54E-05	1.57E-01
2	-1.13E-03	-2.31E-03	3.12E+00	0.456	2.24E-05	1.24E-01
5	-1.62E-03	3.87E-03	3.07E+00	0.443	1.16E-05	8.71E-02
10	-1.44E-04	-4.21E-04	2.99E+00	0.426	6.09E-06	7.53E-02

Table 5.4: GA-TS global search. End values of parameters. Effect of material damping

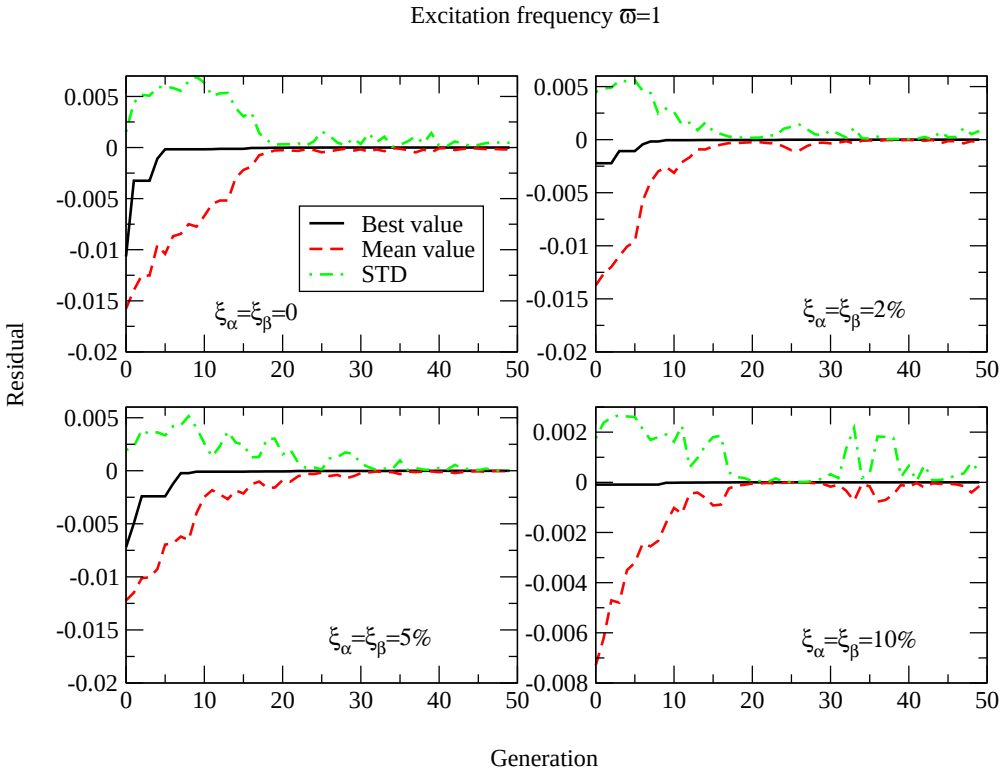

Figure 5.9: GA-TS identification of a cavity. Damping effect at $\bar{\omega} = 1$

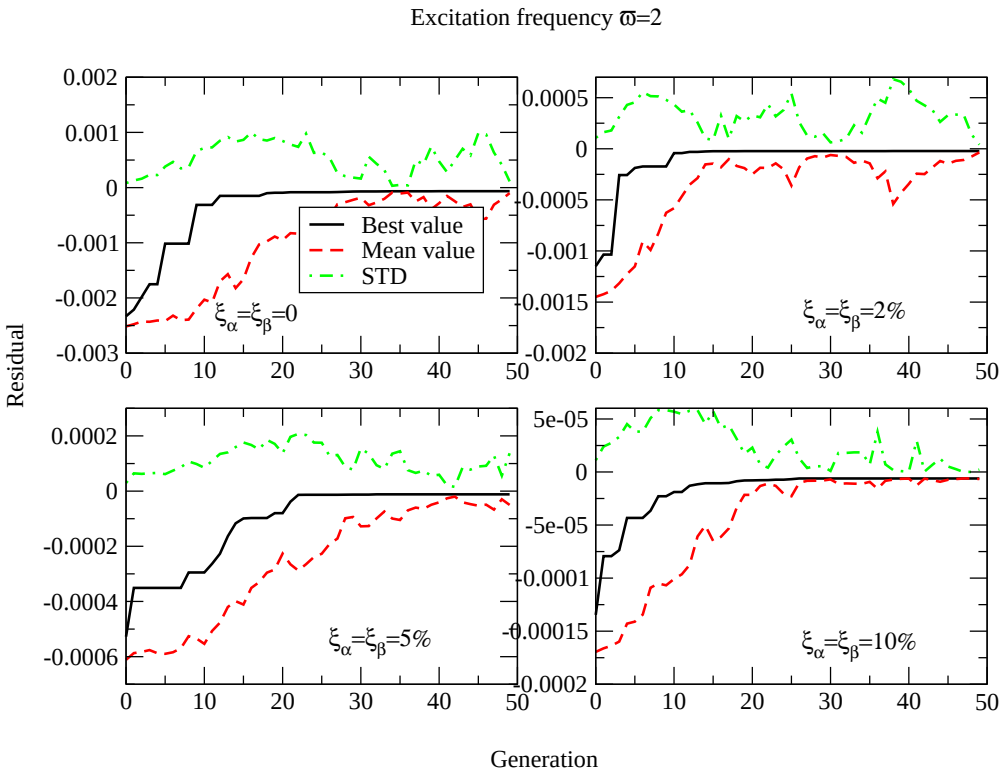

Figure 5.10: GA-TS identification of a cavity. Damping effect at $\bar{\omega} = 2$

Combination of frequencies

At this section, the four frequencies tested are grouped. The new approximed cost function is built by adding the contributions of each single frequency test. Thus, if $\tilde{\mathcal{J}}(\bar{\omega}_i, V)$ denotes the approximed cost function at frequency $\bar{\omega}_i$, depending on V, the combined approximed function is built as:

$$\tilde{\mathcal{J}}(V) = \sum_{i=1}^{NF} \tilde{\mathcal{J}}(\bar{\omega}_i, V) \tag{5.31}$$

with NF the number of frequencies considered. Note that V is an scalar value computed for the combined frequency cost function.

Table 5.5 show the results of parameters, cost function, and normalized error computed with Eq. (5.30). The error reported with the combined cost function is less than errors obtained at each individual frequency, but for $\bar{\omega}$=1.5. This result means that for some individual frequencies, the obtained result might be better, but providing more experiments is an stable approach to determine an optimum value. Figure 5.11 show the GA-TS evolution.

$\bar{\omega}$	c_1/r	c_2/r	c_3/r	a_r/r	$\tilde{\mathcal{J}}/(\mu r^3)$	ε/r
1.0	3.48E-04	5.39E-03	3.09	0.4816	2.26E-06	9.20E-02
1.5	-1.98E-03	-1.39E-03	2.99	0.461	2.29E-01	4.03E-02
2	5.06E-04	3.79E-03	3.15E+00	4.55E-01	6.54E-05	1.57E-01
2.5	-1.44E-01	-9.44E-01	2.44E+00	3.08E-01	3.47E-04	1.12E+00
Combined	7.91E-03	4.66E-03	3.06E+00	0.46246	2.28E-03	7.38E-02

Table 5.5: GA-TS global search. Combination of frequencies. Centered cavity with a symmetric profile of sources and receivers

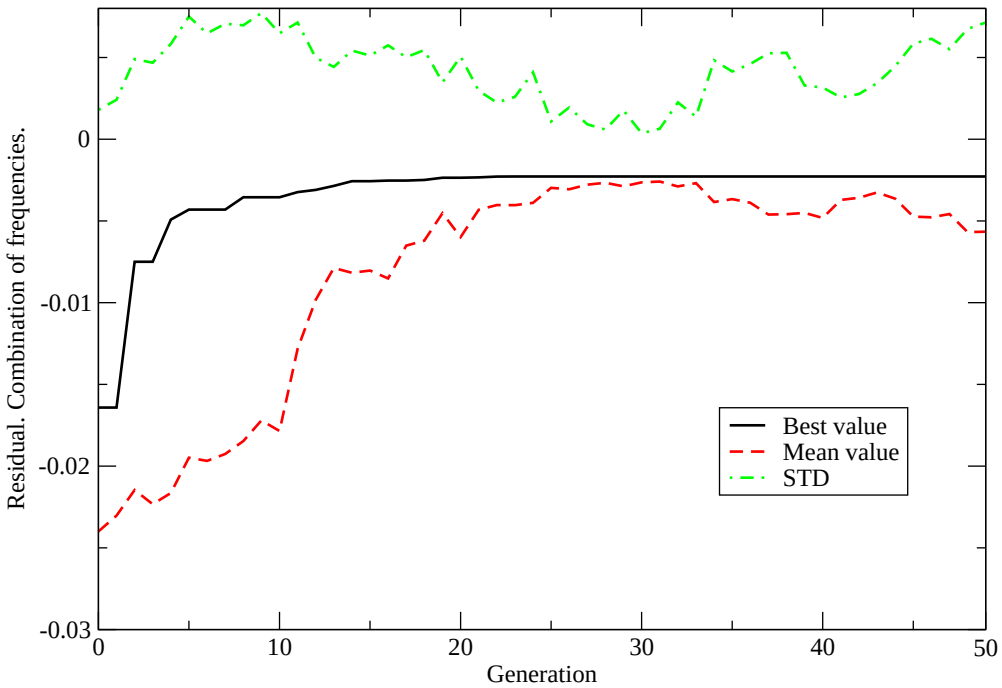

Figure 5.11: GA-TS identification of a cavity. Combination of frequencies.

Cost Function and Topological Sensitivity as Image Methods

The use of small-asymptotic expansion of functionals and variables is an interesting task to minimize the time required to compute the forward problem. It provides the value of the topological sensitivity, and the cost function evaluated at the optimum volume values. The three-dimensional mapping of such parameters is used in the literature as an image method. At this section the two image methods are compared.

The Topological Derivative of the cost function is used in the literature as an image method. When mapped in a 3D region, the negative values of it is understood as point in which the presence of a cavity decreases the cost function. The isosurfaces of some percentage of the negative values might be understood as shapes of the hidden objects (see works by Guzina and Bonnet). This approach is based on heuristic ideas, and no rigorous proof is stablished to define the isosurface corresponding with the boundary of the hidden cavity. In works by Bonnet, Guzina and co-workers ([23, 65, 63]) the delineation of internal cavities and inclusions, and the way to combine frequencies, are carried out by heuristic ideas. The approach to combine the results at different frequencies is not based on cost functions, but on image properties. In such papers, it is observed some cases in which internal shapes are identifies, but also cases in which such heuristic procedure fails. The advantage of this method is that no a-priori shape of the hidden cavity is assumed.

The three-dimensional map provided by the cost function depends on the shape of the assumed cavity. In this sense, it is not an image method, as this method does not pretend to obtain the shape of a hidden object by an isosurface of a particular function evaluated at the domain. Any case, it is interesting the comparison of the TS and the cost function maps. In what follows, it will be observed that the cost function provides a minimum point at the coordinate center of the cavity, when the deffect corresponds with a single cavity. It will be observed that the TS is not a good image method for this problem.

Figures 5.12, 5.14, 5.16 and 5.18 represent the three-dimensional map of the Topological Derivative of the cost function. Two isosurfaces are represented, corresponding with value $\mathcal{T} = 0$ (blue) and $0.5 \min\{\mathcal{T}\}$ (red). The red one surface is the predicted hidden cavity. It is observed that the predicted shape is not an sphere, and that when the frequency increases, the position of the center is wrong.

Figures 5.13,5.15, 5.17 and 5.19 represent the three-dimensional mapping of the cost function (three slices). It has been computed at the optimum volumes at each point. The cost function in all the cases reach a minimum value at the center of the true sphere position. The end point of the GA-TS approach are shown in Table 5.5.

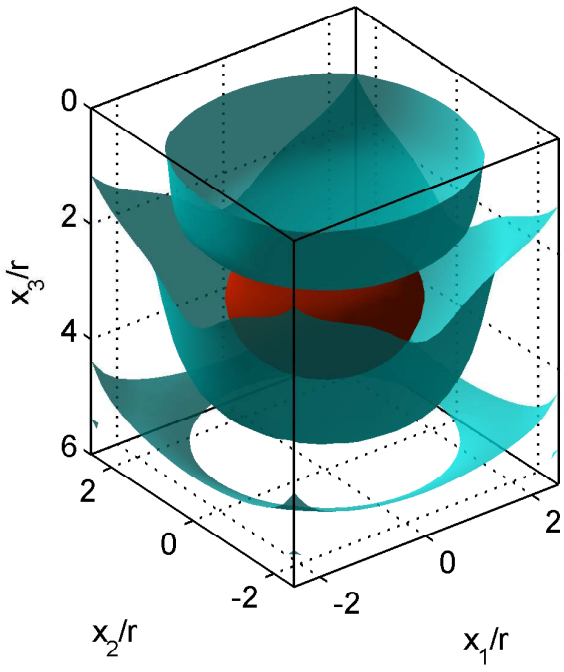

Figure 5.12: Identification of a centered spherical cavity. Isosurfaces of $\mathcal{T}$ at $\bar{\omega} = 1$. Symmetric profile sources/receivers.

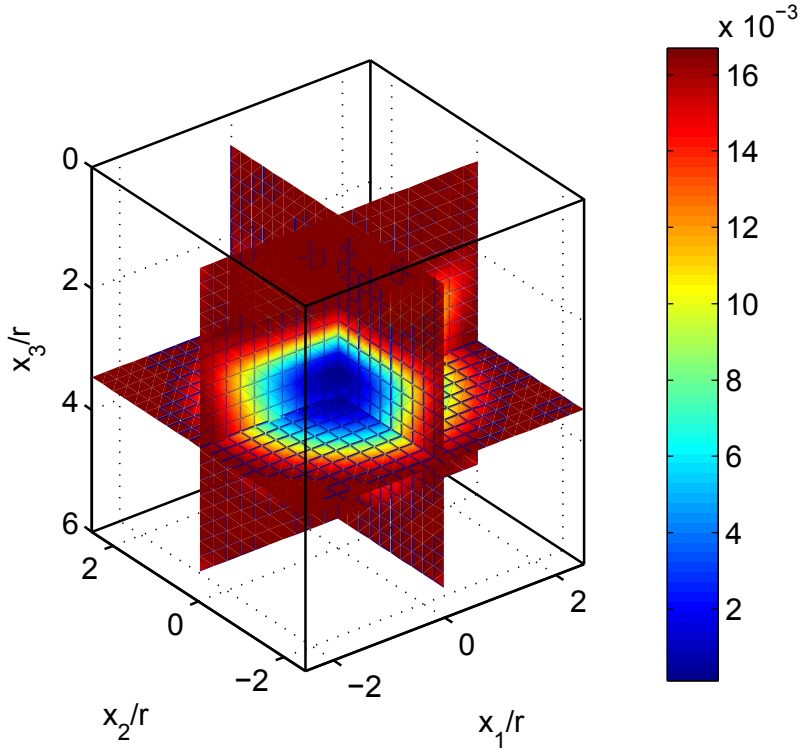

Figure 5.13: Identification of a centered spherical cavity. Linearized Cost Function slices at $\bar{\omega} = 1$. Symmetric profile sources/receivers.

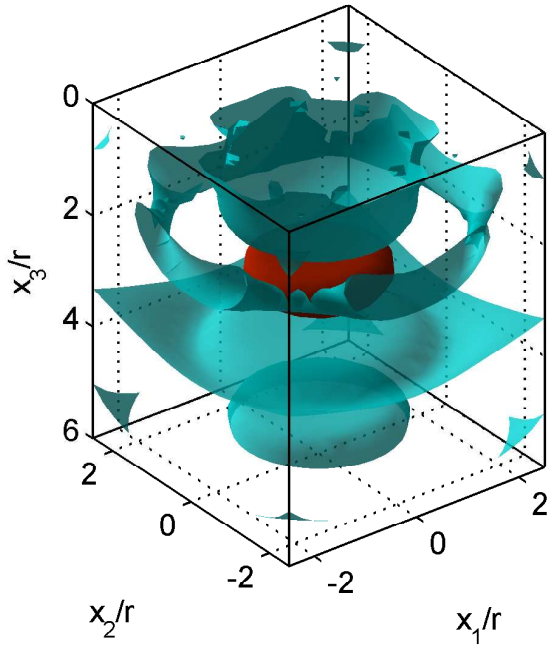

Figure 5.14: Identification of a centered spherical cavity. Isosurfaces of $\mathcal{T}$ at $\bar{\omega} = 1.5$. Symmetric profile sources/receivers.

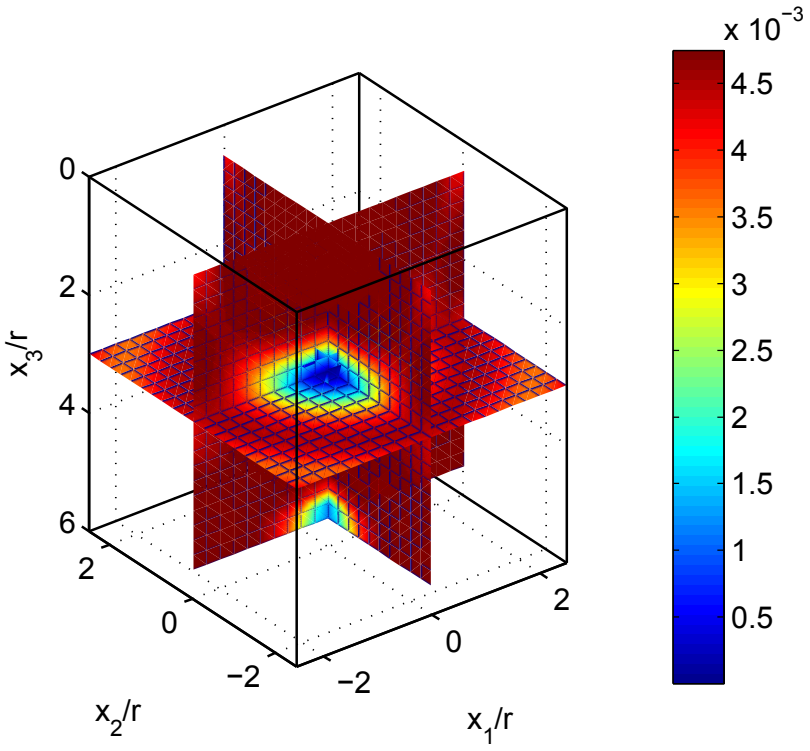

Figure 5.15: Identification of a centered spherical cavity. Linearized Cost Function slices at $\bar{\omega} = 1.5$. Symmetric profile sources/receivers.

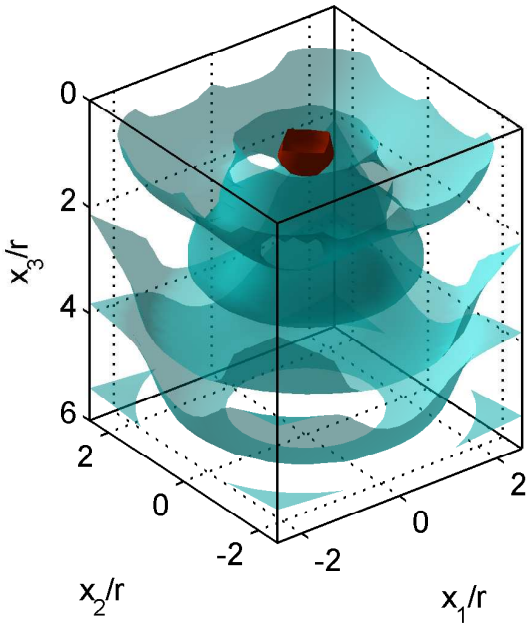

Figure 5.16: Identification of a centered spherical cavity. Isosurfaces of $\mathcal{T}$ at $\bar{\omega} = 2$. Symmetric profile sources/receivers.

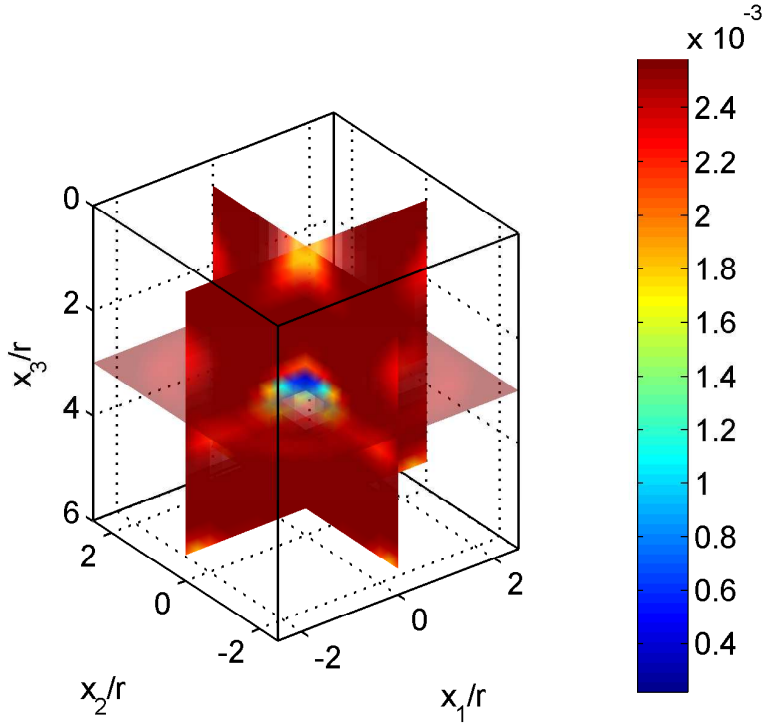

Figure 5.17: Identification of a centered spherical cavity. Linearized Cost Function slices at $\bar{\omega} = 2$. Symmetric profile sources/receivers.

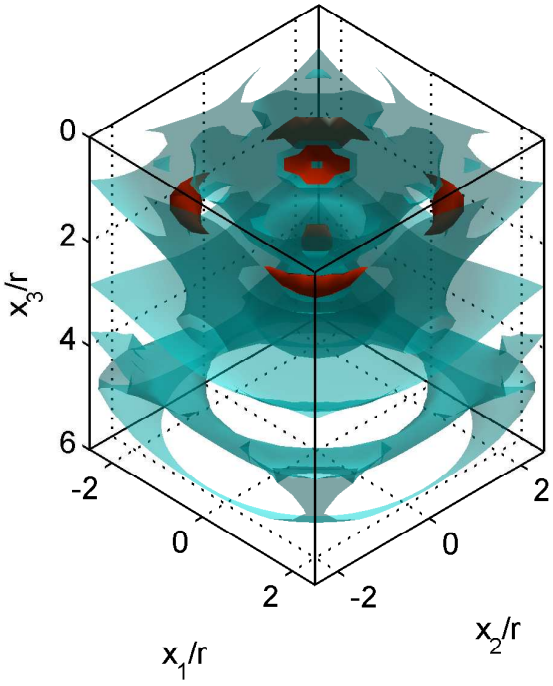

Figure 5.18: Identification of a centered spherical cavity. Isosurfaces of $\mathcal{T}$ at $\bar{\omega} = 2.5$. Symmetric profile sources/receivers.

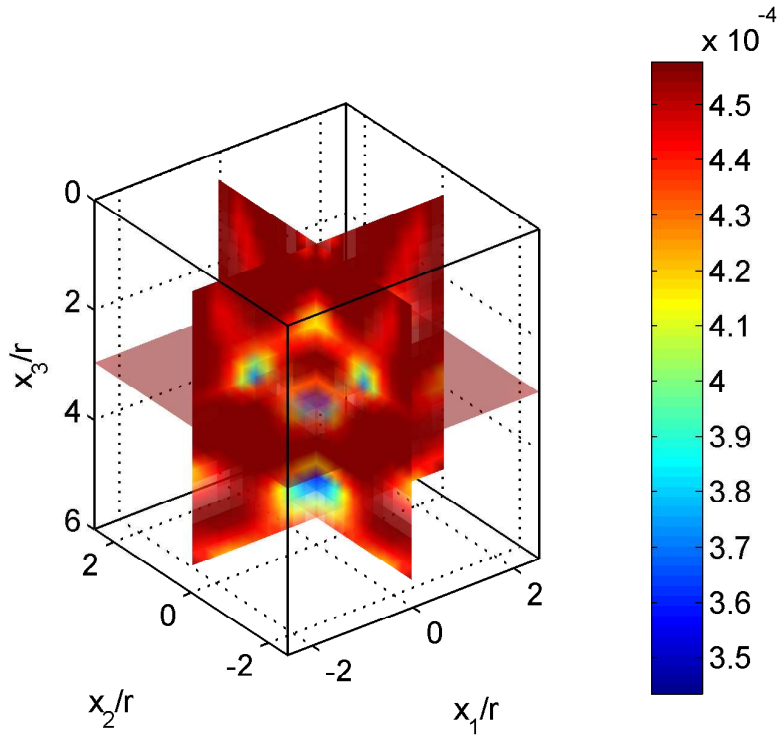

Figure 5.19: Identification of a centered spherical cavity. Linearized Cost Function slices at $\bar{\omega} = 2.5$. Symmetric profile sources/receivers.

Effect of positions of sources/receivers
The identification of the hidden cavity radious $a_r = 0.5r$ centered at $(0, 0, 3r)$ is carried out at this section with a non-symmetric profile of sources and receivers. The effect of multiple wave reflection is the main effect explored here. Figure 5.20 represents the position of the 16 sources (red) and 9 receivers (blue). Sources are centered at $(-1.5r, 0, 0)$, located in a rectangular patch $2r \times 2r$. Receivers are centered at $(1.5r, 0, 0)$ and are disposed in an squared array size $2r$. Figure also represent the Boundary Element Mesh.

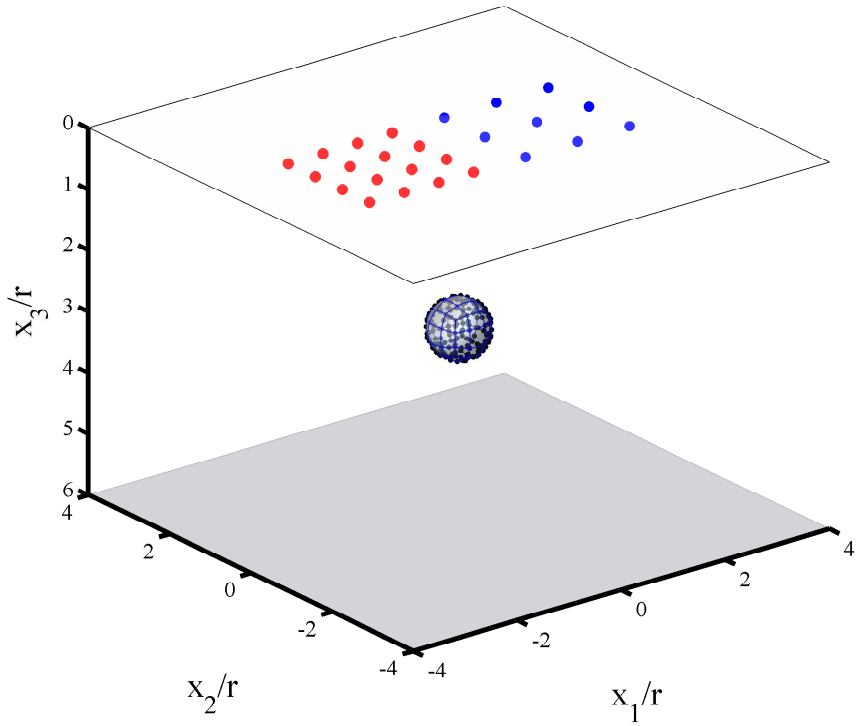

Figure 5.20: Configuration of sources (red) and receivers (blue). Identification of a centered cavity with a non-symmetric profile of sources and receivers

The identification is carried out by a combined GA-TS approach, with parameters shown in table 5.2. The combination of frequencies is also explored. Table 5.6 show the end points, cost function and error ε computed by Equation 5.30. It is observed that despite higher error rates are repored for the lowest frequencies, when compared with Table 5.5, lower errors are reported for the higher frequencies.

The error of the combination of frequencies search is less than the error obtained with any monochromatic test. In comparison with Table 5.5, the magnitude of the error obtained with the combination frequencies approach is similar. The inverse problem depends on the number of experiments. It is expected that the convergence is improved by increasing the number of experimental data.

The evolution of the GA-TS algorithm at each single frequency is shown in figure 5.21. The evolution for the combination of frequencies is shown in figure 5.22.

$\bar{\omega}$	c_1/r	c_2/r	c_3/r	a_r/r	$\tilde{\mathcal{J}}/(\mu r^3)$	ε/r
1	-3.24E-02	1.33E-03	3.153	0.488	3.08E-05	1.57E-01
1.5	1.58E-01	4.79E-03	3.040	0.489	6.35E-05	1.64E-01
2	8.59E-02	8.06E-03	3.028	0.437	4.71E-04	1.11E-01
2.5	2.37E-01	2.71E-03	3.039	0.427	2.27E-04	2.51E-01
Combined	6.92E-02	1.05E-03	3.059	0.463	1.73E-03	9.80E-02

Table 5.6: GA-TS global search. Spherical cavity identification. Non-symmetric profile of sources and receivers

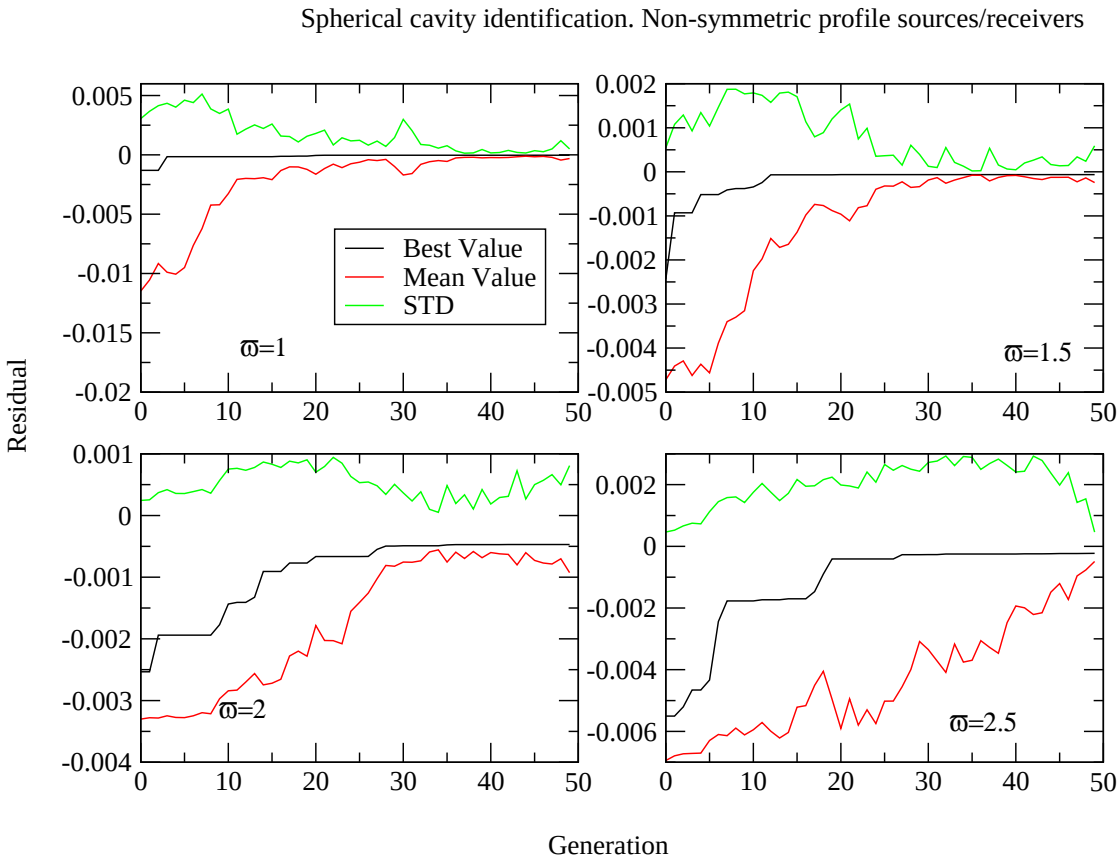

Figure 5.21: GA-TS identification of a cavity. Non-symmetric profile sources/receivers. Results at four frequencies.

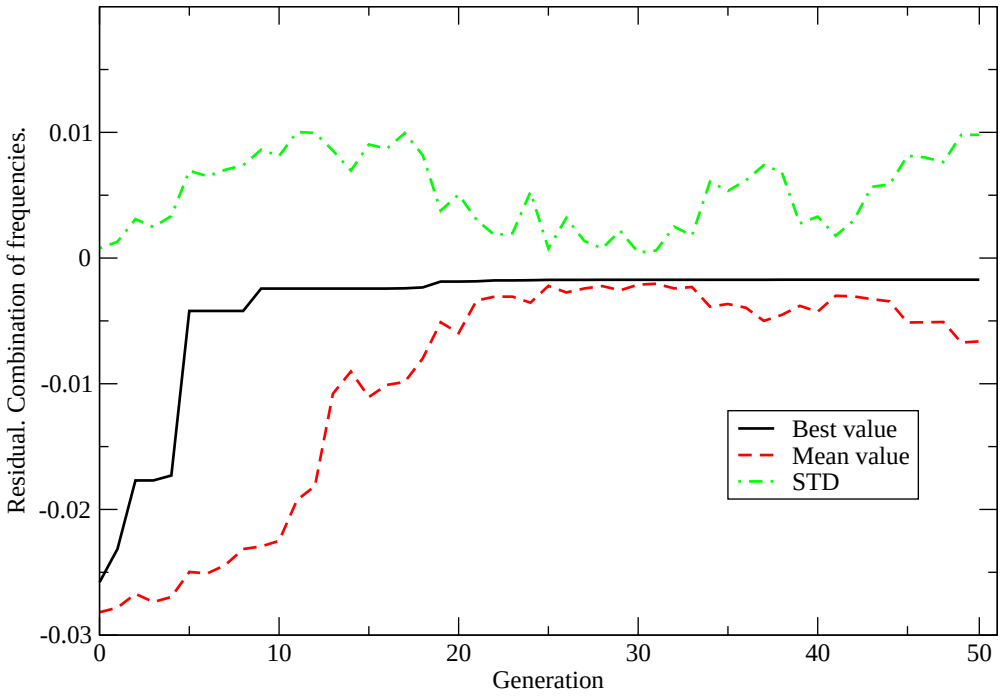

Figure 5.22: GA-TS identification of a cavity. Non-symmetric profile sources/receivers. Combination of frequencies.

The observation of the Topological Sensitivity Map can be done in figures 5.23, 5.25, 5.27, 5.29. The isosurface corresponding with $0.5\min\{\mathcal{T}\}$ is represented in red colour; the isosurface $\mathcal{T} = 0$ is represented in blue colour. For this problem, figures evidences that the minimum value in $\mathcal{T}$ is not reached at the center of the sphere. The isosurfaces does not show any kind of information about the shape of the hidden cavity. On the contrary, the Cost Function, evaluated at each point at the optimum radius, obtain the coordinate center at the true cavity position. Figures 5.24, 5.26, 5.28 and 5.30 represents the cost functon at four frequencies.

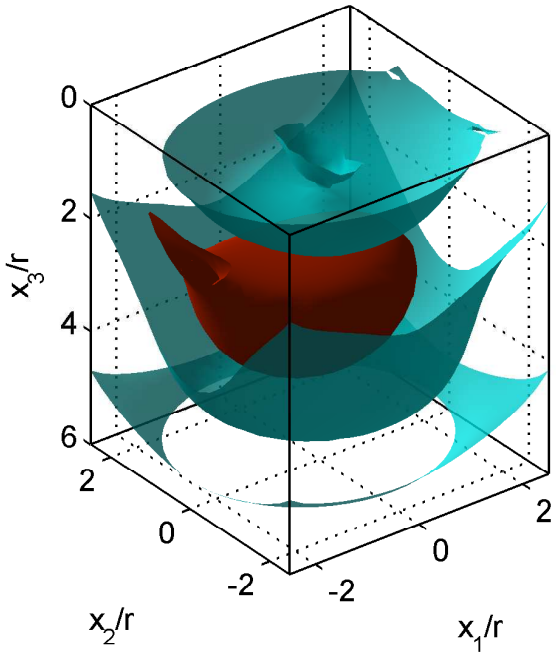

Figure 5.23: Identification of a centered spherical cavity. Isosurfaces of $\mathcal{T}$ at $\bar{\omega} = 1$. Non-symmetric profile sources/receivers.

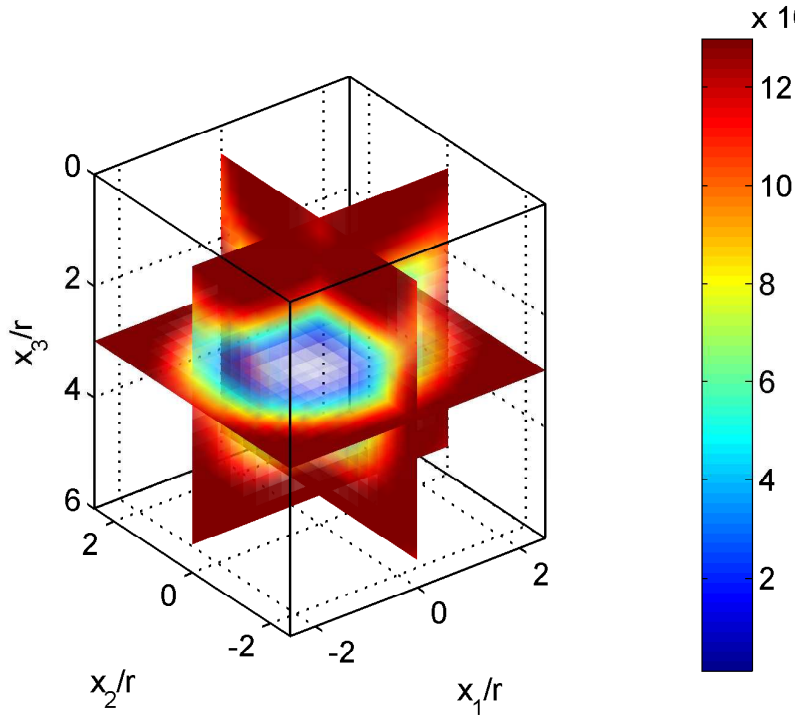

Figure 5.24: Identification of a centered spherical cavity. Linearized Cost Function slices at $\bar{\omega} = 1$. Non-symmetric profile sources/receivers.

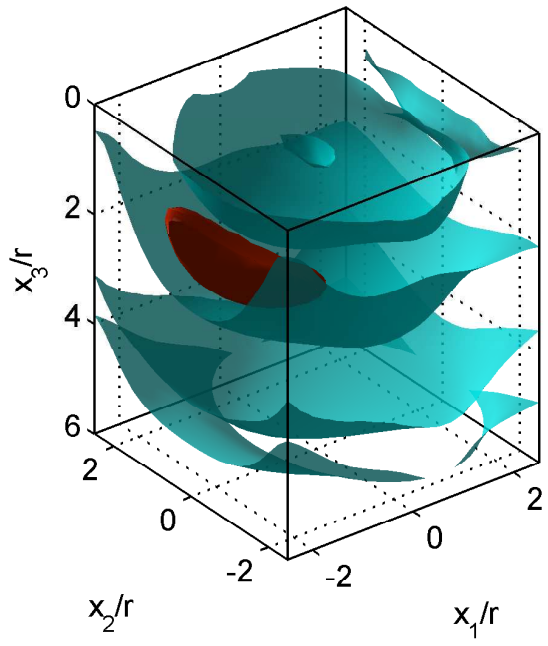

Figure 5.25: Identification of a centered spherical cavity. Isosurfaces of $\mathcal{T}$ at $\bar{\omega} = 1.5$. Non-symmetric profile sources/receivers.

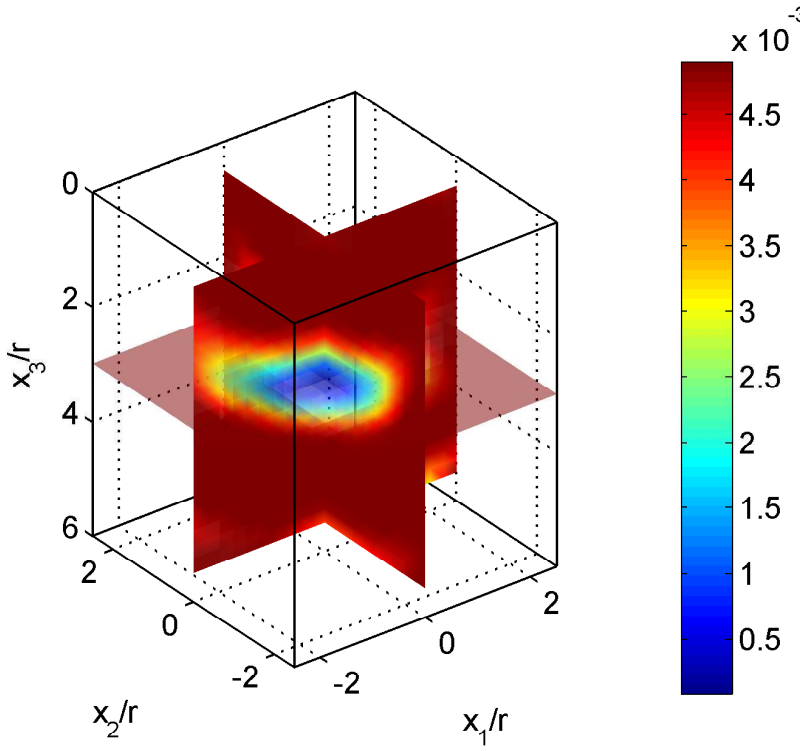

Figure 5.26: Identification of a centered spherical cavity. Linearized Cost Function slices at $\bar{\omega} = 1.5$. Non-symmetric profile sources/receivers.

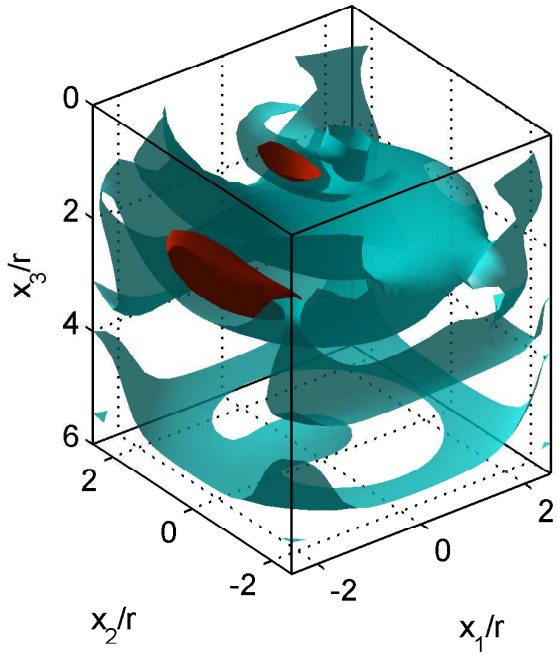

Figure 5.27: Identification of a centered spherical cavity. Isosurfaces of $\mathcal{T}$ at $\bar{\omega} = 2$. Non-symmetric profile sources/receivers.

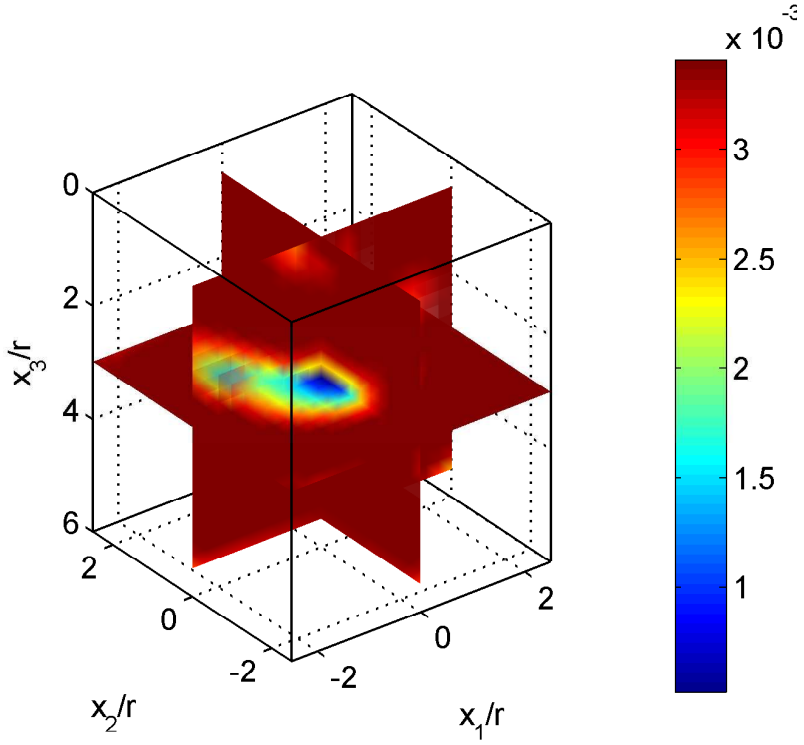

Figure 5.28: Identification of a centered spherical cavity. Linearized Cost Function slices at $\bar{\omega} = 2$. Non-symmetric profile sources/receivers.

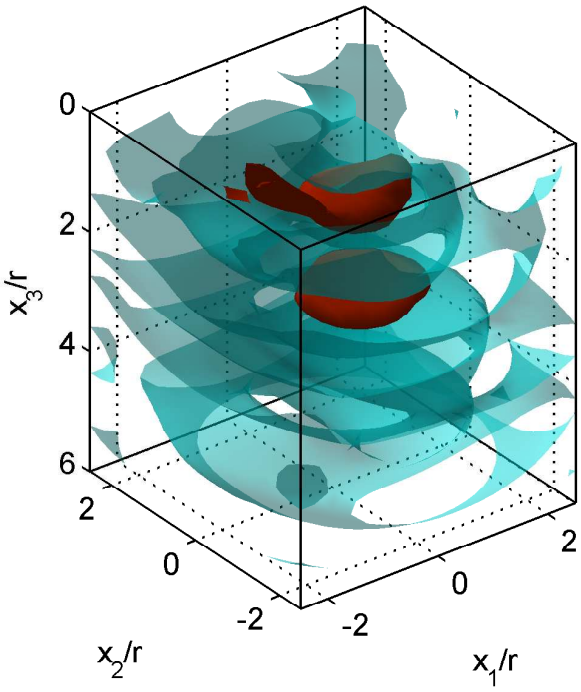

Figure 5.29: Identification of a centered spherical cavity. Isosurfaces of $\mathcal{T}$ at $\bar{\omega} = 2.5$. Non-symmetric profile sources/receivers.

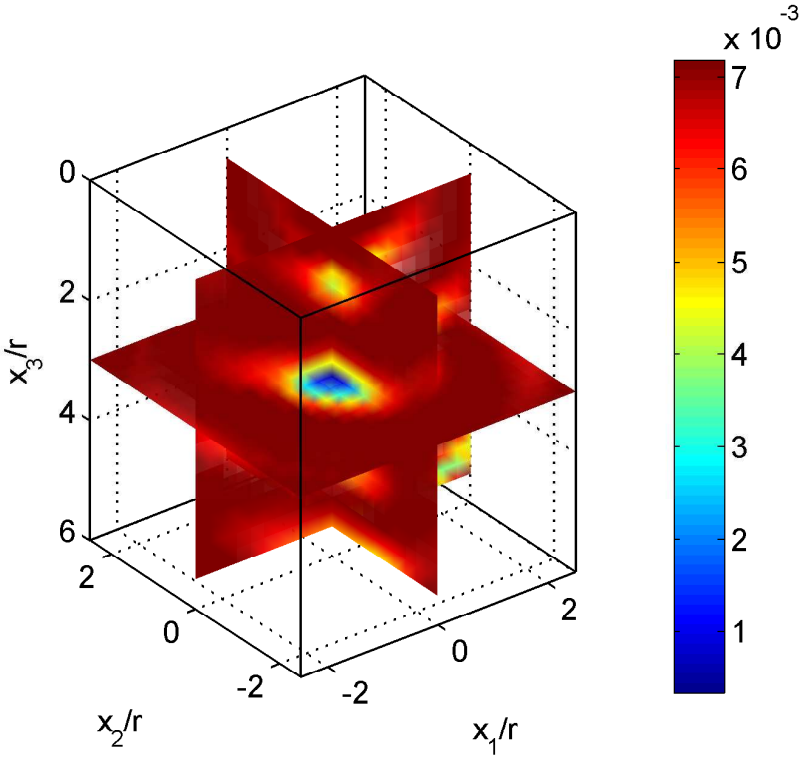

Figure 5.30: Identification of a centered spherical cavity. Linearized Cost Function slices at $\bar{\omega} = 2.5$. Non-symmetric profile sources/receivers.

5.8.3 *Two cavities detection*

The identification of two spherical cavities based on the linearization of the cost function is explored at this section. It must be remarked that it is assumed that the interaction between cavities is small. Damping also minimises the interaction between cavities. Thus, the sensitivity to damping is considered.

The combined GA-TS is used to find the global minimum. For all tests, the aim of the tests is the identification of two cavities. Thus, the number of parameters of the Genetic Algorithm search is 6, the coordinate centers of both cavities: for cavity $\mathcal{C}_1$, the center is (c_1^1, c_2^1, c_3^1) and its volume is v_1. Cavity $\mathcal{C}_2$ is centered at (c_1^2, c_2^2, c_3^2), and volume v_2. Both cavities are spherical.

At each point, a local expansion of the cost function in terms of the two volume is obtained. Optimum volumes are solved by stating a local constrained minimization problem, by the physical consideration that volumes must be positive or zero. Thus, the optimum volumes are search at the boundary $v_1 = 0$ or $v_2 = 0$, when the optimum volume obtained by solving the local minimization problem produces negative values at any of values v_1 or v_2.

Parameters of the combined GA-TS global search are shown in Table 5.7. Note that despite it is a six-parameter identification, the order of the cavity is not fixed; thus, two optimum points might be obtained. Symmetric results are obtained, and a careful analysis of the results reveal the cavity order.

Parameter	Value
Low constrain	$[-2.5, -2.5, 0.5, -2.5, -2.5, 0.5]$
Up constrain	$[2.5, 2.5, 5.5, 2.5, 2.5, 5.5]$
Number of parameters	6
Number of generations	100
Size of the population	50
Probability of crossover	0.8
Probability of mutation	0.02
Tournament probability	0.7
Scale for mutation	0.1

Table 5.7: Parameters of the GA for two cavities identification

Two cavities identification: Different diameters

The first test consists on the identification of two cavities. Cavity $\mathcal{C}_1$ is centered at $(-1.5r, 0, 2r)$ and radius $a_r^1 = 0.5r$. The second cavity $\mathcal{C}_2$ is located at $(1.5r, 2r, 4r)$, radius $a_r^2 = r$. Figure 5.31 represents the BE mesh and the location of sources and receivers. The exitation frequency is fixed in $\bar{w} = 1$. Layer and material properties are analogous to the one considered at the other numerical tests.

The interaction between cavities causes that the approximed topological expansion of the cost function fails. The interaction depends on damping, among other parameters (e.g. relative distance, excitation frequency, sources, receivres, etc). Thus, it is expected that an small damping rate $\xi_\alpha = \xi_\beta = 5\%$ improves the convergence.

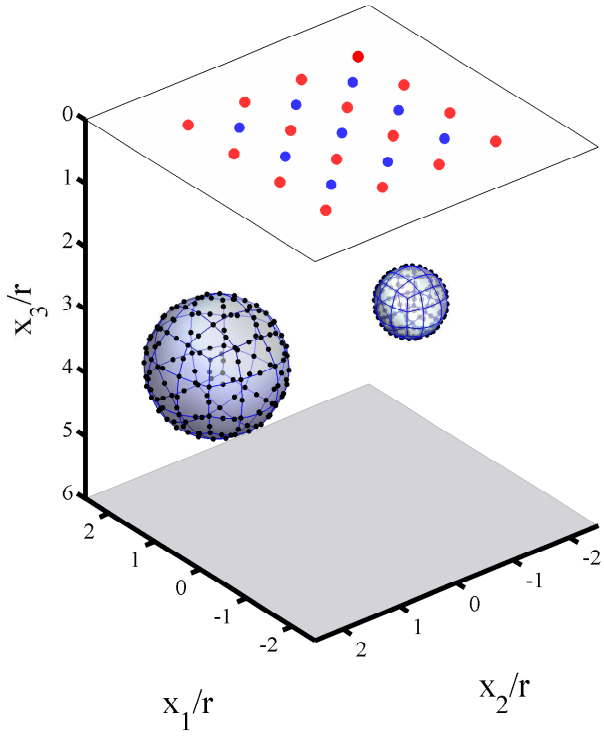

Figure 5.31: Two cavities identification. Different radius. Boundary elements mesh

The combined GA-TS global search produces end points reported in table 5.8. The last column represent the error computed by Eq. 5.30, particularized for each cavity. Damping improves the convergence and minimizes the interaction between cavities, as it can be observed by lesser errors ε. Figure 5.32 show the evolution of the GA-TS. It can be observed that the residual when damping is considered is less than the residual without damping.

Cavity	c_1/r	c_2/r	c_3/r	a_r/r	ε/r
$\xi_\alpha = \xi_\beta = 0\%$					
$\mathcal{C}_1$	-1.80	0.12	2.07	0.48	0.33
$\mathcal{C}_2$	1.69	1.08	4.26	0.96	0.98
$\xi_\alpha = \xi_\beta = 5\%$					
$\mathcal{C}_1$	-1.48	0.15	2.11	0.47	0.19
$\mathcal{C}_2$	1.64	1.11	4.14	0.96	0.92

Table 5.8: GA-TS global search. Two cavities identification, different radius. End values of parameters.

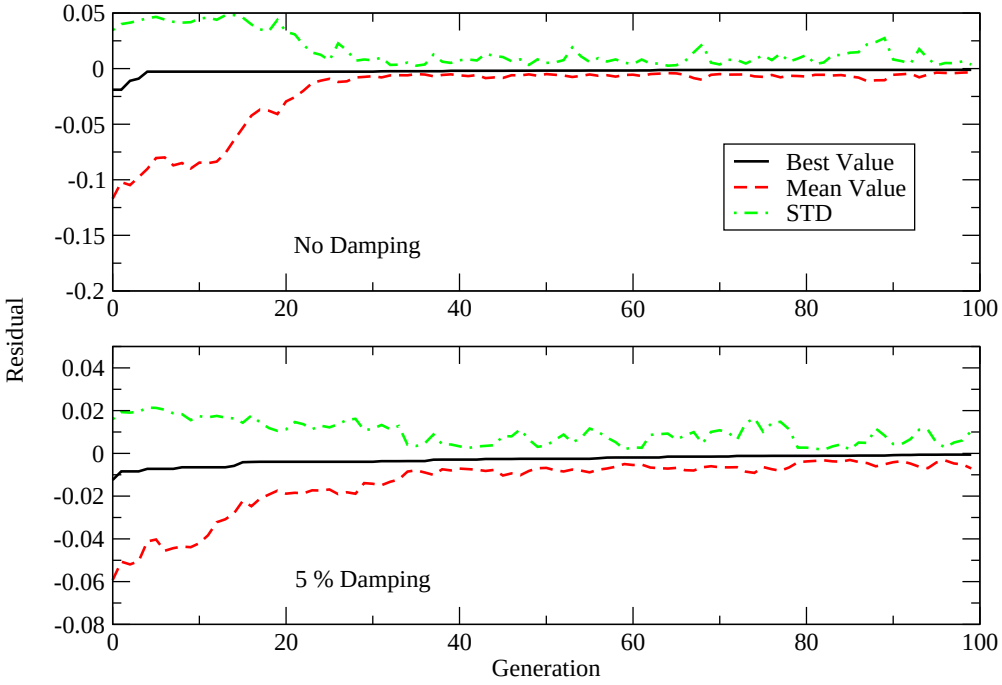

Figure 5.32: GA-TS identification of two cavities with different diameters. Effect of damping at $\bar{\omega} = 1$

Two cavities identification: Equal diameters

At the second test involving two cavities, two small and equal diameters are considered. Cavity $\mathcal{C}_1$ is centered at $(r, -r, 4r)$ and radius $a_r^1 = 0.5r$. The second cavity $\mathcal{C}_2$ is located at $(-2r, 2r, 2r)$, radius $a_r^2 = 0.5r$. Figure 5.33 represents the BE mesh and the location of sources and receivers. The exitation frequency is also fixed in $\bar{\omega} = 1$. The same consideration respect to layer and material properties remains from the previous test.

The interaction between cavities is greater than the one for the previous test. Despite both radii are small, the reflection of waves is important. Table 5.9 show the last point when: a) no damping is provided and b) 5% damping is provided. When no damping is given, no convergence is reached. On the contrary, when damping is included, error decreases drastically. Thus, material damping permit neglecting the interaction between cavities. This different behaviour is also observed in figure 5.34, in which the residual strongly decays when damping is considered.

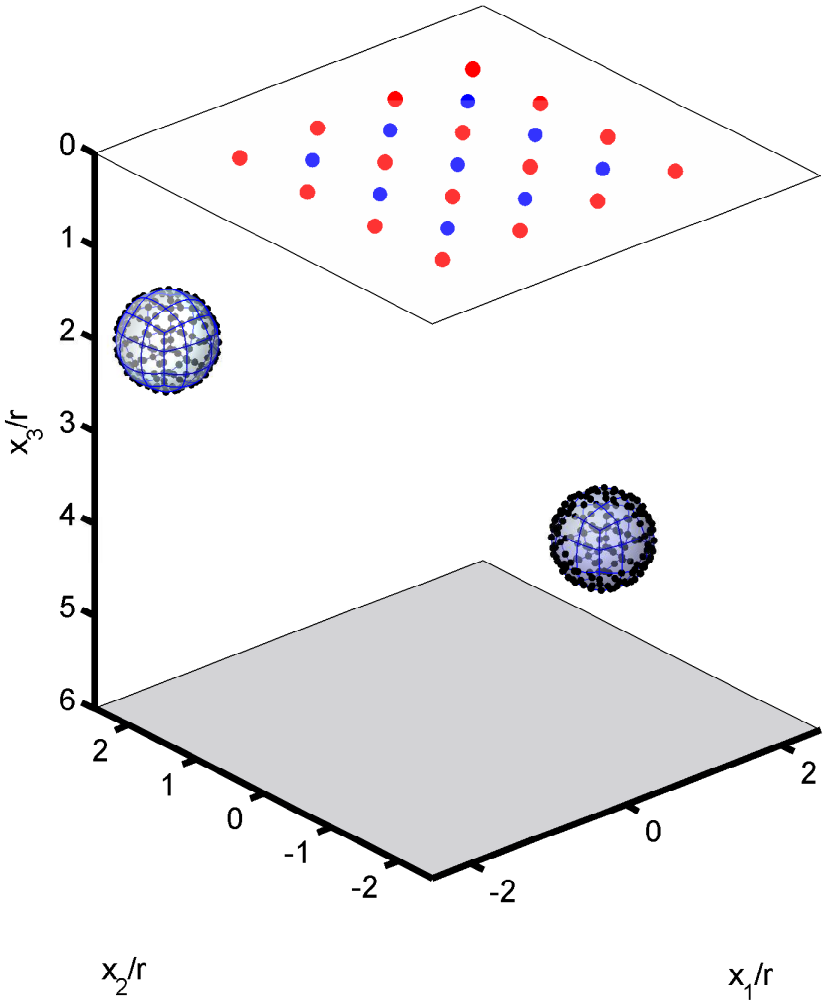

Figure 5.33: Two cavities identification. Same radius. Boundary Element mesh

Cavity	c_1/r	c_2/r	c_3/r	a_r/r	ε/r
$\xi_\alpha = \xi_\beta = 0\%$					
$\mathcal{C}_1$	0.22	0.23	4.66	1.88	2.11
$\mathcal{C}_2$	-1.21	-1.22	2.31	1.19	3.40
$\xi_\alpha = \xi_\beta = 5\%$					
$\mathcal{C}_1$	1.00	-1.01	4.10	0.51	0.10
$\mathcal{C}_2$	-1.92	1.95	2.04	0.47	0.11

Table 5.9: GA-TS global search. Two cavities identification, same radius. End values of parameters

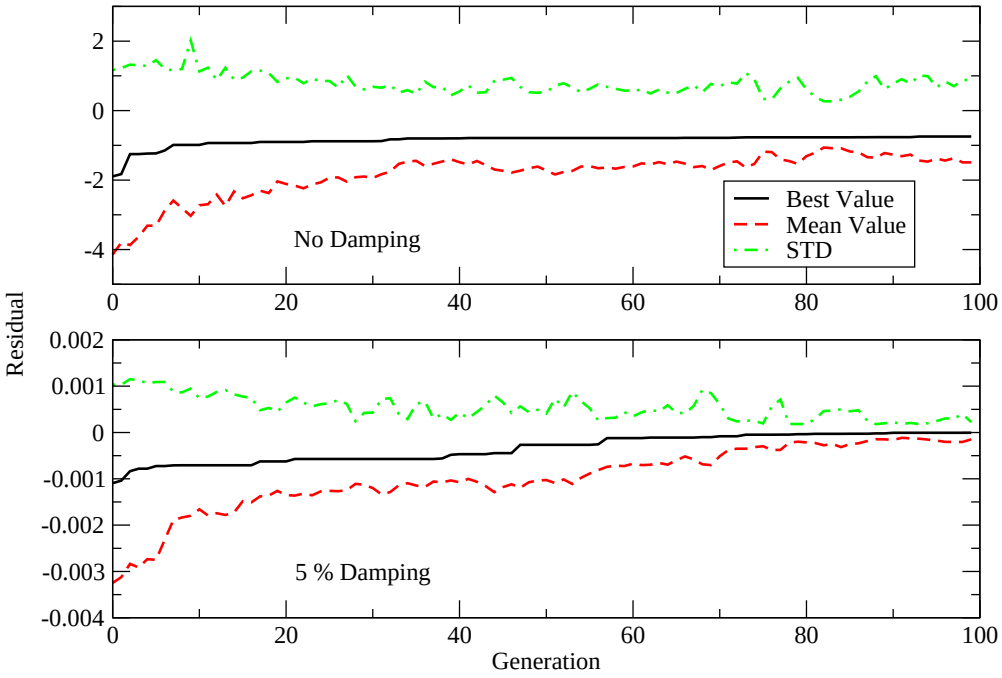

Figure 5.34: GA-TS identification of two cavities with the same diameters. Effect of damping at $\bar{\omega} = 1$

5.8.4 *Multiple deffect identification without a-priori information on the number of cavities*

One of the most interesting applications of the GA-TS approach to find cavities is the possibility of detection of less number of cavities than the number of trial cavities. The main advantage of the topological expansion is that zero volumes are obtained as natural solutions. At each point, the local search is restricted to zero or positive radius, which has proved to be very important to define a cost function with a strong local minimum.

The proposed expansion for the multiple-cavity case is based on the linearization of the cost function considering that the interaction between cavities is small. Terms involved in the interaction are relevant for the problem. Including damping, or considering long distances between deffects, are natural ways to ignore such interaction terms. At this section it is also observed that the effects of the interaction depends on the excitation frequencies. The higher the frequency, the more relevance for such effect.

At this section, the basic cavity identified in section 5.8.2 is considered. A single cavity centered at $(0, 0, 3r)$, radius $a_r = 0.5r$ is identified by a 6-parameter GA-TS search (two cavity centers). Parameters of the Genetic Algorithm global search are reported in table 5.7. The true cavity is centerd at $(0, 0, 3r)$, and radius $a_r = 0.5r$. The symmetric profile of 16 sources and 9 receivers used in section 5.8.2 is considered here.

Table 5.10 show the end point of the GA-TS global search. It is observed that two cavities are obtained. One of them is close to the exact one. The second one has a small radius. This second small cavity depends on some parameters, such as damping, number of experiments, etc. Such kind of solution with two cavities, one a main cavity and a secondary small cavity, is also reported for static problems in Gallego and Rus works. The interaction between cavities is small when the frequency is low. This is the reason that, by increasing the frequency, the higher the error are obtained. At the highest tested frequency, $\bar{\omega} = 2.5$ is observed that two equal-size cavities are obtained, with only one of the positions close to the true cavity. This test reveals that the consideration of the interaction

between cavities become more important at the highest frequencies. As it was reported in tests involving two cavities, the global search can be improved by the consideration of an small material damping rate.

Figure 5.35 show the evolution of the GA-TS global search. For all the problems, the algorithm stop when the number of iterations is reached. Plots suggest that probably the number of iterations and the size of the population should be increased to reach a better best value. Thus, a slow convergence is obtained for this kind of identification, in comparison with the identification of two cavities shown in previous section. To visualize the dependence on the population size and the number of generations, the case for frequency $\bar{\omega} = 2.5$ has been computed, with a population size 80 and number of generations 200. The resulting cavities are: $\mathcal{C}_1$, centered at $(3.69E-02, 1.49E-02, 3.24)r$, radius $a_r = 0.41r$; $\mathcal{C}_2$, centered at $(7.54E-02, 1.33E-02, 2.65)r$, radius $a_r = 0.35r$. This result can be compared with the one obtained in Table 5.10. Figure 5.36 shows the evolution of the Genetic Algorithm with the refined parameters, for the frequency $\bar{\omega} = 2.5$. It is observed, when compared with figure 5.35 that this combined approach requires more iterations when the frequency increases. The interaction between cavities become an important term for this configuration.

Cavity	c_1/r	c_2/r	c_3/r	a_r/r
$\bar{\omega} = 1$				
$\mathcal{C}_1$	4.17E-01	3.36E-01	3.08	0.11
$\mathcal{C}_2$	-5.34E-03	-3.40E-03	3.09	0.48
$\bar{\omega} = 1.5$				
$\mathcal{C}_1$	8.04E-03	8.44E-02	4.22	0.18
$\mathcal{C}_2$	2.613E-03	-2.63E-03	2.99	0.46
$\bar{\omega} = 2$				
$\mathcal{C}_1$	-4.23E-01	8.13E-02	2.23	0.22
$\mathcal{C}_2$	-5.91E-02	3.24E-04	3.16	0.48
$\bar{\omega} = 2.5$				
$\mathcal{C}_1$	2.24E-02	-5.73E-02	3.08	0.36
$\mathcal{C}_2$	4.74E-02	-2.20E-01	5.29	0.36

Table 5.10: GA-TS global search. Identification of a single spherical cavity giving two trial cavities.

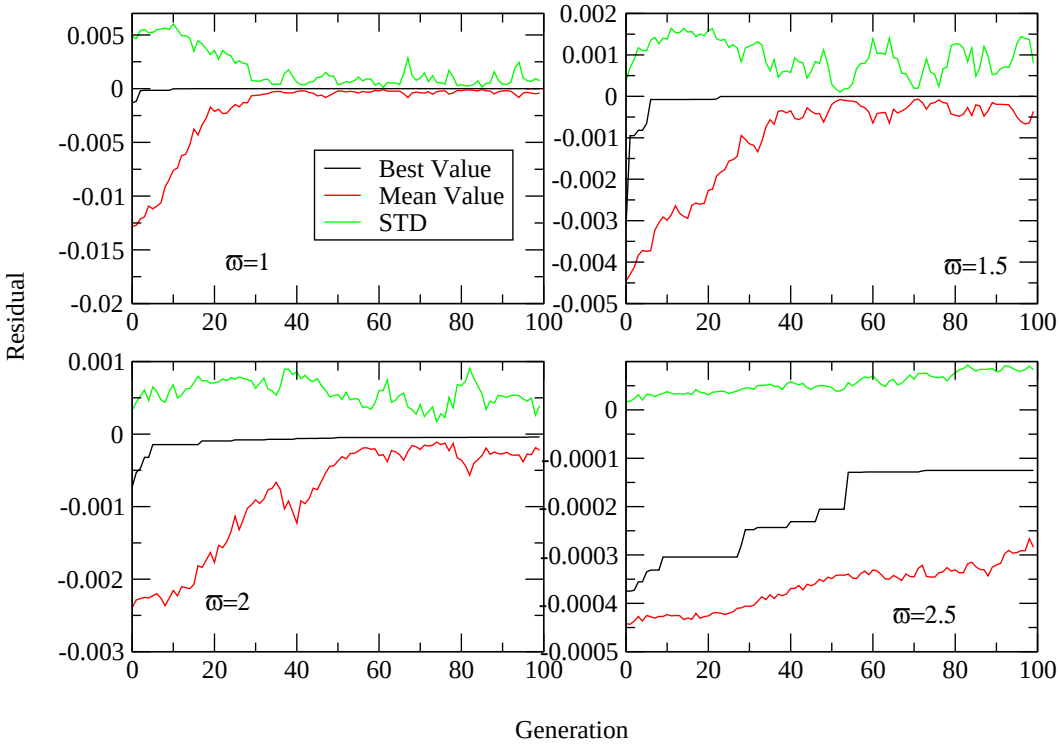

Fi

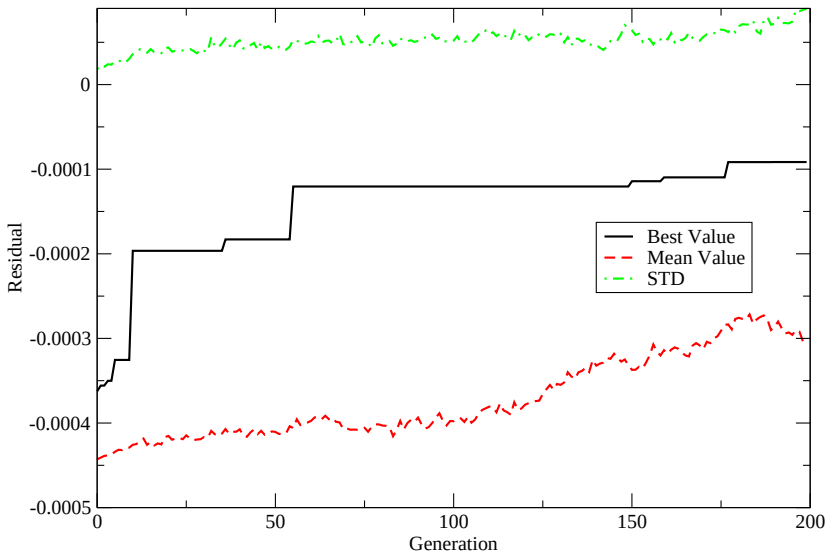

Figure 5.36: GA-TS identification of a spherical cavity with two trial cavities. Refined search at $\bar{\omega} = 2.5$

5.8.5 Ellipsoidal cavity detection: oblate spheroid

At this section the identification of an oblate spheroid is tested. The combined methodology GA-TS is used. Thus, the exact solution is not a possible one. The algorithm is explored to check the potentiallity of the method to provide a location and size of a cavity when the shape is not an sphere.

The ellipsoid $a = b = 2c = 1.1r$ centered at $(0, 0, 3r)$ is considered. The same symmetric profile of sources and receivers used at the identification of an spherical cavity are used. Figure 5.37 show

the BE mesh used to solve the forward problem that provides the pseudo-experimental data. Also,

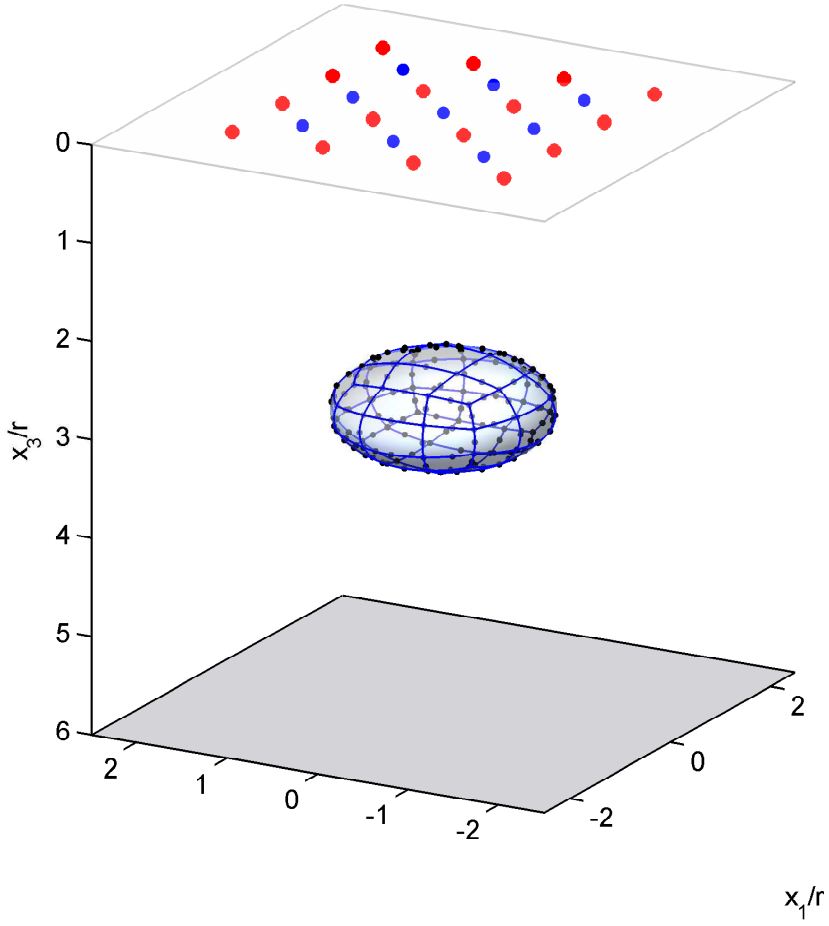

Figure 5.37: Oblate spheroid cavity. Boundary Element mesh

The exact solution is not possible at this test. For each frequency, the end point of the GA-TS approach is shown in table 5.11. For each end-point, the quadratic error ε is computed, in which the volume and the center coordinates are the four parameters considered, Eq. 5.32. The exact volume for the true ellipsoid is $v^{ref} = 2.7876$. It is observed that the spherical cavity obtained as an end point produces a position and volume similar to the position and volume of the exact ellipsoidal cavity. Figure 5.38 show the evolution of parameters in terms of best value, mean value and standard deviation, corresponding with the GA-TS global search.

$$\varepsilon = \sqrt{(c_1 - c_1^{ref})^2 + (c_2 - c_2^{ref})^2 + (c_3 - c_3^{ref})^2 + (v - v^{ref})^2} \tag{5.32}$$

$\bar{\omega}$	c_1/r	c_2/r	c_3/r	v/r^3	$\tilde{\mathcal{J}}/(\mu r^3)$	ε
1	1.38E-03	1.06E-05	3.85E+00	3.0297	8.04E-04	8.83E-01
1.5	-4.13E-04	1.74E-03	3.03E+00	2.1752	1.23E-03	6.13E-01
2	1.66E-03	6.38E-03	3.25E+00	1.2735	5.30E-03	1.53E+00
2.5	2.70E-03	-3.15E-02	2.59E+00	1.1793	8.26E-03	1.66E+00

Table 5.11: GA-TS global search. Oblated ellipsoid. End points and errors

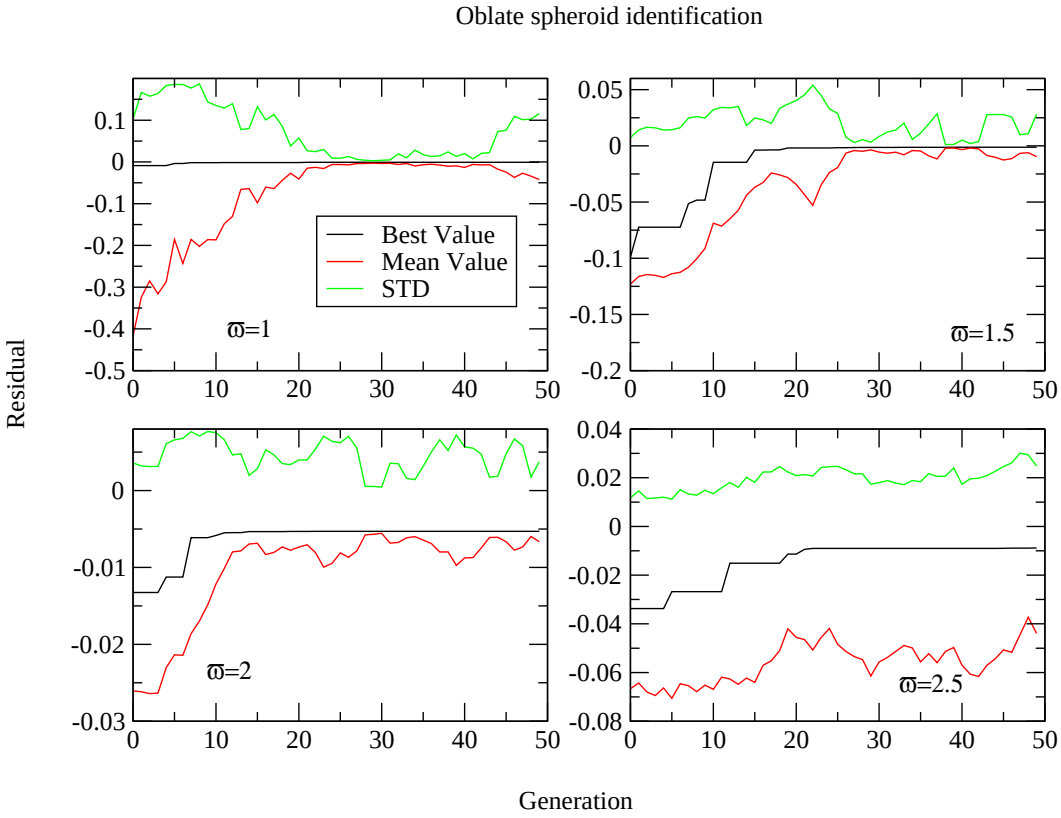

Figure 5.38: GA-TS identification of an oblate ellipsoidal cavity

The observation of the topological sensitivity map, and the cost function, is an interesting task for this problem. Figures 5.39, 5.41,5.43 and 5.45 show the three-dimensional isosurfaces corresponding with the topological derivative $\mathcal{T}$ at four frequencies; the red shape corresponds with value $0.5\min\{\mathcal{T}\}$ value. The blue one, corresponds with $\mathcal{T} = 0$. It is observed that the shape of such surfaces can not be used as an image method to identify the shape of the ellipsoid. Particularly at the higher frequencies, the $\mathcal{T}$ map provides poor information about the location of the cavity. The point with minimum value of $\mathcal{T}$ does not necessarily corresponds with the center of the ellipsoid. On the contrary, the cost function always provide a minimum value at the center of the ellipsoid, for the frequencies tested. The slices of the cost function mapped at three different planes are shown at figures 5.40,5.42,5.44 and 5.46.

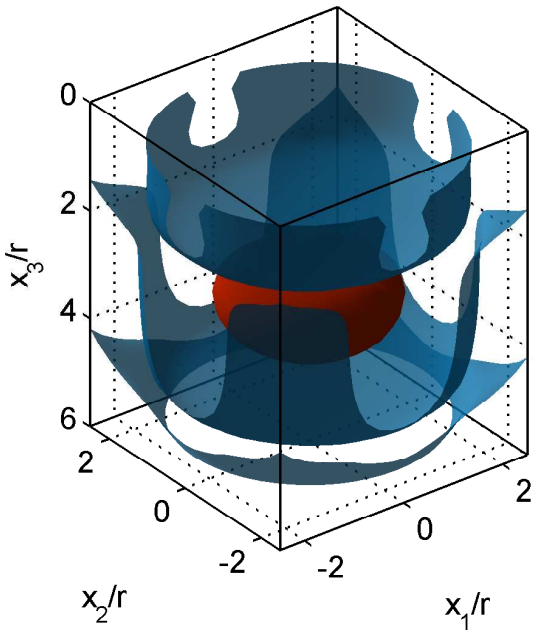

Figure 5.39: Oblate ellipsoid identification. Isosurfaces of $\mathcal{T}$ at $\bar{w} = 1$.

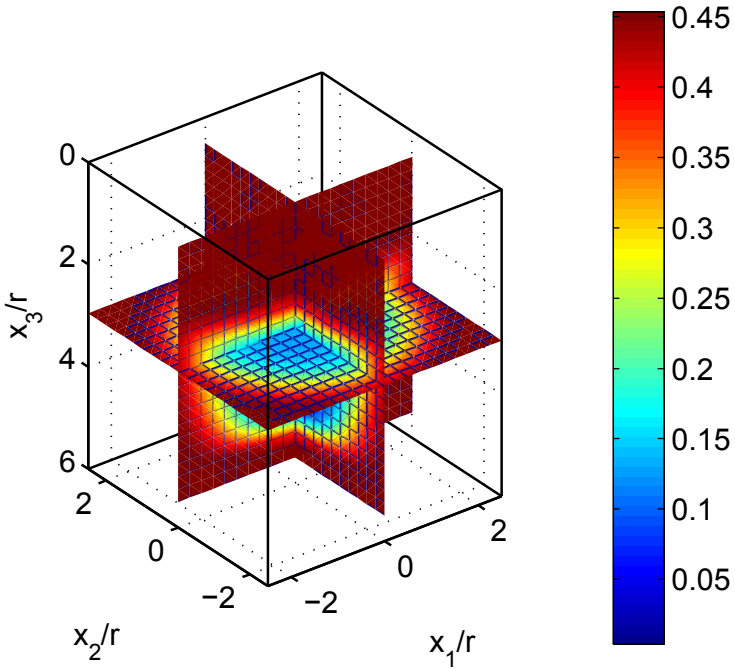

Figure 5.40: Oblate ellipsoid identification. Linearized Cost Function slices at $\bar{w} = 1$.

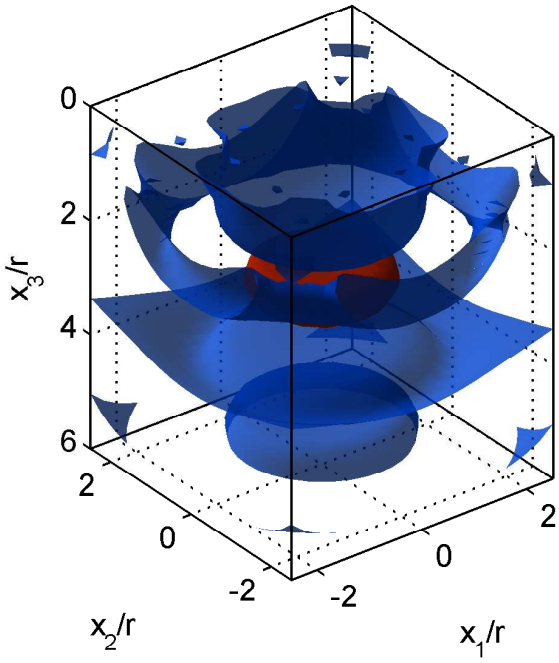

Figure 5.41: Oblate ellipsoid identification. Isosurfaces of $\mathcal{T}$ at $\bar{\omega} = 1.5$.

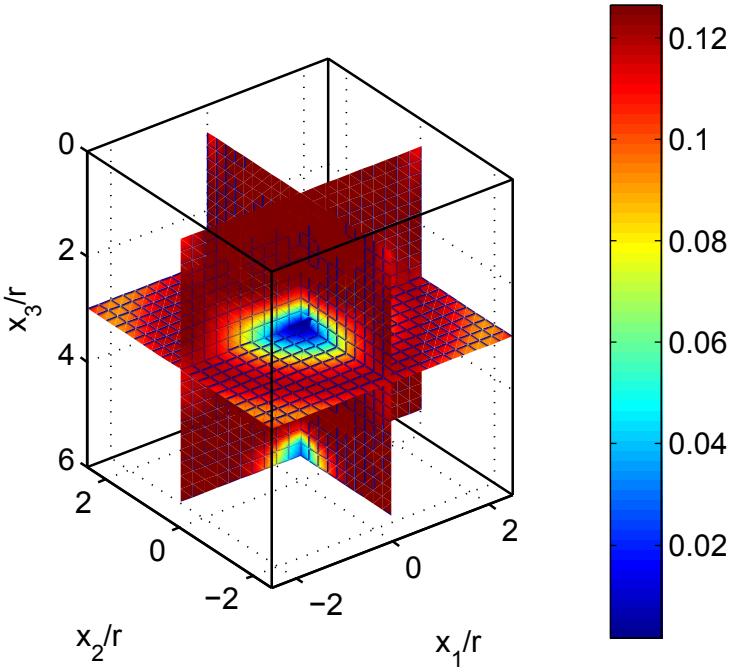

Figure 5.42: Oblate ellipsoid identification. Linearized Cost Function slices at $\bar{\omega} = 1.5$.

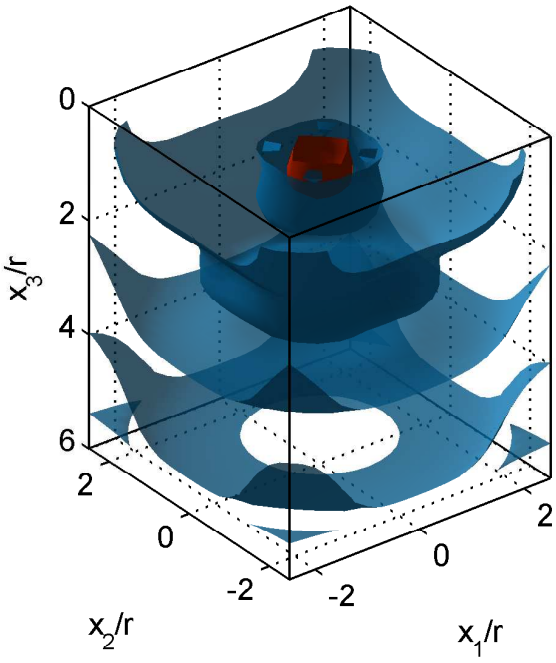

Figure 5.43: Oblate ellipsoid identification. Isosurfaces of $\mathcal{T}$ at $\bar{w} = 2$.

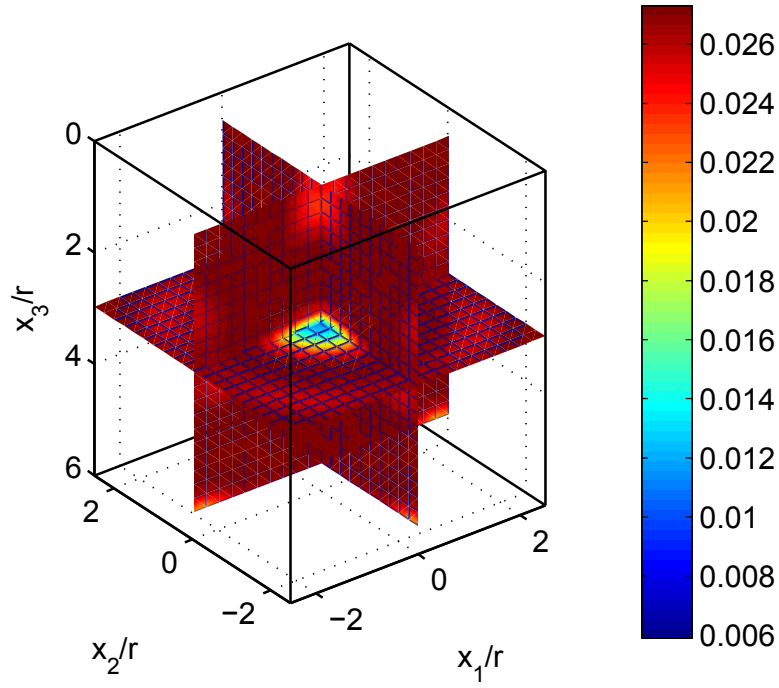

Figure 5.44: Oblate ellipsoid identification. Linearized Cost Function slices at $\bar{w} = 2$.

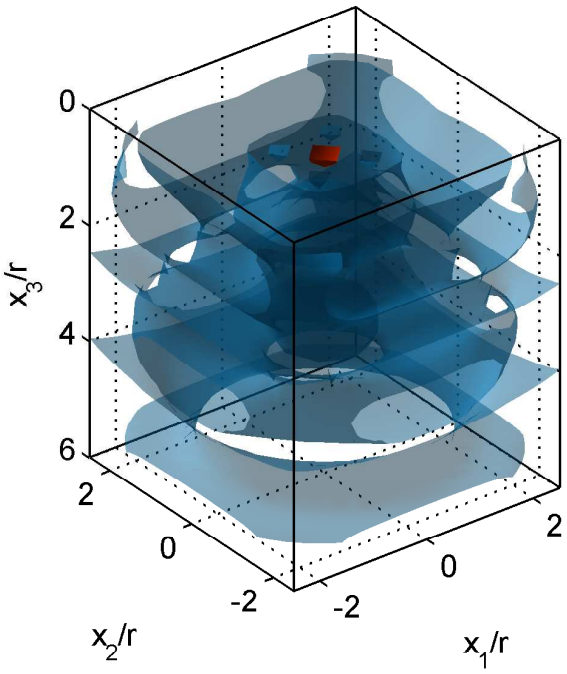

Figure 5.45: Oblate ellipsoid identification. Isosurfaces of $\mathcal{T}$ at $\bar{\omega} = 2.5$.

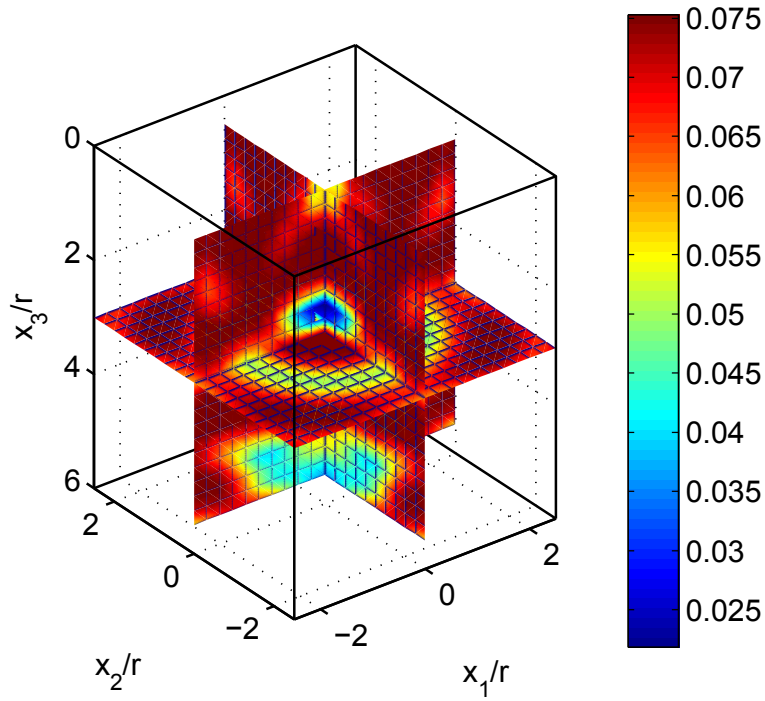

Figure 5.46: Oblate ellipsoid identification. Linearized Cost Function slices at $\bar{\omega} = 2.5$.

5.8.6 *Ellipsoidal cavity detection: prolate spheroid*

The identification of a prolate spheroid is the focus of this section. The combined methodology GA-TS is used. As occured with the previous section, the exact solution is not included in the search space; thus, a best approximation provided by the global search method is obtained. The position of the center and the volume are the adjustement parameters.

The ellipsoid $2a = 2b = c = 1.1r$ centered at $(0, 0, 3r)$ is considered. Figure 5.47 show the BE mesh and the relative positions of sources and receivers.

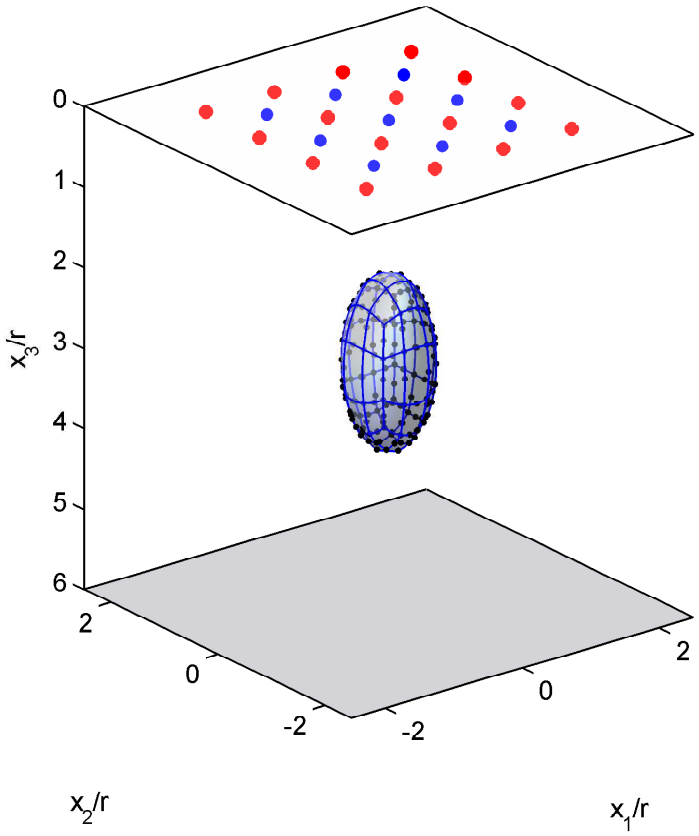

Figure 5.47: Prolate spheroid cavity. Boundary Element mesh

The end point of the GA-TS approach is shown in table 5.12, with the cost function and the quadratic error ε (Eq. 5.32). The exact volume for the ellipsoid is $v^{ref} = 1.3938$. As occured with the oblate spheroid, the volume and center coordinates are close to the exact ellipsoid parameters. Figure 5.48 show the evolution of parameters of the Genetic Algorithm.

$\bar{\omega}$	c_1/r	c_2/r	c_3/r	v/r^3	$\tilde{\mathcal{J}}/(\mu r^3)$	ε
1	1.38E-03	1.06E-05	3.85E+00	3.0297	8.04E-04	1.84E+00
1.5	-4.13E-04	1.74E-03	3.03E+00	2.1752	1.23E-03	7.82E-01
2	1.66E-03	6.38E-03	3.25E+00	1.2735	5.30E-03	2.76E-01
2.5	2.70E-03	-3.15E-02	2.59E+00	1.1793	8.26E-03	4.66E-01

Table 5.12: GA-TS global search. Prolate ellipsoid. End points and errors

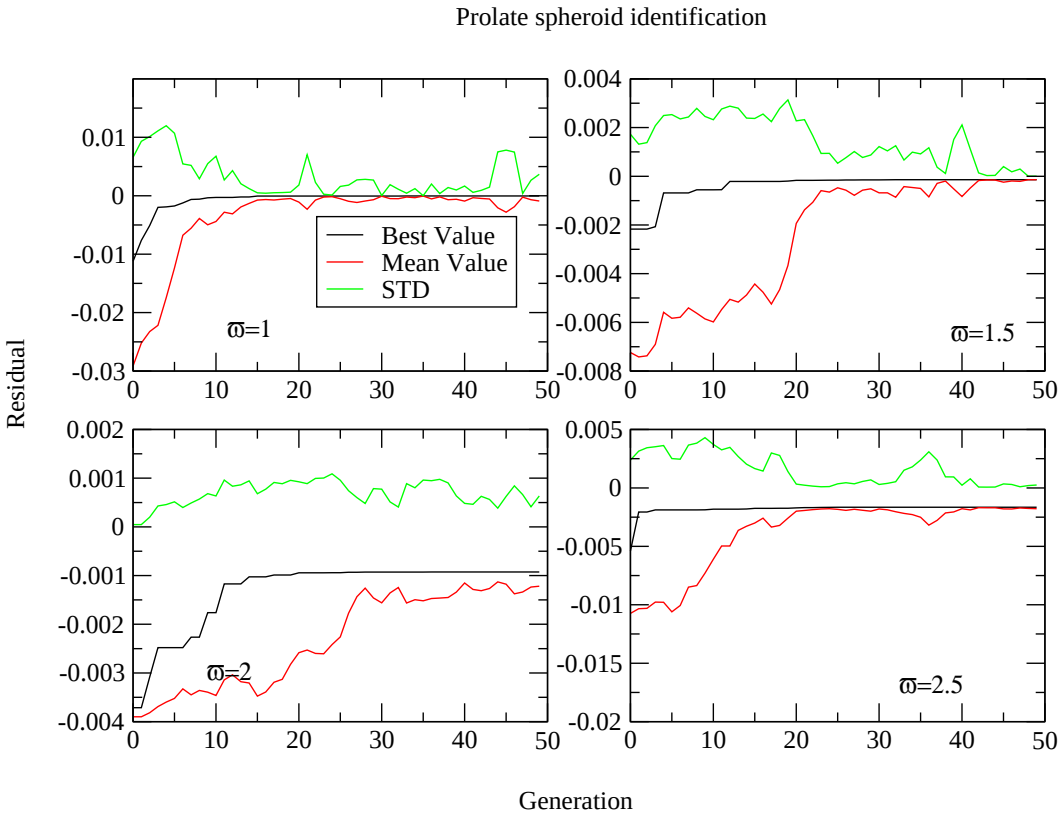

Figure 5.48: GA-TS identification of a prolate ellipsoidal cavity

The topological sensitvity map is shown in figures 5.49, 5.51,5.53 and 5.55. The red shape corresponds with $0.5\min\{\mathcal{T}\}$. The blue one, corresponds with $\mathcal{T}=0$. It is observed that the 3D $\mathcal{T}$ map provides poor information about the location and shape of the cavity. The cost function is shown in figures 5.50,5.52,5.54 and 5.56. The minimum value correspond for the four cases tested with the true coordinate center: the volume at the optimum point is similar to the volume provided by the spheric approximation.

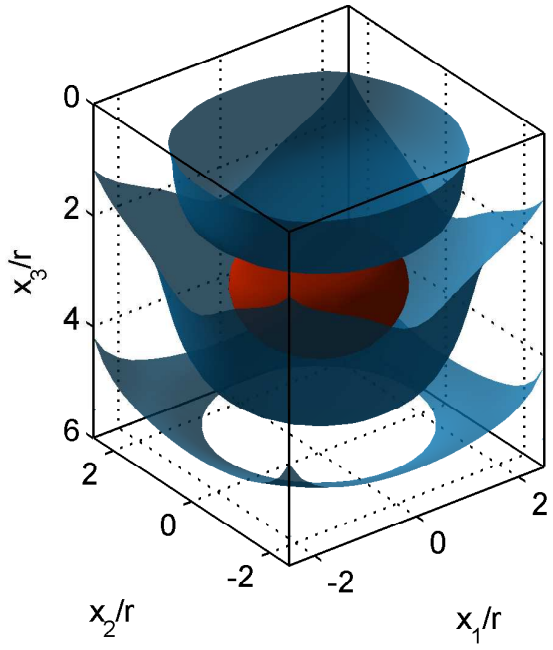

Figure 5.49: Prolate ellipsoid identification. Isosurfaces of $\mathcal{T}$ at $\bar{w} = 1$.

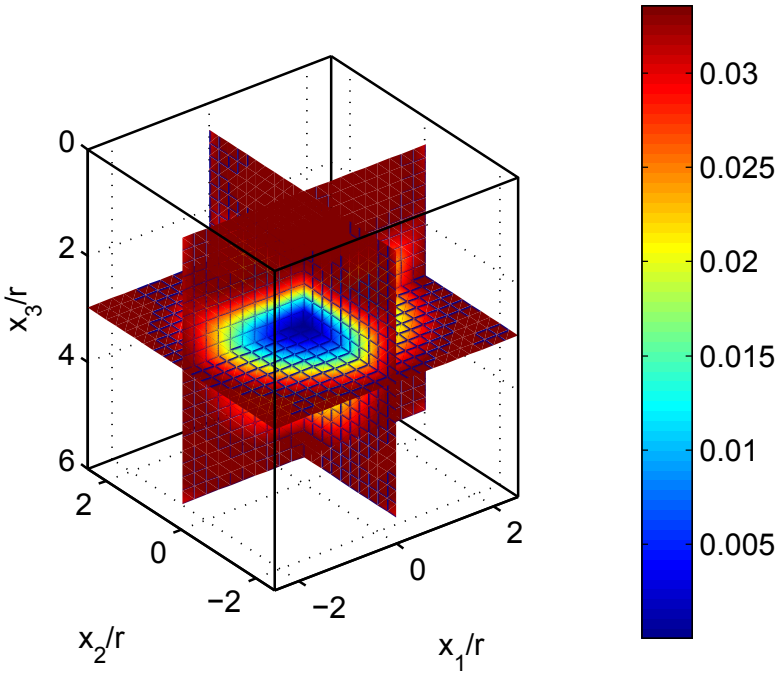

Figure 5.50: Prolate ellipsoid identification.Linearized Cost Function slices at $\bar{w} = 1$.

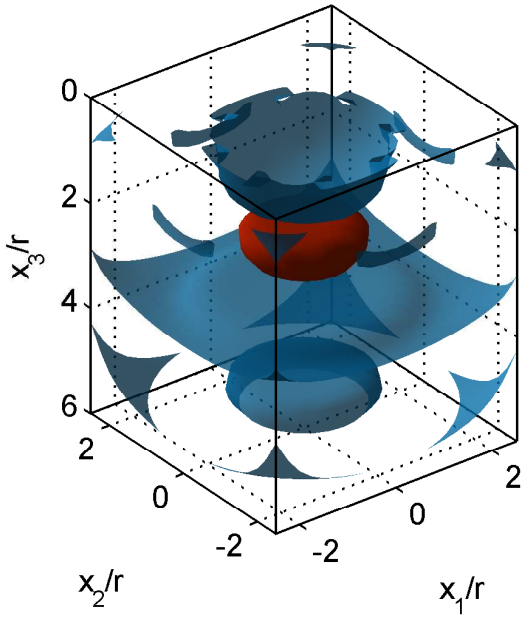

Figure 5.51: Prolate ellipsoid identification. Isosurfaces of $\mathcal{T}$ at $\bar{\omega} = 1.5$.

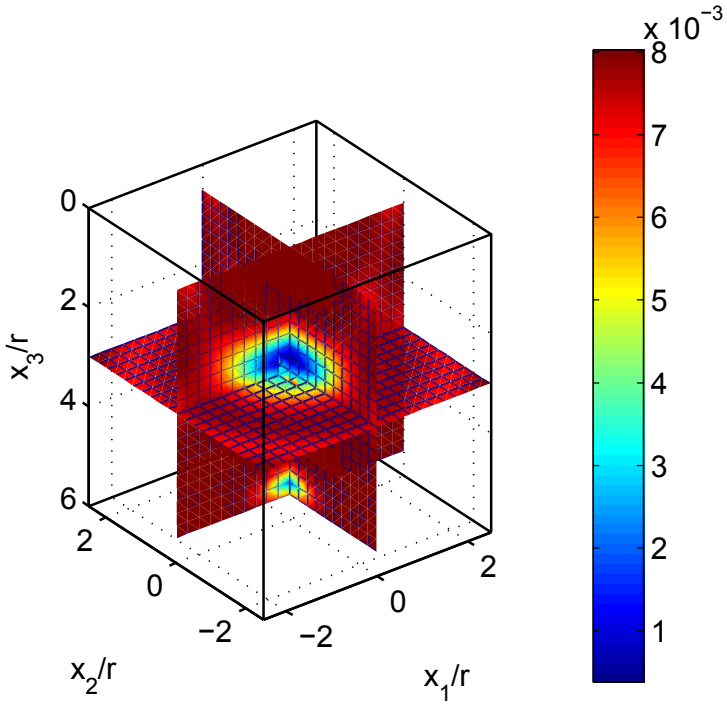

Figure 5.52: Prolate ellipsoid identification. Linearized Cost Function slices at $\bar{\omega} = 1.5$.

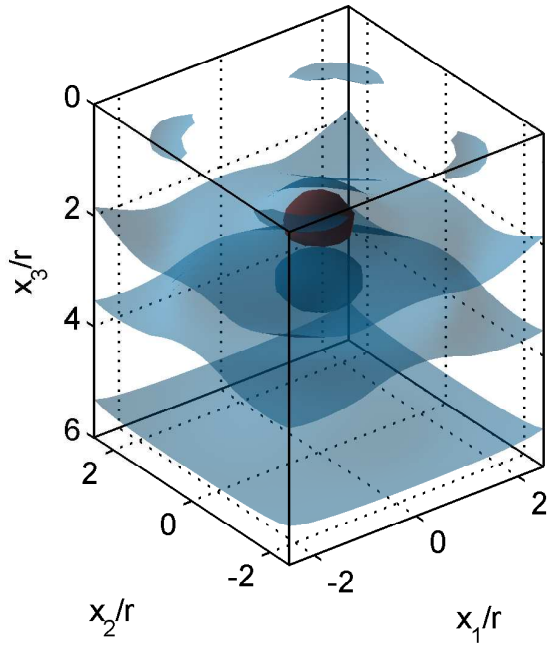

Figure 5.53: Prolate ellipsoid identification. Isosurfaces of $\mathcal{T}$ at $\bar{\omega} = 2$.

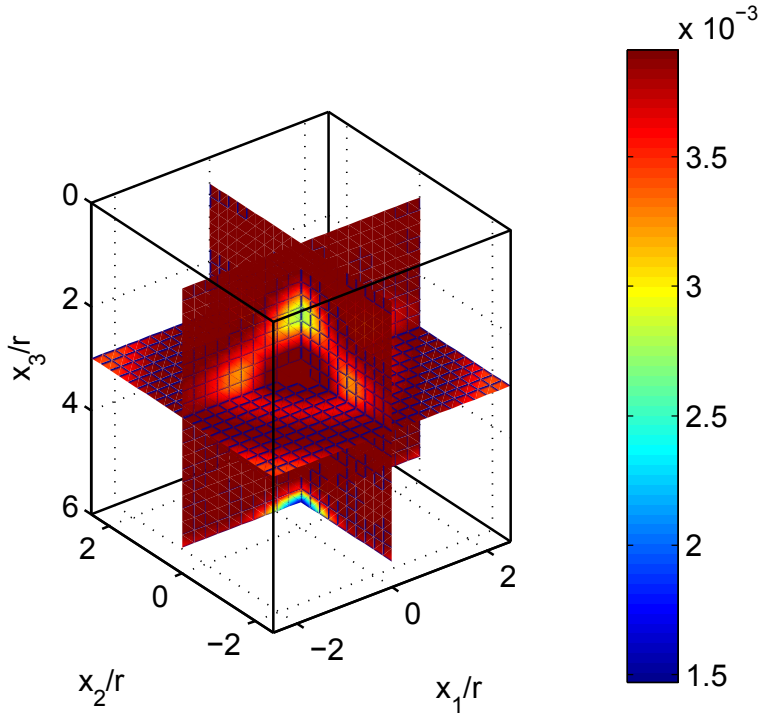

Figure 5.54: Prolate ellipsoid identification. Linearized Cost Function slices at $\bar{\omega} = 2$.

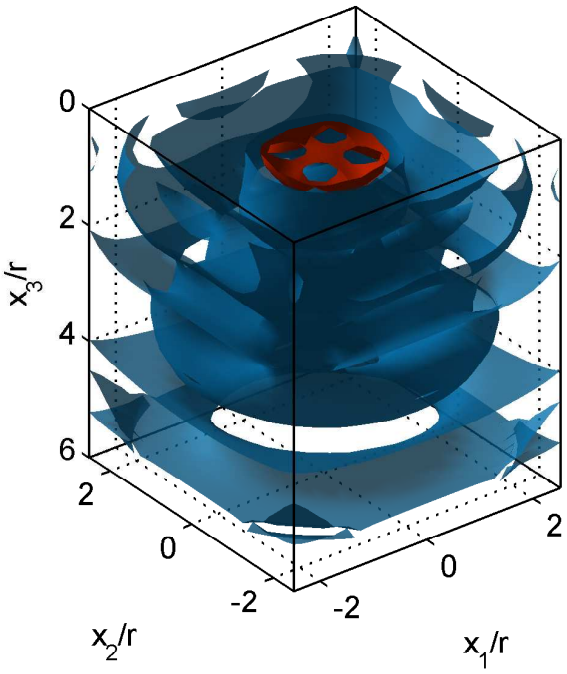

Figure 5.55: Prolate ellipsoid identification. Isosurfaces of $\mathcal{T}$ at $\bar{\omega} = 2.5$.

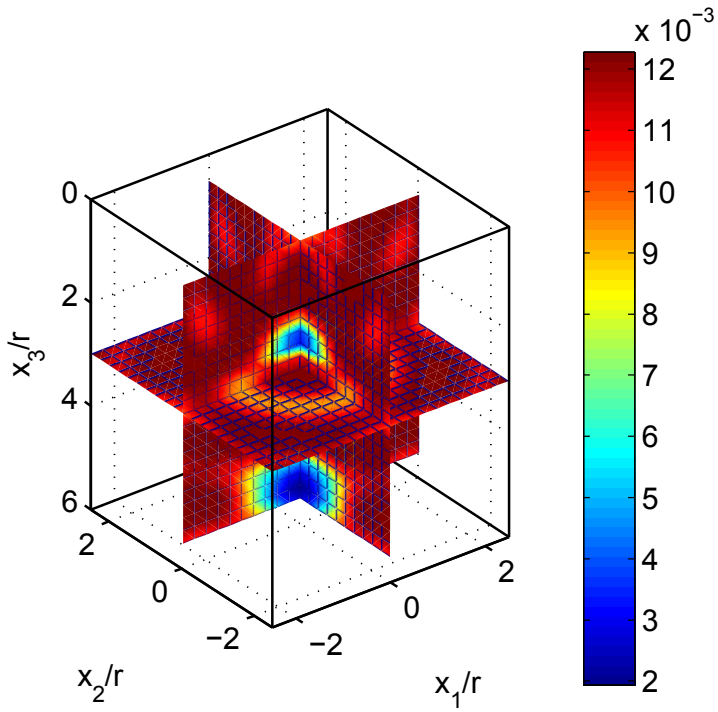

Figure 5.56: Prolate ellipsoid identification. Linearized Cost Function slices at $\bar{\omega} = 2.5$.

5.9 Concluding Remarks

The topological expansion of the cost function is presented for the layer domain in the context of time-harmonic problems. The small-asymptotic expansion of displacements in terms of a single cavity volume is presented and validated. The expansion is extended to the multi-deffect case, neglecting the interaction between deffects terms.

At each three dimensional point, the cost function can be built and optimized in terms of volumes. The volume optimization is carried out by a local constrained minimization. This aspect has been proof to be very important in the context of frequency domain computations, by numerical experiments.

The search of the optimum position and sizes of cavities is carried out by a global zero-order optimization algorithm, in the context of Genetic Algorithms. At each point, the optimum volumes are computed and the linearized cost function is evaluated. This approach is particularly interesting for the multiple-deffect global search. The proposed cost function permits the collapse of some cavities, providing a way to reduce the number of supposed cavities to fit the number of voids proposed with the actual existing one at the specimen. This approach has been demonstrated to be sensitive to frequency, due to the fact that the important terms involving the interaction between cavities are not included here.

The linearized cost function depends on the shape of the deffect. The problem involving shperical shapes has been considered here. Based on it, two examples have been carried out in order to check the possibility of finding ellipsoids based on this formulation. Numerical test show that the center coordinates and the volumes are successfully find with the proposed linealization.

The linealized cost function permits two basic ways to improve the global search. The first one is including terms that represent the interaction between cavities. Such terms requires, in the context of boundary integral equation, the hypersingular boundary integral equation of tractions. Such kernel is not available in the literature for the layer domain at the present context; thus, it is required a previous work with the Green's fuction. The second approach is the definition of a different expansion. The topological expansion migh be carried out in the frequency domain with radial functions depending on the wavenumber. This topological sensitivity become more stable at the highest frequencies.

At the frequency domain, the information provided by different frequencies might be combined to generate a new cost function. Numerical tests confirm that the end point obtained by considering the combination of frequencies is usually better than the ones obtained for a monchromatic test.

The use of the Topological Sensitivity as an image method has been explored also. Numerical tests confirm that it is a difficult task obtaining images of hidden cavities based on the TS values. On the contrary, the approximed cost function show a strong minimum point at the coordinate centers. The optimum volumes are obtained by a local minimization procedure. Combined with a zero order global method of minimization, such as the Genetic Algorithm approach, solutions are obtained close to the exact one.

CHAPTER 6

Conclusions and future works

6.1 Concluding remarks

The analysis of the Inverse Identification problem of hidden objects at a three-dimensional viscoelastic layer is stated at the present PhD work. The identification is based on the scattering of elastic waves, with time-harmonic excitation. The deffect type is limited to ellipsoids inner in a three-dimensional layer. This domain is very interesting for industrial aplications, in which ultrasound testing is used at lamites in the context of non-destructive testing.

At each chapter, particular conclusions are obtained when testing specific aspects of the inversion process. At this section the main contributions of this PhD works are summarized.

- A new Green function has been developed for the three-dimensional viscoelastic layer. New delimitations of the integration paths have been proposed.
- To include sharp geometries, new 8-noded variable-order traction singular elements have been presented.
- The use of an optimization method based on gradients, such as the AVM, has been explored. An exhaustive set of numerical tests have been presented. Conclusions about the use of first order algorithms, based on a quasi-Newton method, for the layer domain are presented. The layer domain, due to its particular geometrical damping, permits the inversion and results report stability respect to random noise at measurements.
- The time-harmonic formulation for the topological sensitivity boundary integral equation is presented. The proposed displacement expansion is tested, and is used as a basis to develop an approximed cost function, free of higher-order displacmente derivatives. Genetic Algorithms have been used to find the location and optimum sizes of hidden cavities. A numerical benchmark have been carried out, in which the sensitivity respect to the most relevant variables of the inverse problem have been tested for this GA-TS approach.

6.2 Future works

The work reported at this document permit the analysis of the inverse problem at a layer. Among the future works proposed based on this work, the following items are proposed.

a) Extension of the TS to different geometries, such as ellipsoids and cracks.
b) Development of a topological expansion depending on the wavelenght. Compare and contrast the results with the expansion presented here.
c) Development of experimental tests, which provide true experimental data for the numerical codes developed at the present work.

Bibliography

[1] R. Aithal and S. Saigal. Shape sensitivity in thermal problems using BEM. *Engineering Analysis with Boundary Elements*, 15:115–120, 1995.

[2] K. Aki and P. Richards. *Quantitative seismology. Theory and methods. Vol I.* Freeman, 1986.

[3] C. J. S. Alves and R. Kress. On the far-field operator in elastic obstacle scattering. *Journal of Applied Mathematics*, 67:1–21, 2002.

[4] R. J. Apsel and J. E. Luco. Radiation pattern of surface waves from point sources in a multilayered medium. *Bull. Seismol. Soc. Am.*, 73:931–951, 1964.

[5] T. Arens. Linear sampling methods for 2d inverse elastic wave scattering. *Inverse Problems*, 17:1445–1464, 2001.

[6] M.P. Ariza, A. Sáez, and J. Domínguez. A singular element for three–dimensional fracture mechanics analysis. *Engineering Analysis with Boundary Elements*, 20:275–285, 1997.

[7] H. Bai, J. Zhu, A. H. Shah, and N. Popplewell. Three-dimensional steady state Green function for a layered isotropic plate. *Journal of Sound and Vibration*, 269:251–271, 2004.

[8] S. Banerjee and A. K. Mal. Acoustic emission waveform simulation in multilayered composites. *Journal of Strain Analysis for Engineering Design*, 40(1):25–32, 2005.

[9] P. Bartholomew. Solution of elastic crack problems by superposition of finite elements and singular fields. *Comp. Meth. Appl. Mech. Eng.*, 13:59–78, 1978.

[10] Z. P. Bažant. Three-dimensional harmonic functions near termination of intersection of gradient singularity lines: a general numerical method. *Int. J. Eng. Sci.*, 12:221–243, 1974.

[11] Z. P. Bažant and L. F. Estenstoro. Surface singularity and crack propagation. *Int. J. Solids Struct.*, 15:405–426, 1979.

[12] F. G. Benítez and A. J. Rosakis. *Three dimensional elastodynamics of a layered medium*. Tech. rep., SM85–22, Division of Engineering and Applied Sciences, California Institute of Technology, 1985.

[13] H. Besserer and P. G. Malishewsky. Mode series expansion at vertical boundaries in elastic waveguides. *Wave Motion*, 51:1–13, 2004.

[14] D. R. Bland. *Wave theory and applications*. Oxford University Press, New York, 1988.

[15] G.E. Blandford, A.R. Ingraffea, and J.A. Liggett. Two dimensional stress intensity factor computations using the boundary element method. *International Journal for Numerical Methods in Engineering*, 17:387–404, 1981.

[16] D. B. Bogy. Edge–bonded dissimilar orthogonal elastic wedges under normal and shear loading. *Journal of Applied Mechanics*, 35:460–466, 1968.

[17] D. B. Bogy and K. C. Wang. Stress singularities at interface corners in bonded dissimilar isotropic elastic materials. *International Journal of Solids and Structures*, 7:993–1005, 1971.

[18] D.B. Bogy. Two edge–bonded elastic wedges in different materials and wedge angles under surface tractions. *Journal of Applied Mechanics*, 38:377–386, 1971.

[19] M. Bonnet. BIE and material differentiation applied to the formulation of obstacle inverse problems. *Engineering Analysis with Boundary Elements*, 15:121–136, 1995.

[20] M. Bonnet. *Boundary Integral Equations Methods for Solids and Fluids*. John Wiley & Sons, New York, 1999.

[21] M. Bonnet, T. Burczyński, and M. Nowakowski. Sensitivity analysis for shape perturbation of cavity or internal crack using BIE and adjoint variable approach. *Int. J. Solids and Structures*, 39:2365–2385, 2002.

[22] M. Bonnet and A. Constantinescu. Inverse problems in elasticity. *Inverse Problems*, 21(2):R1–R50, 2005.

[23] M. Bonnet and B. B. Guzina. Sounding of finite bodies by way of topological derivative. *International Journal for Numerical Methods in Engineering*, 61:2344–2373, 2004.

[24] M. Bonnet and B. B. Guzina. Elasic-wave identification of penetrable obstacles using shape-material sensitivity framework. *Journal of Computational Physics*, 228:294–311, 2009.

[25] Marc Bonnet. Topological sensitivity for 3d elastodynamic and acoustic inverse scattering in the time domain. *Computer Methods in Applied Mechanics and Engineering*, 195(37-40):5239–5254, 2006.

[26] T. Burczyński, J. H. Kane, and C. Balakrishna. Shape design sensitivity analysis via material derivative–adjoint variable technique for 3-D and 2-D curved boundary elements. *International Journal for Numerical Methods in Engineering*, 38:2839–2866, 1995.

[27] A. N. Ceranoglu and Y. H. Pao. Propagation of elastic pulses and acoustic emission in a plate: Part I, Theory; Part II, Epicentral Responses; Part III, General Responses. *Journal of Applied Mechanics (ASME)*, 48:125–147, 1981.

[28] A. Charalambopoulos, D. Gintides, and K. Kiriaki. The linear sampling method for the transmission problem in three-dimensional linear elasticity. *Inverse Problems*, 18:547–558, 2002.

[29] D. H. Chen and H. Nisitani. Singular stress field near the corner of joined dissimilar materials. *ASME J. of Appl. Mech.*, 60:607–613, 1993.

[30] R. M. Christensen. *Theory of viscoelasticity*. Academic Press, New York, 1971.

[31] D. Colton, J. Coyle, and P. Monk. Recent developments in inverse acoustic scattering theory. *SIAM Rev.*, 42:369–414, 2000.

[32] D. Colton, K. Giebermann, and P. Monk. Regularized sampling method for solving three-dimensional inverse scattering problems. *SIAM J. Sci. Comput.*, 21:2316–2330, 2000.

[33] D. Colton and A. Kirsch. A simple method for solving inverse scattering problems in the resonance region. *Inverse Problems*, 12:383–393, 1996.

[34] D. Colton and P. Monk. Linear sampling method for the detection of leukemia using microwaves. *SIAM J. Appl. Math.*, 58:926–941, 1998.

[35] D. Colton and P. Monk. Linear sampling method for the detection of leukemia using microwaves ii siam. *SIAM J. Appl. Math.*, 60:241–255, 1999.

[36] D. Colton, M. Piana, and R. Potthast. A simple method for solving inverse scattering problems in the resonance region. *Inverse Problems*, 13:1477–1493, 1997.

[37] L. Comino, R. Gallego, and G. Rus. Combining topological sensitivity and genetic algorithms for identification inverse problems in anisotropic materials. *Computational Mechanics*, 41:231–242, 2008.

[38] T. A. Cruse and R. B. Wilson. Boundary–integral equation method for elastic fracture mechanics. Technical report, CE-STR-90-27, November 1977.

[39] J. David and N. Cheeke. *Fundamentals and applications of ultrasonic waves*. CRC Press, 2002.

[40] J. P. Dempsey and H. Li. A rigid rectangular footing on an elastic layer. *Geotechnique*, 39(1):147–152, 1989.

[41] J. P. Dempsey and G. B. Sinclair. On the stress singularities in the plane elasticity of the composite wedge. *Journal of Elasticity*, 8:373–391, 1979.

[42] J. P. Dempsey and G. B. Sinclair. On the singular behavior at the vertex of a bi–material wedge. *Journal of Elasticity*, 11(3):317–327, 1981.

[43] J. Dundrus and M. S. Lee. Stress concentration at a sharp edge in contact problem. *Journal of Elasticity*, 2:109–112, 1972.

[44] H. A. Eschenauer, V. V. Kobelev, and A. Schumacher. Bubble method for topology and shape optimization of structures. *Structural Optimization*, 8:42–51, 1994.

[45] J. D. Eshelby. The determination of the elastic field of an ellipsoidal inclusion, and related problems. *Proceedings of the Royal Society of London. Series A. Mathematical and Physical Sciencies*, 241(1226):376–396, 1957.

[46] J. D. Eshelby. The elastic field outside an ellipsoidal inclusion. *Proceedings of the Royal Society of London. Series A. Mathematical and Physical Sciencies*, 252(1271):561–569, 1959.

[47] I. H. Faris and R. Gallego. Determination of the elastic response of materials with deffects in three dimensional domains using BEM and topological derivative. In *Proceedings of the Boundary Element Techniques Conference*, pages 107–112, Seville, Spain, 2008.

[48] S. Nintcheu Fata, B. B. Guzina, and M. Bonnet. Computational framework for the bie solution to inverse scattering problems in elastodynamics. *Computational Mechanics*, 32:370–380, 2003.

[49] Sylvain Nintcheu Fata and Bojan B. Guzina. A linear sampling method for near-field inverse problems in elastodynamics. *Inverse Problems*, 20:713–736, 2004.

[50] M. Fatemi and J. F. Greenleaf. Probing the dynamics of tissue at low frequencies with the radiation force of ultrasound. *Phys. Med. Biol.*, 45:1449–1464, 2000.

[51] G.R. Feijóo. A new method in inverse scattering based on the topological derivative. *Inverse Problems*, 20:1819—-1840, 2004.

[52] G. R. Franssens. Calculation of the elastodynamic Green's functions in a layered media by means of a modified propagator matrix method. *Geophys. J. R. Astron. Soc.*, 75:669–691, 1983.

[53] Rus G. and Gallego R. Solution of identification inverse problems by sensitivity boundary integral equation. In E. Oñate, G. Bugeda, and B. Suárez, editors, *ECCOMAS2000*, Barcelona, September 2000.

[54] R. Gallego and G. Rus. Identification of cracks and cavities using the topological sensitivity boundary integral equation. In *Proceedings of the IABEM 2002 Conference*, Austin, Texas, 2002.

[55] R. Gallego and G. Rus. Identification of cracks and cavities using the topological sensitivity boundary integral equation. *Computational Mechanics*, 33:154–163, 2004.

[56] J. M. Galán and R. Abascal. Numerical simulation of Lamb wave scattering in semi-infinite plates. *International Journal for Numerical Methods in Engineering*, 53:1145–1173, 2002.

[57] J. M. Galán and R. Abascal. Elastodynamic guided wave scattering in infinite plates. *International Journal for Numerical Methods in Engineering*, 58:1091–1118, 2003.

[58] S. Garreau, Ph. Duillaume, and M. Massmoudi. The topological asymptotic for the PDE systems: the elasticity case. *SIAM Journal on Control and Optimization*, 39(6):1756–1778, 2001.

[59] D. Gintides and K. Kiriaki. The far-field equations in linear elasticity–an inversion scheme. *Z. Angew. Math.*, 81:305–316, 2001.

[60] L.J. Gray, A.V. Phan, G.H. Paulino, and T. Kaplan. Improved quarter–point crack tip element. *Engineering Fracture Mechanics*, 70:69–283, 2003.

[61] R. J. Greenfield. Comments on "an efficient method for computing green's functions for a layered half-space with sources and receivers at close depths" by y. hisada. *Bull. Seism. Soc. Am*, 85 (5):1523–1524, 1995.

[62] R. D. Gregory and I. Gladwell. The reflection of a symmetric rayleigh-lamb wave at the fixed or free edge of a plate. *J. Elast.*, 13:185–206, 1983.

[63] B. Guzina and I. Chikichev. From imaging to material identification: a generalized concept of topological sensitivity. *Journal of the Mechanics and Physics of Solids*, 55:245–279, 2007.

[64] B. Guzina and R. Pak. Static fundamental solutions for a bi-material full-space. *Int. J. Solids & Structures*, 36:493–516, 1999.

[65] B. B. Guzina and M. Bonnet. Topological derivative for the inverse scattering of elastic waves. *Quarterly Journal of Mechanics and Applied Mathematics*, 57(Part 2):161–179, MAY 2004.

[66] B. B. Guzina and M. Bonnet. Small–inclusion asymptotic of misfit functionals for inverse problems in acoustics. *Inverse Problems*, 22:1761–1785, 2006.

[67] B. B. Guzina, S. Nintcheu-Fata, and M. Bonnet. On the stress-wave imaging of cavities in a semi-infinite solid. *International Journal of Solids and Structures*, 40:1505–1523, 2003.

[68] B. B. Guzina and R. Y. S. Pak. Static fundamental solutions for a bi-material full-space. *International Journal of Solids and Structures*, 36:493–451, 1999.

[69] B. B. Guzina and R. Y. S. Pak. On the analysis of wave motions in a multi-layered solid. *Quart. J. Mech. Appl. Math*, 54(1):13–31, 2001.

[70] B.B. Guzina, R.Y.S. Pak, and A.E. Martínez-Castro. Singular boundary elements for three-dimensional elasticity problems. *Enginerring Analysis with Boundary Elements*, 30:623–639, 2006.

[71] Bojan B. Guzina. *Seismic response of foundations and structures in multilayered media*. PhD thesis, University of Colorado, 1996.

[72] J. Haataja. Matlab function for simulating a simple real-coded genetic algorithm. Center for Scientific Computing, Box 405, FIN-02101 Espoo. Internet: Juha.Haataja@csc.fi, 2000.

[73] H. Haddar and P. Monk. The linear sampling method for solving the electromagnetic inverse medium problem. *Inverse Problems*, 18:891–906, 2002.

[74] G. K. Haritos and L. M. Keer. Stress analysis for an elastic half-space containing an embedded rigid block. *International Journal of Solids and Structures*, 16:19–40, 1980.

[75] D. G. Harkrider. Surface waves in multilayered elastic media I: Rayleigh and Love waves from buried sources in a multilayered elastic half-space. *Bull. Seismol. Soc. Am.*, 54:627–629, 1964.

[76] N. A. Haskell. The dispersion of surface waves on multilayered media. *Bull. Seism. Soc. Am.*, 43:17–34, 1953.

[77] N. A. Haskell. Radiation pattern of surface waves from point sources in a multilayered medium. *Bull. Seismol. Soc. Am.*, 54:377–393, 1964.

[78] Y. Hisada. An efficient method for computing Green's functions for a layered half-space with sources and receivers at close depths. *Bull. Seismol. Soc. Am.*, 84 (5):1456–1472, 1994.

[79] Y. Hisada. An efficient method for computing Green's functions for a layered half-space with sources and receivers at close depths (Part 2). *Bull. Seismol. Soc. Am.*, 85 (4):1080–1093, 1995.

[80] N. N. Hsu. Dynamic Green's functions of an infinite plate – a computer program. Technical report, NBSIR 85–3234. National Bureau of Standards. Center for Mfg. Engineering., Gaithersburg, MD, 1985.

[81] L. Jackowska-Strumiłło, J. Sokołowski, and A. Żochowski. The topological derivative method and artificial neural networks for numerical solution of shape inverse problems. Rapport de Recherche 3739, Institute National de Recherche en Informatique et en Automatique, 1999.

[82] E. Kausel. Thin-layer method: formulation in the time domain. *International Journal for Numerical Methods in Engineering*, 37:927–941, 1994.

[83] E. Kausel and R. Peek. Dynamic loads in the interior of a layered stratum: an explicit solution. *Bulletin of the Seismological Society of America*, 72 (5):1459–1481, 1982.

[84] H. Koguchi and T. Muramoto. The order of stress singularity near the vertex in three–dimensional joints. *International Journal of Solids and Structures*, 37:4737–4762, 2000.

[85] H. Koguchi and H. Watabe. Improving defects search in structure by boundary element and genetic algorithm scan method. *Engineering Analysis with Boundary Elements*, 19:105–116, 1997.

[86] T. Kowalckzyk, T. Fukukawa, S. Yoshimura, and G. Yagawa. An extensible evolutionary algorithm approach for inverse problems. In M. Tanaka and G. S. Dulikravich, editors, *Inverse problems in Engineering Mechanics*, pages 541–550, 1998.

[87] S. Kubo. Classification of inverse problems arising in field problems and their treatments. In M. Tanaka and H. D. Bui, editors, *Inverse Problems in Engineering Mechanics*, pages 51–60, Tokyo (Japan), 1992. Springer-Verlag.

[88] T. Kundu. *Ultrasonic nondestructive evaluation. Engineering and biological material characterization*. CRC Press, 2004.

[89] T. Kundu and A. K. Mal. Elastic waves in a multilayered solid due to a dislocation source. *Wave Motion*, 7:459–471, 1985.

[90] J.C. Lachat and J.O. Watson. Effective numerical treatment of boundary integral equations. *International Journal for Numerical Methods in Engineering*, 10(10):991–1005, 1976.

[91] H. Lamb. On waves in an elastic plate. *Proc. Royal Soc. London*, 93:114–128, 1917.

[92] E. Le Clezio, M. V. Predoi, M Castaings, B. Hosten, and M. Rousseau. Numerical predictions and experiments on the free-plate edge mode. *Ultrasonics*, 41:25–40, 2003.

[93] B. Y. Lee and B. M. Kwak. Shape optimization of two-dimensional thermoelastic structures using boundary integral equation formulation. *Computers and Structures*, 41(4):709–722, 1991.

[94] N. Levy and A. K. Mal. Calculation of ground motion in a three-dimensional model of the 1966 Parkfield earthquake. *Bull. Seism. Soc. Am*, 66:405–423, 1976.

[95] T. Lewiński and J. Sokołowski. Topological derivative for nucleation of non-circular voids. Rapport de Recherche 3798, Institute National de Recherche en Informatique et en Automatique, 1997.

[96] T. Lewiński and J. Sokołowski. Optimal shells formed on a sphere. the topological derivative method. Rapport de Recherche 3495, Institute National de Recherche en Informatique et en Automatique, 1998.

[97] T. Lewiński and J. Sokołowski. Energy change due to the appearance of cavities in elastic solids. *Int. J. Solids and Structures*, 40:1765–1803, 2003.

[98] K.M. Lim, K. H. Lee, A. A. O. Tay, and W. Zhou. A new variable–order singular boundary element for two–dimensional stress analysis. *International Journal for Numerical Methods in Engineering*, 55:293–316, 2002.

[99] M. J. S. Lowe. Matrix techniques for modeling ultrasonic waves in multilayered media. *IEEE Transactions on Ultrasonics, Ferroelectrics, and Frequency Control*, 42 (4):525–542, 1995.

[100] M.L. Luchi and S. Rizzuti. Boundary elements for three–dimensional elastic crack analysis. *International Journal for Numerical Methods in Engineering*, 24:2253–2271, 1987.

[101] J. E. Luco and R. J. Apsel. On the Green's functions for a layered half-space: Part I. *Bull. Seismol. Soc. Am.*, 73:909–929, 1983.

[102] E. Hinton M. Papadrakakis, Y. Tsompanakis and J. Sienz. Advanced solution methods in topology optimisation and shape sensitivity analysis. *Engineering Computations*, 13(5):57–90, 1996.

[103] A. K. Mal and S. J. Singh. *Deformation of Elastic Solids*. Prentice Hall, New Jersey, 1991.

[104] A. Malcolm and B. Guzina. On the topological sensitivity of transient acoustic fields. *Wave Motion*, 45:821—834, 2008.

[105] V. M. Malhotra and N. J. Carino. *Nondestructive testing of concrete*. CRC Press, 2004.

[106] J. Martínez and J. Domínguez. On the use of quarter-point boundary elements for stress intensity factor computations. *International Journal for Numerical Methods in Engineering*, 20:1941–1950, 1984.

[107] J. M. Martinez-Esnaola. Stress singularity at the junction of three dissimilar materials. *International Journal of Fracture*, 113:133–137, 2002.

[108] A. Martínez-Castro and R. Gallego. Three-dimensional green's function for time-harmonic dynamics in a viscoelastic layer. *International Journal of Solids and Structures*, 44:4541–4558, 2007.

[109] M. Masmoudi, J. Pommier, and B. Samet. The topological asymptotic expansion for the maxwell equations and some applications. *Inverse Problems*, 21:547—-564, 2005.

[110] M. Melkoumian, S. M. Mkhitaryan, and B. B. Lin. Stress-strain state of a cracked elastic wedge under anti-plane deformation with mixed boundary conditions on its faces. *International Journal of Fracture*, 108:291–315, 2001.

[111] S. C. Mellings and M. H. Aliabadi. Flaw identification using the boundary element method. *International Journal for Numerical Methods in Engineering*, 38:399–419, 1995.

[112] R. A. Meric. Differential and integral sensitivity formulations and shape optimization by BEM. *Engineering Analysis with Boundary Elements*, 15:181–188, 1995.

[113] Z. Michaelewicz and D. B. Fogel. *How to Solve It: Modern Heuristics*. Springer, Berlin, 2004.

[114] J. Miklowitz. *The theory of elastic waves and waveguides*. North-Holland, Amsterdam, 1978.

[115] P. Millot, X. Ferriers, J. Pommier, and Mohamed Masmoudi. A new method for solving an inverse scattering problem using topological sensitivity in the context of detection of buried objects with a ground-penetrating radar. In *Proceedings of the European Symposium on numerical methods in electromagnetics*, March 2002.

[116] R. D. Mindlin. Force at a point in the interior of a semi-infinite solid. *Pysics*, 7:195–201, 1936.

[117] R. D. Mindlin. *Waves and vibrations in isotropic, elastic plates.* In Book: *Structural Mechanics,* by Goodier, J. N. and Hoff, N. J. editors. Pergamon Press, New York, 1960.

[118] N. Nishimura and S. Kobayashi. Determination of cracks having arbitrary shapes with the boundary integral equation method. *Engineering Analysis with Boundary Elements*, 15:189–195, 1994.

[119] J. Nocedal and S.J. Wright. *Numerical Optimization*. Springer-Verlag, 2006.

[120] S. S. Pageau and S. B. Biggers. A finite element approach to three–dimensional singular stress states in anysotropic multi–material wedges and junctions. *International Journal of Solids and Structures*, 33(1):33–37, 1996.

[121] S. S. Pageau, P. F. Joseph, and S. B. Biggers. The order of stress singularities for bonded and disbonded three–material junctions. *International Journal of Solids and Structures*, 31(21):2979–2997, 1994.

[122] V. Pagneaux. Revisiting the edge resonance for lamb waves in a semi-infinite plate. *J. Acoust. Soc. Am. 120*, pages 649–656, 2006.

[123] R. Y. S. Pak. Asymmetric wave propagation in a half-space by a method of potentials. *Journal of Applied Mechanics. ASME*, 434:121–126, 1987.

[124] R. Y. S. Pak and B. Guzina. Three-dimensional Green's funcions for a multilayered half-space in displacement potentials. *Journal of Engineerng Mechanics*, 128(4):449–461, 2002.

[125] R. Y. S. Pak and B. B. Guzina. Seismic soil–structure interaction analysis by direct boundary element methods. *International Journal of Solids and Structures*, 36:4743–4766, 1999.

[126] R.Y.S. Pak and F. Ji. Rational mechanics of axial soil–pile interaction. *Journal of Engineering Mechanics, ASCE*, 119(4):813–832, 1993.

[127] R.Y.S. Pak and F. Ji. Mathematical boundary integral equations analysis of an embedded shell under dynamic excitations. *International Journal for Numerial Methods in Engineering*, 37(14):2501–2520, 1994.

[128] G. Pelekanos and V. Sevroglou. Inverse scattering by penetrable objects in two-dimensional elastodynamics. *Journal of Computational Applied Mathematics*, 151:129–140, 2003.

[129] H. Petryk and Z. Mroz. Time derivatives of integrals functionals defined on varying volume and surface domains. *Applied Numerical Mathematics*, 38:694–724, 1986.

[130] G. M. Pharr. Understanding nanoindentation unloading curves. *J. Mater. Res.*, 17:660–2671, 2002.

[131] P. Pintado and F. G. Benítez. Three-dimensional elastodynamics of a plate subjected to concentrated internal loads under uniform motion. *Computers & Structures*, 36:355–368, 1990.

[132] R. E. Plessix, Y. H. de Roeck, and G. Chavent. Localizar. *SIAM J. Sci. Comput.*, 20:1033–1052, 1999.

[133] A.D. Poularikas. *The Transforms and Applications Handbook*. CRC and IEEE Press, 2000.

[134] L. Rayleigh. On the free vibration of an infinite plate of homogeneous isotropic elastic matter. *Proc. London Math. Soc.*, 20 (357):225–234, 1888–1889.

[135] J.J. Rego Silva, H. Power, and L.C. Wrobel. Boundary element xv: Stress analysis. In *Proc. of the International Conference on Boundary Element Methods (BEM XV)*, pages 423–439, Worcester, MA, USA, 1993.

[136] G. Rus and R. Gallego. Optimization algorithms for identification inverse problems with the boundary element method. *Engineering Analysis with Boundary Elements*, 26:315–327, 2002.

[137] G. Rus and R. Gallego. Boundary integral equation for inclusion and cavity shape sensitivity in harmonic elastodynamics. *Engineering Analysis with Boundary Elements*, 25:77–91, 2005.

[138] G. Rus and R. Gallego. Solution of identification inverse problems in elastodynamics using semi-analytical sensitivity computation. *Engineering Analysis with Boundary Elements*, 31, 2007.

[139] L. W. Schmerr. *Fundamentals of ultrasonic nondestructive evaluation — A modeling approach*. Plenum Press, New York, 1998.

[140] A. Schumacher. *Topologieoptimierung von Bauteilstrukturen unter Verwendung von Lochpositionierungskriterien*. PhD thesis, University of Siegen, Germany, 1995.

[141] E. A. G. Shaw. On the resonant vibrations of thick barium titane disks. *J. Acoust. Soc. Am.*, 28:38–50, 1956.

[142] R. E. Sheriff and L. P. Geldart. *Exploration Seismology*. Cambridge University Press, 1995.

[143] J. Sokołowski and A. Żochowski. On topological derivative in shape optimization. Rapport de Recherche 3170, Institute National de Recherche en Informatique et en Automatique, 1997.

[144] J. Sokołowski and A. Żochowski. Topological derivatives for elliptic equations. In *Proc. Inverse Problems, Control and Shape Optimization*, pages 129—-136, April 1998.

[145] N. Somaratna and T. C. T. Ting. Three–dimensional stress singularities in anisotropic materials and composites. *International Journal of Engineering Sciences*, 24(7):1115–1134, 1986.

[146] A.A. Stamos and D.E. Beskos. Dynamic analysis of large 3–D underground structures by the bem. *Earthquake Engineering & Structural Dynamics*, 26(6):917–934, 1995.

[147] G. E. Stavroulakis. *Inverse and crack identification problems in engineering*. Kluwer Academic Publishers, 2001.

[148] G. E. Stavroulakis and H. Antes. Crack detection in elastostatics and elastodynamics. a BEM modelling - neural network approach. In M. Tanaka and G. Dulikravich, editors, *Inverse problems in engineering mechanics*, 1998.

[149] G. E. Stavroulakis and H. Antes. Flaw identification in elastomechanics: BEM simulation with local and genetic optimization. *Structural Optimization*, 16:162–175, 1998.

[150] C. R. Steele and Y. Y. Kim. Modified mixed variational principle and the state–vector equation for elastic bodies and shells of revolution. *J. Theory Appl. Mech.*, 59:587–595, 1992.

[151] F. J. Suárez and R. Gallego. Numerical solution of the variation boundary integral equation for inverse problems. *International Journal for Numerical Methods in Engineering*, 48:111–135, 2000.

[152] M. Tanaka and M. Nakamura. Application of genetic algorithm to plural defects identification. In H. Bui, M. Tanaka, et al., editors, *Inverse problems in Engineering Mechanics*, 1994.

[153] A. Tarantola. *Inverse Problems Theory and Methods for Model Parameter Estimation*. SIAM, Philadelphia, 2005.

[154] P. S. Theocaris. The order of singularity at a multi-wedge material corner of a composite plate. *Int. J. Eng. Sci.*, 12:107–120, 1974.

[155] G. Thierauf. Optimal topologies of structures: homogenization, pseudo-elastic approximation and the bubble method. *Engineering Computations*, 13(1):86–102, 1996.

[156] W. T. Thompson. Transmission of elastic waves through a stratified soil medium. *Journal of Applied Physics*, 21:89–93, 1950.

[157] E. C. Titchmarsh. *Introduction to the theory of Fourier integrals*. Chelsea Publ. Co, New York, 1986.

[158] P. J. Torvik. Reflection of wave trains in semi-infinite plates. *J. Acoust. Soc. Am.*, 41:346–353, 1967.

[159] N. Vasudevan and A. K. Mal. Response of an elastic plate to localized transient sources. *Journal of Applied Mechanics (ASME)*, 52:356–362, 1985.

[160] I. A. Viktorov. *Rayleigh and Lamb Waves*. Plenum Press, New York, 1967.

[161] R. L. Weaver and Y. H. Pao. Axisymmetrix waves excited by a point source in a plate. *Journal of Applied Mechanics (ASME)*, 49:821–836, 1982.

[162] N. Wilkie-Chancelier, H. Duflo, A. Tinel, and J. Duclos. Numerical description of the edge mode at the beveled extremity of a plate. *J. Acousti. Soc. Am.*, 100:92–97, 2005.

[163] M. L. Williams. Stress singularities resulting from various boundary conditions in angular corners of plates in extension. *J. Appl. Mech.*, 74:526–528, 1952.

[164] P. Xu and A. K. Mal. An adaptive integration scheme for irregularly oscillatory functions. *Wave Motion*, 7:235–243, 1985.

[165] H. W. Zhang and W. X. Zhong. Hamiltonian principle based stress singularity analysis near corners of multi–material junctions. *International Journal of Solids and Structures*, 40:493–510, 2003.

[166] W Zhou, K.M. Lim, K.H. Lee, and A. A. O. Tay. A new variable-order singular boundary element for calculating stress intensity factors in three-dimensional elasticity problems. *International Journal of Solids and Structures*, 42:152–189, 2005.